

Hybrid Systems, Iterative Learning Control, and Non-minimum Phase

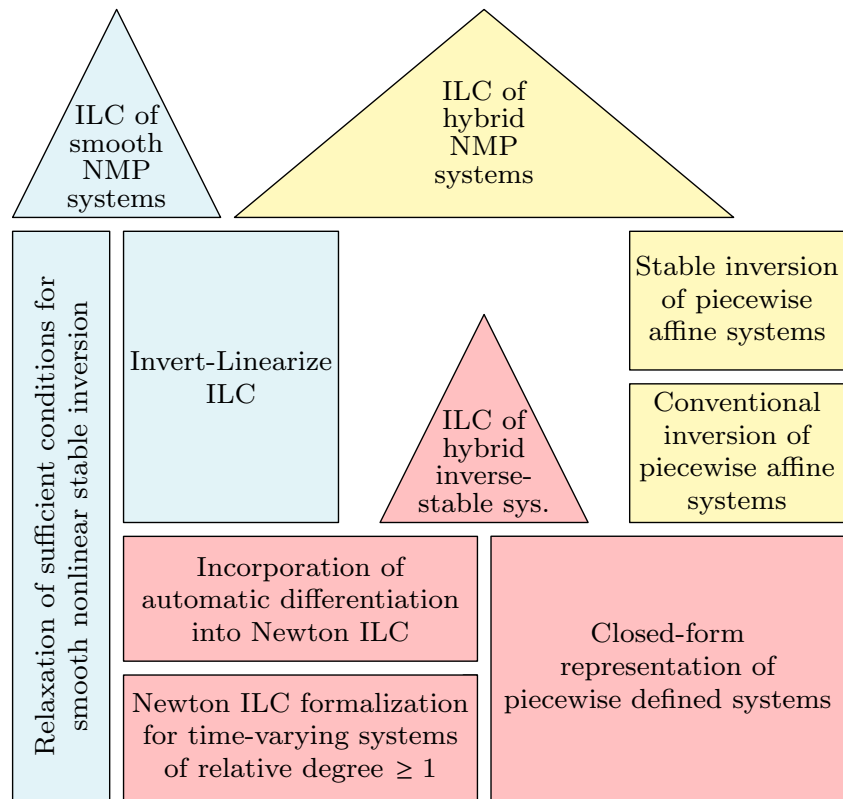
by

Isaac A. Spiegel

A dissertation submitted in partial fulfillment
of the requirements for the degree of
Doctor of Philosophy
(Mechanical Engineering)
in the University of Michigan
2021

Doctoral Committee:

Associate Professor Kira Barton, Chair
Associate Research Scientist Tulga Ersal
Associate Professor Chinedum Okwudire
Associate Professor Necmiye Ozay



□ Fundamental contribution △ Enabled class of control systems

● Ch. 3 ● Ch. 4 ● Ch. 5

Isaac A. Spiegel

ispiegel@umich.edu

ORCID iD: [0000-0002-4415-9190](https://orcid.org/0000-0002-4415-9190)

© Isaac A. Spiegel 2021

To those who value this, and to those who benefit from it.

ACKNOWLEDGMENTS

It is difficult to find the right words for this acknowledgement. There are so many people I want to address in so many different ways.

This dissertation would not have been possible without funding from the University of Michigan Department of Mechanical Engineering, the National Science Foundation, and the National Institute of Standards and Technology. Equally essential are the members of my doctoral committee: Kira Barton, Tulga Ersal, Chinedum Okwudire, and Necmiye Ozay. And I am especially grateful for all the collaborators that have contributed to this research: Kira Barton, Tom Oomen, Nard Strijbosch, Robin de Rozario, Patrick Sammons, and Tom van de Laar.

As I conclude this doctoral program, I have also been reflecting on a bigger picture that sprawls beyond the walls of graduate schools and my time within them. To me, this dissertation has not been 5 years, but rather 13-20 years in the making. Because I see this as the culmination of my life to date, I keep thinking back over my life's full span. There's a lot to be humble about.

I bring this up because over time I've accrued a great list people to whom I'm deeply indebted, but have not repaid and probably cannot repay, and that's a humbling feeling. To thank in words is not enough. These are debts of friendship, time, effort, grace, pain, forgiveness, and love. I wish I could give you all what you are worth or at least give you the feeling deep inside that you are worth more than can be given, and that you are loved in kind. I realize this is a bit dramatic, but what can I do? So much of me has been shaped by you. I'm carried by the gifts you've given me. And I know that you are carried by gifts given to you by others. There are all these gifts begetting gifts, rippling outward. So if it is not within my power to repay you, I hope to at least pay it forward as best I can.

You've made my life special. I will do my best by you, and by those I meet as time goes on.

So here's to those that shaped me, from the beginning:

Lisa Spiegel
David Spiegel
Daniel Spiegel
Breanna Spiegel
Lauren Ruge
Jessica Ruge
Sean Kennedy
Dick Ruge
Marilyn Stamper
Hannah Rosenfeld
Colleen Rosenfeld
Marc Rosenfeld
Ian Rosenfeld
Master Mark W. Pattison,
Sir
Master Danielle Page-Pattison
Kevin Shaw
Dani Gradisher
Lauren Shaw
Anita Hayworth
Dave Shaw
Henry Sweat
Pauline Disch
Alex Sweat
Jola Prosceno
Mark Sweat
Ryan Giza
John McBlair
Master Matt Goodsell
Merl Goodsell
Master Adam Rosenberg
Amanda Rosenberg
Master David Lam
Dan Gehlhaar
Heidi Hill
Michael Eckstein

Dave Lambillotte
Nick Lococo
Erika Shaw,
Honorary High Admiral V
Matthew Eliceiri
Margie Wilhelm
Judy Holland
Linda Rohmund
Jon Rasmussen
Steven Walker
Eric Smith
Tyler Workinger
Christian Workinger
Lynn Light
Sally Ptak
Sydney Spiegel
Ezra Spiegel
Charlene Spiegel
Charles Spiegel
Lily-Jean Ciccotelli
Tony Ciccotelli
Steve Ciccotelli
Fred Ciccotelli
Eleonore Stump
Donald Stump
Nathan Stump
Aaron Stump
Monica Stump
Cathy Noord
Thomas Noord
Mick Noord
Francesca Noord
Jake Bert
Jason Marshal
McKenna Taylor
Andrew Rappolt

Ben Love
Jen Wilson
Matt Golman,
Founder
Asa Puckette,
Co-Founder
Alec Asperslag,
Honorary High Admiral I
Grant Lawrence Thompson,
Honorary Vice Admiral I
Elena Cléménçon-Charles
Megan Gaffney
Andrea Reyes
Ana Reyes
Micael Maya-Peinl
Julian Noble
Natalie Van Valkenberg
Geoff Van Valkenberg
Alex Van Valkenberg
Maria Van Valkenberg
William Van Valkenberg
Max Van Valkenberg
George Stimson
Rie Tsuboi
Darlene Blanchard
Justin Conn
Michael Santos
Tatiana Roy
Suki Berry
Annie Tarabini
Lonnie Safarik
Amy Kuo
Emma Lindley
Ariel Jones,
Honorary High Admiral III
Stan Austin,
Honorary High Admiral IV

Sammy Ness	Megan Bradley	Pol Llado
Savannah Turner	Sean Holcomb	Alex Cuevas
Jaden Pratt	Greg Jackson	Mandy Huo
Mike Shook	Yukina Tanaka	Marc Russel
Blaze Newman	Haruka Nomura	Stephen Rhodes
Ryan Cardenes	Satoru Takagi	Taito Nabeshima
Caroline Pollock	Ali Candlin	Hiroo Yugami
Scott Huntley	Zoë Winkworth	Fumitada Iguchi
Jason Berend	Michael Reza Farzi	Makoto Shimizu
Karen des Jardins	Sydney Lefabvre	Asaka Kohiyama
Stephen des Jardin	Emily Doherty	Kyotaka Konno
Darryl Walton	Michael McCutchen	Hiroaki Kobayashi
Bobbie Walton	Lara Harding	Mari Suzuki
Nick Foote	Alyx Barbeau	Kunihiko Yanagisawa
Kevin Brice	Delani Davis	Hiroki Sato
Willie Saake	Drew Spiller	Kasemchai Chaiprasobphol
Karen Saake	Haley Kovacs	Syo Onodera
Andrew Dalager	Claire Li	Taro Fukushige
Gabe Cemaj	Jessica Resnick	Jun Sakai
Andy Colletta	Adam Resnick	Yuta Fujiwara
Mark Leon	Andy Packard	Yoshikazu Shibata
Dana Pede	Emily Jensen	Ryusuke Mihara
Betty Huang	Oliver O'Reilly	Takahiro Kumagai
Kyla Wilson	James Casey	Shoya Murayama
Victoria Ly	Amando Miller	Shoma Onuki
Olivia Perry	Chris Bulpitt	Daniel Kenji Pederson
Linda Lam	Cynthia Tan	Lea Rossander
Logan Mercer	Danny Wilson	Frej Rossander
Zack Mayeda	Louis Malito	Eivind Rossander
Cassidy Mayeda	Bardia Ganji	Jenny Rossander
Laura O'Hagan	Roshena Macpherson	Tatsuki Momose
Dustin Atlas	John Wallace	Sayaka Ono
Ben Atlas	Ben Chen	Shogo Onishi
Tory Bader	Brian Graf	Nick Gustafson
Evan Wong	Nicole Schauser	Charlie Heckroth
Zyad Hammad	Derek Chou	Lei Lee

Perry Hobbs	Xiao-Yu Fu	Robin Rodríguez
Yuri Hobbs	CJ Linton	Ahmet Mazacioglu
Nick Ong	Meg Brennan	Nils Smit-Anseeuw
Juri Mizuki	Kira Barton	Audrey Sedal
Haruka Ochisai	Alex Shorter	Mario Medina
Meng Han	Efe Balta	Suhak Lee
Robert Baumann	Ilya Kovalenko	Matthew Porter
Gracie Burdeos	Shreyas Kousik	Rachel Vitali
Oskar Södergren	Miguel Saez	Patrick Holmes
Kaori Ohrui	Zheng Wang	Dan Bruder
Marian Lumongsod	Deema Totah	Kim Ingraham
Ryan Thompson	Mike Quann	Misaki Nozawa
Takuya Yashima	Ding Zhang	Hasnaa Rabbat
Mizuki Temma	Delaramm Afkhami	Remy Pelzer
Lauri Pokka	Nazanin Farjam	Nico Mbolamena
Samuli Koivu	Anne Gu	Sherry Lin
Philip Grajetzki	Joaquin Gabaldon	Shuyu Long
Megumi Sugano	Meghna Menon	Tom Oomen
Midori Hirose	Max Wu	Nard Strijbosch
Heraldo Stefanon	Dory Yang	Noud Mooren
Christopher Tacub	Yaqing Xu	Nic Dirx
Amrita Srinivasan	Loubna Baroudi	Robin de Rozario
Ammama	Max Toothman	Lennart Blanken
Tathappa	Mingjie Bi	Enzo Evers
Ganesh Srinivasan	Tyler Toner	Fahim Sakib
Terri Srinivasan	Yassine Qamsane	Camiel Beckers
Gita Srinivasan	Lai-Yu Leo Tse	Robert van der Weijst
Michael Srinivasan	Christopher Pannier	Joey Reinders
Raghu Srinivasan	Berk Altın	Chyannie Amarillio
Lisa Tran	Max Toothman	Rishi Mohan
Melis Şahinöz	Bo Fu	Daniel Veldman
Narayanan Kidambi	Allison White	Frans Verbruggen
Katie McLaughlin	C. David Remy	Tom van de Laar

PREFACE

Technology advances. As it does so, both the complexity of our machines and the performance demands upon them grow. To meet these performance demands, ever more sophisticated automatic control schemes are developed for these machines. Most controllers are designed based on knowledge—i.e. a mathematical model—of a machine’s dynamics, and the performance achievable by such controllers is usually a function of how well the dynamical model represents the true system behavior. The simultaneous increases in system complexity and performance requirements thus clash when the system complexity exceeds the ability of a mathematical modeling framework to capture.

The development of new, more flexible dynamical modeling frameworks (hybrid systems) is a clear response to this problem, one to which the controls engineering community has taken heartily [1, 2, 3]. However, improved model fidelity is only half the battle. There must also be *compatibility* between a controller synthesis method and a model framework. In other words, a second clash occurs when model complexity exceeds the ability of a control framework to utilize.

The main purpose of this dissertation is to bridge the gap between high fidelity modeling and controller synthesis for systems required to perform a task repetitively, such as manufacturing robots producing many copies of the same product. This gap-bridging is done by contributing new mathematical tools to both the theory of modeling and the theory of controller synthesis for repetitive systems (Iterative Learning Control (ILC)).

There are three primary contributions. First is a new mathematical representation of hybrid systems that admits several mathematical operations crucial to ILC synthesis, but that had been undefined for prior hybrid system representations. The second and third contributions deal with the particularly challenging case of dynamical models that have unstable inverses (often called Non-minimum Phase (NMP) models). Because many ILC syntheses use model inversion [4], such NMP models can cause instability of the overall controlled system. To combat this problem for both hybrid and non-hybrid systems, the second contribution is a new ILC framework that enables the incorporation of alternative notions of model inversion with ILC, circumventing the instability problem. Finally, the third contribution is a method for deriving such an alternative, stable inverse specifically for a class of hybrid NMP models. Thus, the three primary contributions culminate in

the ability to perform ILC with hybrid models, even when the models have unstable inverses.

These results address challenges faced by a broad array of systems, from pick-and-place robots to piezoactuators [5, ch. 6], [6, 7]. However, the original impetus for this research is Electrohydrodynamic Jet (e-jet) Printing, which epitomizes the challenges arising from the tandem growth of performance demands and system complexity. E-jet printing, like commonplace inkjet printing, revolves around the ejection of liquid from a nozzle onto a target surface. Unlike inkjet printing, e-jet printing is driven by the delicate interaction of applied electric fields with particles in the liquid meniscus at the nozzle tip. See Figure P.1 for illustration. This gives e-jet the capacity for submicron resolution patterning for printed optics and electronics [8, 9]. But e-jet printers are sensitive machines, and require automatic control to perform reliably. Unfortunately, the ejection process is too small and too fast for online control of the fluid flow *during* ejection to be practical. Thus, the clearest path to control e-jet printing is by analyzing performance *after* each ejection and seeking to improve performance from ejection to ejection, i.e. ILC.

However, the system electrohydrodynamics are complicated enough that no traditional control-oriented modeling effort has been able to capture the complete ejection process's dynamics. Thus began research on the hybrid modeling of e-jet printing and the ILC of hybrid systems, resulting in the first primary contribution. The hybrid e-jet modeling research is provided in this dissertation as an application-focused contribution motivating the theoretical work.

Because the complexity and sensitivity of e-jet printing produces substantial confounding factors, preliminary physical implementation of this new theory was attempted on a comparatively simple inkjet printhead positioning system. The ILC scheme in focus failed to produce stable control. This spurred the research into the ILC failure mechanisms, leading to the discovery of the ILC scheme's fundamental inability to leverage models with unstable inverses, which the printhead positioning system happened to have. The second and third major contributions address this problem.

In other words, this dissertation contributes new broadly applicable control-theoretic tools born from challenges encountered in practice on physical systems.

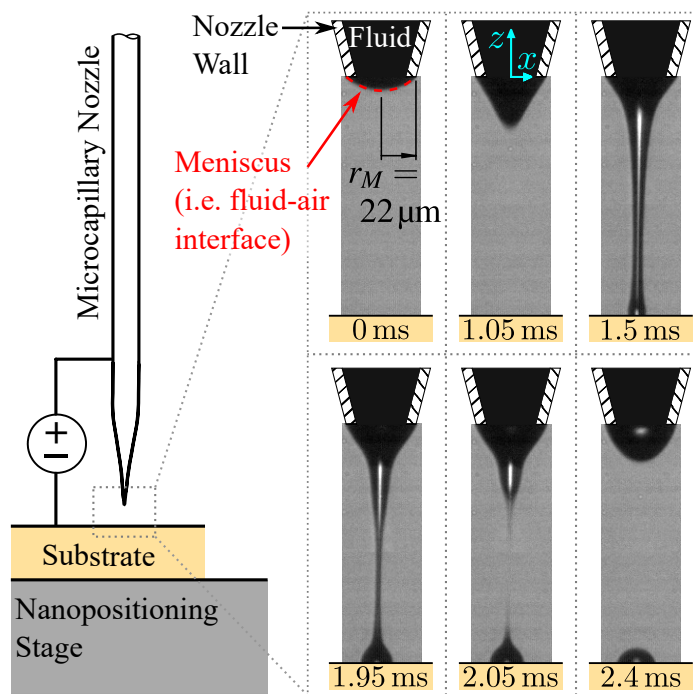
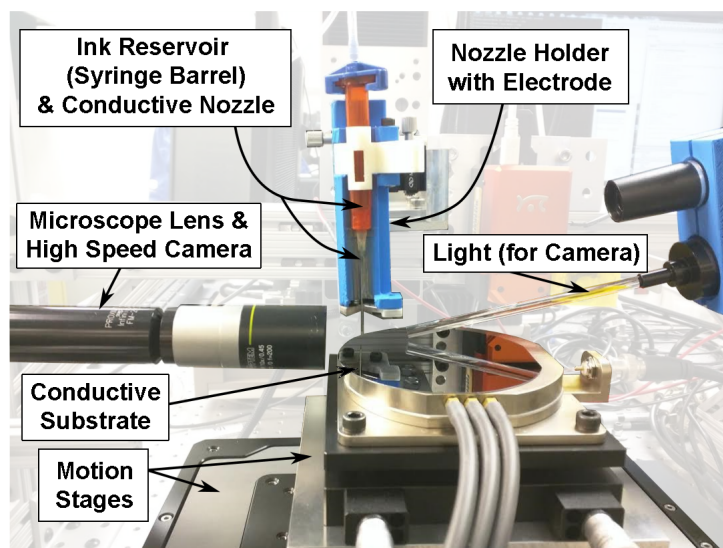


Figure P.1: *Top*: Photograph of the e-jet printer at the University of Michigan. The conductive nozzle and substrate are connected by a high voltage amplifier to apply electric fields to the fluid at the nozzle tip. *Bottom*: Schematic and time lapse photography illustrating the ejection process (with 0 ms set at the beginning of a voltage pulse). The meniscus base radius r_M , determined by the nozzle outer diameter, is $22\ \mu\text{m}$ here, and in general can be as small as $1\ \mu\text{m}$. The speed of the ejection is determined largely by the fluid viscosity, and can be as fast as $10\ \mu\text{s}$ for inviscid fluids such as water. The 2.4 ms process shown here is for a fluid 300 times the viscosity of water, i.e. about the viscosity of castor oil. Further details are given in Chapter 2.

TABLE OF CONTENTS

Dedication	ii
Acknowledgments	iii
Preface	vii
List of Figures	xiii
List of Tables	xviii
List of Abbreviations	xix
Abstract	xx
 Chapter	
1 Introduction	1
1.1 Motivation: E-jet Printing	1
1.2 Aim 1: ILC of Piecewise Defined Systems	2
1.3 Aim 2: Versatile, Fast ILC of NMP Nonlinear Systems	5
1.4 Aim 3: (Stable) Inversion of Piecewise Affine Systems	6
1.5 Contribution Synergy	7
1.6 A Note On Notation	7
2 Repetitive Processes Needing Hybrid Modeling: Electrohydrodynamic Jet Printing Studies	9
2.1 Electrohydrodynamic Jet Printing	12
2.2 First-Principles-Based Modeling	14
2.2.1 Hybrid System Model Framework	14
2.2.2 Experimental Methods	27
2.2.3 Model Validation	30
2.2.4 Physics-Focused Hybrid E-jet Modeling Conclusion	37
2.3 Piecewise Affine Modeling	37
2.3.1 Dynamical Deposited Volume Model	38
2.3.2 Experimental Methods	43
2.3.3 Results & Discussion	47
2.3.4 Piecewise Affine E-jet Modeling Conclusion	50
2.4 Overarching E-jet Printing Conclusion	52

3 Enabling ILC of Hybrid Systems:	
Closed-Form Hybrid System Representation	54
3.1 Closed Form Piecewise Defined Systems	55
3.2 Newton Iterative Learning Control	58
3.3 Validation	62
3.3.1 Model and Software Implementation	62
3.3.2 Methods	64
3.3.3 Results & Discussion	65
3.4 Conclusion	69
4 Nonlinear Systems with Unstable Inverses:	
Invert-Linearize ILC and Stable Inversion	70
4.1 Nonlinear Stable Inversion Background	72
4.2 Novel ILC Analysis and Development	75
4.2.1 Failure for Models with Unstable Inverses	75
4.2.2 Alternative Learning Matrix Synthesis	76
4.3 Novel Stable Inversion Development	77
4.3.1 Fixed-Point Problem Solution	77
4.3.2 Initial Picard Iterate $\tilde{\eta}_{(0)}$ Selection and Implementation	82
4.4 Validation	83
4.4.1 Benchmark Technique: Gradient ILC	84
4.4.2 Example System	84
4.4.3 Simulation and Analysis Methods	87
4.4.4 Results and Discussion	89
4.5 Conclusion	91
5 Hybrid Systems with Unstable Inverses:	
Stable Inversion of Piecewise Affine Systems	93
5.1 System Definition	94
5.2 Conventional PWA System Inversion	96
5.2.1 Unique Exact Inversion For $\mu_g = 0$	96
5.2.2 Non-unique Exact Inversion For $\mu_g \geq 1$	98
5.2.3 Unique Exact Inverses For $\mu_g \in \{1, 2\}$	103
5.3 Stable Inversion of PWA Systems	106
5.3.1 Exact Stable Inversion	106
5.3.2 Practical Considerations	110
5.4 Validation: Application to ILC	112
5.4.1 Example System	112
5.4.2 ILC Schemes	117
5.4.3 Methods	119
5.4.4 Results and Discussion	120
5.5 Conclusion	124

6 Conclusion 125
 6.1 Synthesis of Research Contributions 125
 6.2 Broader Impacts 126
 6.3 Future Directions 128
Appendices 130
Appendix A: Neglect of Inverse Instability by Non-NILC Prior Art 130
Bibliography 132

LIST OF FIGURES

P.1	<p><i>Top</i>: Photograph of the e-jet printer at the University of Michigan. The conductive nozzle and substrate are connected by a high voltage amplifier to apply electric fields to the fluid at the nozzle tip. <i>Bottom</i>: Schematic and time lapse photography illustrating the ejection process (with 0 ms set at the beginning of a voltage pulse). The meniscus base radius r_M, determined by the nozzle outer diameter, is 22 μm here, and in general can be as small as 1 μm. The speed of the ejection is determined largely by the fluid viscosity, and can be as fast as 10 μs for inviscid fluids such as water. The 2.4 ms process shown here is for a fluid 300 times the viscosity of water, i.e. about the viscosity of castor oil. Further details are given in Chapter 2.</p>	ix
1.1	<p>Castle of Control Contributions. Rectangular “building blocks” represent the fundamental control-theoretic contributions. Conical “spires” represent a class of nonlinear, potentially time-varying systems supported by the underlying theoretical contributions. Note that more elevated rectangular building blocks also depend on the building blocks beneath them. For example, theory for the stable inversion of Piecewise Affine (PWA) systems <i>requires</i> theory for the conventional inversion of PWA systems. The validation of the theory in each chapter is executed via control of an example system from the corresponding spire. Practical target applications for each class include (i) piecewise mass-spring-dampers (e.g. ankle-foot orthosis emulation [47, ch. 3-4]), (ii) cart-and-pendulum systems (e.g. bridge and tower cranes [48, 49]), and (iii) micro-positioning systems (See Chapter 5.4).</p>	8
2.1	<p>(<i>Top</i>) Schematic of e-jet printing setup. Dimensions represent signed displacements in the direction of the single-sided arrows with respect to the inertial (x, z) coordinate system. The volumetric flow rate Q, labeled via block arrow, is also a signed quantity, but its sign is with respect to the control volume denoted by the dashed box. (<i>Bottom</i>) Time lapse photography of an ejection with time stamps from the rising edge of a voltage pulse.</p>	13
2.2	<p>Ejection process in terms of the physical phenomena at the liquid-air interface. Distinction is drawn between the process under a constant DC applied voltage, for which ejections begin and end repeatedly under the natural high voltage electrohydrodynamics, and under a single subcritical pulse, which yields a single ejection whose cessation is induced by the falling of the pulse.</p>	15
2.3	<p>Schematic of the system as a hybrid automaton. The transition inequalities are labeled explicitly on the automaton edges for completeness, and are derived in section 2.2.1.3.</p>	17

2.4	To-scale schematic of a critically deformed meniscus and the prolate spheroidal coordinate system (with horizontal axis at $z' = 0$) used to describe the geometry of the meniscus and its local electric field (ellipses) and electric potential contours (hyperbolae). The focus is marked by the white dot at $z' = a$. For $z' < 0$ the field and potential contours are assumed “Cartesian.” Note that by the z -axis sign convention, h -values are negative, and a is positive.	25
2.5	Training error, Err , and standard deviation of Q in the build-up state with respect to $c_{\delta E}$ and c_{r_I} . The color bar across the top of the figure applies to both plots, and gives the logarithmic relationship between pixel brightness and the magnitude of the mean and standard deviation in picoLiters per millisecond ($\frac{pL}{ms}$). The hatched regions represent $(c_{\delta E}, c_{r_I})$ combinations corresponding to <code>Inf</code> error values. The circled point in both images represents the global minimum Err found in this analysis. . . .	31
2.6	Time constants (τ) and DC Gains (G) of Q and h jetting models versus V_h . For comparability between Q and h , τ and G are normalized by their mean value. No correlation is apparent between τ and V_h . However, DC Gain and V_h are clearly correlated.	32
2.7	Complete model error given as the RMSE normalized by the range of measured data within each location. Each bar is computed from 100 measured timeseries averaging 23 points each for build-up, 34 points for Jetting, and 237 points for relaxation. Error bars represent plus/minus one standard deviation.	34
2.8	Plot of the simulation and measured data for h , Q , and the individual pressure components contributing to Q for $T_p = 2$ ms and $V_h = 1150$ V. P_E and P_g are combined because P_g is constant and they are both always positive, meaning that their sum should be balanced against P_γ with the assistance of P_μ	35
2.9	Paraboloidal and hyperboloidal electrode geometry approximations overlaid on nozzle/meniscus photographs at a low voltage equilibrium (left), and at the critical Taylor cone preceding jetting (right). The “underdetermined” hyperboloid is given only at the critical meniscus because the necessary prior information (in this case, the value of ξ) is only known for the critical meniscus (see section 2.2.1.3).	36
2.10	Schematic of the two CVs used in this work superimposed over an illustration of a jet immediately after breaking.	38
2.11	System Architecture. <i>Top</i> : Automaton illustrating the timed switching behavior of the system model and the reset determining the initial contiguity droplet volume. Each automaton location is accompanied by photographs of the first and final samples of the corresponding partial process from a video with $V_h = 1300$ V and $T_p = 1.5$ ms. <i>Bottom</i> : Block diagram illustrating breakdown of a complete input-to-droplet-volume model into a nozzle flow rate model f_Q and a droplet volume model f_{V_d} , both of which are piecewise defined to capture the switching and reset behavior of the automaton. . . .	40
2.12	Measured data from a particular ejection video illustrating the motivation for a proportional Q_d model. <i>Left</i> : Half-outline of fluid body (the jet is roughly symmetric about z -axis) at the onset of contiguity and at the end of the voltage pulse, representing a 7% increase in volume outside the droplet CV. <i>Right</i> : Flow rate time series data during contiguity illustrating roughly proportional signals between Q and Q_d	41

2.13	Depiction of the two CVs described in Section 2.3.1.1, the distinction between the direct and reflection-augmented measurement regions, and the estimated jet break position superposed on the final contiguity frame and first retraction frame for a particular trial ($V_h = 1300$ V, $T_p = 1.5$ ms). Δz is the distance from either fluid body tip to the jet break position.	45
2.14	Retraction-stage droplet volume measurement taken by direct and reflection-augmented measurement techniques. Light and dark points represent raw and filtered data, respectively. As \mathcal{V}_d is expected to be constant during retraction, this plot illustrates the reflection-augmented technique’s superiority in that it maintains a roughly constant value of 5.3 pL after the transient (i.e. for $t \geq 2.5$ ms), while the direct measurement steadily decreases until about $t = 9$ ms.	48
2.15	Percent error in final deposited droplet volume, $\mathcal{V}_d(t_r)$, using measured and simulated Q . The lowest voltage experiment exceeds 100% error in both cases. Each bar represents the mean value of $N = 10$ samples. Measured Q results illustrate the high quality of equation (2.54) for all but the lowest voltage case. Simulated Q results illustrate increased error associated with increased uncertainty in the cascaded model, motivating future flow rate modeling work.	49
2.16	Time series plots of droplet volume \mathcal{V}_d for a representative experiment and the experiment of lowest high voltage V_h . Plotted measured data is the mean of the validation data ($N = 10$ samples for each time series) with an envelope of plus or minus the standard deviation. The data suggests that the reset is the main source of error in low V_h experiments.	50
2.17	Jet break positions of each experiment’s validation data against high voltage. The nozzle outlet is located at $0 \mu\text{m}$ and the substrate at $-150 \mu\text{m}$. $N = 10$ samples for all high voltages except $V_h = 1300$ V, for which $N = 40$ samples because four pulse widths are tested at $V_h = 1300$ V. The modest spread of data points at $V_h = 1300$ V suggests that high voltage (equivalent to the difference between high and low voltage in this data set) has a greater influence on jet break position than pulse width in the subcritical jetting regime.	51
2.18	Mean unsigned percent error and standard deviation (given by error bars) of final droplet volume over all validation trials except those of lowest high voltage ($N = 110$ samples).	51
3.1	Block diagram of the closed-form Piecewise Defined (PWD) system representation . . .	57
3.2	An \mathbb{R}^2 topology representable by (3.6) with 14 hyperplanes (dashed lines) having 1 convex (a) and 2 nonconvex (b and c) dynamic regimes.	59
3.3	Mass-spring-damper system used for validation. The spring stiffness is a piecewise defined function of the spring extension and the applied force is a nonlinear function of actuator voltage u	63
3.4	<i>Above:</i> Histogram of final-trial NRMSE for all experiments. All but the highest error bin are defined by a 0.005 range of NRMSE. <i>Middle:</i> Average trajectory of NRMSE vs. Trial number for all completely convergent simulations. <i>Bottom:</i> Same on a logarithmic scale, for perspective.	67
3.5	Timeseries evolution over multiple trials for a simulation with $\ e_\theta\ _2 = 0.27$. This simulation took 8 trials to completely converge.	68

3.6	Percentage of experiments that converge for each 0.05 range of relative model error from 0 to 1. The dashed line is a least squares model of the decay in the probability of convergence as model error increases.	68
4.1	Cart and pendulum system. Dimension, position, and mass annotations are in grey. Force and torque annotations are in black.	85
4.2	Reference	87
4.3	System Block Diagram. The control law outputting u is synthesized from the control models defined by the behatted parameters of Table 4.1 and by $\omega_c(k) = \omega_y(k) = 0$. The plant and controller gain blocks are defined with the truth model parameters generated according to Section 4.4.3. Inter-trial signals from trial ℓ are stored and used to compute the input for trial $\ell + 1$	88
4.4	Representative input solution trajectories from low- and high-model-error ILILC simulations compared with the solution to the zero-model-error problem. The zero-model-error solution is the input trajectory that would be chosen for feedforward control in the absence of learning, and differs notably from both minimum-error trajectories found by ILILC with stable inversion.	90
4.5	<i>Top:</i> Histogram giving the percentage of simulations converged in each bin of the model error metric $\ e_\theta\ _2$. <i>Bottom:</i> Mean value of NRMSE for each ILC trial over all simulations that are convergent for both gradient ILC and ILILC with stable inversion. This illustrates that for comparable robustness to model error, ILILC converges substantially faster than gradient ILC.	91
5.1	Photo of desktop inkjet printer with the case removed. The motor actuates the print-head motion along a guide rail via a timing belt, and the motion is measured by a linear optical encoder with resolution of $50\ \mu\text{m}$ (about 600 dots per inch).	113
5.2	System block diagram. The plant block uses the truth model of the printer system obtained by experimental system identification while the ILC law is synthesized using the control model. The downsample and upsample blocks account for the difference in sample period between the ILC law and the truth model.	113
5.3	Bode plot of the experimental plant data, truth model of the plant, and control model of the plant.	114
5.4	Reference. The reference is 1999 samples long for the truth model, and is downsampled to 1000 samples for the control model.	117
5.5	NRMSE of each ILC trial, illustrating convergence of ILILC to a plateau determined by the noise injected to the system, and dramatically surpassing the convergence speed of both benchmark ILC techniques. The NRMSE of the learning-free stable inversion simulation is also pictured. It is 4% smaller than the feedback-only simulation (ILILC trial 0), but is much larger than the performance achievable with learning. Because the noise injected in this chapter is of the same distribution and injection location as the noise in Chapter 4, the same convergence threshold can be used to approximate the minimum NRMSE achievable by ILILC.	121

5.6 Error (top) and Input (bottom) time series data for the feedback-only simulation, learning-free stable inversion simulation, and the final trial of the ILILC simulation. Both stable inversion and ILILC perform as expected, but due to model error learning is required to reap the full benefit of feedforward control. 122

5.7 Error (top) and Input (bottom) time series data for the three ILC simulations. Even the worst-performing ILC technique—P-type ILC—yields a reduction in maximum error magnitude when compared to the learning-free techniques of Figure 5.6, but Invert-Linearize Iterative Learning Control (ILILC) clearly yields the lowest-error performance. This superiority is in spite of ILILC acquiring more high frequency content via learning than the other ILC schemes, which appear less noisy but appear to contain higher amplitude, lower frequency oscillations that degrade performance. 123

6.1 Castle of Control Contributions, revisited for visualization of this dissertation’s potential broader impacts. These may take the form of other new classes of control systems leveraging the theoretical contributions presented here. 127

A.1 NRMSE versus trial number of past works’ ILC schemes (A.2) applied with learning gain (A.4) to the system (A.3). These NRMSEs monotonically increase, confirming the inability of the past work on ILC with discrete-time nonlinear systems to account for unstable inverses. The NRMSE trajectory yielded by the stable-inversion-supported ILILC scheme proposed by this article is also displayed. The convergence of this ILC scheme when applied to (A.3) reiterates its ability to control such non-minimum phase systems. 131

LIST OF TABLES

2.1	Experimental Setup and Process Parameters	28
2.2	The set Ω of $\omega = (T_p, V_h)$ pairs	28
2.3	p-values and correlation coefficients for LTI Metrics vs. V_h^2	33
2.4	Transition Timing Error Mean (e_μ) & Standard Deviation (e_σ)	33
2.5	Experimental High Voltage and Pulse Width Pairs	44
4.1	Cart-Pendulum Control Model Parameters	88
4.2	Transient Convergence Rates for ILILC and Gradient ILC	91
5.1	Simulation Model Parameters	116
5.2	NRMSE and Peak Error Magnitude of Truth Model Simulations	121

LIST OF ABBREVIATIONS

AM Additive Manufacturing

μ -AM Microscale Additive Manufacturing

CV Control Volume

DoD Drop on Demand

e-jet Electrohydrodynamic Jet

FDM Fused Deposition Modeling

ILC Iterative Learning Control

ILILC Invert-Linearize Iterative Learning Control

LTI Linear Time Invariant

MLD Mixed Logical Dynamical

MPC Model Predictive Control

NILC Newton Iterative Learning Control

NMP Non-minimum Phase

ODE Ordinary Difference/Differential Equation

PWA Piecewise Affine

PWD Piecewise Defined

ZPETC Zero Phase Error Tracking Control

ABSTRACT

Hybrid systems have steadily grown in popularity over the last few decades because they ease the task of modeling complicated nonlinear systems. Legged locomotion, robotic manipulation, and additive manufacturing are representative examples of systems benefiting from hybrid modeling. They are also prime examples of repetitive processes; gait cycles in walking, product assembly tasks in robotic manipulation, and material deposition in additive manufacturing. Thus, they would also benefit substantially from Iterative Learning Control (ILC), a class of feedforward controllers for repetitive systems that achieve high performance in output reference tracking by learning from the errors of past process cycles. However, the literature is bereft of ILC syntheses from hybrid models. The main thrust of this dissertation is to provide a broadly applicable theory of ILC for deterministic, discrete-time hybrid systems, i.e. piecewise defined (PWD) systems.

A type of ILC called Newton ILC (NILC) serves as the foundation for this mission due to its admittance of an unusually broad range of nonlinearities. Preventing the synthesis of NILC from hybrid models is the fact that contemporary hybrid modeling frameworks do not admit closed-form function composition of a single state transition formula capturing the complete hybrid system dynamics. This dissertation offers a new, closed-form PWD modeling framework to solve this problem.

However, NILC itself is not without flaw. This dissertation's research reveals that it generally fails to converge when synthesized from models with unstable inverses (i.e. non-minimum phase (NMP) models), a class that includes flexible-link robotic manipulators. Thus, to fulfill the goal of providing the most broadly applicable control theory possible, improvement to NILC must be

made to avoid the operation that causes divergence when applied to NMP systems (a particular matrix inversion).

Stable inversion—a technique for generating stable state trajectories from unstable systems by decoupling their stable and unstable modes—is identified as a valuable tool in this endeavor. This concept is well-explored for linear time invariant systems, but stable inversion for hybrid systems has not been explored by the prior art. Thus, to focus the research, this dissertation specifically examines piecewise affine (PWA) systems (a subset of PWD systems) for the study of NMP hybrid system control. For PWA systems (and their PWD superset), in addition to a lack of stable inversion, a general, closed-form solution to the conventional inversion problem is also absent from the literature. Having a closed-form conventional inverse model is a prerequisite for stable inversion, but inversion of PWA models is nontrivial because the uniqueness of PWA system inverses is not guaranteed as it is for ordinary affine systems. Therefore, to achieve the first ILC of a hybrid system with an unstable inverse, theory for both conventional inversion and stable inversion must be delivered for PWA systems.

In summary, the three main gaps addressed by this dissertation are (1) the lack of compatibility between existing hybrid modeling frameworks and ILC synthesis techniques, (2) the failure of NILC for NMP systems, and (3) the lack of inversion and stable inversion theory for PWA systems. These issues are addressed by (1) developing a closed-form representation for PWD systems, (2) developing a new ILC framework informed by NILC but free of matrix inversion, and (3) deriving conventional and stable model inversion theories for PWA systems.

CHAPTER 1

Introduction

1.1 Motivation: E-jet Printing

The main contributions to hybrid systems and control theory are presented in Chapters 3-5. These chapters validate their theoretical contributions with simulations on a diverse set of example systems derived from mechanics principles or data collected from physical systems. Additionally, the simulations feature numerous types of model errors in order to stress test the proposed controllers. However, it is desirable to further ground theoretical controls research in the needs of application-based research. To this end Chapter 2 presents Electrohydrodynamic Jet (e-jet) printing in detail, specifically the first efforts to create end-to-end Ordinary Difference/Differential Equation (ODE)-based models of the fluid flow from the nozzle to the substrate over the course of an ejection.

Two models are derived. The first is focused on extending physics-based nonlinear modeling as much as possible to achieve an end-to-end dynamical model of the flow rate of fluid through the nozzle outlet. The second is focused on capturing the volume of fluid actually deposited on the substrate. Additionally, the second model seeks to accomplish this while limiting the system nonlinearities to a Piecewise Affine (PWA) definition of the dynamics.

As explained thoroughly in the chapter, this modeling research is a direct response to the future desire to achieve high performance control of deposited droplet volume. In this endeavor, automatic control is required due to the high uncertainty in system behavior, and Iterative Learning Control (ILC) is the clearest choice because physical sensing limitations preclude real-time feedback control. The desire for ILC motivates the desire for an ODE-based model for controller synthesis. As demonstrated in Chapter 2.2, hybridness is ultimately necessary to capture the end-to-end process dynamics. This is in spite of contributing substantial improvements to the physics-based smooth nonlinear electrohydrodynamics model, resulting in a five-fold increase to the range of well-modeled meniscus deformation. Thus, in addition to raw scientific contributions to e-jet modeling, Chapter 2 concretely establishes the need for a theory merging ILC and hybrid systems.

Note however, that this dissertation does not contain a physical implementation of the de-

veloped ILC theory on an e-jet printer. This is because the main objective here is to deliver a foundational theory of ILC for hybrid systems, and e-jet printing presents additional challenges to ILC beyond model hybridness. These challenges are explained in the description of future work, Section 6.3. For a foundational ILC theory such issues were deemed less critical than the treatment of the Non-minimum Phase (NMP) behavior described later in this chapter, which fundamentally impacts the stability of ILC for many systems. In other words, while e-jet printing is representative of systems requiring iterative learning for control and requiring hybridness for end-to-end ODE-based modeling, more e-jet-printing-specific research is necessary before safe and effective automatic control is achievable.

1.2 Aim 1: ILC of Piecewise Defined Systems

Concretely defined, ILC is the process of learning an optimal feedforward control input over multiple trials of a repetitive process based on feedback measurements from previous trials. ILC is used when typical real-time-feedback and/or feedforward control techniques yield too much output tracking error (as determined by case-specific criteria) because of their reactive nature or model error, respectively. Notable past applications include robot-assisted stroke rehabilitation [10], high speed train control [11], and laser additive manufacturing [12], all of which use nonlinear models. In fact, while the majority of ILC literature focuses on linear systems, the prevalence of nonlinear dynamics in real-world systems has motivated the development of numerous ILC syntheses from discrete-time nonlinear models [13, 14, 15, 16].

Nonlinear modeling can be extremely challenging. Chapter 2 illustrates that there are repetitive systems for which even extensive traditional (i.e. continuous) nonlinear modeling is insufficient for capturing a process’s full dynamics. Hybrid system modeling offers a more flexible formal modeling framework.

The term “hybrid systems” encompasses a wide variety of modeling frameworks that are composed of a set of traditional dynamical models—e.g. systems of ODEs—and a set of rules regarding switching between which of these “component” models is governing the system state evolution at a particular point in time [2]. The set of switching rules can usually be interpreted as a discrete event system [3, 1]. Each discrete state, or “location,” is associated with one of the component dynamical models. The transitioning between locations is conditioned on the dynamical states and control inputs. This dissertation specifically considers deterministic hybrid systems, in which satisfaction of any transition condition enforces a location switch at the moment in time the condition is satisfied. This is in opposition to frameworks based on transition guard conditions and location invariant conditions, which may *allow* a transition if satisfied, but do not typically *enforce* switching. Deterministic switching behavior (and state resets) can in general be captured by piece-

wise definition of a state space system via augmentation of the state dimension [17]. Thus, most deterministic hybrid system frameworks are a subset of Piecewise Defined (PWD) systems [2].

In the past couple decades, hybrid systems have become broadly popular because their ability to stitch simple dynamical systems together to produce complicated state trajectories has greatly eased the task of modeling many physical systems. Examples include cyber-physical systems in general [1], automobile driver behavior [18], power systems [19], legged locomotion [20], conveyor systems [21], and additive manufacturing [22].

Clearly, there is overlap between repetitive systems and systems well-modeled as hybrid systems: gait cycles in legged locomotion are repetitive, as are many manufacturing processes. In fact, of myriad robotics-related uses, manufacturing is one of the primary fields in which ILC is applied [4]. However, the combination of ILC and hybrid modeling is absent from the literature. This is the main gap of Chapter 3.

The first step to achieving ILC of PWD systems is to choose a particular ILC scheme to build off of. However, literature on the ILC of nonlinear systems can trend towards hyper-specialization with respect to the system model, making it more restrictive than desired. Even amongst the more general literature such as [13, 14, 15, 16, 23] mentioned above, nearly all published ILC theory for discrete-time nonlinear systems feature at least one of the following model restrictions

(R1) relative degree of either 0 or 1 [14, 15],

(R2) affineness in the input [13, 14, 15, 23],

(R3) time-invariance [13, 16], and

(R4) smoothness of the state transition formula and output functions (Lipschitz continuity at the most relaxed) [13, 14, 15, 16, 23].

This is problematic because many practical systems violate these constraints. (R1) may be violated in the position control of myriad systems including piezoactuators [24], motors [25], robotic manipulators [26], and vehicles [27]. (R2) may be violated by piezoactuators [24], electric power converters [28], wind energy systems [29], magnetic levitation systems [30], e-jet printing (Chapter 2.2) and flexible-link manipulators [26]. (R3) may be violated by any feedforward-input-to-output model of systems using both feedforward and feedback control, as is often done for robotic manipulation [31]. Finally, and of primary concern here, (R4) may be violated by gain switching feedback control systems (e.g. for motor control [32]), power converters [28], legged locomotion [33], e-jet printing (Chapter 2), and robotic manipulation [6]. The fact that many of these example systems violate multiple restrictions illustrates that it can be challenging to find a model-based ILC synthesis scheme appropriate for many real-world applications. Indeed, flexible-link manipulators violate all four, and they are relevant to the fast and cost-effective automation of pick-and-place

and assembly tasks as well as to the control of large structures such as cranes [5, ch. 6]. Such application spaces would benefit from having a versatile ILC scheme free from (R1)-(R4).

Additionally, while ILC seeks to converge to a satisfactorily low error, this learning is not immediate, and trials executed before the satisfactory error threshold is passed may be seen as costly failures from the perspective of the process specification. It is thus desirable to develop ILC schemes that converge as quickly as possible.

There is one published ILC scheme that meets the need for versatility and speed: the application of Newton's root finding algorithm to a complete finite error time series (as opposed to individual points in time). This technique was first proposed in [34], and is called Newton Iterative Learning Control (NILC) here. NILC's synthesis procedure and convergence analysis are unusually broad in that they are free of (R1)-(R4) [34]. Additionally, Newton's method has been shown to deliver faster convergence in ILC than more basic schemes such as P-type ILC [35, ch. 5].

However, while the convergence conditions of NILC do not preclude their application to hybrid systems, the synthesis of NILC requires a closed-form lifted system model. This lifted model is a vector-input-vector-output function taking in the control input time series and outputting the system output time series. To construct this model from state space systems requires function composition and differentiation of a single closed-form state transition formula capturing the model's entire dynamics. Existing hybrid system formalisms rarely possess such monolithic state transition formulas, and the ones that do cannot explicitly nest calls to them via function composition (further details on this point are given in the introduction to Chapter 3). Thus the approach to addressing the first main gap, i.e. the first main contribution, is the development of a closed-form state space representation of PWD systems. This enables ILC of a large swath of hybrid systems.

To support this main contribution, Chapter 3 also delivers two ancillary contributions related to the implementation of NILC. The original NILC literature [34] assumes an appropriate lifted model is given. Synthesis of this model from state-space systems requires careful handling of the system relative degree, which has been neglected in subsequent works leveraging NILC, such as [36]. Neither have time-varying nonlinear system dynamics been considered in the lifted system derivation. Thus, the first ancillary contribution is an explicit formalization of NILC for time-varying nonlinear systems of any relative degree ≥ 1 . Additionally, the differentiation in Newton's method has been challenging for past authors due to computational cost. The second ancillary contribution is the incorporation of automatic differentiation (see [37, 38]) into NILC implementation, dramatically reducing this cost.

1.3 Aim 2: Versatile, Fast ILC of NMP Nonlinear Systems

NILC has one of the least restrictive sets of sufficient conditions for convergence published in the prior art. However, Chapter 4 reveals that when synthesized from models with unstable inverses¹, NILC typically generates control signals that diverge to enormous magnitudes. In other words NILC is not compatible with these models, which are often called NMP models. This is problematic because a number of important physical systems are well represented by NMP models. Examples include piezoactuators [7], electric power converters [28], wind energy systems [29], DC motor and tachometer assemblies [39], and flexible-link manipulators [26]. Thus, incompatibility of NILC and NMP models is the main gap of Chapter 4.

Note that the full original definition of NMP refers to the property of a frequency response function having the minimum possible phase change from $\omega = 0$ to $\omega \rightarrow \infty$ for a given magnitude trajectory. For Linear Time Invariant (LTI) systems this is achieved if and only if the system and its inverse are causal and stable. In other words, strictly proper systems cannot be minimum phase regardless of the stability of their inverses. However, because the lack of causality is rarely an obstacle in feedforward control when the entire reference is known in advance, NMP is often used as jargon for inverse instability (equivalently, as an abbreviation for “non-minimum phase *zero dynamics*”) in the feedforward control community, and thus in this dissertation as well.

For linear models with unstable inverses, a common way to obtain feedforward control signals is to systematically synthesize approximate dynamical models with stable inverses by individually changing the model zeros and poles, e.g. Zero Phase Error Tracking Control (ZPETC) [40]. However, it is difficult to prescribe analogous systematic approximation methods for nonlinear models because the poles and zeros do not necessarily manifest as distinct binomial factors that can be individually inverted or modified in the system transfer function.

An alternative is to harness the fact that a scalar difference equation that is unstable when evolved forward in time from an initial condition is stable if evolved backwards in time from a terminal condition. If the stable and unstable modes of a system are decoupled and evolved in opposite directions, a stable total trajectory can be obtained. This process is called stable inversion. For linear systems on a bi-infinite timeline, with boundary conditions at time $\pm\infty$, stable inversion gives an exact solution to the output tracking problem posed by the unstable inverse model. In practice on a finite timeline, a high-fidelity approximation is obtained by ensuring the reference is designed with sufficient room for pre- and post-actuation, i.e. with a “flat” beginning and end. Additionally, unlike ILC, stable inversion alone cannot account for model error. To address this, [41] details stable inversion and presents an ILC scheme for linear systems that incorporates a

¹More specifically: models for which the inverse’s linearization about the input trajectory is unstable. See Section 4.2.1 for details.

process similar to stable inversion.

The main contribution of Chapter 4 is to fill the gap of NILC's failure for NMP systems by developing a new nonlinear systems ILC framework, Invert-Linearize Iterative Learning Control (ILILC), which has the ability to incorporate stable inversion into the controller synthesis. ILILC also retains NILC's advantages in speed and broad applicability because it preserves the fundamental learning structure on which the NILC convergence analysis is founded.

Because stable inversion for hybrid systems does not appear in the prior art, Chapter 4 focuses on smooth nonlinear systems. Consequently, a supporting contribution is made to the theory of smooth nonlinear discrete-time stable inversion to expand its domain of applicability to include representations of systems under both feedback and feedforward control. Specifically, a relaxed set of sufficient conditions is proven for the convergence of the stable inversion procedure.

1.4 Aim 3: (Stable) Inversion of Piecewise Affine Systems

The aforementioned lack of stable inversion theory for Hybrid systems provides an obvious final gap that must be filled to achieve the first ILC of a hybrid system with unstable inverse dynamics. However, such a gap statement belies the fact that there is no published general solution to the conventional inversion of PWD systems, let alone stable inversion. To focus the research on solving both the inversion and stable inversion problems for a class of hybrid system, Chapter 5 considers a subset of PWD systems called PWA systems.

PWA systems are simply PWD systems with the component dynamics restricted to affine models. Examples include current transformers [42], one-sided spring supports [43], gain switching [32], and e-jet printing (Chapter 2.3). As with hybrid systems in general, the mathematical rigor provided by the PWA framework facilitates analysis and control theory development for these systems. Examples include stabilizing state feedback control [44] and model reference adaptive control [45].

To date, such research has focused primarily on feedback control. Feedforward control has not been thoroughly addressed in the PWA literature. In addition to preventing the control of systems with specific needs for feedforward control, this gap inhibits the implementation of existing feedback control theory that requires feedforward control components. Indeed, [46] presents a solution to the output reference tracking problem for a class of PWA systems using both feedback and feedforward control elements, but does not present a method to compute the feedforward signal. The validation is instead limited to a master-slave synchronization example in which the feedforward input to the master system is known in advance.

In other words, while Chapter 5's contributions of rigorous theory for the inversion and stable inversion of PWA systems do yield the first ILC of an NMP hybrid system, they also have broader

ramifications for the control of PWA systems.

1.5 Contribution Synergy

One can see that the control-theoretic contributions of Aims 1-3 are not wholly independent of one another. Instead, they build off one another and share responsibility for enabling the ILC of different classes of systems. Figure 1.1 gives a graphical representation of this synergy by treating the fundamental contributions as building blocks that work together to hold up both each other and the specific classes of systems for which they enable control.

1.6 A Note On Notation

Chapter 2 prioritizes the modeling of e-jet printing, while Chapters 3-5 prioritize hybrid systems and ILC theory. Thus, other than the most basic conventions, effort to unify the notation between these two sections has been limited. Overloaded symbol definitions occur, but are highly distinguished by context. For example Q is used to indicate volumetric flow rate in Chapter 2 and a set of subspaces of the real vector space \mathbb{R}^n in Chapters 3-5.

Within Chapters 3-5 notation is unified with one exception. Chapters 3-4 represent the time argument in functions of discrete time as $x(k)$, with k as the time step index. Chapter 5 uses the subscript notation x_k . This is done to compact a number of otherwise very long expressions.

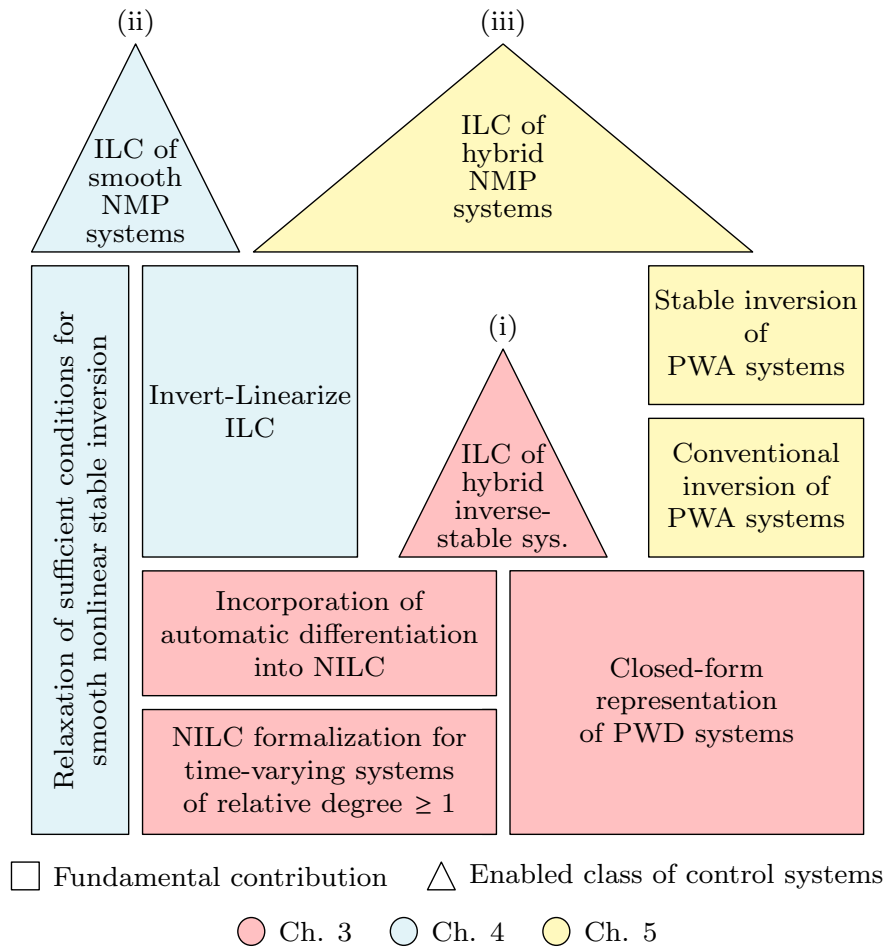


Figure 1.1: Castle of Control Contributions. Rectangular “building blocks” represent the fundamental control-theoretic contributions. Conical “spires” represent a class of nonlinear, potentially time-varying systems supported by the underlying theoretical contributions. Note that more elevated rectangular building blocks also depend on the building blocks beneath them. For example, theory for the stable inversion of PWA systems *requires* theory for the conventional inversion of PWA systems. The validation of the theory in each chapter is executed via control of an example system from the corresponding spire. Practical target applications for each class include (i) piecewise mass-spring-dampers (e.g. ankle-foot orthosis emulation [47, ch. 3-4]), (ii) cart-and-pendulum systems (e.g. bridge and tower cranes [48, 49]), and (iii) micro-positioning systems (See Chapter 5.4).

CHAPTER 2

Repetitive Processes Needing Hybrid Modeling: Electrohydrodynamic Jet Printing Studies

Additive Manufacturing (AM) is a growing class of processes that fabricate components in a layer-by-layer fashion. However, several obstacles inhibit the widespread adoption of AM. Chief among these is the lack of appropriate process descriptions for both implementing satisfactory process planners and integrating process feedback control to enable repeatable, accurate part fabrication. A major reason for this is that many AM processes are governed by complex physical phenomena, e.g. the melting, heat transfer and solidification processes in Laser Engineered Net Shaping (LENS) and Selective Laser Melting (SLM) [50], and the jetting and binder-burnout processes in Binder Jetting [51], resulting in strongly nonlinear mappings between process inputs and process outputs. Because of these nonlinearities, models that may be useful for control design are only applicable in small regions of the operating space, accounting for only short periods within the total process. Therefore, in order to enable control that addresses AM processes in a holistic manner, there is a need to develop models that are capable of describing the complex, interconnected, physical phenomena of AM processes.

One important subdivision of AM that has attracted significant attention is Microscale Additive Manufacturing (μ -AM). μ -AM comprises a number of processes characterized by their ability to produce feature sizes on the order of 100 nm to 100 μ m. Processes typically classed as μ -AM include ink jet [52] and other direct-write technologies such as dip-pen nanolithography [53], and stereolithography [54]. Applications for these processes include patterning, printed

Content of this chapter also published as:

I. A. Spiegel, P. Sammons and K. Barton, "Hybrid Modeling of Electrohydrodynamic Jet Printing," in *IEEE Transactions on Control Systems Technology*, vol. 28, no. 6, pp. 2322-2335, Nov. 2020, <https://doi.org/10.1109/TCST.2019.2939963> ©IEEE 2020. Reprinted with permission.

I. A. Spiegel, T. van de Laar, T. Oomen and K. Barton, "A Control-Oriented Dynamical Model of Deposited Droplet Volume in Electrohydrodynamic Jet Printing," in *Proceedings of the ASME 2020 Dynamic Systems and Control Conference*. Virtual: ASME, 2020. <https://doi.org/10.1115/DSCC2020-3238> ©ASME 2020. Reprinted with permission.

electronic components, and biological and pharmaceutical devices. For such applications, μ -AM offers potential advantages in operating cost, speed, waste reduction, buildable geometries, and integration of fabricated components with larger systems compared to more traditional fabrication techniques involving lithography, spin-coating, or gas deposition [55, 56, 57]. However, many μ -AM technologies suffer from having coarser resolutions and smaller portfolios of usable materials than traditional technologies.

Electrohydrodynamic jet (e-jet) printing is a relatively nascent μ -AM technology that seeks to overcome both of these challenges, and already has proven applications in printed electronics such as thin film transistors [56] and resistive sensors [57], and in biotechnology such as patterned cell cultures [58]. In e-jet printing, a microcapillary nozzle filled with a polarizable ink is suspended above a flat substrate and an electric potential is applied between the two. The resultant electric field induces a stress in the liquid surface. When this stress reaches a critical value, a thin jet of ink issues from the liquid surface towards the substrate. Once a 2D pattern of liquid has been deposited on the substrate, a process such as sintering or curing solidifies the liquid. More liquid can then be deposited atop the previously solidified liquid to build 3D structures [59].

Unlike back-pressure-driven processes such as inkjet and aerosol jet printing, the physical phenomenon driving jetting in e-jet printing is localized to the fluid surface. Consequently, e-jet can print liquids with viscosities multiple orders of magnitude greater than inkjet printing's max viscosity [60], allowing the use of new polymers and metallic nanoparticle solutions with higher concentrations of the active ingredient. Also due to the surface-localization of the electrohydrodynamics, while inkjet droplets pinch off the meniscus near the nozzle tip and thus have diameters approximately equal to that of the nozzle, electrohydrodynamic jets thin considerably as they extend to strike the substrate. This enables submicron line widths and gap sizes compared to inkjet printing's $\sim 10\ \mu\text{m}$ minimum [61].

Reliably fulfilling the potential for submicron resolution requires closed-loop control for the rejection of disturbances introduced by variations in nozzle shape, fluid properties, and environmental factors like temperature and humidity [62]. However, the computer-vision-based measurement process, [22], is too slow compared to the jetting process for traditional real-time feedback control to be practical. Thus, recent research has focused on closing the loop in the iteration domain rather than the time domain. Specifically, this research uses measurements from previous trials of an e-jet printing task in conjunction with dynamical models of nominal system behavior to inform the feedforward control input signal for the subsequent trial [63, 64, 65], a technique known as iterative learning control (ILC).

Thus far, this research has been limited to using models of droplet spreading over a substrate to determine the droplet volume necessary for achieving a desired final print topography. It has not used knowledge of the dynamics between the applied voltage signal and the volume of fluid ulti-

mately ejected from the nozzle, instead assuming perfectly known static relationships. Dynamical models relating applied voltage to fluid flow could be used to decouple the problems of learning the correct volume to deposit and learning the applied voltage signal necessary to achieve that volume, potentially decreasing the number of trials required to achieve satisfactory performance.

For a model to be compatible with ILC it must be founded on ordinary differential or difference equations (ODEs), but the majority of current modeling efforts for e-jet printing can be broadly classified as either partial-differential-equation-driven finite element/volume methods or static scaling laws. In the former category, a significant amount of work has been aimed at studying the fluid-air surface profile as a function of electric field and, to a lesser extent, specific material properties such as fluid conductivity [66, 67, 68]. Additionally, there has been work towards developing models of the spreading and coalescence of e-jet-printed droplets on substrates [69, 70], as well as developing relationships between input parameters, (e.g. applied voltage), and deposited droplet properties (e.g. contact angle and volume). In the latter category, several authors proposed static scaling law relationships between process inputs such as applied voltage and certain process outputs such as the frequency at which jets issued from the fluid [71, 72, 73]. While both the high fidelity simulation models and the static scaling models provide benefits for some applications, they are not suitable for use in model-based feedback control algorithms. In particular, there is a lack of compact models that are capable of holistically describing the distinct dynamic regimes in e-jet printing. An attractive framework for accomplishing this task is that of hybrid dynamical systems, as they enable the capture of complicated, varying dynamics while still maintaining a foundation in ODEs rather than in partial differential equations.

After some necessary further technical details on e-jet printing in Section 2.1, this chapter presents two hybrid modeling frameworks for e-jet printing. First, Section 2.2 presents a continuous-time model with nonlinear components that highlights the necessity of hybridness for ODE-based modeling of e-jet printing by using as much physics-based modeling as possible and then capturing the remaining unmodeled parts of the ejection process with data driven techniques. These physics- and data-driven models are linked by a hybrid framework. This constitutes the first-ever complete model of the ejection process based on ODEs. However, this model only captures fluid flow at the nozzle outlet, and does not explicitly output the final droplet volume deposited on the substrate. Thus, Section 2.3 presents a discrete-time, piecewise affine (PWA) model featuring simplified flow dynamics and a new framework for capturing the final droplet volume. Both sections feature empirical validation of their models.

2.1 Electrohydrodynamic Jet Printing

The conventional e-jet printing setup requires an ink-filled emitter, typically a conductive (or conductively coated) microcapillary nozzle, and an attractor, typically a flat, conducting, grounded substrate. The emitter is positioned vertically above the attractor and an electric potential is applied between the two components. Figure 2.1 gives a schematic of this configuration, labeling both the important geometric constants of the printer setup and two important dynamical process variables: volumetric flow rate of ink out of the nozzle, Q , and the position of the meniscus tip in space, h . Volumetric flow rate Q is important because of its obvious relevance to the fluid volume ultimately deposited on the substrate. Meniscus position h is important both because it captures important “milestones” in the ejection process (e.g. the transition between dynamic regimes, impingement of the jet on the substrate, and the breaking of the jet) and because its dynamics are coupled to those of Q by capturing the change in the system’s capacitor geometry.

The electric field induced between the liquid meniscus and the attractor causes the meniscus to deform. This deformation can be stable at low voltages, and as applied voltage increases the equilibrium shape of the meniscus changes from a spherical cap to a sharp point known as a Taylor cone. If the applied voltage is high enough, the meniscus becomes unstable and a jet of ink issues from the tip of the Taylor cone towards the attractor. While the voltage difference between the emitter and attractor is maintained and there exists material contiguity between the emitter and attractor, a redistribution of charge occurs in the fluid until the electrically induced surface stress becomes weak enough that the natural liquid surface tension causes the jet to retract, leaving a droplet of ink on the attractor.

If voltage is held high after this ejection, charge will again accumulate at the meniscus and another ejection will occur. The indefinite repetition of this cycle at constant high voltage is termed DC printing. Drop on Demand (DoD) printing is an alternative method in which distinct pulses of length T_p and high voltage V_h are used against a constant low voltage bias V_l to control the timing and size of droplet deposition [22]. DoD printing can be further subdivided into subcritical printing and the complementary supercritical printing. Subcritical printing, upon which this work focuses, is defined as DoD printing in which T_p is short enough that the high voltage pulse falls before the natural cessation of the jet can begin [22]. In other words, subcritical printing is where each pulse corresponds to a single ejection which is stopped artificially by the falling edge of the pulse. (Supercritical printing is any DoD printing that is not subcritical, and is not considered in this work).

The remaining sections in this chapter subdivide the ejection process itself into a set of distinct dynamic regimes. These regimes are the locations of the hybrid model. For both hybrid models in this chapter, the division of the total ejection process into partial processes is based on physically

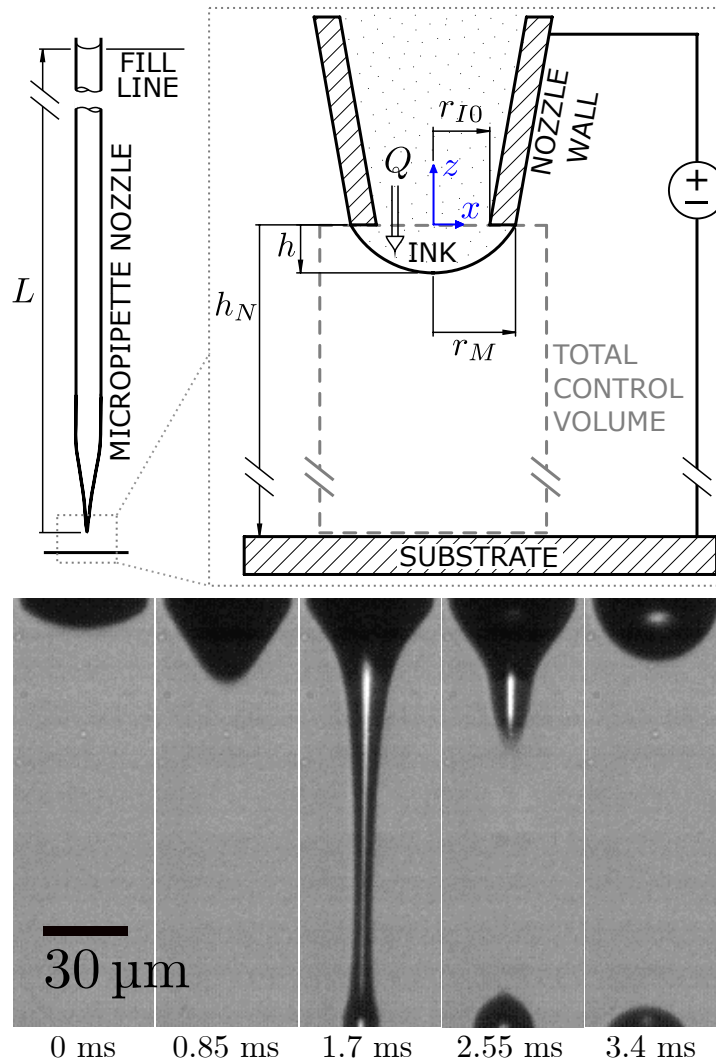


Figure 2.1: (*Top*) Schematic of e-jet printing setup. Dimensions represent signed displacements in the direction of the single-sided arrows with respect to the inertial (x, z) coordinate system. The volumetric flow rate Q , labeled via block arrow, is also a signed quantity, but its sign is with respect to the control volume denoted by the dashed box. (*Bottom*) Time lapse photography of an ejection with time stamps from the rising edge of a voltage pulse.

significant events. However, because the priorities of the two models differ, so do the location definitions. Section 2.2 partitions the system dynamics about the extension of the meniscus tip beyond its maximum stable elongation, while Section 2.3 partitions the system dynamics about impingement of the jet on the substrate.

2.2 First-Principles-Based Modeling

To leverage as much as possible existing knowledge of e-jet printing physics, this section divides the ejection process into the following three partial processes. The “build-up” regime describes the initial deformation of the meniscus into a Taylor Cone when voltage is stepped high. The “jetting” regime describes the development of the jet at the Taylor cone tip, its approach towards the attractor, the fluid flow while the jet is fully developed, and the retraction of the jet back to the Taylor cone. Finally, the “relaxation” regime describes the settling of the meniscus from a Taylor cone back to a stable equilibrium position while the voltage is low. A complete ejection consists of switching from build-up to jetting to relaxation. This process, and the distinction between dynamic regimes and actuation methods, is illustrated in Figure 2.2.

The rest of the section is structured as follows. Section 2.2.1 defines the mathematical representation of e-jet as a hybrid dynamical system, and derives the individual model components. Section 2.2.2 describes the experimental system, the procedure for collecting and processing data, and the system identification techniques for defining the data-driven portions of the model. Section 2.2.3 presents a validation of the identified model. Finally, Section 2.2.4 provides a conclusive summary of the section.

2.2.1 Hybrid System Model Framework

A hybrid dynamical system is a synthesis of a discrete event system and a dynamical system governed by differential or difference equations. Because this section emphasizes the physics-driven modeling of e-jet printing, continuous-time differential equations are used¹. Like discrete event systems, hybrid systems are often formalized as a set, called a hybrid automaton, in which each element describes a different feature of the system behavior. Here, the hybrid automaton definition of Cassandras and Lafortune [3] serves as a basis for this work’s formalism, in which a hybrid system is given as a 10-tuple $\mathcal{G} = (P, X, U, Y, f, g, \phi, \psi, p_0, \mathbf{x}_0)$. P is a set of discrete states or “locations,” $X = \mathbb{R}^n$ is the dynamical state space, $U = \mathbb{R}^m$ is the dynamical control input space, $Y = \mathbb{R}^q$ is the dynamical output space, $f : P \times X \times U \rightarrow X$ is a vector field denoting the

¹This section is the exception to the rule of using discrete-time systems in this dissertation. This section thus uses a somewhat different hybrid system formalization than Section 2.3 onwards.

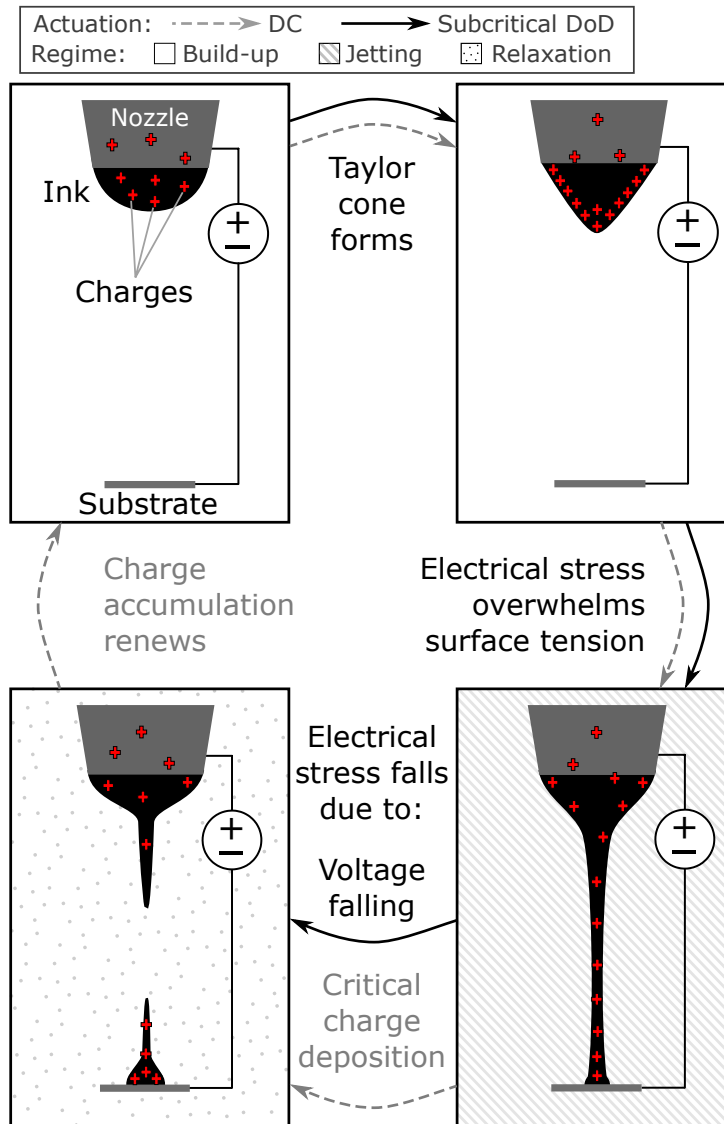


Figure 2.2: Ejection process in terms of the physical phenomena at the liquid-air interface. Distinction is drawn between the process under a constant DC applied voltage, for which ejections begin and end repeatedly under the natural high voltage electrohydrodynamics, and under a single subcritical pulse, which yields a single ejection whose cessation is induced by the falling of the pulse.

dynamics of each location, $g: P \times X \rightarrow Y$ is the arithmetic map from the dynamical states to the output space in a given location, $\phi: P \times Y \rightarrow P$ is the transition function determining the discrete state based on the dynamical output (usually an inequality condition), $\psi: P \times P \times X \rightarrow X$ is the reset function which can instantaneously change the dynamical state when a transition occurs, and p_0, \mathbf{x}_0 are initial conditions of the discrete and dynamical states. This definition is reminiscent of a PWD nonlinear system. However, here the automaton structure helps guide the modeling effort, and the use of continuous time rather than discrete time complicates the translation of resets into a strict PWD framework, which usually relies on a notion of sample period [17].

Furthermore, this definition features one significant structural simplification when compared to most general contemporary hybrid systems, which imposes a limitation on system behavior. It does not allow for uncertain discrete transitions because it does not have invariants on the locations or guards on the transitions. (Invariants and guards allow for separate, potentially overlapping, restrictions on the viability of each location and transition). Instead, the transition function ϕ enforces a one-to-one mapping from the dynamic outputs and the current location to the next location. This limitation is imposed to keep the scope of the mathematical framework comparable to the physical modeling objectives of this work—in which system stochasticity is not considered.

In this work, the e-jet system is modeled with three locations, $P = \{p_1, p_2, p_3\}$ corresponding to build-up, jetting, and relaxation, respectively. Thus, at any point in time, the state of the system is described by $p(t) \in P$ and the dynamical state vector $\mathbf{x}(t) \in X$, and is driven by the input vector $\mathbf{u}(t) \in U$ via the differential equations

$$\dot{\mathbf{x}}(t) = f(p(t), \mathbf{x}(t), \mathbf{u}(t)) = \begin{cases} f_1(\mathbf{x}(t), \mathbf{u}(t)) & p(t) = p_1 \\ f_2(\mathbf{x}(t), \mathbf{u}(t)) & p(t) = p_2 \\ f_3(\mathbf{x}(t), \mathbf{u}(t)) & p(t) = p_3 \end{cases} \quad (2.1)$$

$$\mathbf{y}(t) = g(p(t), \mathbf{x}(t)) = \begin{cases} g_1(\mathbf{x}(t)) & p(t) = p_1 \\ g_2(\mathbf{x}(t)) & p(t) = p_2 \\ g_3(\mathbf{x}(t)) & p(t) = p_3 \end{cases} \quad (2.2)$$

$$p(t) = \phi(p_-(t), \mathbf{y}(t)) \quad (2.3)$$

Note that (2.3) captures the instantaneousness of discrete transitions, with $p_-(t)$ being the value of $p(t)$ prior to ϕ evaluation.

In this work the outputs are the physical system values, $\mathbf{y}(t) = [h(t), Q(t)]^T$. The exact definitions of \mathbf{x} and \mathbf{u} depend on the details of the differential equations to be derived, but for the

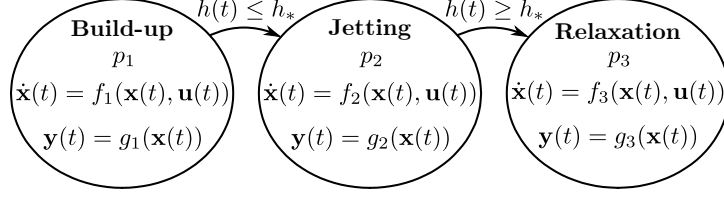


Figure 2.3: Schematic of the system as a hybrid automaton. The transition inequalities are labeled explicitly on the automaton edges for completeness, and are derived in section 2.2.1.3.

sake of clarity, they are preemptively defined as

$$\mathbf{x}(t) = \begin{bmatrix} \delta h(t) \\ \delta Q(t) \\ \delta \dot{Q}(t) \end{bmatrix} = \begin{cases} \begin{bmatrix} h(t) - 0 \\ Q(t) - 0 \\ \dot{Q}(t) \end{bmatrix} & p(t) \in \{p_1, p_3\} \\ \begin{bmatrix} h(t) - h_N \\ Q(t) - Q_f \\ \dot{Q}(t) \end{bmatrix} & p(t) = p_2 \end{cases} \quad (2.4)$$

$$\mathbf{u}(t) = u(t) = \begin{cases} V(t)^2 - 0^2 & p(t) \in \{p_1, p_3\} \\ V(t)^2 - V_h^2 & p(t) = p_2 \end{cases} \quad (2.5)$$

where h_N is the displacement of the substrate from the nozzle outlet and Q_f is the flow rate at the end of the voltage pulse. This model structure allows for the dynamical states δh and δQ to be equal to the outputs h and Q during build-up and relaxation (i.e. when the models are physics-based), and equal to deviations from output equilibria h_N and Q_f during jetting (i.e. when the model is a black box).

A graphical representation of the hybrid automaton for an e-jet ejection is given in Figure 2.3.

The remainder of this section focuses on deriving f_1 , f_2 , f_3 , ϕ , and ψ . For all these derivations, it is assumed that nozzle and the substrate have zero velocity with respect to one another, and that the substrate is flat and clean (i.e. free of pre-deposited substances).

2.2.1.1 Build-up & Relaxation

Physically, the build-up location represents the accumulation of charge and mass in the meniscus under high voltage leading up to jetting. The relaxation state represents the convergence of the meniscus to an equilibrium shape at low voltage. Despite involving nontrivial changes to the meniscus volume and shape, throughout both of these states the liquid's form factor is approximately that of a typical pendant droplet, whose deformations under applied electric fields have

been the subject of much study [74, 75, 76]. This prior art enables these locations to be modeled from a perspective of physical first-principles. Such a model was first proposed by Wright, Krein, and Chato [77] in 1993, further developed by Yang, Kim, Cho and Chung [78] in 2014, and serves as a foundation for the physics-driven modeling in this work.

The premise of Wright’s dynamic model is a 1-dimensional (along the nozzle axis) Newtonian force balance across the plane of the nozzle outlet (i.e. across the boundary of the control volume via which Q is defined). Algebraic manipulation of this force balance yields the derivative of flow rate as a function of pressures at the plane. This is represented as

$$\dot{Q} = \frac{\pi r_{I0}^2}{\rho L} P_{net} \quad (2.6)$$

where r_{I0} is the inner radius of the nozzle outlet, ρ is the mass density of the ink, L is the length of the fluid column, and P_{net} is the net pressure difference across the nozzle outlet, equal to the sum of pressure changes arising from the dominant physical phenomena in the system. These physical phenomena are the pressure due to gravity P_g (taken to be hydrostatic pressure), the pressure due to viscous flow P_μ (assumed equal to Hagen-Poiseuille flow in the nozzle), the pressure due to surface tension P_γ (from the Young-Laplace equation applied to the meniscus tip), and the electric pressure due to applied field P_E (equal to the electrical energy density of the system at the meniscus tip [79, 80]). Mathematically, these pressures are given by

$$P_g = \rho g L \quad (2.7)$$

$$P_\mu(t) = -\frac{8\mu L Q(t)}{\pi r_I^4} \quad (2.8)$$

$$P_\gamma(t) = -\frac{2\gamma}{R(t)} \quad (2.9)$$

$$P_E(t) = \frac{1}{2} \varepsilon E(t)^2 \quad (2.10)$$

where g is the gravitational constant, μ is the dynamic viscosity of the ink, r_I is a measure of the nozzle shaft inner radius, γ is the liquid-air surface tension coefficient of the ink, R is the radius of curvature of the meniscus tip, ε is the permittivity of the medium between the meniscus and the ground plate (usually air), and E is the electric field at the liquid-air interface at the meniscus tip.

This model provides a concrete ODE-based representation of flow rate dynamics in e-jet printing. However, Wright does not perform any empirical validations of this model. The model variant presented by Yang in [78] sees some validation, but is limited by the fact that it relies on a time-varying variable that is not explicitly modeled, and whose value must be gleaned from measured data and updated at each time-step or approximated as constant. Indeed, while the current work

uses equations (2.6-2.10) virtually unchanged as a model framework, several of their constitutive elements are substantially modified to facilitate the model's practical implementation. Specifically, $P_\mu(t)$, $R(t)$, and $E(t)$ are addressed in this work.

In past works P_μ is given by the Hagen-Poiseuille equation, which describes the pressure drop through a long tube of constant cross-section due to shear forces, and uses $r_I = r_{I0}$. However, the nozzles used in e-jet printing do not have constant cross-sections. To achieve the small outlet diameters required, the nozzles are made from pulled-glass micropipettes, which do not have easily defined axial cross-sections. Thus, this work treats r_I in (2.8) as an *effective* inner tube radius,

$$r_I = c_{r_I} r_{I0} \quad (2.11)$$

where c_{r_I} is a correction coefficient to be found via a system identification process described in section 2.2.2.2. This modeling strategy keeps the shear term physically meaningful while enabling a degree of flexibility required for dealing with uncertain nozzle geometry.

Both $R(t)$ and $E(t)$ depend on the shape of the meniscus. For the purpose of modeling $R(t)$ in the surface tension term, equation (2.9), Wright and Yang both assume the meniscus is a spherical cap. This assumption is clearly only valid for small deformations of the meniscus under an electric field. As the meniscus sharpens into a Taylor cone, it achieves a much smaller $R(t)$ than can be captured with a spherical model.

Wright does not offer a physics-based model for $E(t)$, but Yang models the meniscus (assumed to be conducting) and nozzle together as the one half of a two-sheeted hyperboloid of revolution. To fully determine this hyperboloid the following constraints are imposed:

(C2.1) the surface vertex position is fixed to the meniscus tip,

(C2.2) the surface center of symmetry is fixed to the substrate,

(C2.3) $R(t)$ is equal to the meniscus tip radius of curvature measured from photographs.

These constraints enable the use of an analytical solution for electric field, but (C2.3) makes the model dependent on an enormous quantity of measured data, as each time step of every voltage step (characterized by the combination of V_l and V_h) requires a different value of $R(t)$. Yang circumvents this need by considering only small meniscus deformations, up to roughly 40% increases in $h(t)$ from an initial condition where the spherical cap assumption holds, and assuming $R(t)$ is constant. Additionally, to make up for differences between the theoretical electrode configuration described above and the physical system, the theoretical electric field is multiplied by a time-varying model adjustment coefficient, which itself is a function requiring the system identification of two parameters.

The current work presents a model seeking to capture large meniscus deformations (greater than 200% increases in $h(t)$) while reducing the need for measured data to define the model. This is done by modeling the meniscus as a paraboloid of revolution for all dynamical equation derivations (rather than the mixed spherical and hyperboloidal paradigm), and by leveraging knowledge of the force balance at low voltage equilibrium.

To fully determine the paraboloid at any point in time, only two constraints are necessary: (C2.1) and

(C2.4) The surface intersects the nozzle-ink interface (i.e. the outer edge of the nozzle outlet).

Under these constraints, the radius of curvature and theoretical electric field are given by [81]

$$R(t) = \frac{r_M^2}{-2h(t)} \quad (2.12)$$

$$E_t(t) = \frac{2V(t)}{R(t) \ln\left(\frac{2(h(t)-h_N)}{R(t)}\right)} \quad (2.13)$$

The adjusted electrical field to be plugged into equation (2.10) is chosen to be

$$E(t) = c_{E_{eq}} E_{t,eq} + c_{\delta E} \delta E_t(t) \quad (2.14)$$

$$\delta E_t(t) = E_t(t) - E_{t,eq} \quad (2.15)$$

where $E_{t,eq}$ is the unadjusted field at low voltage equilibrium, δE_t is the change in unadjusted field from $E_{t,eq}$, and the correction coefficients $c_{E_{eq}}$ and $c_{\delta E}$ are both constants. Only $c_{\delta E}$ need be found via system identification involving measured timeseries data. $c_{E_{eq}}$ can be found analytically from the fact that at equilibrium the sum of all forces (equivalent to $P_g + P_\mu + P_\gamma + P_E$ in this case) must be zero. This relation yields

$$c_{E_{eq}} = -\frac{r_M \ln\left(\frac{4h_{eq}(h_N-h_{eq})}{r_M^2}\right) \sqrt{-gL\rho r_M^2 - 4\gamma h_{eq}}}{2\sqrt{2\varepsilon} h_{eq} V_l} \quad (2.16)$$

where the only empirical information required is the meniscus position at low voltage equilibrium, h_{eq} , which is a single datum as opposed to a model parameter that must be regressed on a data set. Thus the paraboloidal meniscus approximation enables modeling of larger meniscus deformations by capturing the sharpening of the meniscus as it grows in size via equation (2.12). Equation (2.12) also eliminates the need for $R(t)$ to be defined by measured timeseries data, and basing the electric field adjustment scheme on perturbation from equilibrium via (2.14) and (2.16) eliminates a parameter in $E(t)$ requiring system identification, thereby reducing the model's dependence on empirical data to be fully defined.

The final point to be addressed in the physics-driven modeling of flow rate is the difference between the build-up and relaxation states, which revolves around $c_{\delta E}$. The high voltage during build-up, which pushes the system well beyond the region of attraction of any stable equilibria, makes δE_t a significant overapproximation, necessitating $c_{\delta E} < 1$. However, in relaxation, when the system is under a low voltage yielding a stable equilibrium, the changes in unadjusted field are smaller. Reducing them is both unnecessary for convergence to equilibrium, and can cause surface tension to unrealistically overwhelm electric stress. Thus during relaxation, $c_{\delta E}$ is simply set to 1.

This fully defines the flow rate dynamics for build-up and relaxation, leaving the dynamics of meniscus position to be derived. To do this, an equation for the volume of the fluid outside the nozzle may be differentiated. This yields Q as a function of \dot{h} , which can then be rearranged.

The volume equation is that of a paraboloid truncated at the nozzle outlet:

$$\mathcal{V}(t) = -\frac{\pi}{2}r_M^2 h(t) \quad (2.17)$$

The time derivative of this equation, rearranged, yields

$$\dot{h}(t) = \frac{-2}{\pi r_M^2} Q(t) \quad (2.18)$$

Equations (2.6) and (2.18) can be used to describe the evolution of flow rate and meniscus position during build-up, but two small formalities must be addressed before it can be incorporated with the hybrid model. First, it is a model in Q and h whereas the hybrid system definition has dynamical states of δQ and δh . Second, this model is not second-order in Q , while the hybrid system definition is.

Both of these issues are remedied by choosing

$$g_1(\mathbf{x}(t)) = g_3(\mathbf{x}(t)) = \begin{bmatrix} 1 & 0 & 0 \\ 0 & 1 & 0 \end{bmatrix} \mathbf{x}(t) \quad (2.19)$$

This implies that during build-up, $\delta Q = Q$, $\delta h = h$. Thus, the final form of f_1 and f_3 is

$$f_{1,3}(\mathbf{x}, \mathbf{u}) = \begin{bmatrix} \frac{-2}{\pi r_M^2} \delta Q \\ \frac{\pi r_{I0}^2}{\rho L} \left(\rho g L - \frac{8\mu L}{\pi r_I^4} \delta Q + \frac{4\gamma}{r_M^2} \delta h + \frac{\varepsilon}{2} E^2 \right) \\ 0 \end{bmatrix} \quad (2.20)$$

$$E = -\sqrt{\frac{-8h_{eq}\gamma - 2g L r_M^2 \rho}{\varepsilon r_M^2}} - \frac{4c_{\delta E} \delta h \sqrt{u}}{r_M^2 \ln\left(\frac{4\delta h(h_N - \delta h)}{r_M^2}\right)} \quad (2.21)$$

where time argument (t) has been dropped for compactness, $c_{\delta E} < 1$ for f_1 , and $c_{\delta E} = 1$ for f_3 .

Finally, because the actuating voltage pulses in e-jet typically rise while the system is at some low-voltage equilibrium, the initial conditions of the system are within the build-up state. Here, we assume simulations to start from a stationary meniscus. Thus

$$\mathbf{x}_0 = \begin{bmatrix} h_{eq} & 0 & 0 \end{bmatrix}^T, \quad p_0 = p_1 \quad (2.22)$$

2.2.1.2 Jetting

The physics-driven models f_1 and f_3 describe meniscus deformations up to the critical Taylor cone. However, as the jet forms at the cone tip, the capacitor geometry, charge flow, and fluid flow become more complicated, and these models cease to represent the system's dynamics. At this point, the system transitions to the data-driven model of jetting dynamics. This model is developed by finding differential equations yielding signal shapes similar to those of empirical data and fitting the parameters of those differential equations to measurements.

Classification of the empirical signal profiles is dependent on the actuation method. DC printing and frequently supercritical DoD printing can yield highly nonlinear dynamics in that flow rate will fall and the jet will cease automatically due to critical charge ejection despite a constant input. In subcritical printing, however, the falling edge of the voltage pulse is directly responsible for the fall in flow rate and jet cessation. This causality enables the input/output dynamics to be well-captured by a linear time invariant (LTI) model defined in terms of change from the locally steady high-voltage flow, i.e. from the flow with a fully developed contiguous jet. Thus, this work limits the scope of the jetting model to subcritical printing.

Based on qualitative observations of measured jetting signals, a second order LTI system is chosen for flow rate, with model coefficients to be found by least squares regression. For mathematical consistency with the physics-driven models, the continuous-time model

$$\delta\ddot{Q}(t) = a_{Q1}\delta\dot{Q}(t) + a_{Q0}\delta Q(t) + b_Q u(t) \quad (2.23)$$

is desired. However, because jetting is a high-speed, small-scale phenomenon, sampling can be relatively coarse and noisy. Regression performance is thus significantly improved when using the discrete time model given by

$$\delta Q(k+2) = \tilde{a}_{Q1}\delta Q(k+1) + \tilde{a}_{Q0}\delta Q(k) + \tilde{b}_Q u(k) \quad (2.24)$$

where k is the discrete time index.

To get the continuous-time model coefficients a_{Q1} , a_{Q0} , and b_Q from the regressed discrete

time coefficients \tilde{a}_{Q1} , \tilde{a}_{Q0} , and \tilde{b}_Q , the poles and final values of the two systems are matched. First, the two poles of the discrete time system are converted to their continuous-time equivalents via

$$p_{si} = \frac{\ln(p_{zi})}{T_s} \quad i \in \{1, 2\} \quad (2.25)$$

where p_{si} is a continuous-time pole, p_{zi} is a discrete time pole, and T_s is the sampling period. Solving the characteristic equation of the continuous-time system then yields

$$a_{Q1} = p_{s1} + p_{s2} \quad a_{Q0} = -p_{s1}p_{s2} \quad (2.26)$$

For the input coefficient, the final value theorem expressions at low voltage for the continuous and discrete time systems can be equated to yield

$$\lim_{s \rightarrow 0} s \frac{\delta Q(s)}{U(s)} \frac{(V_l^2 - V_h^2)}{s} = \lim_{z \rightarrow 1} (z - 1) \frac{\delta Q(z)}{U(z)} \frac{z(V_l^2 - V_h^2)}{z - 1}$$

$$b_Q = \frac{\tilde{b}_Q a_{Q0}}{\tilde{a}_{Q1} + \tilde{a}_{Q0} - 1} \quad (2.27)$$

where $\frac{\delta Q(s)}{U(s)}$ is the transfer function from input to δQ .

The above analysis fully defines the flow rate model for jetting, and one may note that it is independent of meniscus position. However, the meniscus position is still important in the jetting model, particularly during jet retraction, because it will trigger the transition to the relaxation location.

Inspection of measured meniscus position signals during jet retraction suggest it may be approximated by exponential decay, i.e. a first order LTI system. However, the retraction does not begin until some time after the falling edge of the voltage pulse. This is accounted for by adding a delay on the input. This system will be identified in much the same way as flow-rate, with regression and delay identification being performed on the discrete time system

$$\delta h(k + 1) = \tilde{a}_{h0} \delta h(k) + \tilde{b}_h u(k - d) \quad (2.28)$$

where d is the delay in time steps between the step down in voltage and the beginning of retraction. The continuous-time model parameters arising from pole matching and final value theorem matching, respectively, are

$$a_{h0} = \frac{\ln(\tilde{a}_{h0})}{T_s} \quad b_h = \frac{\tilde{b}_h a_{h0}}{\tilde{a}_{h0} - 1} \quad (2.29)$$

which are then plugged into the continuous-time form of the system, given by

$$\delta \dot{h}(t) = a_{h0} \delta h(t) + b_h \mathcal{T}^{-dT_s} u(t) \quad (2.30)$$

where \mathcal{T} is the shift operator, making $\mathcal{T}^{-dT_s} u(t) = u(t - dT_s)$.

With this, f_2 is fully defined as

$$\dot{\mathbf{x}}(t) = f_2(\mathbf{x}(t), u(t)) = \begin{bmatrix} a_{h0} & 0 & 0 \\ 0 & 0 & 1 \\ 0 & a_{Q0} & a_{Q1} \end{bmatrix} \mathbf{x}(t) + \begin{bmatrix} b_h \mathcal{T}^{-dT_s} \\ 0 \\ b_Q \end{bmatrix} u(t) \quad (2.31)$$

g_2 will account for the fact that unlike the physics-driven models, the jetting model is not derived in terms of absolute Q and h . Instead, it is assumed that in subcritical DoD printing, the flow at the falling edge of the voltage pulse is fully developed and locally steady. Thus

$$\mathbf{y}(t) = g_2(\mathbf{x}(t)) = \begin{bmatrix} 1 & 0 & 0 \\ 0 & 1 & 0 \end{bmatrix} \mathbf{x} + \begin{bmatrix} h_N \\ Q_f \end{bmatrix} \quad (2.32)$$

where Q_f is the empirically determined flow rate at $t = T_p$.

2.2.1.3 Transition & Reset

This work uses analysis of system stability to concretely define the points in the ejection process at which transitions between the physics- and data-driven models should occur. As described in section 2.1, up to a critical magnitude of deformation each meniscus shape is a stable equilibrium of the system for a particular input. Deformation in excess of that critical shape marks the transition from build-up to jetting. Likewise, the complementary condition—the point during jet retraction at which the meniscus shape becomes a stable equilibrium for some applied voltage—is used to mark the transition from jetting to relaxation.

This notion of the transition condition was first proposed by the authors in [22], which leverages the physics-based work of Yarin, Koombhongse, and Reneker on deriving the range of stable equilibria in terms of meniscus shape [82]. In this work, Yarin models the meniscus as a hyperboloid in a prolate spheroidal coordinate system (η, ξ) with the horizontal axis free to move between the nozzle and substrate, equivalent to replacing (C2.2) and (C2.3) with (C2.4) in the surface definition. This results in hyperboloids that are underdetermined given the information available for dynamic simulation, but can fit the true meniscus shape more closely if extra information is available at a given point.

In the prolate spheroidal coordinate system, $\xi \in [0, 1]$ denotes a hyperbola, and $\eta \in [1, \infty)$

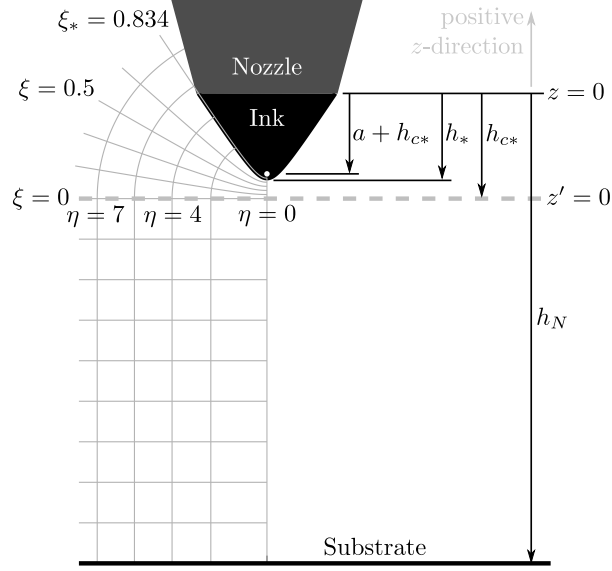


Figure 2.4: To-scale schematic of a critically deformed meniscus and the prolate spheroidal coordinate system (with horizontal axis at $z' = 0$) used to describe the geometry of the meniscus and its local electric field (ellipses) and electric potential contours (hyperbolae). The focus is marked by the white dot at $z' = a$. For $z' < 0$ the field and potential contours are assumed “Cartesian.” Note that by the z -axis sign convention, h -values are negative, and a is positive.

denotes an ellipse (see Figure 2.4). Yarin shows that regardless of surface tension coefficient, the maximum stable deformation of the meniscus corresponds to the shape of the critical hyperbola $\xi_* \approx 0.834$. This extra datum fully determines the surface of the critical Taylor cone.

In [22], ξ is estimated from measured data, and the jetting state is isolated from the build-up state empirically. For simulations independent of measured data, the transition condition must be defined in terms of the model’s dynamical states. In other words, for this work a critical meniscus position h_* must be found in terms of ξ_* .

The derivation of this relationship starts with the transformation equations between the 2D cross section of the prolate spheroidal coordinate system and a Cartesian coordinate system (x', z') with the same horizontal and vertical axes:

$$\eta = \frac{1}{2a} \left(\sqrt{x'^2 + (z' + a)^2} + \sqrt{x'^2 + (z' - a)^2} \right) \quad (2.33)$$

$$\xi = \frac{1}{2a} \left(\sqrt{x'^2 + (z' + a)^2} - \sqrt{x'^2 + (z' - a)^2} \right) \quad (2.34)$$

$$z' = a\eta\xi \quad (2.35)$$

While both coordinate systems are two-dimensional, three equations are needed to relate them. This is because in addition to ξ and η , the prolate spheroidal coordinate system is also parame-

terized by the distance a from the horizontal z' -axis to the focus of the coordinate system. The application of (C2.4) to equation (2.34) and (C2.1) to equation (2.35) yields

$$\xi_* = \frac{\sqrt{r_M^2 + (a - h_{c*})^2} - \sqrt{r_M^2 + (-a - h_{c*})^2}}{2a} \quad (2.36)$$

$$h_* = a\xi_* + h_{c*} \quad (2.37)$$

where h_{c*} is the displacement of the prolate spheroidal coordinate system from the inertial coordinate system (x, z) .

As is, the system is underdetermined, having unknowns a , h_* , and h_{c*} . This is remedied by reformulating the theory in [82] to yield h_{c*} as a function of h_* and constant system properties via

$$h_{c*} = \sqrt{\alpha^2 + 2\alpha h_*} - \alpha \quad (2.38)$$

$$\text{where } \alpha = \frac{2\pi\gamma h_N^2 (1 - \xi_*^2) \left(\ln \frac{1+\xi_*}{1-\xi_*}\right)^2}{(CV_*)^2}, \quad (2.39)$$

$C \approx 1.05\text{E-}5 \frac{\text{kg}^{\frac{1}{2}} \text{m}^{\frac{1}{2}}}{\text{sV}}$ is the conversion from volts to statvolts in SI units, and V_* is the maximum non-jetting applied voltage. V_* is empirically determined, providing the extra datum required to fully determine the critical hyperboloid.

Now solving the system (2.36), (2.37) will yield four sets of solutions for h_* , and a . Three of these solutions are spurious: two for returning meniscus positions inside the nozzle and another for yielding η outside of its domain when plugged into equation (2.33). This leaves a single solution for the maximum stable meniscus length, thereby defining the transitions into and out of jetting via the transition function

$$p_+ = \phi(p_-, \mathbf{y}) = \begin{cases} p_1 & h \geq h_* \wedge p_- = p_1 \\ p_2 & h < h_* \\ p_3 & h \geq h_* \wedge p_- \neq p_1 \end{cases} \quad (2.40)$$

$$\text{where } h_* = \alpha - \frac{\beta}{1 - \xi_*^2} - \sqrt{\frac{2\alpha(\alpha(1 - \xi_*^2) - \beta)}{1 - \xi_*^2}} \quad (2.41)$$

$$\text{and } \beta = \sqrt{(1 - \xi_*^2)(\alpha^2(1 - \xi_*^2) - r_M^2 \xi_*^2)} \quad (2.42)$$

The $(-)$ subscript indicates the state value preceding transition and the $(+)$ subscript indicates the state value after transition. The transition is instantaneous.

While the outputs \mathbf{y} representing the absolute flow rate and meniscus position should be con-

tinuous over transitions between locations, the dynamical states \mathbf{x} must undergo a reset at each transition because the build-up and jetting dynamics use different set points from which δh and δQ are defined.

The reset's objective is thus to ensure \mathbf{y} is continuous despite discontinuities in \mathbf{x} . For δh and δQ , this amounts to subtracting and adding the output offsets of the jetting model when entering and exiting the jetting state, respectively. For $\delta \dot{Q}$, the flow rate dynamics in equations (2.20-2.21) can be used to set the initial $\delta \dot{Q}$ when entering jetting, and the state can be set to zero when exiting jetting, as it is unused by the build-up dynamics.

Thus

$$\mathbf{x}_+ = \psi(p_-, p_+, \mathbf{x}_-) = \begin{cases} \mathbf{x}_- + \begin{bmatrix} -h_N \\ -Q_f \\ \begin{bmatrix} 0 & 1 & 0 \end{bmatrix} f_1(\mathbf{x}_-, \mathbf{u}_-) \end{bmatrix} & \begin{bmatrix} p_- \\ p_+ \end{bmatrix} = \begin{bmatrix} p_1 \\ p_2 \end{bmatrix} \\ \mathbf{x}_- + \begin{bmatrix} h_N \\ Q_f \\ \begin{bmatrix} 0 & -1 & 0 \end{bmatrix} f_2(\mathbf{x}_-, \mathbf{u}_-) \end{bmatrix} & \begin{bmatrix} p_- \\ p_+ \end{bmatrix} = \begin{bmatrix} p_2 \\ p_3 \end{bmatrix} \end{cases} \quad (2.43)$$

Now, with the dynamics of all locations and the process for transitioning between them defined, a complete end-to-end model of the e-jet cycle under subcritical actuation is achieved. The following sections discuss the experimental procedures and data processing involved in model verification.

2.2.2 Experimental Methods

2.2.2.1 Data Collection and Processing

There are two main components of the process used for collecting data for system identification and validation of the hybrid e-jet model proposed above: the physical system used to generate high speed videos and image processing code that is used to extract signals of interest from the raw high speed videos.

The experimental setup consists of an e-jet printer (custom built at the University of Michigan), and a high speed camera (Vision Research, Phantom V9.0) which are automated and synchronized via the drivers of an X-Y-Z nanopositioning stage (Aerotech, "Planar_{DL}") and software written in the Aerotech A3200 Motion Composer Integrated Development Environment. The high speed camera is fixed with a 20x microscope lens assembly yielding $0.65 \frac{\mu\text{m}}{\text{pixel}}$ resolution. Norland Optical Adhesive 81, a UV curable monomer-photocatalyst mixture, is used as the ink for all experiments in this work. A silicon wafer serves as the substrate. The microcapillary nozzle is supplied by Word Precision Instruments (product TIP30TW1), and sputter coated in house with gold-palladium alloy

Table 2.1: Experimental Setup and Process Parameters

Parameter	Symbol	Value
Nozzle outlet inner radius	r_{I0}	15 μm
Nozzle outlet outer radius (meniscus radius)	r_M	21.8 μm
Fluid column height	L	5 cm
Substrate position	h_N	150 μm
Ink Density	ρ	1200 $\frac{\text{kg}}{\text{m}^3}$ [83]
Ink Dynamic Viscosity	μ	0.3 Pa s [84]
Surface Tension Coefficient	γ	0.039 $\frac{\text{N}}{\text{m}}$ [69]
Low Voltage	V_l	525 V
Sample Period	T_s	50 μs

Table 2.2: The set Ω of $\omega = (T_p, V_h)$ pairs

V_h [V]	1100	1150	1200	1250	1300	1300	1300	1300	1350	1370
T_p [ms]	2.0	2.0	2.0	2.0	1.5	1.8	2.0	2.3	2.0	2.0

for conductivity.

Important physical parameters of the printer setup and video capture process are tabulated in table 2.1. Twenty single-droplet ejections are recorded for each element of a set Ω of ten (T_p, V_h) pairs, listed in table 2.2. All trials begin from the low voltage equilibrium meniscus position over a clean region of substrate with no prior fluid depositions. For each pair, 10 of the 20 recordings are designated as training data, and the remaining as validation data. These pairs are chosen to approximately cover the range of voltages within the subcritical regime for the given printer configuration and ink, as well as to offer some variation in T_p where possible (the subcritical regime may be “narrow” at particularly low or high values of V_h).

The experimental setup and procedure (other than the specific (T_p, V_h) pairs tested) is identical to those of [22], which may be referenced for greater detail. Additionally, Figure P.1 contains a photograph of the experimental system.

Once the videos are captured, h and Q signals are extracted for each trial via an image processing protocol consisting of substrate position identification, ink-nozzle interface identification, edge finding, region area/volume computation, and numerical differentiation. These operations are also described in detail in [22]. The only procedure change from [22] is that where the previous work discarded trials for which the algorithm failed to identify the ink-nozzle interface (a task made difficult by the dullness of the feature corners), this work retains all recorded video and uses manual

interface identification for trials where the algorithm failed.

2.2.2.2 System Identification

For the physics-driven locations, there are two major parameters that must be found via system identification: c_{r_I} and $c_{\delta E}$. The system identification is done via the minimization of flow rate error in simulations performed over a mesh of parameter test values.

Each parameter is given a set of 100 linearly spaced test values on the ranges $c_{r_I} \in [1, 35]$ and $c_{\delta E} \in [0.3, 0.6]$, yielding 10,000 models in total. For c_{r_I} , this range allows r_I to vary from the nozzle outlet radius to approximately the radius of the main body of the micropipette. For $c_{\delta E}$, this range is found by trial and error with boundaries chosen such that no r_I in the aforementioned range yields simulation timeseries sufficiently approximating the empirical signals under holistic qualitative assessment.

Each of the 10,000 models is given a scalar error value, Err , by the the metric

$$Err(c_{\delta E}, c_{r_I}) = \text{mean}_{\omega \in \Omega, i \in I} \left(\text{RMS}_{k \in K_{p_1}(\omega, i)} \left(Q_{\omega, i}(kT_s) - \hat{Q}_{\omega, c_{\delta E}, c_{r_I}}(kT_s) \right) \right) \quad (2.44)$$

where $i \in I = \{1, 2, \dots, 10\}$ is the index of the training data recording for a given ω , $K_{p_1}(\omega, i)$ is the set of time steps in the build-up state for the (ω, i) recording, $Q_{\omega, i}$ is the measured flow rate trajectory of the (ω, i) recording, and $\hat{Q}_{\omega, c_{\delta E}, c_{r_I}}$ is the simulated flow rate trajectory generated with the given test values of $c_{\delta E}$ and c_{r_I} , and the input dictated by ω . These simulations are performed using a fourth order Runge-Kutta method with step-size $T_s = 100$ ns.

In addition to c_{r_I} and $c_{\delta E}$, the low-voltage equilibrium position h_{eq} , the maximum non-jetting voltage V_* , and the input delay d for the jetting dynamics of meniscus position must be determined empirically. h_{eq} is found by averaging the empirical $h(0)$ over all training trials. V_* is set to 1000 V based on the results in [69], which uses the same ink and printer setup as the current work. For each $\omega \in \Omega$, d is the median number of time steps during jetting for which $V(t) = V_l$ and $|\delta h(t)| \leq \text{tol}$, where tol is a tolerance close to 0.

For the jetting location, this work assumes that

(A2.1) each (T_p, V_h) pair requires a different set of LTI model parameters, and

(A2.2) these parameter sets must be derived independently from one another.

The LTI models for each (T_p, V_h) pair are thus derived from only the 10 training recordings corresponding to that pair. The discrete-time LTI model parameters for Q , \tilde{a}_{Q0} , \tilde{a}_{Q1} , and \tilde{b}_Q , are to be fit by basic least squares regression. For h , however, a standard least squares regression runs the risk of returning an LTI model whose steady state value under low voltage is near h_* but does not

cross h_* . Such a model would prevent a transition from jetting to relaxation from ever happening. Thus the system identification for meniscus position will constrain the least squares optimization such that the final value theorem applied to the model under low voltage yields

$$h(t \rightarrow \infty) \geq 0.95h_* \quad (2.45)$$

Because the optimization is carried out over the decision variables \tilde{a}_{h0} and \tilde{b}_h , this inequality constraint is realized as

$$\begin{bmatrix} h_N - 0.95h_* & V_h^2 - V_l^2 \end{bmatrix} \begin{bmatrix} \tilde{a}_{h0} \\ \tilde{b}_h \end{bmatrix} \leq h_N - 0.95h_* \quad (2.46)$$

which can be implemented via MATLAB's `lsqlin` function.

2.2.3 Model Validation

This section first presents the results of the system identification processes described above, and uses these results to assess this work's approach to integrating data-driven components into e-jet modeling. Then, an error breakdown of the fully defined model against the validation data is presented, and analysis is given.

2.2.3.1 System Identification Results

Figure 2.5 gives the error and standard deviation of the build-up Q models over the 100-by-100 array of c_{r_I} and $c_{\delta E}$ choices. The parameter values yielding minimum error are $c_{r_I} = 7.87$ and $c_{\delta E} = 0.44$, which are applied to all (T_p, V_h) pairs for the given ink and printer configuration. This value of c_{r_I} yields an effective inner shaft radius of $r_I = 118 \mu\text{m}$. This is nearly an order of magnitude larger than the nozzle outlet inner radius, $r_{I0} = 15 \mu\text{m}$. However, it is still significantly closer to r_{I0} than it is to the capillary radius preceding the taper ($\sim 400\text{-}500 \mu\text{m}$), which makes up $\sim 90\%$ of the fluid column. This verifies the necessity of using c_{r_I} to find an effective radius for the fluid column in the physics-based modeling, as the true nozzle outlet radius and mean column radius would both fall outside of the low error valley seen in Figure 2.5, regardless of choice of $c_{\delta E}$.

For the choice of $c_{\delta E}$ itself, the low error valley apparent in Figure 2.5 may tempt one to believe that the global minimum within this valley is not substantially different from other points along some "minimum trajectory" across the mesh, and that choosing a point in the valley yielding the least aggressive model adjustment (i.e. $c_{\delta E}$ closest to 1) may be a better modeling choice. However, in fact the model behavior changes as $c_{\delta E}$ increases and c_{r_I} correspondingly decreases.

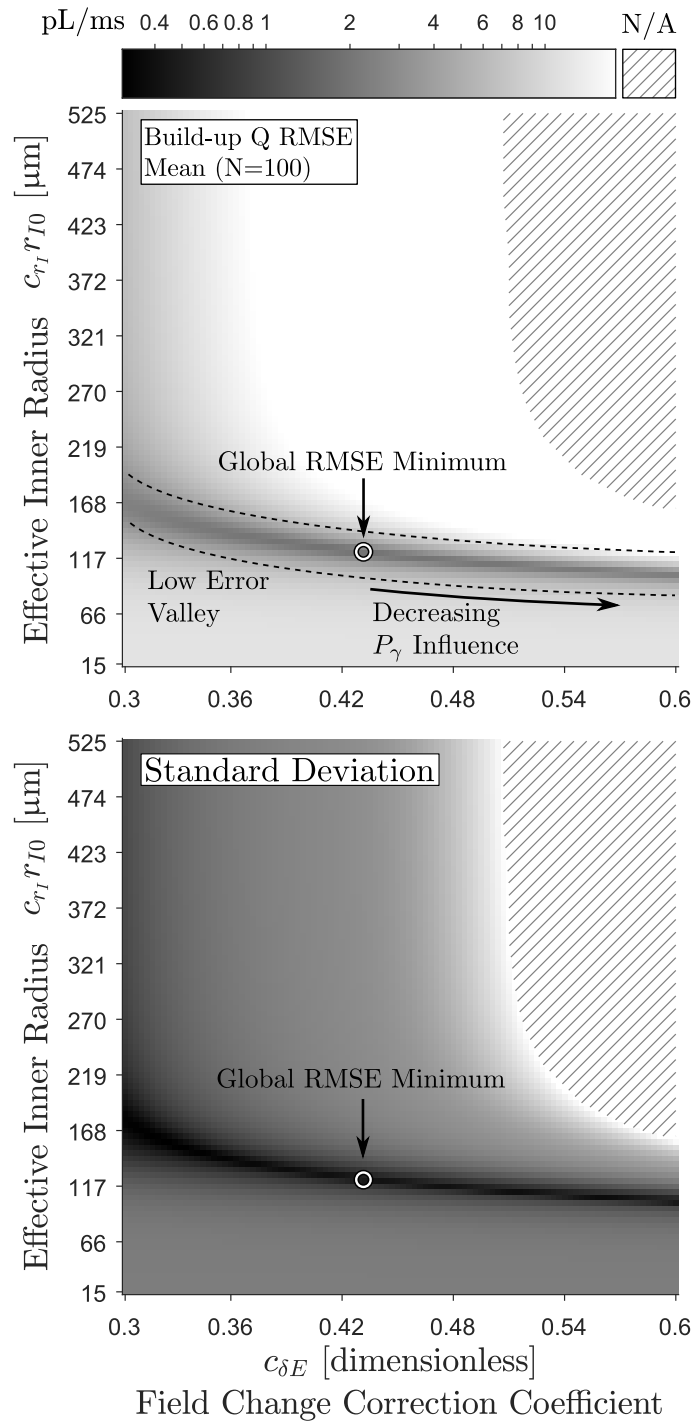


Figure 2.5: Training error, Err , and standard deviation of Q in the build-up state with respect to $c_{\delta E}$ and c_{r_I} . The color bar across the top of the figure applies to both plots, and gives the logarithmic relationship between pixel brightness and the magnitude of the mean and standard deviation in picoLiters per millisecond ($\frac{\text{pL}}{\text{ms}}$). The hatched regions represent $(c_{\delta E}, c_{r_I})$ combinations corresponding to Inf error values. The circled point in both images represents the global minimum Err found in this analysis.

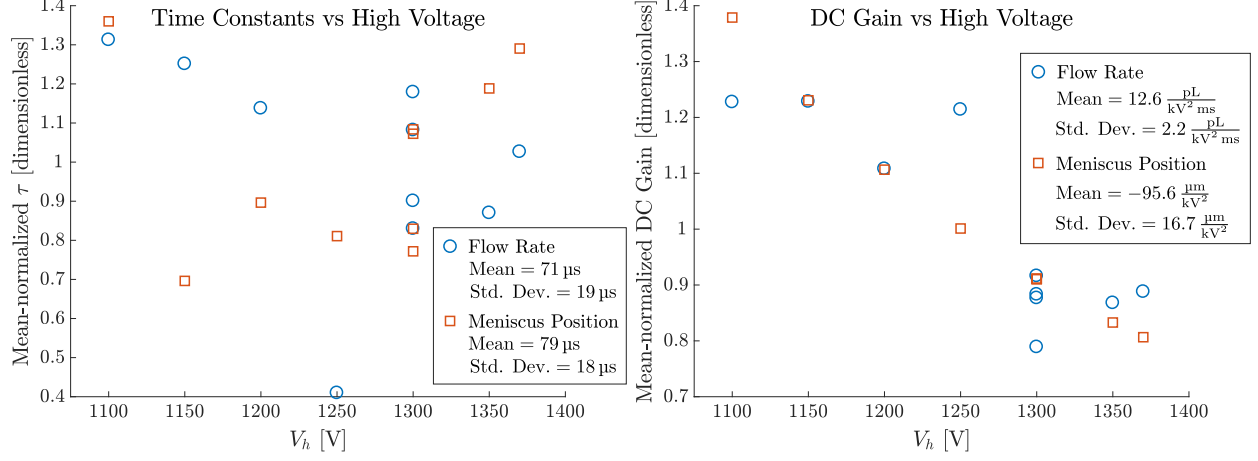


Figure 2.6: Time constants (τ) and DC Gains (G) of Q and h jetting models versus V_h . For comparability between Q and h , τ and G are normalized by their mean value. No correlation is apparent between τ and V_h . However, DC Gain and V_h are clearly correlated.

Specifically, the pressure due to surface tension (P_γ) loses influence over the flow rate dynamics compared to the pressures due to electric field (P_E) and shear forces (P_μ), as can be seen by inspection of equation (2.20). This degrades the model's ability to capture the system's transient response to the step increase in applied voltage, which is governed largely by the balance of P_E and P_γ due to P_μ being zero at $t = 0$. Thus, while the error increases incurred by choosing $c_{\delta E}$ closer to 1 may be relatively small, this choice has nontrivial ramifications for the physical meaning of the model, which justifies the selection of $c_{\delta E}$ based on global minimum RMSE.

To assess the system identification approach taken for the jetting location, specifically the necessity of assumptions (A2.1) and (A2.2), Figure 2.6 illustrates how the transient and steady state behavior of the LTI models vary with applied voltage. This is done by plotting the time constants, τ , and DC gains, G , for each ω against V_h . τ and G come from the roots of a system's characteristic polynomial (which determine the rate of exponential decay of transient responses in stable LTI systems) and the final value theorem applied to a system with a unit step input, respectively, and are given by

$$\tau_h = \frac{-1}{a_{h0}} \quad \tau_Q = \frac{-2}{a_{Q1}} \quad (2.47)$$

$$G_h = \frac{-b_h}{a_{h0}} \quad G_Q = \frac{-b_Q}{a_{Q0}} \quad (2.48)$$

Pearson correlation coefficients, r , and the corresponding \mathfrak{p} -values (stylized with a fraktur font to distinguish \mathfrak{p} from the hybrid system's discrete state, $p(t)$) of the τ and G magnitudes versus V_h^2 are given in table 2.3. $r \in [-1, 1]$ quantifies the degree to which two variables are linearly

Table 2.3: p-values and correlation coefficients for LTI Metrics vs. V_h^2

LTI Metric	p	r
$ \tau_h $	0.67	Irrelevant
$ \tau_Q $	0.23	Irrelevant
$ G_h $	$7_{\text{E}-8}$	-0.99
$ G_Q $	0.002	-0.85

Table 2.4: Transition Timing Error Mean (e_μ) & Standard Deviation (e_σ)

Transition	e_μ [ms]	e_σ [ms]
Build-up to Jetting	-0.26	0.12
Jetting to Relaxation	-0.04	0.05

correlated (and the direction in which they are correlated). p-values indicate the probability that the measured r could arise from randomness given a true relationship of zero correlation. Thus, correlation coefficients associated with high p-values are marked irrelevant. r and p are computed with respect to V_h^2 because the input to the dynamic system is based on squared voltage.

The fact that the τ and G values are far from constant across all V_h^2 clearly demonstrates the validity of (A2.1). (A2.2) is more interesting. Time constant shows no correlation with V_h^2 . This means that there is unlikely to be a meaningful linear relationship between τ and ω , and that some independent system identification may be necessary for each ω . However, DC Gain exhibits strong correlation. This is a desirable result because it suggests the possibility of reducing the strictness of (A2.2) by incorporating the dependence of DC Gain on ω into the framework of jetting-state dynamics, which may reduce the burden of system identification in future work.

2.2.3.2 Total Model Validation

To represent the results of the complete model, Figure 2.7 gives a normalized root mean squared error (NRMSE) breakdown of the model for each location with respect to the measured data across all (T_p, V_h) pairs from the rising edge of the voltage pulse, $t = 0$, to $t = 14.65$ ms. For each location $p \in \{p_1, p_2, p_3\}$ and each output $y \in \{h, Q\}$ the NRMSE is calculated by

$$NRMSE(p, y) = \frac{\text{RMS}_{\omega \in \Omega, i \in I, k \in K_p(\omega, i)} y_{\omega, i}(kT_s) - \hat{y}_\omega(kT_s)}{\text{range}_{\omega \in \Omega, i \in I, k \in K_p(\omega, i, p)} y_{\omega, i}(kT_s)}$$

where \hat{y}_ω is the simulated output trajectory generated with the input dictated by ω , and $K_p(\omega, i)$ is the set of time-steps for which the physical system trial (ω, i) is in state p .

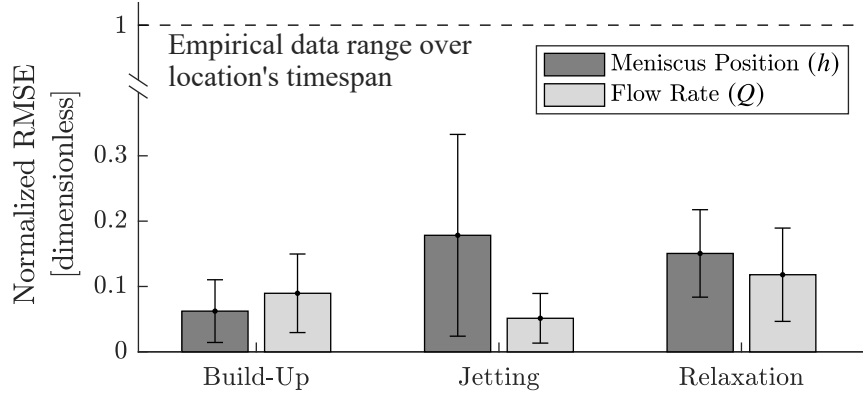


Figure 2.7: Complete model error given as the RMSE normalized by the range of measured data within each location. Each bar is computed from 100 measured timeseries averaging 23 points each for build-up, 34 points for Jetting, and 237 points for relaxation. Error bars represent plus/minus one standard deviation.

Error of state transition times is reported in table 2.4. These errors are given as a simple mean and standard deviation, rather than an RMSE-style metric. This is done in order to preserve the sign of the error, and thus indicate whether the simulation transitions early (positive error) or late (negative error).

Finally, a representative timeseries plot showing the simulated output trajectories against the measured trajectories is given in Figure 2.8.

A qualitative assessment of Figure 2.8 shows that despite some notably erroneous features, the overall model reproduces the empirical timeseries satisfactorily. This holistic satisfaction is supported quantitatively by the NRMSE values presented in Figure 2.7, which illustrates that the range-normalized timeseries errors average to only 11% for both outputs across all locations (where the average is evenly weighted with respect to the locations, not individual points in time). However, the standard deviations on these NRMSEs are relatively large, such that the maximum sum of standard deviation and NRMSE reaches 33%. While the average sum of the NRMSE and standard deviation is still just 18%, indicating that overall the error is acceptable despite some nontrivial spread, the standard deviations still warrant discussion.

A key reason the standard deviation is large is that the error within a single timeseries is not evenly distributed. Instead, there are areas of small and large errors. Take, for example, the meniscus position during jetting, which has the largest NRMSE and standard deviation. Figure 2.8 shows that towards the end of the jetting state, there is very little error between the measured and simulated h trajectories. However at the beginning of the measured trajectory's jetting state (upon which the NRMSE computation is based), there is a brief period of large error while the simulated system is still in the build-up state. As can be seen from table 2.4, the simulations' delayed transition into jetting (and thus the large error in h during the period where the location of the simulation and experiment are mismatched) is consistent, and is likely the cause of the

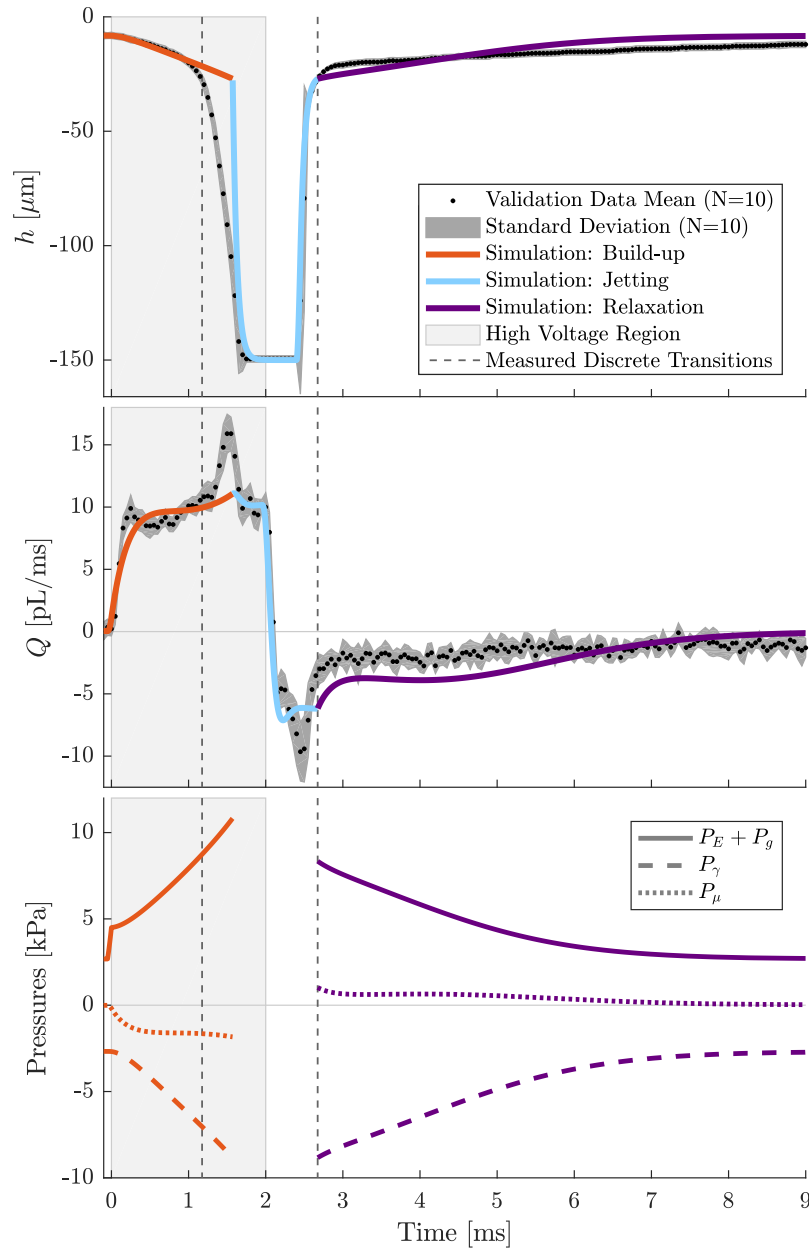


Figure 2.8: Plot of the simulation and measured data for h , Q , and the individual pressure components contributing to Q for $T_p = 2$ ms and $V_h = 1150$ V. P_E and P_g are combined because P_g is constant and they are both always positive, meaning that their sum should be balanced against P_γ with the assistance of P_μ .

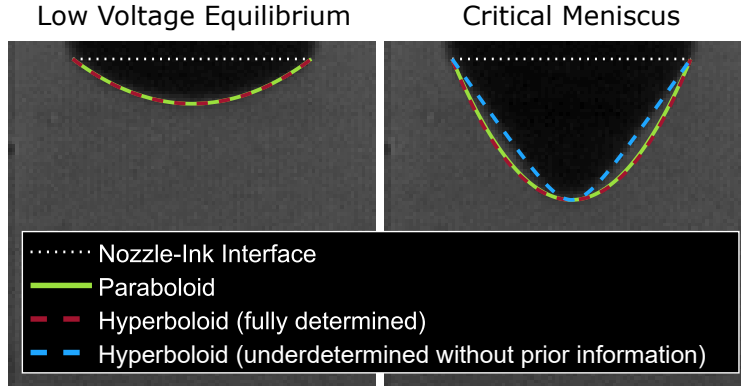


Figure 2.9: Paraboloidal and hyperboloidal electrode geometry approximations overlaid on nozzle/meniscus photographs at a low voltage equilibrium (left), and at the critical Taylor cone preceding jetting (right). The “underdetermined” hyperboloid is given only at the critical meniscus because the necessary prior information (in this case, the value of ξ) is only known for the critical meniscus (see section 2.2.1.3).

relatively large standard deviations. In fact, if the error analysis is restricted to the time span in which the measured and simulated trajectories are in the same location, the sum of the standard deviation and NRMSE for h in jetting decreases by 23%.

While location mismatch is not the only factor contributing to the observed errors, it is worth focusing on in particular not only because of its numerical impact illustrated above, but also because it can be ascribed to a specific modeling assumption: that of the meniscus’s shape. While the paraboloidal shape assumption is clearly more accurate than the spherical cap assumption, it still increasingly overestimates the volume of the meniscus as the meniscus elongates, with the critical meniscus volume being overestimated by 16% on average (compare to 75% for the spherical cap). This means the model requires a greater liquid volume change per unit change in h than the true system. Consequently, for the same Q the simulated h in this work grows more slowly than the physical system the nearer h draws to h_* . On top of this, any retardation of h due to geometric model mismatch is amplified through the positive coupling of h and Q . In other words, the geometric mismatch also causes a reduction in \dot{Q} , which further slows meniscus elongation beyond the direct effect of geometric mismatch on \dot{h} . This combination of factors ultimately results in delayed transitions to jetting.

Note that a hyperboloidal shape assumption is not intrinsically better than the paraboloidal model in this regard. Indeed, while combining constraints (C2.1), (C2.2), and (C2.4) can be used to produce fully determined hyperboloids for use in the dynamic equations, these hyperboloids are virtually identical to the mathematically simpler paraboloids used in this work. This is illustrated in Figure 2.9. In other words, the ability of hyperboloids to capture the sharpness of the critical meniscus is contingent on the relaxation of (C2.2), and the alternative constraint used to derive the transition condition ($\xi = \xi_*$) is only valid at the critical meniscus.

Thus, while there is room for future studies to polish the model minutiae, the above results demonstrate the efficacy of the given hybrid system framework, along with this work's contributions to each of the component models, in capturing the end-to-end dynamics of an e-jet printing process.

2.2.4 Physics-Focused Hybrid E-jet Modeling Conclusion

In summary, this section delivers the first end-to-end ODE-driven model of an e-jet printing process. This is achieved by the combination of three major types of contribution. First, a hybrid systems framework is presented for combining multiple partial process models into an end-to-end model. Second, the scope of prior partial process models is expanded by means such as increasing the sophistication of geometric modeling, leveraging equilibrium information to structure dynamical equations, and analysis of the necessary areas in which to incorporate data-driven modeling elements. Lastly, transitions between the hybrid system's component models are determined via consideration of the partial process's stability.

2.3 Piecewise Affine Modeling

The physics-focused model of Section 2.2 does not explicitly model the deposited fluid volume, instead only modeling the volumetric flow rate of fluid out of the nozzle. This is in large part because past works have considered droplet volume ill-defined until the jet breaks, at which point the droplet volume was considered constant. Thus, there remains a gap in the satisfaction of the requirements that a model be both control-oriented (i.e. ODE-based) and explicitly output deposited droplet volume.

The main contribution of the present section is a hybrid system model framework for e-jet printing that bridges this gap. Specifically, this section

- defines the droplet volume as a dynamical state variable that may evolve over time,
- presents a new division of the ejection process into partial processes to facilitate droplet volume modeling,
- proposes and experimentally validates a mapping between nozzle flow rate and deposited droplet volume enabled by the preceding bullets, and
- presents a new computer vision technique for taking consistent droplet volume measurements from high speed microscope video.

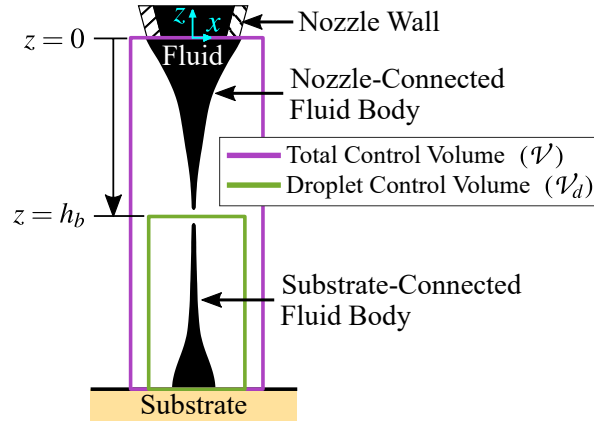


Figure 2.10: Schematic of the two CVs used in this work superimposed over an illustration of a jet immediately after breaking.

The remainder of the section is organized as follows. Section 2.3.1 presents the model (i.e. the first three bullets). Section 2.3.2 presents the experimental methods for measurement, system identification, and model verification, including the final bullet. Section 2.3.3 presents and discusses the model verification results. Finally, concluding remarks are given in section 2.3.4.

2.3.1 Dynamical Deposited Volume Model

2.3.1.1 Droplet Volume Definition

The plane of the nozzle outlet and the solid substrate surface provide obvious boundaries for a Control Volume (CV) through which the total volume of fluid outside the nozzle, $\mathcal{V}(t)$, and the total flow rate through the nozzle outlet, $Q(t)$, may be analyzed and modeled. Similarly, to analyze deposited droplet volume, $\mathcal{V}_d(t)$, as a dynamically evolving variable a droplet CV must be defined. This CV cannot be the same as the total fluid CV because only a fraction of the cumulative flow out of the nozzle up until the jet breaks is deposited on the substrate. The remainder of the fluid is retracted back into the nozzle under the power of surface tension after the jet breaks and the nozzle-connected fluid body and substrate-connected fluid body become disjoint.

This work introduces a CV with an upper boundary at the z -coordinate h_b , where the jet ultimately pinches closed and breaks into two disjoint fluid bodies, as shown in Figure 2.10. This CV allows measurements of droplet volume to be made as time series data while remaining consistent with prior notions of droplet volume in that after the jet breaks the volume of fluid in the droplet CV remains constant (assuming negligible evaporation).

To avoid dramatic increases in complexity, this work's model does not explicitly use h_b . The jet break point is only used to facilitate defining droplet volume as a time series signal and for extracting time series measurements of droplet volume from microscope videos. Theoretical derivation

of the jet break point's position is thus beyond the scope of this work, and it is estimated independently for each material ejection as described in Section 2.3.2.3.

2.3.1.2 Hybrid System Architecture

Ultimately, this work's model is given as the cascading of two discrete-time state-space systems with state transition formulas of the form $f : X \times U \times T \rightarrow X$ where X is the state vector space, U is the input vector space, and T is the time vector, all over the field \mathbb{R} . These two systems are the input-to-nozzle-flow-rate model

$$\begin{bmatrix} Q(t + T_s) \\ Q(t + 2T_s) \end{bmatrix} = f_Q \left(\begin{bmatrix} Q(t) \\ Q(t + T_s) \end{bmatrix}, V(t)^2 - V_l^2, t \right), \quad (2.49)$$

and the nozzle-flow-rate-to-droplet-volume model

$$\begin{bmatrix} \mathcal{V}(t + T_s) \\ \mathcal{V}_d(t + T_s) \end{bmatrix} = f_{\mathcal{V}_d} \left(\begin{bmatrix} \mathcal{V}(t) \\ \mathcal{V}_d(t) \end{bmatrix}, \begin{bmatrix} Q(t) \\ Q(t + T_s) \end{bmatrix}, t \right). \quad (2.50)$$

T_s is the sample period in seconds, t is the time from the rising edge of the voltage pulse in seconds, and $V(t)$ is the applied voltage signal.

Both f_Q and $f_{\mathcal{V}_d}$ are piecewise defined to capture switching between partial process dynamics and to capture state resets—functions that execute upon certain switches and alter the dynamical states before the first evaluation of the newly active partial process dynamics.

In Section 2.2 the division of the material ejection process into partial processes was done to maximize the use of physics-driven first principles model components, and was based on the stretching of the meniscus beyond its maximum stable non-jetting equilibrium extension.

This work presents an alternate breakdown of the material ejection process designed to facilitate modeling of the deposited droplet volume. This breakdown revolves around whether or not there exists a contiguous fluid stream between the nozzle and substrate, as the cessation of this contiguity is synonymous with the cessation of flow into or out of the droplet CV. Specifically, the complete process is broken into an “approach” stage, a “contiguity” stage, and a “retraction” stage. To better focus on the mapping between Q and \mathcal{V}_d , instead of modeling the meniscus tip position dynamics this work assumes that the timing of jet impingement and breaking are determined solely by the pulse parameters V_l , V_h , and T_p . Switching is thus governed by time: with the rising edge of the voltage pulse set to $t = 0$, transition from approach to contiguity occurs when t exceeds $t_c(V_l, V_h, T_p)$ and transition from contiguity to retraction occurs when t exceeds $t_r(V_l, V_h, T_p)$, where t_c and t_r are identified from data for each set of pulse parameters as described in Section 2.3.2.3.

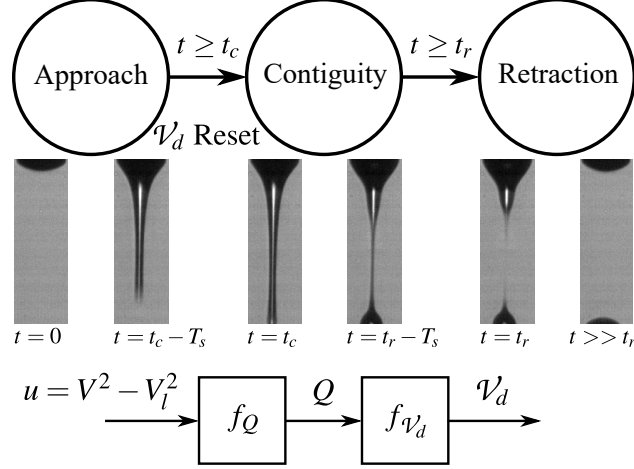


Figure 2.11: System Architecture. *Top*: Automaton illustrating the timed switching behavior of the system model and the reset determining the initial contiguity droplet volume. Each automaton location is accompanied by photographs of the first and final samples of the corresponding partial process from a video with $V_h = 1300$ V and $T_p = 1.5$ ms. *Bottom*: Block diagram illustrating breakdown of a complete input-to-droplet-volume model into a nozzle flow rate model f_Q and a droplet volume model $f_{\mathcal{V}_d}$, both of which are piecewise defined to capture the switching and reset behavior of the automaton.

The lone reset in the system is applied to \mathcal{V}_d upon the switch from approach to contiguity. The complete model architecture is thus visualized by Figure 2.11.

2.3.1.3 Deposited Droplet Volume Model

If the shape of the fluid-air interface were constant over time and the fluid incompressible, the volumetric flow rate out of the nozzle, Q , would be equal to the volumetric flow rate into the droplet control volume, Q_d . However, observation of video data indicates that the interface broadens slowly but steadily while voltage is high during contiguity. This implies that Q_d is only some fraction of Q . The video observation is corroborated by observation of the extracted time series data, such as that shown in Figure 2.12. This motivates a simple proportional model between Q and Q_d during contiguity:

$$Q_d(t) = b_{Q_d} Q(t) \quad (2.51)$$

where b_{Q_d} is a constant.

Trapezoidal integration of $Q_d(t)$ in equation (2.51) yields the first-order discrete-time droplet volume model for the contiguity stage

$$\mathcal{V}_d(t + T_s) = \mathcal{V}_d(t) + \frac{T_s}{2} b_{Q_d} Q(t + T_s) + \frac{T_s}{2} b_{Q_d} Q(t) \quad (2.52)$$

where \mathcal{V}_d is the droplet volume and T_s is the sample period.

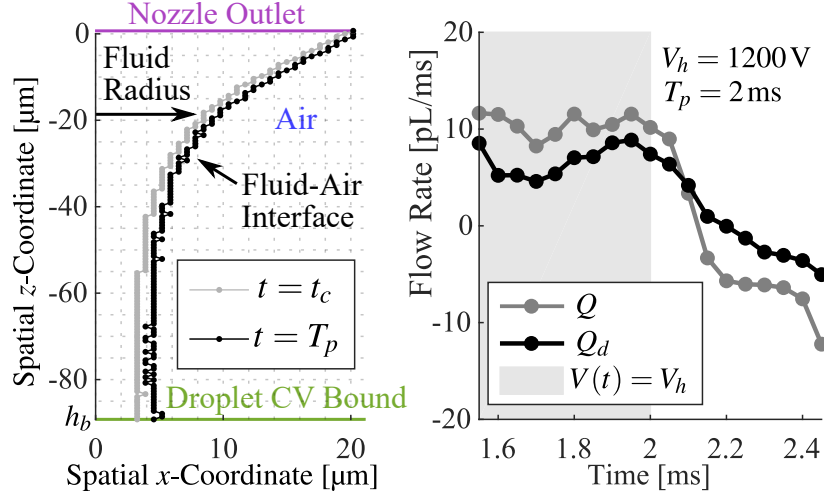


Figure 2.12: Measured data from a particular ejection video illustrating the motivation for a proportional Q_d model. *Left*: Half-outline of fluid body (the jet is roughly symmetric about z -axis) at the onset of contiguity and at the end of the voltage pulse, representing a 7% increase in volume outside the droplet CV. *Right*: Flow rate time series data during contiguity illustrating roughly proportional signals between Q and Q_d .

Volume is also added to the droplet CV during the approach stage when the tip of the meniscus crosses the upper boundary of the droplet CV but has not yet struck the substrate. However, each ejection video only provides a few samples of this situation, as the jet traverses the distance from the jet break position to the substrate relatively quickly. It may thus be impractical to identify a dynamical model of volume increase during the approach stage. Instead, this work sets $\mathcal{V}_d(t + T_s)$ to $\mathcal{V}_d(t)$ during approach, and uses a reset to give \mathcal{V}_d an initial condition in the contiguity stage, which accounts for the fluid added to the droplet CV during approach.

The total volume of the fluid outside the nozzle, \mathcal{V} , at the moment of jet collision with the substrate, t_c , may be roughly modeled as the volume of the Boolean union of a cylinder and a cone arranged to approximate the fluid body shape. \mathcal{V}_d is then some fraction of the cylinder volume. This is equivalent to some fraction, ψ_0 , of the total volume minus the Boolean difference of the cone and the cylinder, ψ_1 . Physics-driven modeling of the jet diameter and break position necessary to explicitly calculate ψ_0 and ψ_1 are beyond the scope of this work, but the structure of the mapping between \mathcal{V} and \mathcal{V}_d at $t = t_c$ arising from this geometric analysis may still be used:

$$\mathcal{V}_d^+ = \mathcal{V}_d^- + \psi_0 \mathcal{V}^- + \psi_1 \quad (2.53)$$

where ψ_0 and ψ_1 require data-driven identification and the subscripts $+$ and $-$ indicate a state's value before and after reset. \mathcal{V}_d^- will be 0 unless there was already fluid in the droplet control volume (e.g. if a second pulse is fired over an existing droplet).

Equation (2.53) requires total volume \mathcal{V} be captured by the state dynamics, which can be

done with a trapezoidal integration of the input Q similar to that of equation (2.51). This addition completes the hybrid model of droplet volume evolution in terms of total flow rate input, which can be given in totality as

$$\begin{bmatrix} \mathcal{V}(t+T_s) \\ \mathcal{V}_d(t+T_s) \end{bmatrix} = f_{\mathcal{V}_d} \left(\begin{bmatrix} \mathcal{V}(t) \\ \mathcal{V}_d(t) \end{bmatrix}, \begin{bmatrix} Q(t) \\ Q(t+T_s) \end{bmatrix}, t \right) = \begin{cases} \begin{bmatrix} \mathcal{V}(t) + \mathcal{Q} \\ \mathcal{V}_d(t) \end{bmatrix} & t < t_c \vee t \geq t_r \\ \begin{bmatrix} \mathcal{V}(t) + \mathcal{Q} \\ \psi_0 \mathcal{V}(t) + \mathcal{V}_d(t) + b_{Q_d} \mathcal{Q} + \psi_1 \end{bmatrix} & t_c \leq t < t_c + T_s \\ \begin{bmatrix} \mathcal{V}(t) + \mathcal{Q} \\ \mathcal{V}_d(t) + b_{Q_d} \mathcal{Q} \end{bmatrix} & t_c + T_s \leq t < t_r \end{cases} \quad (2.54)$$

where

$$\mathcal{Q} = \frac{T_s}{2} (Q(t+T_s) + Q(t)) \quad (2.55)$$

and $t < t_c$ corresponds to the approach stage, $t \geq t_r$ corresponds to the retraction stage, $t_c + T_s \leq t < t_r$ corresponds to all but the first time step of the contiguity stage, and $t_c \leq t < t_c + T_s$ corresponds to the first time step of contiguity, in which the reset is applied.

2.3.1.4 Nozzle Flow Rate Model

The main focus of this chapter is the development and validation of the mapping between nozzle flow rate Q and deposited droplet volume \mathcal{V}_d . This could be done by simply injecting measured Q data into equation (2.54) and assessing the generated \mathcal{V}_d signals against measured droplet volumes. However, for control there must ultimately be a model with input based on applied voltage $V(t)$ rather than $Q(t)$. To demonstrate the viability of equation (2.54) for this purpose, this section presents a simple V -to- Q model based on Section 2.2, which is cascaded with the \mathcal{V}_d model.

The jetting model in Section 2.2 is a second-order LTI system, which may be represented in discrete time as

$$Q(t+2T_s) = a_{Q,1}(V_l, V_h, T_p)Q(t+T_s) + a_{Q,2}(V_l, V_h, T_p)Q(t) + b_{Q,2}(V_l, V_h, T_p)u(t) \quad (2.56)$$

where the input $u(t)$ is given as

$$u(t) = V(t)^2 - V_l^2 \quad (2.57)$$

This choice of input is made because the physics-based first principles models of flow rate are

driven by the applied voltage squared, and because at the low voltage stable equilibrium, Q should be zero. The model parameters $a_{Q,1}$, $a_{Q,2}$, and $b_{Q,2}$ are identified independently for each pulse definition in Section 2.2.

Section 2.2 uses equation (2.56) when the nonlinear physics first principles models cease to capture the observed dynamics. This happens during contiguity and in approach and retraction when the meniscus is sufficiently elongated. Because the nonlinear models cannot capture the entirety of approach or contiguity, incorporating them into this work's deposited-volume-focused switching framework would substantially complicate the model. Thus to preserve the model's focus and manage complexity while still accounting for changes in dynamical behavior over the course of ejection, the structure of equation (2.56) is applied to the entire model with separate parameters identified for contiguity and non-contiguity partial processes. This results in the model

$$\begin{aligned} \begin{bmatrix} Q(t+T_s) \\ Q(t+2T_s) \end{bmatrix} &= f_Q \left(\begin{bmatrix} Q(t) \\ Q(t+T_s) \end{bmatrix}, u(t), t \right) = \\ &\begin{cases} \begin{bmatrix} 0 & 1 \\ \tilde{a}_{Q,2} & \tilde{a}_{Q,1} \end{bmatrix} \begin{bmatrix} Q(t) \\ Q(t+T_s) \end{bmatrix} + \begin{bmatrix} 0 \\ \tilde{b}_{Q,2} \end{bmatrix} u(t) & t < t_c \vee t \geq t_r \\ \begin{bmatrix} 0 & 1 \\ \bar{a}_{Q,2} & \bar{a}_{Q,1} \end{bmatrix} \begin{bmatrix} Q(t) \\ Q(t+T_s) \end{bmatrix} + \begin{bmatrix} 0 \\ \bar{b}_{Q,2} \end{bmatrix} u(t) & t_c \leq t < t_r \end{cases}, \quad (2.58) \end{aligned}$$

where the tilde-topped and overlined parameters are separately identified (and have the input arguments (V_l, V_h, T_p) dropped for compactness) and correspond to the approach and retraction stages and the contiguity stage, respectively.

2.3.2 Experimental Methods

2.3.2.1 Experimental Setup

The e-jet printing setup is identical to that of Section 2.2.2.1.

Twelve sets of (V_l, V_h, T_p) parameters, referred to as ‘‘experiments,’’ are tested, with 20 trials of each experiment being recorded. All trials begin from the low voltage equilibrium meniscus position over a clean region of substrate with no prior fluid depositions: $V(0) = V_l$, $Q(0) = Q(T_s) = 0$, $\mathcal{V}_d(0) = 0$, and $\mathcal{V}(0)$ is the small total fluid volume outside the nozzle at low voltage equilibrium (see Figure 2.1, 0 ms). Time $t = 0$ is defined at the rising edge of the voltage pulse. $V_l = 525$ V for all experiments. V_h and T_p values are tabulated in Table 2.5.

Table 2.5: Experimental High Voltage and Pulse Width Pairs

V_h [V]	T_p [ms]	V_h [V]	T_p [ms]	V_h [V]	T_p [ms]
1100	2.0	1300	1.5	1350	2.0
1150	2.0	1300	1.8	1370	2.0
1200	2.0	1300	2.0	1420	1.5
1250	2.0	1300	2.3	1470	1.5

2.3.2.2 High Speed Microscopy & State Extraction

Each frame of video is a grayscale image containing the nozzle tip, the fluid outside the nozzle, and—if there is fluid near enough to the substrate—a reflection of the fluid off of the substrate. The image processing protocol used to extract time series measurements of \mathcal{V} and \mathcal{V}_d from these images is nearly the same as that of [22]. Edge finding identifies the (x, z) coordinates for the silhouette of the nozzle tip, fluid, and reflection. Corner finding and extremum finding identify the z -coordinates of the nozzle-fluid interface and the substrate-fluid interface. Finally, the width of the silhouette at each z -coordinate is treated as the diameter of a disk of height equal to the image resolution (i.e. the height of one pixel) for volume determination. Q and Q_d measurements are numerical derivatives of \mathcal{V} and \mathcal{V}_d measurements. On top of this established procedure, this work introduces a method to harness the reflection for improving volume measurement consistency near the substrate and a method for estimating jet break position, both of which are illustrated in Figure 2.13 and explained in detail below.

In previous works, the reflection was eliminated from volume calculations entirely. However, due to the quantization error associated with fixing the substrate position measurement to a pixel edge (and possibly other optical or image processing imperfections), this direct calculation leads to nonzero flow of fluid through the bottom of the droplet CV as the droplet spreads. This change in droplet volume measurement during the retraction stage makes identifying a final droplet volume value difficult. Thus this work introduces reflection-augmented volume measurement to maintain conservation of volume near the substrate. Given images that extend Δp_r pixels below the estimated substrate position, a region $2\Delta p_r$ pixels tall centered on the estimated substrate position is defined as the “reflection-augmented measurement region.” The volume of fluid contained in the upper half of this region (i.e. the portion of the region containing direct fluid silhouette rather than reflection) is taken as half the volume computed in the total reflection-augmented measurement region. In other words, the true fluid volume is taken as the average of the silhouette volume and reflection volume.

The jet break position for each trial is measured from the first video frame in which there are two disjoint fluid bodies (i.e. the first frame of retraction). The jet break position is estimated to be

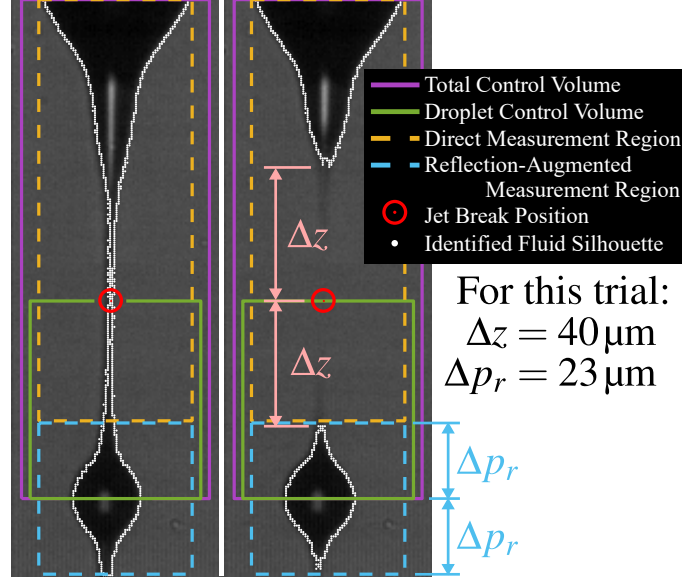


Figure 2.13: Depiction of the two CVs described in Section 2.3.1.1, the distinction between the direct and reflection-augmented measurement regions, and the estimated jet break position superposed on the final contiguity frame and first retraction frame for a particular trial ($V_h = 1300$ V, $T_p = 1.5$ ms). Δz is the distance from either fluid body tip to the jet break position.

the midpoint between the tips of these bodies based on the assumption that the initial droplet and meniscus tip velocities and accelerations are equal and opposite at the moment the jet breaks. This assumption is driven by the fact that the initial jet-breaking and retraction behavior is dominated by surface tension. While this assumption neglects much of the complexity of the true retraction physics, Figure 2.13 suggests it does an acceptable job of identifying the thinnest portion of the jet immediately before breaking, and it circumvents image resolution and noise issues associated with directly computing the thinnest jet point in the final frame of contiguity.

2.3.2.3 System Identification

The parameters to be identified can be grouped into two categories. First are the primary model parameters making up the dynamics of the Q -to- \mathcal{V}_d model (2.54): b_{Q_d} , ψ_0 , and ψ_1 , which are constant over all experiments. Second are the supporting model parameters determining the timing of switching in the volume model (2.54) and the simulated nozzle flow rate model (2.58): $t_c(V_l, V_h, T_p)$, $t_r(V_l, V_h, T_p)$, $\tilde{a}_{Q,1}(V_l, V_h, T_p)$, $\tilde{a}_{Q,2}(V_l, V_h, T_p)$, $\tilde{b}_{Q,2}(V_l, V_h, T_p)$, $\bar{a}_{Q,1}(V_l, V_h, T_p)$, $\bar{a}_{Q,2}(V_l, V_h, T_p)$, and $\bar{b}_{Q,2}(V_l, V_h, T_p)$, whose values vary with the the experiment parameters. The measured data is divided evenly into training and validation data. For each experiment, 10 trials are reserved for training and 10 for validation.

In order to keep the timing of switching fixed to a particular sample, for each experiment t_c and

t_r are taken as the median time of the first frame of contiguity and retraction over the 10 training trials of that experiment (1 parameter from 10 samples). All other parameters are identified via least squares regression. The model coefficients for equation (2.58) are trained independently for each experiment on all the available data in the corresponding process stage (3 parameters from 353 samples for approach and 194 samples for contiguity, on average). The reset parameters ψ_0 and ψ_1 are trained on the set of first frames of contiguity (i.e. the $t_c \leq t < t_c + T_s$ sample) from all trials (2 parameters from 120 samples). Finally, b_{Q_d} is trained on all contiguity training data (1 parameter from 2337 samples).

2.3.2.4 Error Metrics

This section presents metrics for validating the reflection-augmented volume measurement technique, and the ability of the total model to predict deposited droplet volume.

The improvement yielded by reflection-augmented volume measurement over direct measurement is quantified as the mean percent decrease in total variation of the filtered retraction-stage \mathcal{V}_d timeseries between the two techniques. The total variation L of a time-varying parameter is its total change (as opposed to net change) over a given period of time T_L . In theory, the total variation of \mathcal{V}_d in the retraction stage is zero, making its reduction a practical improvement metric. However, high frequency measurement noise also contributes to L . To moderate noise's influence, the \mathcal{V}_d signal is filtered before its total variation is computed. Thus, the total variation of a trial j is given by

$$L_j = \sum_{t=t_r}^{t_r+T_L} |\mathcal{V}_d^f(t+T_s) - \mathcal{V}_d^f(t)| \quad (2.59)$$

where \mathcal{V}_d^f is the filtered volume signal. The final metric for reflection-augmented volume measurement performance is

$$\Delta L\% = 100 \operatorname{mean}_{j \in \text{All Validation Trials}} \frac{L_j^{\text{direct}} - L_j^{\text{augmented}}}{L_j^{\text{direct}}} \quad (2.60)$$

Here, a Savitzky-Golay filter with a window size of 15 samples is used. $T_L = 10$ ms (200 samples), roughly the time it takes for the droplet to spread and settle to its final shape on the substrate.

The efficacy of the overall model in predicting deposited droplet volume is measured by the mean unsigned error between the modeled $\mathcal{V}_d(t_r)$ (equal to $\mathcal{V}_d(t > t_r)$) and the measured final

droplet volume. Measured final droplet volume is taken as

$$\mathcal{V}_{d,j}^{\text{final}} = \text{mean}_{t \in [t_r, t_r + 10 \text{ ms}]} \mathcal{V}_{d,j}^{\text{meas}}(t) \quad (2.61)$$

where $\mathcal{V}_{d,j}^{\text{meas}}(t)$ is the measured droplet volume time series for a particular trial j , making the mean unsigned error

$$e_{\mathcal{V}_d} = \text{mean}_{j \in J} |\mathcal{V}_{d,j}^{\text{final}} - \mathcal{V}_{d,j}(t_r)| \quad (2.62)$$

This metric is evaluated over multiple sets of trials J . In addition to an aggregate $e_{\mathcal{V}_d}$ in which J contains the validation trials of all but one experiment (that of lowest V_h , see Section 2.3.3.2 for discussion of this exclusion), individual $e_{\mathcal{V}_d}$ values are computed for each experiment. This is done to examine how model performance changes with the pulse parameters. Additionally, for each of these sets J , both an $e_{\mathcal{V}_d}$ using $\mathcal{V}_d(t_r)$ generated from injecting measured nozzle flow rate into equation (2.54) and an $e_{\mathcal{V}_d}$ using $\mathcal{V}_d(t_r)$ generated from nozzle flow rate simulated by equation (2.58) are computed. This is done to enable both focus on the quality of equation (2.54) and broader consideration of the ultimate needs for a control-oriented e-jet printing model, respectively. Finally, along with each $e_{\mathcal{V}_d}$, a corresponding standard deviation of the signed error is presented.

2.3.3 Results & Discussion

2.3.3.1 Droplet Volume Measurement

Equations (2.59) and (2.60) show that the reflection-augmented image processing yields a 42% decrease in total variation of measured droplet volume time series data compared to direct measurement, with an associated standard deviation of 10%. This substantial performance improvement can be visualized through the example retraction-stage droplet volume time series in Figure 2.14, in which the direct measurement yields a steady decrease while the reflection-augmented measurement yields a relatively constant droplet volume.

However, in both measurement schemes there is a steep transient at the start of retraction. This arises from an inability of these measurement techniques to conserve volume over the collapse of the relatively tall and thin droplet tail (observable in Figure 2.13, right) into the larger and wider main droplet body.

Thus, these results demonstrate that the reflection-augmented volume measurement scheme is an effective tool that may be useful for future e-jet printing research, but does not address every artifact associated with video-based measurement, which may serve as the subject of future investigations.

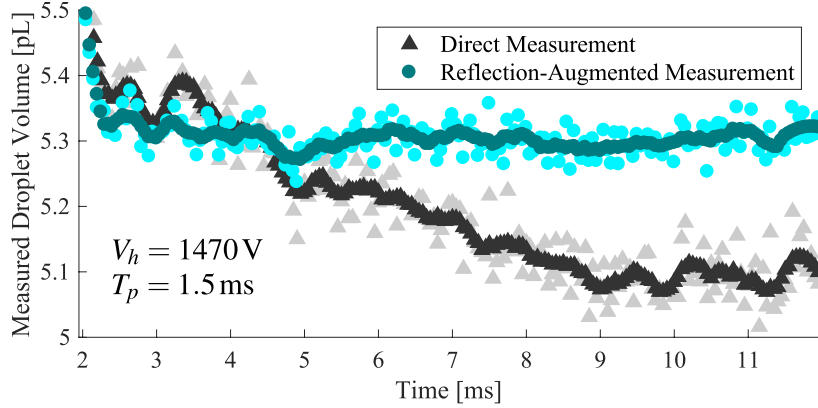


Figure 2.14: Retraction-stage droplet volume measurement taken by direct and reflection-augmented measurement techniques. Light and dark points represent raw and filtered data, respectively. As \mathcal{V}_d is expected to be constant during retraction, this plot illustrates the reflection-augmented technique’s superiority in that it maintains a roughly constant value of 5.3 pL after the transient (i.e. for $t \geq 2.5$ ms), while the direct measurement steadily decreases until about $t = 9$ ms.

2.3.3.2 Deposited Droplet Volume Error

Figure 2.15 presents the mean percent error in the final droplet volume as computed by equation (2.62), for each experiment. The experiment of lowest high voltage ($V_h = 1100$ V) clearly represents an outlier in this data, having a percent error of 130% for the predictions driven by measured nozzle flow rate and 170% for the predictions using simulated nozzle flow rate, more than triple the next highest percent error.

To better discuss this outlying experiment, time series plots of $\mathcal{V}_d(t)$ and a plot of each trial’s estimated jet break position, h_b , versus V_h are presented in Figures 2.16 and 2.17, respectively. From the time series plot, one observes that the reset—the initial step change from zero to non-zero volume—is the most clearly erroneous feature of the low V_h time series. The reset causes a large overestimation of the initial volume in the contiguity stage that cannot be compensated for by the contiguity dynamics models, which only capture the change in droplet volume from the beginning to the end of contiguity.

The plot of h_b in Figure 2.17 lends insight into why this reset error may arise. While the experiments well within the subcritical jetting regime (those from 1150 V to 1420 V) show comparable h_b values, the experiment of lowest V_h shows a jet break position markedly closer to the substrate. Because h_b marks the upper boundary of the droplet control volume (a condition necessary for droplet flow rate to be zero after the jet breaks), this lowered jet break position substantially reduces the fraction of total volume that is in the droplet control volume at the first moment of contiguity. This change in the fraction of total volume is not accounted for by the reset model (2.53), which assumes only the total volume itself is changing (e.g. because of jet diameter variations over

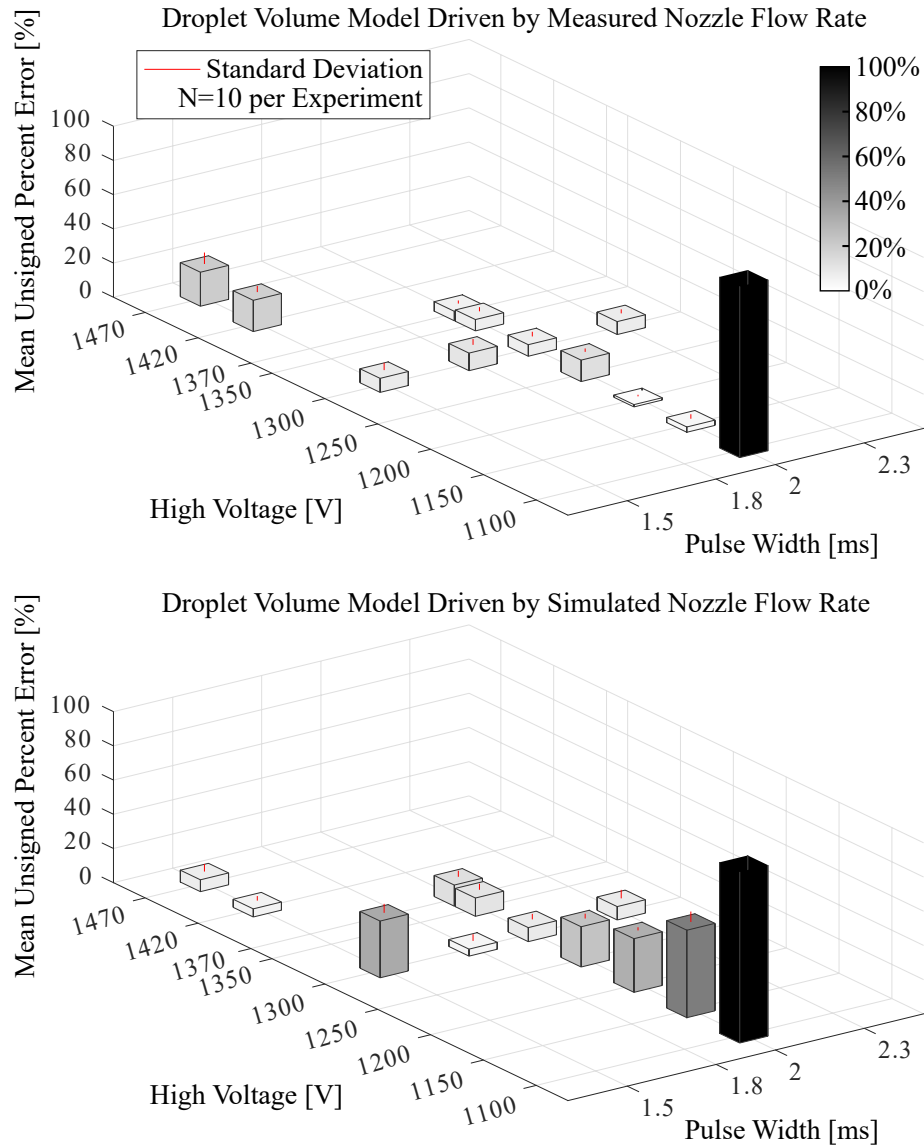


Figure 2.15: Percent error in final deposited droplet volume, $\mathcal{V}_d(t_r)$, using measured and simulated Q . The lowest voltage experiment exceeds 100% error in both cases. Each bar represents the mean value of $N = 10$ samples. Measured Q results illustrate the high quality of equation (2.54) for all but the lowest voltage case. Simulated Q results illustrate increased error associated with increased uncertainty in the cascaded model, motivating future flow rate modeling work.

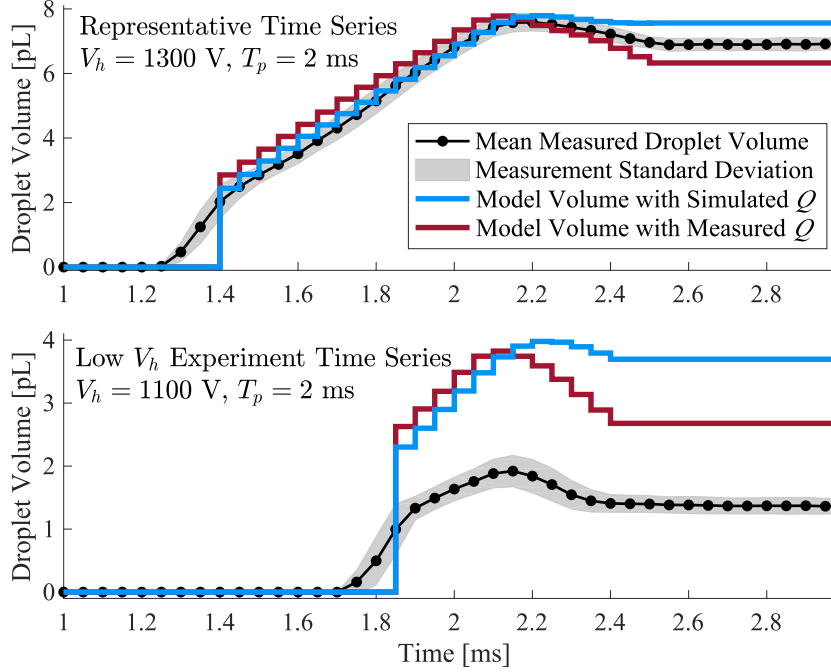


Figure 2.16: Time series plots of droplet volume \mathcal{V}_d for a representative experiment and the experiment of lowest high voltage V_h . Plotted measured data is the mean of the validation data ($N = 10$ samples for each time series) with an envelope of plus or minus the standard deviation. The data suggests that the reset is the main source of error in low V_h experiments.

applied voltage).

Because the given model structure does not account for the changing jet break position near the boundaries of the subcritical jetting regime, the low V_h experiment is deemed to be outside the applicable domain of the model, and is thus removed from the aggregate model error data, given in Figure 2.18. The lower error yielded when the droplet volume model is driven by measured nozzle flow rate illustrates the validity of the Q -to- \mathcal{V}_d model (2.54). When equation (2.54) is driven by the nozzle flow rate simulated by equation (2.58), making a complete model from V to \mathcal{V}_d , the error increases. This is due to increased model uncertainty associated with equation (2.58) and its cascading with equation (2.54). While reducing this model uncertainty will be an important future endeavor, these results demonstrate the foundation of a dynamical V -to- \mathcal{V}_d model that may be integrated with iterative learning control for the sake of e-jet printing control.

2.3.4 Piecewise Affine E-jet Modeling Conclusion

This section presents a hybrid system model framework for dynamical droplet volume modeling in e-jet printing based on contiguity of the fluid jet between the nozzle and the substrate. This overarching modeling framework involves the contributions of several novel model elements whose

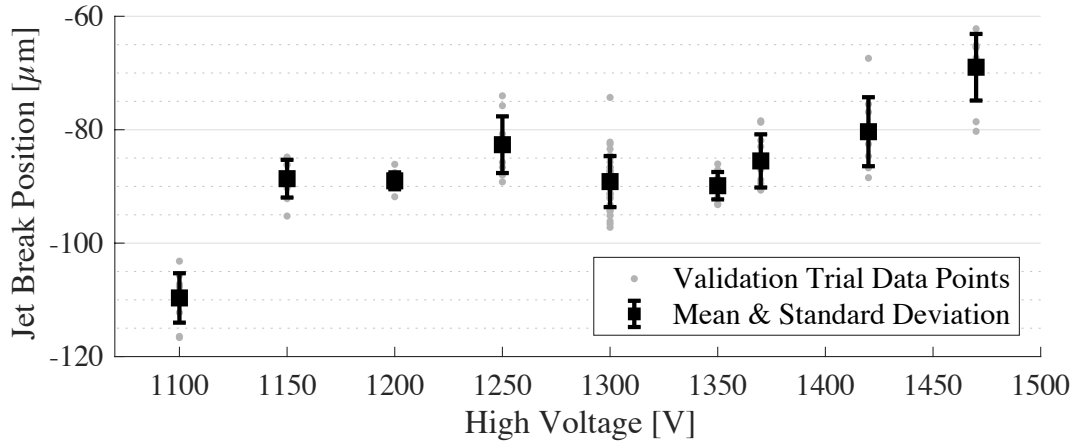


Figure 2.17: Jet break positions of each experiment’s validation data against high voltage. The nozzle outlet is located at $0 \mu\text{m}$ and the substrate at $-150 \mu\text{m}$. $N = 10$ samples for all high voltages except $V_h = 1300$ V, for which $N = 40$ samples because four pulse widths are tested at $V_h = 1300$ V. The modest spread of data points at $V_h = 1300$ V suggests that high voltage (equivalent to the difference between high and low voltage in this data set) has a greater influence on jet break position than pulse width in the subcritical jetting regime.

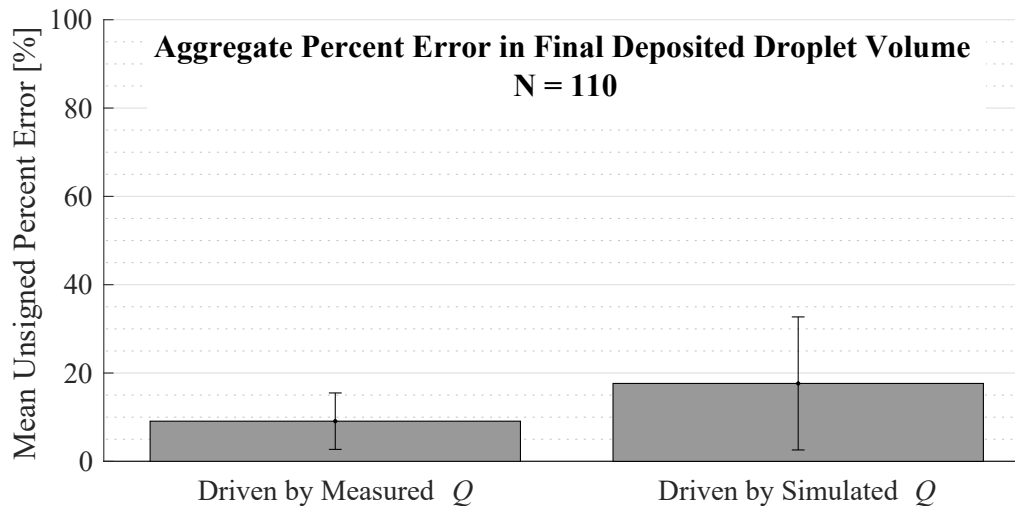


Figure 2.18: Mean unsigned percent error and standard deviation (given by error bars) of final droplet volume over all validation trials except those of lowest high voltage ($N = 110$ samples).

structures are motivated by physical analysis of the material ejection process. These contributions include a new droplet control volume definition enabling the treatment of droplet volume as a dynamically evolving parameter, a dynamical mapping between nozzle flow rate and droplet volume during contiguity, and a reset map circumventing the need for dynamical modeling of droplet volume before contiguity, when data is of limited availability. Additionally, this section contributes a new computer vision method for extracting time series volume data from videos that, while simple, substantially improves the consistency of volume measurements. These contributions are validated with physical experiments that show good model performance in the interior of the subcritical jetting regime, but reveal system behaviors not captured by the model towards the boundaries of the subcritical jetting regime, specifically unmodeled changes in the jet break position.

The presented work thus represents an important step towards model-based control of deposited droplet volume in e-jet printing. To further pursue this goal, future work will focus on refining the reset model to account for the entire subcritical jetting regime, and on finding an ideal balance between simplicity and fidelity in applied-voltage-to-nozzle-flow-rate models. Finally, relaxation of the time-based switching assumption and reintroduction of meniscus position as the switching criterion, and thus as a dynamical state, will substantially improve the flexibility and utility of the droplet volume modeling framework.

2.4 Overarching E-jet Printing Conclusion

This chapter has contributed two hybrid models for e-jet printing: one focused on fidelity to the first principles of the physical system and the other on capturing the final volume of the droplet on the substrate.

Specifically, the former contributes new geometrical and equilibrium analysis, extending the amount of the ejection process that can be modeled by first principles and reducing model reliance on measured data. Additionally, Section 2.2 introduces and validates hybrid modeling as a means to merge physics-driven modeling with data-driven modeling to produce an ODE-based model of the end-to-end electrohydrodynamic ejection process.

The latter hybrid model of Section 2.3 introduces an alternative division of the total ejection process into partial process and defines a new CV for droplet volume. These contributions enable dynamical modeling of the droplet volume ultimately deposited on the substrate via PWA framework.

The bigger picture delivered by this chapter is that e-jet printing exemplifies a class of physical systems for which hybrid modeling is thus far the only path to ODE-based modeling, and thus to control-oriented modeling. E-jet printing also represents a class of systems for which ILC is necessary to improve performance because of the impracticality of real-time feedback. Thus, while it

is certainly not the only motivation, e-jet printing provides a concrete motivation for the integration of hybrid systems theory and ILC theory, upon which the subsequent chapters focus. Finally, because e-jet's modeling and control challenges are shared by numerous other AM technologies, the validation of this modeling philosophy may lower the boundary for the development of similar models for these AM processes. Fused Deposition Modeling (FDM), perhaps the most ubiquitous AM technology, serves as a prime example. While formal hybrid modeling has not been attempted, [85] identifies several distinct regimes for the filament deposition dynamics. As these regimes arise due to the physical state of the printhead and filament, these dynamics may be well-unified by a hybrid framework.

CHAPTER 3

Enabling ILC of Hybrid Systems: Closed-Form Hybrid System Representation

In most cases, even when hybrid system control takes inspiration from preexisting control theories, significant work must be done to redevelop the theory specifically for hybrid systems [45, 86, 87]. One reason for this difficulty is that the hybrid systems are, in general, mathematically represented as a type of automaton [1, 3] rather than as a closed-form system of ODEs as is typical for control systems. This lack of a closed-form system representation prevents the direct application of many analytical mathematical operations that would ordinarily accompany dynamical system analysis and controller design (e.g. function composition, Jacobian).

The importance of performing such operations on piecewise functions, and thus the importance of having closed form representations of piecewise functions, was originally identified by the nonlinear circuit theory community well before the modern notion of hybrid systems were developed. In fact, in 1977 Chua and Kang published a canonical, closed-form representation of piece-wise linear functions to close this gap [88]. However, their representation was not designed with dynamical systems in mind, and thus has several features making it incompatible with hybrid systems analysis and control. Most importantly, it is based on interpolation between the breakpoints of the piecewise functions, precluding it from representing nonlinear dynamics within a particular discrete state. Secondly, rather than representing each “piece” of a piecewise function independently, [88] treats each “piece” as a superposition of components from all “pieces” corresponding to lesser values of the independent variable. Finally, higher dimensional functions are represented by nesting functions of 1 or 2 dimensions, which results in structures far more convoluted than the state-space models employed by today’s control engineers.

Content of this chapter also published as:

I. A. Spiegel and K. Barton, “A Closed-Form Representation of Piecewise Defined Systems and their Integration with Iterative Learning Control,” in *2019 American Control Conference (ACC)*, Philadelphia, PA, USA, 2019, pp. 2327-2333, <https://doi.org/10.23919/ACC.2019.8814823> ©IEEE 2019. Reprinted with permission.

In the more contemporary literature, Bemporad and Morari’s seminal Mixed Logical Dynamical (MLD) Systems seek to provide a more analytical hybrid system representation, which is composed entirely of systems of algebraic equalities and inequalities [89]. However, like the systems of [88], MLD systems cannot contain nonlinear dynamics within a discrete state. More importantly, while MLD systems integrate readily with control frameworks that involve online optimization, such as Model Predictive Control (MPC), they can be difficult to integrate with other classes of controllers because they require the solution of a mixed integer program at each time step to determine the system’s discrete state.

This restriction on controller options is particularly problematic when real time feedback is unavailable, or when model errors are substantial enough to prevent the fulfillment of performance goals. In such cases, ILC is attractive. However, to date no implementation of ILC has been made with hybrid system models. This is in part because the mathematical operations required to synthesize the controller cannot be performed on contemporary hybrid system representations.

The primary contribution of the present chapter is to deliver a closed-form representation of a particular class of hybrid systems: PWD systems (i.e. a generalization of the popular PWA system class). This closed-form representation is shown to bridge the gap between system representation and control via the application of ILC to an example hybrid system. Minor contributions are made to the selected ILC method (applicable to both hybrid and non-hybrid systems): it is reformalized to enable application to systems of any relative degree, and a novel recommendation is made vis-à-vis implementation in order to facilitate direct application of the control theory and to improve controller scalability. No special modifications are made for the hybrid nature of the example system, thereby illustrating the utility of the closed-form representation.

The rest of the chapter is organized as follows. Section 3.1 presents the closed-form piecewise defined system representation, i.e. this work’s main contribution, via a proposition and constructive proof. Section 3.2 details the iterative learning controller to be used. Section 3.3 presents the example hybrid system, the methods of controller performance analysis, and presents and discusses the results of the simulation experiments. Finally, Section 3.4 provides concluding remarks and suggests future work.

3.1 Closed Form Piecewise Defined Systems

Definition 3.1 (PWD System). A discrete-time PWD system is a system defined by

$$\begin{aligned} x(k+1) &= f_q(x(k), u(k), k) \\ y(k) &= h_q(x(k), u(k), k) \end{aligned} \quad \text{for } \begin{bmatrix} x(k) \\ u(k) \end{bmatrix} \in Q_q \quad (3.1)$$

where k is the discrete time index, $x \in \mathbb{R}^{n_x}$ is the state vector, $u \in \mathbb{R}^{n_u}$ is the control input, $y \in \mathbb{R}^{n_y}$ is the output vector, $q \in \{1, 2, \dots, |Q|\}$, $Q_q \in Q = \{Q_1, Q_2, \dots, Q_{|Q|}\}$ is a convex polytope (i.e. an intersection of half-spaces) in $\mathbb{R}^{n_x+n_u}$, $f_q : \mathbb{R}^{n_x} \times \mathbb{R}^{n_u} \times \mathbb{Z} \rightarrow \mathbb{R}^{n_x}$ is a closed-form function representing the potentially nonlinear state dynamics in Q_q , and $h_q : \mathbb{R}^{n_x} \times \mathbb{R}^{n_u} \times \mathbb{Z} \rightarrow \mathbb{R}^{n_y}$ is the potentially nonlinear closed-form output function in Q_q . All polytopes in Q are disjoint, and their union is equal to $\mathbb{R}^{n_x+n_u}$.

The following theorem and constructive proof constitute the primary contribution of this chapter.

Theorem 3.1 (Closed-Form PWD System Representation). *Any PWD system (3.1) can be represented in closed form as*

$$\begin{aligned} x(k+1) &= f(x(k), u(k), k) \\ y(k) &= h(x(k), u(k), k) \end{aligned} \quad (3.2)$$

where f and h explicitly encapsulate both the component dynamics and switching behavior of the PWD system.

Proof. Because Q_q are convex polytopes, their boundaries are hyperplanes, which can be represented via

$$p^T \begin{bmatrix} x(k) \\ u(k) \end{bmatrix} = b \quad (3.3)$$

where $p \in \mathbb{R}^{n_x+n_u}$ describes the orientation of the hyperplane and $b \in \mathbb{R}$ is an offset. To capture the partitioning of $\mathbb{R}^{n_x+n_u}$ into $|Q|$ regions by n_P hyperplanes in the system dynamics, this work introduces the auxiliary logical state vector

$$\begin{aligned} \delta(k) &= f_\delta(x(k), u(k)) = H \left(P \begin{bmatrix} x(k) \\ u(k) \end{bmatrix} - \beta \right) \\ P &= \begin{bmatrix} p_1 & p_2 & \dots & p_{n_P} \end{bmatrix}^T \\ \beta &= \begin{bmatrix} b_1 & b_2 & \dots & b_{n_P} \end{bmatrix}^T \end{aligned} \quad (3.4)$$

where H is the element-wise Heaviside step function¹ with convention $H(0) = 1$, and the relationship between $|Q|$ and n_P depends on the exact configuration of the hyperplanes. The i^{th} element of δ indicates on which side of the i^{th} hyperplane the system vector $\begin{bmatrix} x(k)^T & u(k)^T \end{bmatrix}^T$ falls (with points on hyperplanes being included in the space corresponding to $p_i^T \begin{bmatrix} x(k)^T & u(k)^T \end{bmatrix}^T - b_i > 0$,

¹Some communities may not consider the Heaviside function to be closed-form. Many others do [90, 91, 92, 93, 94, 95, 96]. This classification as closed-form is supported by its seamless integration into most symbolic math software, in which its derivative is well-defined.

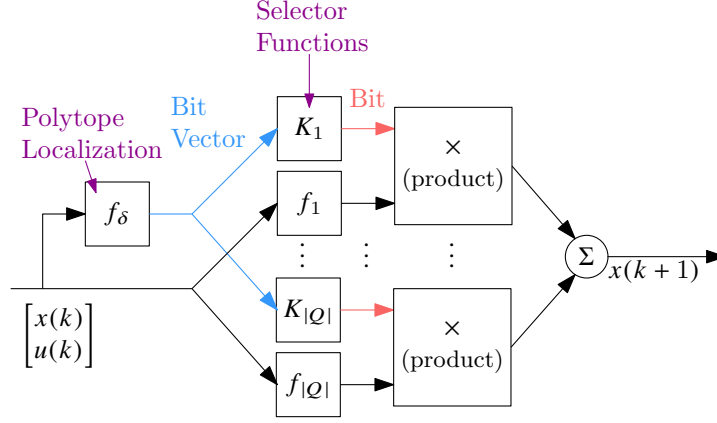


Figure 3.1: Block diagram of the closed-form PWD system representation

see Remark 3.2). In this manner, each Q_q uniquely corresponds to a particular value of δ , which will be denoted δ_q^* .

As the system evolves δ will be compared to each δ_q^* via a set of selector functions given by

$$K_q(\delta(k)) = 0^{\|\delta_q^* - \delta(k)\|} = \begin{cases} 1 & \delta_q^* = \delta(k) \\ 0 & \delta_q^* \neq \delta(k) \end{cases} \quad (3.5)$$

Note that this equation is equivalent to the Kronecker delta of 0 and $\|\delta_q^* - \delta(k)\|$ for any norm, but is left in the given zero exponential form for explicitness.

With these selector functions, the original state dynamics and outputs can be represented by the closed-form equations

$$\begin{aligned} x(k+1) &= f(x(k), u(k), k) = \sum_{q=1}^{|Q|} f_q(x(k), u(k), k) K_q(f_\delta(x(k), u(k))) \\ y(k) &= h(x(k), u(k)) = \sum_{q=1}^{|Q|} h_q(x(k), u(k), k) K_q(f_\delta(x(k), u(k))) \end{aligned} \quad (3.6)$$

This completes the closed-form representation of (3.1). A block diagram of the representation's structure is given in Figure 3.1 □

Remark 3.1 (Continuity). This representation makes no assumptions regarding the continuity of either the state transition formula f or the output function h over the switching hyperplanes. The representation may model both continuous and discontinuous hybrid systems.

Remark 3.2 (Hyperplane Inclusion in Polytopes). The use of the Heaviside function in equation (3.4) systematically includes each hyperplane in the polytopes lying to a particular side. In other

words, a hyperplane serving as a boundary/face for two adjacent polytopes is included in only one of them, such that one polytope is closed on that face and the other polytope is open. To which side the hyperplane belongs can be chosen by manipulation of P and β . For example, $(P = [0, 1], \beta = 0)$ and $(P = [0, -1], \beta = 0)$ both define the horizontal axis in \mathbb{R}^2 . Under (3.4), the former definition yields the same value of δ ($\delta = 1$) for points on the hyper plane *and* in top half of \mathbb{R}^2 , while the bottom half of \mathbb{R}^2 *excluding* the horizontal axis yields $\delta = 0$. The latter definition yields $\delta = 1$ for the hyperplane *and* the *bottom* half of \mathbb{R}^2 , while the top half of \mathbb{R}^2 *excluding* the hyperplane yields $\delta = 0$. In this manner, the hyperplane can be included in either the top or bottom polytope, but not both. The inability to include the hyperplane in both polytopes is desirable because if the polytopes have a non-null intersection there is uncertainty regarding the state dynamics in the intersection.

In many cases this method of determining which polytope contains a face (i.e. which polytope is closed) and which polytope is open at the same face is amply flexible, and ensures that there are an equal number of polytopes and δ^* values. However, if a system designer desires greater flexibility, the Heaviside function can be replaced with the signum function. In this case, each polytope interior and each face uniquely corresponds to a different δ , and the designer must assemble the complete polytope from an interior and the desired faces. For example, if Q_q corresponds to the interior and face associated with $\delta_{q,1}^*$ and $\delta_{q,2}^*$, then $K_q(\delta) = 0 \left\| \delta_{q,1}^* - \delta(k) \right\| \left\| \delta_{q,2}^* - \delta(k) \right\|$.

Remark 3.3 (Location Non-Convexity and Switching Condition Nonlinearity). Despite the convexity requirements of the $\mathbb{R}^{n_x+n_u}$ partitioning, and consequential affine-in- x requirement of the switching behavior governed by equations (3.4) and (3.5), the representation (3.6) can encompass a wide range of complex system structures. There need not be a one-to-one correspondence between the quantity of discrete dynamic regimes and the quantity of polytopes in system (3.6). Indeed, while each polytope Q_q must be convex, one may construct many interesting nonconvex topologies by stitching together adjacent polytopes Q_e and Q_d by setting $f_e = f_d, h_e = h_d$. This is illustrated in Figure 3.2. Additionally, nonlinear switching conditions such as $\sin(x^i) > 0$ (where x^i is the i^{th} element of x) can obviously be accommodated by simply making the nonlinear expression of x into a new state. This of course increases the dimension of the system, but it notably does *not* increase the dimension of the NILC problem, which depends solely on the outputs and quantity of samples in a trial timeseries.

3.2 Newton Iterative Learning Control

NILC, first introduced in terms of abstract Banach space operators by [34], is the use of the Newton-Raphson root-finding algorithm to derive a trial-varying learning matrix L_ℓ for the classi-

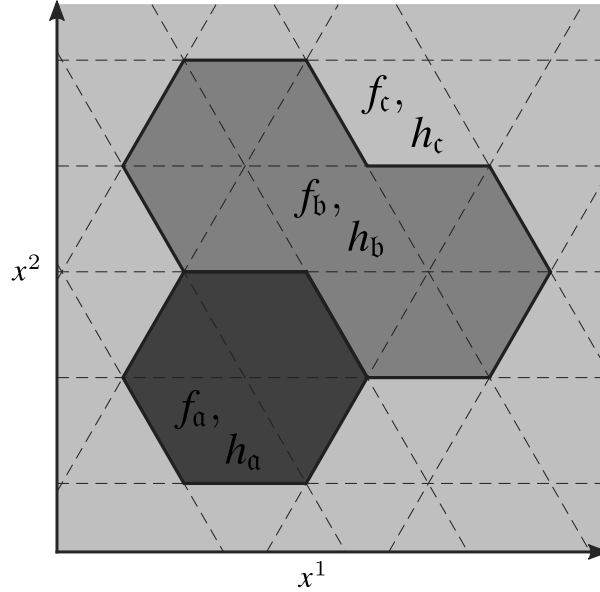


Figure 3.2: An \mathbb{R}^2 topology representable by (3.6) with 14 hyperplanes (dashed lines) having 1 convex (a) and 2 nonconvex (b and c) dynamic regimes.

cal ILC law

$$\mathbf{u}_{\ell+1} = \mathbf{u}_{\ell} + L_{\ell} \mathbf{e}_{\ell} \quad (3.7)$$

where \mathbf{u} is a control input timeseries vector, or “lifted” vector, \mathbf{e} is a lifted error vector, and $\ell \in \{0, 1, \dots\}$ is the trial index².

NILC was first formalized for discrete-time state space systems by [36]. However, the treatment of NILC in [36] is limited in that it only considers time-invariant systems and is only applicable to systems with a relative degree, μ , of 1. For discrete-time systems, the relative degree of an output is the number of time steps that must transpire before the explicit representation of the output, in terms of inputs and initial conditions, contains any input [97]. In many cases this notion of relative degree is adequate for the synthesis of NILC from PWD systems. However, there are also PWD models for which alternative notions of relative degree are useful for managing issues related to the switching behavior of hybrid systems. A rigorous treatment of such issues and the definition of an alternative relative degree is given in Chapter 5. For now, the present section presents an NILC framework generalized for time-varying discrete-time SISO systems of any relative degree ≥ 1 . For all systems, the purpose of incorporating knowledge of the relative degree into NILC synthesis is to guarantee that L_{ℓ} is well-defined regardless of model relative degree. Specifically, L_{ℓ} being well-defined is contingent on L_{ℓ} being invertible, and any notion of relative degree yielding

²In the literature, j or k is usually used for the trial index. Here, ℓ is used for the trial index because i and j will be used for matrix element indexing, k is used for the discrete time index, t is avoided to prevent confusion with continuous time, and ℓ is the next letter in the alphabet and thus commonly used for indexing.

this invertibility is acceptable.

Consider the SISO, discrete-time time-varying nonlinear model

$$\hat{x}_\ell(k+1) = \hat{f}(\hat{x}_\ell(k), u_\ell(k), k) \quad (3.8a)$$

$$\hat{y}_\ell(k) = \hat{h}(\hat{x}_\ell(k)) \quad (3.8b)$$

where $\hat{x} \in \mathbb{R}^{n_x}$, $u \in \mathbb{R}$, $\hat{y} \in \mathbb{R}$, $f : \mathbb{R}^{n_x} \times \mathbb{R} \times \mathbb{Z} \rightarrow \mathbb{R}^{n_x}$, and $h : \mathbb{R}^{n_x} \rightarrow \mathbb{R}$. Hats, $\hat{\cdot}$, are used to emphasize that (3.8) is an imperfect model of some true system, though it is assumed that the control input and initial condition are perfectly known.

Let the system describe a repetitive process with finite duration. This translates to the assumptions:

(A3.1) A trial must have a duration of N time steps,

$$k \in \{0, 1, \dots, N\}.$$

(A3.2) The initial conditions are trial invariant,

$$\hat{x}_\ell(0) = x_0 \quad \forall \ell.$$

(A3.3) The desired output values, $r(k) \in \mathbb{R}$, are trial invariant.

By (A3.1), the input and output trajectories can be represented as timeseries vectors of the same length for every trial:

$$\hat{\mathbf{y}}_\ell = \begin{bmatrix} \hat{y}_\ell(\mu) & \hat{y}_\ell(\mu+1) & \cdots & \hat{y}_\ell(N) \end{bmatrix}^T \in \mathbb{R}^{N-\mu+1} \quad (3.9)$$

$$\mathbf{u}_\ell = \begin{bmatrix} u_\ell(0) & u_\ell(1) & \cdots & u_\ell(N-\mu) \end{bmatrix}^T \in \mathbb{R}^{N-\mu+1} \quad (3.10)$$

Note that $\hat{\mathbf{y}}_\ell$ is time-shifted forward by the relative degree μ , which is a function of the specific definitions of f and h .

By (A3.2) and (3.8), if x_0 is known then $\hat{\mathbf{y}}_\ell$ is entirely a function \mathbf{u}_ℓ given by $\hat{\mathbf{g}} : \mathbb{R}^{N-\mu+1} \rightarrow \mathbb{R}^{N-\mu+1}$

$$\hat{\mathbf{y}}_\ell^i = \hat{\mathbf{g}}^i(\mathbf{u}_\ell) = \hat{y}_\ell(\mu+i-1) \quad (3.11a)$$

$$\hat{y}_\ell(k) = \hat{h}\left(\hat{f}^{(k-1)}(\mathbf{u}_\ell)\right) \quad k \in \{\mu, \mu+1, \dots, N\} \quad (3.11b)$$

where the non-parenthetical superscript i denotes the i^{th} element of a vector, indexing from 1, and the parenthetical superscript (k) denotes function composition of the form

$$\hat{f}^{(k)}(\mathbf{u}_\ell) = \hat{f}(\hat{x}_\ell(k), u_\ell(k), k) = \hat{f}\left(\hat{f}\left(\cdots, u_\ell(k-1), k-1\right), u_\ell(k), k\right) \quad (3.12)$$

The recursion of the state dynamics f expressed by (3.12) has a terminal condition of $\hat{f}(\hat{x}_\ell(0), \mathbf{u}_\ell(0), 0)$. Because $\hat{x}_\ell(0) = x_0$ is known in advance and the time argument is determined by the element index of the lifted representation, $\hat{\mathbf{y}}_\ell$ is a function of only \mathbf{u}_ℓ . Note that because the first element of $\hat{\mathbf{y}}_\ell$ is $\hat{y}_\ell(\mu)$ it explicitly depends on $\mathbf{u}^1 = \mathbf{u}_\ell(0)$.

Similarly, by (A3.3), the reference

$$\mathbf{r} = \begin{bmatrix} r(\mu) & r(\mu+1) & \cdots & r(N) \end{bmatrix}^T \in \mathbb{R}^{N-\mu+1} \quad (3.13)$$

is fixed, causing the output error timeseries, \mathbf{e}_ℓ to be approximable by a function of only \mathbf{u}_ℓ . This relationship is given by

$$\mathbf{e}_\ell(\mathbf{u}_\ell) = \mathbf{r} - \mathbf{y}_\ell = \mathbf{r} - \mathbf{g}(\mathbf{u}_\ell) \approx \mathbf{r} - \hat{\mathbf{g}}(\mathbf{u}_\ell) \quad (3.14)$$

where $\mathbf{g} : \mathbb{R}^{N-\mu+1} \rightarrow \mathbb{R}^{N-\mu+1}$ represents the unknowable dynamics of the true system, and \mathbf{y}_ℓ is the measured value of this true system output. Newton's method can thus be applied to iteratively find an argument \mathbf{u}_ℓ bringing $\mathbf{e}_\ell(\mathbf{u}_\ell)$ toward 0. This naturally yields a control law of the form (3.7) with

$$L_\ell = \left(\frac{\partial \hat{\mathbf{g}}}{\partial \mathbf{u}}(\mathbf{u}_\ell) \right)^{-1} \quad (3.15)$$

where $\frac{\partial \hat{\mathbf{g}}}{\partial \mathbf{u}}$ is the Jacobian (in numerator layout) of $\hat{\mathbf{g}}$ with respect to \mathbf{u} as a function of \mathbf{u} .

However, (3.7), (3.15) is not strictly Newton's method applied to \mathbf{e}_ℓ because $\hat{\mathbf{g}}(\mathbf{u}_\ell)$ is, like all models, only an approximation of the true physical dynamics $\mathbf{g}(\mathbf{u}_\ell)$. Because of this, convergence of \mathbf{y}_ℓ to \mathbf{r} is linear (rather than quadratic) and guaranteed if the following sufficient conditions are satisfied [34].

(A3.4) The true dynamics $\mathbf{g}(\mathbf{u}_\ell)$ are continuously differentiable and their Jacobian $\frac{\partial \mathbf{g}}{\partial \mathbf{u}}$ is Lipschitz continuous with respect to \mathbf{u} within some ball around the solution trajectory \mathbf{u}_{soln} .

(A3.5) The inverse of the model Jacobian (i.e. the learning matrix) always has a bounded norm:

$$\|L_\ell\|_2 < \varepsilon_1 \in \mathbb{R}_{>0} \quad \forall \ell$$

(A3.6) The learning matrix is sufficiently similar to the inverse of the true lifted system Jacobian:

$$\left\| I - L_\ell \frac{\partial \mathbf{g}}{\partial \mathbf{u}}(\mathbf{u}_\ell) \right\|_2 < 1 \quad \forall \ell$$

(A3.7) The initial guess \mathbf{u}_0 is in some basin of attraction around the solution \mathbf{u}_{soln} (guaranteed to exist by (A3.4)-(A3.6)),

$$\|\mathbf{u}_0 - \mathbf{u}_{\text{soln}}\|_2 < \varepsilon_2 \in \mathbb{R}_{>0}$$

Note that the continuous differentiability and Lipschitz continuity conditions are on the sufficient condition for the true system, not the model.

In the implementation of this controller, the Jacobian as a function of \mathbf{u}_ℓ only needs to be derived once (in advance of trial 0). Still, large sample quantities (i.e. long trial durations and/or high temporal resolution) have historically made deriving this matrix a significant computational burden. This has forced past authors to approximate $\frac{\partial \hat{\mathbf{g}}}{\partial \mathbf{u}}$ using techniques ranging from the coarse and simple chord method [34], to more accurate but computationally expensive methods like gradient-based optimization [98]. However, advances in automatic differentiation techniques, such as those in the software tool CasADi [37], now enable rapid derivation of Jacobian functions that are exact to nearly machine precision [38]. This largely eliminates the need for Jacobian approximation methods in many scenarios where a system model is available.

Finally, note that the class of systems (3.1) treated by the closed-form representation in this work is broader than the class of systems (3.8) to which the controller may be applied, and that (3.8) itself is broader than the class of systems guaranteed to satisfied (A3.4)-(A3.6). However, this work chooses to present a broad closed-form representation both because there may be other controllers for which the representation is useful, and because there exists systems of class (3.1) that do converge under the given controller and are not contained by narrower popular subclasses such as piecewise affine and affine-in-the-input systems. An example of such a system is given in Section 3.3.

3.3 Validation

This section demonstrates both the closed form system representation and NILC through the simulated control of a nonlinear mass-spring-damper system over an increasing degree of mismatch between the truth model and control model.

3.3.1 Model and Software Implementation

The truth model is given by the continuous-time mass-spring-damper system pictured in Figure 3.3. The system's equation of motion is

$$\ddot{y}(t) = -\frac{\kappa}{m}y(t)^3 - \frac{\nu}{m}\dot{y}(t) + \frac{\rho_0}{m}u(t) + \frac{\rho_1}{m}\tan^{-1}(u(t)) \quad (3.16)$$

$$\kappa = \begin{cases} \kappa_0 & y(t) > 0 \\ \kappa_1 & y(t) \leq 0 \end{cases} \quad (3.17)$$

where $y(t)$ is the displacement of the mass from the neutral position (positive in direction of spring extension), $u(t)$ is an applied actuator voltage, m is the mass, κ is the stiffness coefficient, ν is

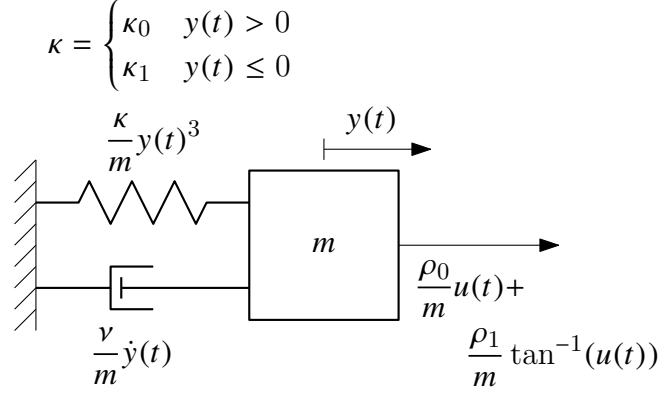


Figure 3.3: Mass-spring-damper system used for validation. The spring stiffness is a piecewise defined function of the spring extension and the applied force is a nonlinear function of actuator voltage u .

a damping coefficient, and ρ_0, ρ_1 are constant coefficients mapping from applied voltage to applied force. The stiffness coefficient depends on whether the system is in compression (softer) or extension (stiffer), and the spring hardens with displacement in either direction due to the cubic exponent on $y(t)$ in (3.16). The “measurements” given to the controller after each trial are generated from this model using Runge Kutta 4-step integration and a step size of $T_s = 0.001$ s.

The controller itself requires a discrete time model, which is derived from (3.16) using the forward Euler method. This yields output and switching equations identical to those of the continuous-time system, but the state dynamics become

$$\hat{x}(k+1) = \begin{bmatrix} \hat{y}(k+1) & \hat{y}(k+2) \end{bmatrix}^T \quad (3.18)$$

where

$$\hat{y}(k+2) = 2\hat{y}(k+1) - \hat{y}(k) + \frac{\hat{T}_s^2}{\hat{m}} \left(-\hat{\kappa}\hat{y}(k)^3 - \frac{\hat{v}}{\hat{T}_s}\hat{y}(k+1) + \hat{\rho}_0 u(k) + \hat{\rho}_1 \tan^{-1}(u(k)) \right) \quad (3.19)$$

where $\hat{T}_s = 0.01$ s, an order of magnitude coarser than the truth model. This model is nonlinear in the states and the input, has relative degree $\mu = 2$, 2 dynamic regimes and can be represented in closed form with one auxiliary variable. The hyperplane corresponding to this auxiliary variable is given by

$$P = \begin{bmatrix} -1 & 0 & 0 \end{bmatrix} \quad \beta = \begin{bmatrix} 0 \end{bmatrix} \quad (3.20)$$

which gives rise to 2 polytopes.

Note that because neither the switching function nor the output function in equation (3.17) depends on the input, and because the system is SISO, this system’s closed form representation

(3.6) is equivalent to (3.8), the system form accepted by the ILC.

Assumptions (A3.1)-(A3.3) are enforced as follows. Each trial lasts 9.5 seconds (approximately 3π seconds), making the length of $\hat{\mathbf{g}}(\mathbf{u}_\ell)$ equal to $N - \mu + 1 = 949$. The trial invariant initial conditions are 0 for both $\hat{y}(k)$ and $\hat{y}(k + 1)$. The trial invariant reference is chosen to be

$$r(k) = \begin{cases} \sin((k - 1)\hat{T}_s) & k > 0 \\ 0 & k = 0 \end{cases} \quad (3.21)$$

where the delay in the sinusoid and the leading 0 ensure that the reference does not demand that the controller alter the initial conditions.

For the derivation of the control law (3.7), (3.15) from the closed form system representation, this work uses the open source software tool CasADi. CasADi is chosen because its combination of symbolic framework, sparse matrix storage, and automatic differentiation make for the rapid computation of exact $\hat{\mathbf{g}}(\mathbf{u}_\ell)$ and $\frac{\partial \hat{\mathbf{g}}}{\partial \mathbf{u}}$ functions. However, the Heaviside function in CasADi uses the trinary “0.5-at-origin” convention rather than the binary “1-at-origin” convention, making it equivalent to signum in the context of determining on which side of a hyperplane a point lies. Because of this, selector functions in CasADi must be written by assembling the polytope interiors and faces as in Remark 3.2. Here this assembly is done to be equivalent to a “1-at-origin” Heaviside convention.

3.3.2 Methods

There are two simulation design objectives. The first is to assess the utility of the closed form system representation in enabling the control of a hybrid system via a controller developed for non-hybrid systems. The second is to assess the sensitivity of the combination of NILC with this system representation. Here, “sensitivity” is characterized by the likelihood that the controller will diverge given a particular degree of modeling error. Both of these goals are accomplished with simulations wherein the controller is synthesized via increasingly erroneous models and its convergence behavior is analyzed.

In this study, a “simulation” is an attempt to produce \mathbf{r} within 20 process trials under NILC for a particular set of mismatched truth and control model parameters. The control model is identical for all simulations, with parameters given by the vector

$$\hat{\theta} = \begin{bmatrix} \hat{m} & \hat{\rho}_0 & \hat{\rho}_1 & \hat{\nu} & \hat{\kappa}_0 & \hat{\kappa}_1 \end{bmatrix}^T \quad (3.22)$$

$$= \begin{bmatrix} 1 & 1 & 1 & 1 & 4 & 1 \end{bmatrix}^T \quad (3.23)$$

The truth model parameters are perturbations of the control model parameters by a random relative error. Mathematically this is given by the random vector

$$\theta = \left(\mathbf{1}_{6 \times 1} e_{\theta}^T \odot I + I \right) \hat{\theta} \quad (3.24)$$

where $\mathbf{1}_{6 \times 1} \in \mathbb{R}^6$ is a vector with every element equal to 1, $e_{\theta} \in \mathbb{R}^6$ is a random vector, \odot is the matrix Hadamard product, and I is the identity matrix. Each element of e_{θ} is the (positive or negative) relative error

$$e_{\theta}^i = \frac{\theta^i - \hat{\theta}^i}{\hat{\theta}^i} \quad (3.25)$$

and is regenerated for each simulation. A scalar parameter describing the degree of modeling error can thus be given by $\|e_{\theta}\|_2$.

Simulations are organized with respect to increasing $\|e_{\theta}\|_2$. There are 20 sets of 50 simulations each. Sets are defined by bounds on $\|e_{\theta}\|_2$, and each simulation in a set is characterized by a random e_{θ} such that $\|e_{\theta}\|_2$ falls within the specified bounds. These bounds are given by 0.05 increments from 0 to 1. For the sake of comparison, one additional simulation is run with zero modeling error ($\|e_{\theta}\|_2 = 0$). To ensure the model mismatch is truly 0, the truth model in this simulation is taken to be the forward Euler discrete model rather than a Runge Kutta integration of the continuous model.

The efficacy of the controller in a simulation is quantified by the normalized root mean square error (NRMSE) between \mathbf{r} and \mathbf{y}_{20} . The RMSE is normalized by the amplitude of \mathbf{r} , which in this work is 1. Thus the normalization does not alter the numerics here, but it formally nondimensionalizes the results. \mathbf{y}_{ℓ} is said to have ‘‘completely’’ converged to \mathbf{r} if this NRMSE is less than 0.005.

Holistic analysis of the integration of the closed-form system representation and ILC is based on the spread of NRMSE values over all sets and the average trajectory of NRMSE versus trial number ℓ for all completely convergent simulations. Comparisons between simulation sets are made by the percentage of simulations within each set that completely converge.

3.3.3 Results & Discussion

For the controller derivation, on a desktop computer with 16 GB of RAM and a 4 GHz CPU, CasADi performs the repeated function composition to acquire $\hat{\mathbf{g}}$ and the differentiation to acquire the 949-by-949 Jacobian $\frac{\partial \hat{\mathbf{g}}}{\partial \mathbf{u}}$ in 29 seconds. Once these functions are derived for the first time, before the first learning operation, they need not be derived again, and can be called ordinarily to generate the trial-varying learning matrix for each subsequent trial. MATLAB symbolic toolbox is used as a traditional symbolic math tool for comparison on the same task. MATLAB fails to com-

plete the task, running out of memory after 1.3 hours. This illustrates the substantial computational advantage of automatic differentiation in this context, and its ability to enable direct application of Newton’s method in ILC.

To confirm the efficacy of the combination of NILC and the closed-form hybrid system representation, Figure 3.4 presents the trajectory of output convergence over trial iteration. The controller reaches the complete convergence threshold in 8 trials under 0 model error, in 12 trials for the mean trajectory over all convergent simulations with erroneous models, and in 14 trials for a simulation with one standard deviation greater NRMSE than the mean trajectory. This illustrates that while increases in model error can slow convergence, this retardation is modest. Additionally, it can be noted that nearly all experiments (96.5%) either completely converge or diverge entirely, yielding final trial NRMSE values in excess of the zero-input NRMSE. This is illustrated by the large gap in the Figure 3.4 histogram between the final-trial RMSEs. The remaining experiments are either almost convergent (likely requiring several more trials to completely converge), or are divergent but with the “blowing up” limited to very few points at the very end of the timeseries, thereby having only a small affect on NRMSE. Finally, to supplement above statistical analysis and to show that the converged simulations indeed yield qualitatively reasonable input trajectories, the timeseries data for a representative simulation is shown in Figure 3.5.

The results in the preceding paragraph follow the convergence behavior predicted by [34] for a generic input-output model under NILC with static modeling error. The adherence of this work’s results to prior predictions illustrates that, as expected, the hybrid nature of the example system does not intrinsically necessitate special accommodation in the controller. Instead, all that is needed to apply the controller is the closed-form input-output model, the construction of which is enabled by the closed-form piecewise defined system representation presented.

Finally, to practically evaluate (A3.6), Figure 3.6 gives the percentage of experiments that converge within each experiment set. Up to $\|e_\theta\|_2 = 0.15$, 100% of the experiments converge. Beyond a relative model error of 0.15, the convergent experiment percentage decays in a reasonably linear fashion. Taking the conservative assumption that the probability of experiment convergence begins to decay for model error greater than 0, a linear least squares model yields a decay rate of -49% convergence probability per unit increase in relative model error (or -0.49 percent convergence probability per unit increase in percent model error), with an RMSE of 6% between the decay model and data.

Naturally, the convergence probability of other systems may behave differently under increasing $\|e_\theta\|_2$, and the above analysis clearly does not constitute a definitive theory. However, because the set of values of e_θ for which (A3.6) is satisfied is usually impossible to compute in practice (because \mathbf{g} is unknown), it is important to have practical references for understanding system convergence. Because mass-spring-damper-like oscillators are ubiquitous across most fields of

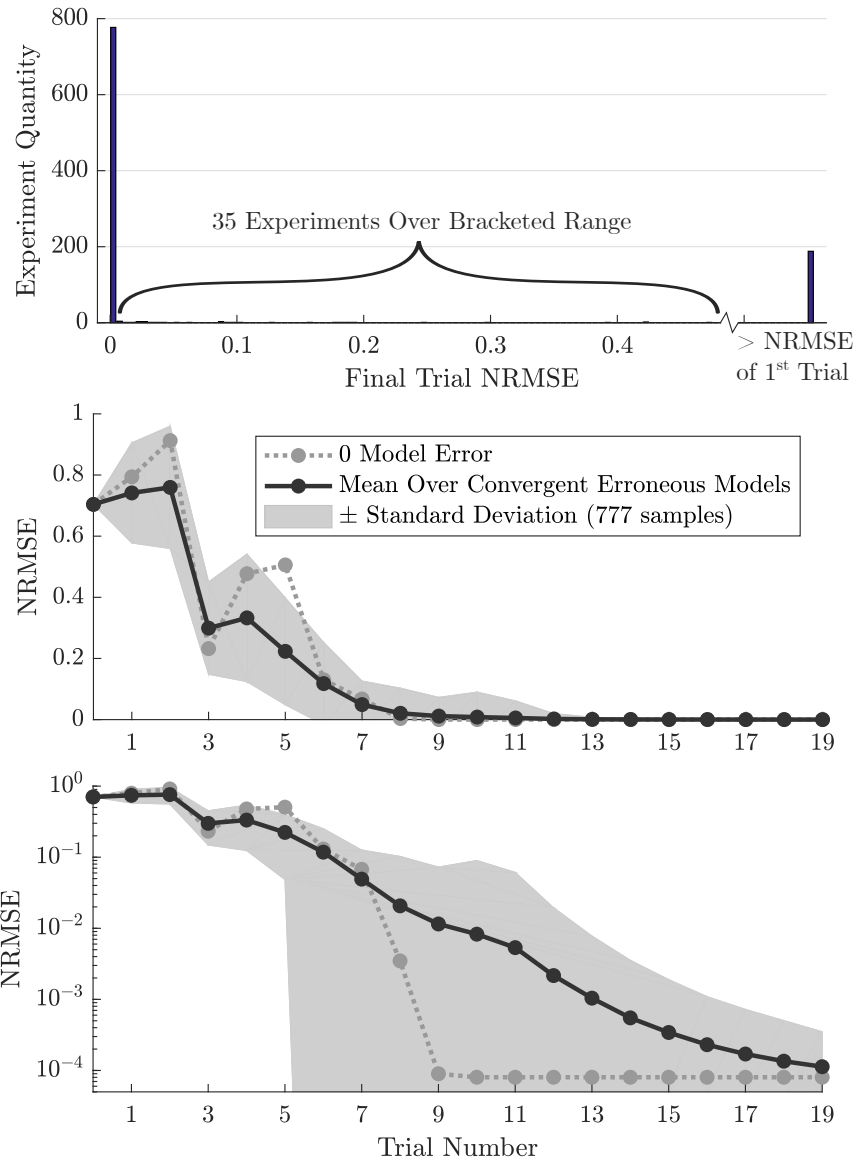


Figure 3.4: *Above*: Histogram of final-trial NRMSE for all experiments. All but the highest error bin are defined by a 0.005 range of NRMSE. *Middle*: Average trajectory of NRMSE vs. Trial number for all completely convergent simulations. *Bottom*: Same on a logarithmic scale, for perspective.

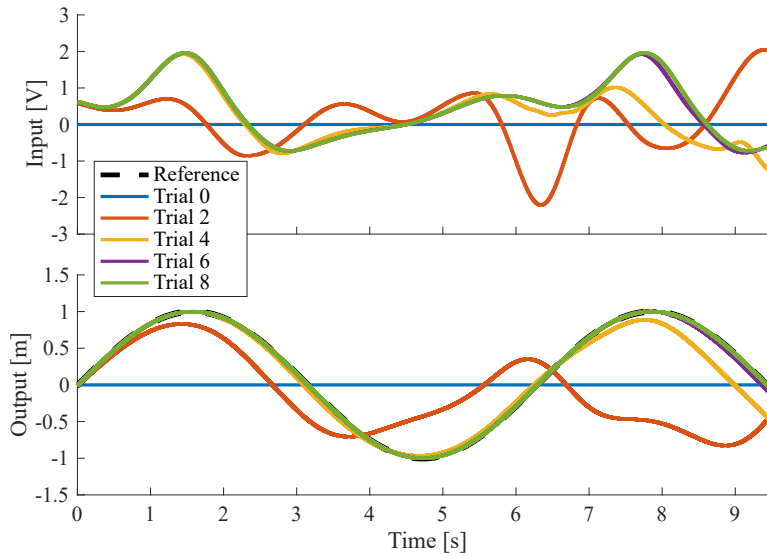


Figure 3.5: Timeseries evolution over multiple trials for a simulation with $\|e_\theta\|_2 = 0.27$. This simulation took 8 trials to completely converge.

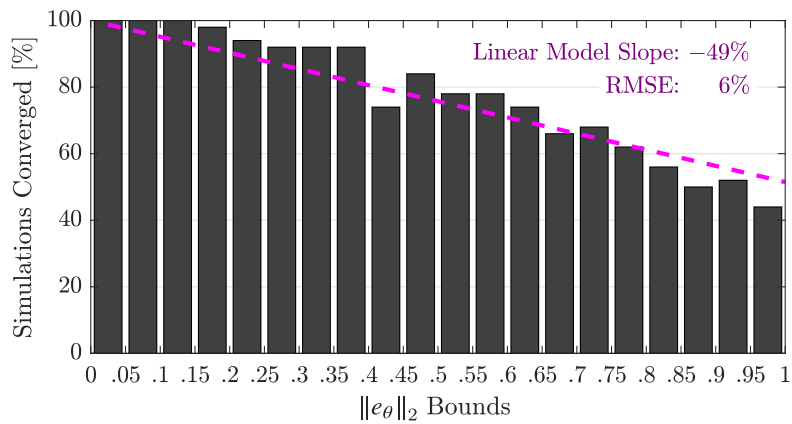


Figure 3.6: Percentage of experiments that converge for each 0.05 range of relative model error from 0 to 1. The dashed line is a least squares model of the decay in the probability of convergence as model error increases.

engineering, the above analysis serves as the first such point of reference for NILC.

3.4 Conclusion

This chapter contributes a closed-form representation of piecewise defined dynamical systems. The utility of having this representation is demonstrated by the application to a hybrid system of an iterative learning controller based on Newton's method, which was hitherto impossible because of the controller's need for a dynamical system model supporting function composition and Jacobian operations.

Additionally, the controller derivation itself is formally generalized for systems of relative degree greater than 1, and for time-varying systems. Additionally, automatic differentiation is used to enable faster and more accurate implementation of Newton's method than prior works, which required coarser and/or more computationally expensive approximation of the model Jacobian.

Future work for the closed-form system representation revolves around expanding the representation to facilitate specification of more complicated switching logic and dynamical state resets upon discrete transitions. While all discrete-time hybrid automaton topologies may be captured by piecewise definition [17], doing so often requires augmentation of the state vector and may make model synthesis more challenging.

CHAPTER 4

Nonlinear Systems with Unstable Inverses: Invert-Linearize ILC and Stable Inversion

Recall from Chapter 1 that NILC is chosen as the foundational ILC technique for this dissertation because of its fast convergence rate and because it is synthesizable from a broader range of systems than is considered by other publications on ILC synthesis from nonlinear models. Specifically, other published ILC laws are subject to at least one of the following restrictions on the control model:

- (R1) having relative degree of either 0 or 1 [14, 15],
- (R2) being affine in the input [13, 14, 15, 23],
- (R3) being time-invariant [13, 16], and
- (R4) being smooth (Lipschitz continuous at the most relaxed) [13, 14, 15, 16, 23]

from all of which NILC is free. Models used to synthesize NILC are, however, subject to the restriction of

- (R5) having a stable inverse.

Note that the non-NILC prior art [13, 14, 15, 16] also suffers from (R5). While the prior art does not explicitly reveal this shortcoming, evidence of it is given in the appendix. The ultimate goal of this chapter is a new ILC framework inheriting the benefits of NILC while surmounting this shortcoming.

Content of this chapter also published as:

I. A. Spiegel, N. Srijbosch, T. Oomen and K. Barton, "Iterative Learning Control with Discrete-Time Nonlinear Nonminimum Phase Models via Stable Inversion," in *International Journal of Robust and Nonlinear Control*. pp. 1-22. Aug. 2021, <https://doi.org/10.1002/rnc.5726> ©John Wiley & Sons Ltd 2021. Reprinted with permission.

Recall too that stable inversion is considered as a foundation for the treatment of unstable inverses in this dissertation, and that for linear systems stable inversion can be summarized as the forward-in-time evolution of a system's stable modes and the backward-in-time evolution of its unstable modes.

Extension of stable inversion to nonlinear models involves additional complexities. Some of these challenges, e.g. the difficulty of completely decoupling the stable and unstable parts of a nonlinear system, have been addressed by works such as [99, 100] for continuous-time systems and [101] for discrete-time systems. However, the following challenges remain. First, for nonlinear models, stable inversion requires Picard iteration to solve a fixed-point-finding problem, and the computational complexity of the solution grows exponentially with the number of iterations. Thus it is desirable to reach a satisfactory point in as few iterations as possible. Secondly, the quality, i.e. proximity to the solution, of the initial guess strongly influences these early iterates, but the initial Picard iterate prescribed by [101]—the zero state trajectory—can be improved upon for many representations of practical systems, such as those employing both feedback and feedforward control. In fact, the convergence proof in [101] relies on an assumption that precludes many representations of these systems. First, this prior art assumes that if the state and input are both zero at a particular time step, then the state will be zero at the next time step. This is not true for most representations of systems employing both feedback and feedforward control because the reference becomes a time-varying parameter embedded in the dynamics of the closed loop system. The reference thus drives state change via the feedback controller despite the initial state and feedforward input being zero. Stable inversion erroneously based on this assumption can have poor performance, and stable inversion has not been proven to converge when this assumption is relaxed. Secondly, [101] lacks discussion of the translation from the theoretical solution on a bi-infinite timeline to an implementable solution on a finite timeline, let alone a validation of such. This chapter addresses these challenges.

In short, while the work to date on NILC and stable inversion has made great strides, gaps remain between the prior art and a synthesis scheme for ILC that is fast and applicable to a wide variety of models—including nonlinear NMP models. This chapter first contributes mathematical analysis concretely identifying the failure mechanism of NILC when synthesized from models with unstable inverses. This leads to the core contribution of a novel ILC framework for controlling nonlinear, NMP systems. The key elements of this framework are

- restructuring of the linearization and model inversion processes in NILC to circumvent issues associated with matrix inversion,
- reformulation of the model inversion in NILC as stable inversion,
- proof of stable inversion convergence with relaxed assumptions on state dynamics, enabling

treatment of a wider array of feedback control and other time-varying models, and

- development of a structured method for implementing the stable inversion technique proposed in this work.

As a final contribution, the proposed framework is validated in simulation on a nonlinear, relative degree 2, time-varying, NMP cart-and-pendulum system with model error and process and measurement noise.

The remainder of the chapter is organized as follows. Section 4.1 provides technical details from the prior art in nonlinear stable inversion [101] necessary to present the novel contributions of the present work. Section 4.2 presents analysis that justifies the attribution of a class of NILC failures to inverse instability, and provides a new ILC framework that enables the circumvention of this failure mechanism by incorporating stable inversion. Section 4.3 provides proof of convergence of stable inversion for an expanded class of systems and provides improved methods for practical implementation. Section 4.4 details and discusses the validation of the new ILC framework with stable inversion through benchmark simulations on an NMP cart-and-pendulum system. This includes demonstration of conventional NILC's divergence when applied to the same system. Section 4.5 presents conclusions and areas for future work.

As a final note: because this chapter seeks to present a new ILC framework that is general enough for both hybrid systems and non-hybrid nonlinear systems, this chapter does not explicitly discuss hybrid systems. Furthermore, the stable inversion techniques discussed in this chapter are focused on smooth nonlinear systems. Consequently, the example system used for validation in this chapter is a smooth nonlinear system. The stable-inversion-based solution to inverse instability will be brought to bear on hybrid systems in Chapter 5.

4.1 Nonlinear Stable Inversion Background

The first step of stable inversion is deriving the conventional inverse. To synthesize a minimal inverse system representation, first assume (3.8) is in the normal form

$$\hat{x}^i(k+1) = \hat{x}^{i+1}(k) \quad i < \mu \quad (4.1a)$$

$$\hat{x}^i(k+1) = \hat{f}^i(\hat{x}(k), u(k), k) \quad i \geq \mu \quad (4.1b)$$

$$\hat{y}(k) = \hat{x}^1 \quad (4.1c)$$

where $\hat{x}(0) = 0$, and the superscripts i indicate the vector element index, starting from 1. Note the ILC trial index subscript ℓ is omitted in this section, as stable inversion on its own does not involve incrementing ℓ . Equation (4.1a) captures the time delay arising from the system relative

degree, while equation (4.1b) captures the remaining system dynamics. One method of deriving this normal form from a system not in normal form is given in [102].

Given this normal form, use (4.1c) to replace the first μ state variables with output variables via

$$\hat{x}^i(k) = \hat{y}(k + i - 1) \quad i \leq \mu \quad (4.2)$$

Similarly, replace the μ^{th} state variable incremented by one time step (i.e. the left side of (4.1b) for $i = \mu$) with an output variable via

$$\hat{x}^\mu(k + 1) = \hat{y}(k + \mu) \quad (4.3)$$

These substitutions are made to facilitate the inversion of system (4.1), as the inverse of a system with relative degree $\mu \geq 1$ is necessarily acausal with dependence on some subset of $\{\hat{y}(k), \hat{y}(k + 1), \dots, \hat{y}(k + \mu)\}$ at each time step k . For notational compactness, define the \hat{y} -preview vector $\hat{\mathcal{Y}}(k) := [\hat{y}(k), \dots, \hat{y}(k + \mu)]^T$. Then inverting (4.1b) with $i = \mu$ yields the conventional inverse output function

$$u(k) = \hat{f}^{\mu-1} \left(\left[\hat{x}^{\mu+1}, \dots, \hat{x}^{n_x} \right]^T, \hat{\mathcal{Y}}(k), k \right) \quad (4.4)$$

where $\hat{f}^{\mu-1}$ is the inverse of \hat{f}^μ , i.e. (4.1b, $i = \mu$) solved for $u(k)$. This output equation is substituted into (4.1b) with $i > \mu$ along with (4.2)-(4.3) to yield the entire inverse state dynamics

$$\hat{\eta}(k + 1) = \hat{f}_\eta(\hat{\eta}(k), \hat{\mathcal{Y}}(k), k) \quad (4.5a)$$

$$u(k) = \hat{f}^{\mu-1}(\hat{\eta}(k), \hat{\mathcal{Y}}(k), k) \quad (4.5b)$$

where $\hat{\eta} \in \mathbb{R}^{n_\eta}$ ($n_\eta = n_x - \mu$) is the inverse state vector defined

$$\hat{\eta}^i(k) := \hat{x}^{\mu+i}(k) \quad (4.6)$$

and $\hat{f}_\eta : \mathbb{R}^{n_\eta} \times \mathbb{R}^{\mu+1} \times \mathbb{Z} \rightarrow \mathbb{R}^{n_\eta}$ is the inverse state dynamics

$$\hat{f}_\eta^i(\hat{\eta}(k), \hat{\mathcal{Y}}(k), k) := \hat{f}^{i+\mu}(\hat{x}(k), u(k), k) \quad (4.7)$$

Next, this inverse system is to be similarity transformed to decouple the stable and unstable modes of its linearization about the initial condition. Consider the Jacobian

$$A = \frac{\partial \hat{f}_\eta}{\partial \hat{\eta}} \left(\hat{\eta} = 0, \hat{\mathcal{Y}} = \hat{\mathcal{Y}}^\dagger, k = 0 \right) \quad (4.8)$$

where $\hat{\mathcal{U}}^\dagger$ is the solution to $\hat{f}_\eta(0, \hat{\mathcal{U}}^\dagger, 0) = 0$. Then let V be the similarity transform matrix such that

$$\tilde{A} = V^{-1}AV = \begin{bmatrix} \tilde{A}_s & 0 \\ 0 & \tilde{A}_u \end{bmatrix} \quad (4.9)$$

where $\tilde{A}_s \in \mathbb{R}^{n_s \times n_s}$ has all eigenvalues inside the unit circle, and $\tilde{A}_u \in \mathbb{R}^{n_\eta - n_s \times n_\eta - n_s}$ has all eigenvalues outside the unit circle. This can be satisfied by deriving the real block Jordan form of A . The corresponding inverse system state dynamics are

$$\tilde{\eta}(k+1) = \tilde{f}_\eta(\tilde{\eta}(k), \hat{\mathcal{U}}(k), k) := V^{-1} \hat{f}_\eta(V\tilde{\eta}(k), \hat{\mathcal{U}}(k), k) \quad (4.10)$$

where the tilde on \tilde{f}_η indicates application to $\tilde{\eta}$ rather than $\hat{\eta}$. Note that despite using a linearization-derived linear similarity transform, (4.10) describes the same nonlinear time-varying dynamics as (4.5a), but with the linear parts of the stable and unstable modes decoupled.

If (3.8) has an unstable inverse, then (4.10) is unstable and $\tilde{\eta}(k)$ will be unbounded as k increases. However, given an infinite timeline in the positive and negative direction, the equation

$$\tilde{\eta}(k) = \sum_{\kappa=-\infty}^{\infty} \phi(k-\kappa) (\tilde{f}_\eta(\tilde{\eta}(\kappa-1), \hat{\mathcal{U}}(\kappa-1), \kappa-1) - \tilde{A}\tilde{\eta}(\kappa-1)) \quad (4.11)$$

where

$$\phi(k) = \begin{cases} \begin{bmatrix} \tilde{A}_s^k & 0_{n_s \times n_\eta - n_s} \\ 0_{n_\eta - n_s \times n_s} & 0_{n_\eta - n_s \times n_\eta - n_s} \end{bmatrix} & k > 0 \\ \begin{bmatrix} I_{n_s \times n_s} & 0_{n_s \times n_\eta - n_s} \\ 0_{n_\eta - n_s \times n_s} & 0_{n_\eta - n_s \times n_\eta - n_s} \end{bmatrix} & k = 0 \\ \begin{bmatrix} 0_{n_s \times n_s} & 0_{n_s \times n_\eta - n_s} \\ 0_{n_\eta - n_s \times n_s} & -\tilde{A}_u^k \end{bmatrix} & k < 0 \end{cases} \quad (4.12)$$

is an exact, bounded solution to (4.10) provided the right hand side of (4.11) exists for all $k \in \mathbb{Z}$. However, (4.11) is implicit, and thus cannot be directly evaluated. A fixed-point problem solver—past work uses Picard iteration—must be used to find $\tilde{\eta}$, and sufficient conditions for the solver convergence and solution uniqueness must be determined.

4.2 Novel ILC Analysis and Development

4.2.1 Failure for Models with Unstable Inverses

The NILC scheme (3.7), (3.15) provides convergence of \mathbf{e}_ℓ to 0 in theory. However, this assumes perfect computation of the matrix inversion in (3.15). In practice, the precision to which $\left(\frac{\partial \hat{\mathbf{g}}}{\partial \mathbf{u}}(\mathbf{u}_\ell)\right)^{-1}$ can be accurately computed is directly dependent on the condition number of $\frac{\partial \hat{\mathbf{g}}}{\partial \mathbf{u}}(\mathbf{u}_\ell)$. If the condition number of a matrix is large enough, the values computed for its inverse may become arbitrary, and their order of magnitude may grow directly with the order of magnitude of the condition number [103, ch. 3.2], [104]. This “blowing up” of the matrix inverse can cause divergence of (3.7), (3.15).

Large $\frac{\partial \hat{\mathbf{g}}}{\partial \mathbf{u}}$ condition numbers have been previously observed for NMP linear systems, both time-invariant [105], [106, ch. 5.3-5.4] and time-varying [107], [108, ch. 4.1.1]. The fact that the minimum singular value of $\frac{\partial \hat{\mathbf{g}}}{\partial \mathbf{u}}(\mathbf{u}_\ell)$ decreases with increases in the system frequency response function magnitude at the Nyquist frequency [109] contributes to this ill-conditioning. For linear systems, this magnitude is directly dependent on the zero magnitudes, and thus on the inverse systems’ stability. These phenomena generalize to nonlinear systems because the Jacobian evaluated at a particular input trajectory, $\frac{\partial \hat{\mathbf{g}}}{\partial \mathbf{u}}(\mathbf{u}^*)$, is equal to the constant matrix $\frac{\partial \bar{\mathbf{g}}}{\partial \mathbf{u}}$ where $\bar{\mathbf{g}}$ is the lifted input-output model of the linearization of (3.8) about the trajectory \mathbf{u}^* .

To illustrate this equality, first consider that the elements of $\frac{\partial \hat{\mathbf{g}}}{\partial \mathbf{u}}(\mathbf{u}^*)$ are given by (3.11b) and the chain rule as

$$\frac{\partial \hat{y}(k)}{\partial u(j)}(\mathbf{u}^*) = \frac{\partial \hat{h}}{\partial \hat{x}}\left(\hat{f}^{(k-1)}(\mathbf{u}^*)\right) \frac{\partial \hat{f}^{(k-1)}}{\partial \mathbf{u}}(\mathbf{u}^*) \frac{\partial \mathbf{u}}{\partial u(j)} \quad (4.13)$$

where

$$\frac{\partial \mathbf{u}}{\partial u(j)} = \begin{bmatrix} \mathbf{0}_{1 \times j} & 1 & \mathbf{0}_{1 \times N - \mu + 1 - j} \end{bmatrix}^T \quad (4.14)$$

and $\frac{\partial \hat{h}}{\partial \hat{x}}$ is a row vector.

Then consider the linearization of (3.8) about \mathbf{u}^* :

$$\begin{aligned} \delta \hat{x}(k+1) &= \bar{f}(\delta \hat{x}(k), \delta u(k), k) \\ &= \frac{\partial \hat{f}}{\partial \hat{x}}(\hat{x}^*(k), u^*(k), k) \delta \hat{x}(k) + \frac{\partial \hat{f}}{\partial u}(\hat{x}^*(k), u^*(k), k) \delta u(k) \end{aligned} \quad (4.15a)$$

$$\delta \hat{y}(k) = \bar{h}(\delta \hat{x}(k)) = \frac{\partial \hat{h}}{\partial \hat{x}}(\hat{x}^*(k)) \delta \hat{x}(k) \quad (4.15b)$$

where $\hat{x}^*(k) = \hat{f}^{(k-1)}(\mathbf{u}^*)$ and the δ notation denotes $\delta \hat{x}(k) = \hat{x}(k) - \hat{x}^*(k)$ for \hat{x} and similar for u .

Lifting (4.15) in the same manner as (3.8) yields the output perturbation as a function of the input perturbation time series $\delta \mathbf{u}$ via

$$\delta \hat{y}(k) = \frac{\partial \hat{h}}{\partial \hat{x}} \left(\hat{f}^{(k-1)}(\mathbf{u}^*) \right) \bar{f}^{(k-1)}(\delta \mathbf{u}) \quad (4.16)$$

Because of (4.15)'s linearity, $\bar{f}^{(k-1)}(\delta \mathbf{u})$ can be explicitly expanded as

$$\bar{f}^{(k-1)}(\delta \mathbf{u}) = \left(\prod_{\kappa=0}^{k-1} \frac{\partial \hat{f}^{(\kappa)}}{\partial \hat{f}^{(\kappa-1)}}(\mathbf{u}^*) \right) \delta \hat{x}(0) + \frac{\partial \hat{f}^{(k-1)}}{\partial \mathbf{u}}(\mathbf{u}^*) \delta \mathbf{u} \quad (4.17)$$

where \prod is ordered with the factor of least ℓ on the right and the factor of greatest ℓ on the left. The terminal condition of the recursive function composition is $\hat{f}^{(-1)} = \hat{x}(0)$. From (4.16) and (4.17) it is clear that the elements of $\frac{\partial \hat{\mathbf{g}}}{\partial \delta \mathbf{u}}$ are given by

$$\frac{\partial \delta \hat{y}(k)}{\partial \delta u(j)} = \frac{\partial \hat{h}}{\partial \hat{x}} \left(\hat{f}^{(k-1)}(\mathbf{u}^*) \right) \frac{\partial \hat{f}^{(k-1)}}{\partial \mathbf{u}}(\mathbf{u}^*) \frac{\partial \delta \mathbf{u}}{\partial \delta u(j)} \quad (4.18)$$

which is equal to (4.13) because $\frac{\partial \delta \mathbf{u}}{\partial \delta u(j)} = \frac{\partial \mathbf{u}}{\partial u(j)}$ due to the identical structures (3.10) of \mathbf{u} and $\delta \mathbf{u}$ with respect to u and δu time indexing. Thus, if (3.8) is such that its linearization (4.15) is unstable it will suffer ill-conditioning and (3.15) may be so difficult to compute in practice that attempts to do so yield a matrix with large erroneous elements. Such a learning gain matrix may in turn cause $\mathbf{u}_{\ell+1}$ to contain large erroneous elements, causing the learning law to diverge.

Therefore, for the learning law (3.7) to converge for a system with an unstable inverse in practice, a learning matrix synthesis that does not require matrix inversion of $\frac{\partial \hat{\mathbf{g}}}{\partial \mathbf{u}}(\mathbf{u}_\ell)$ is desired.

4.2.2 Alternative Learning Matrix Synthesis

To circumvent issues associated with inverting $\frac{\partial \hat{\mathbf{g}}}{\partial \mathbf{u}}(\mathbf{u}_\ell)$ this work introduces a new learning matrix definition seeking to satisfy the requirements (A3.4)-(A3.6) in the spirit of Newton's method, but without the matrix inversion requirement of (3.15). The new learning matrix is given by

$$L_\ell = \frac{\partial \hat{\mathbf{g}}^{-1}}{\partial \hat{\mathbf{y}}}(\mathbf{y}_\ell) \quad (4.19)$$

where $\hat{\mathbf{g}}^{-1} : \mathbb{R}^{N-\mu+1} \rightarrow \mathbb{R}^{N-\mu+1}$ is a lifted model of the inverse of (3.8). This makes $\frac{\partial \hat{\mathbf{g}}^{-1}}{\partial \hat{\mathbf{y}}}$ a function of the output of (3.8), namely $\hat{\mathbf{y}}_\ell$. As stated in Section 3.2, $\hat{\mathbf{y}}_\ell$ is merely a prediction of the accessible, measured output \mathbf{y}_ℓ . Hence \mathbf{y}_ℓ is used as the input to $\frac{\partial \hat{\mathbf{g}}^{-1}}{\partial \hat{\mathbf{y}}}$. In short, this work proposes using the linearization of the inverse of (3.8) rather than the inverse of the linearization, and thus

the new framework (3.7), (4.19) will be referred to as ‘‘Invert-Linearize ILC’’ (ILILC).

A direct method of inverting (3.8) is to solve

$$\hat{y}_\ell(k + \mu) = \hat{h}(\hat{f}^{(k+\mu-1)}(\mathbf{u}_\ell)) \quad (4.20)$$

for $u_\ell(k)$, and substitute the resulting function of $\{\hat{y}_\ell(k), \hat{y}_\ell(k + 1), \dots, \hat{y}_\ell(k + \mu)\}$ into (3.8a). However, if (3.8) has an unstable inverse, this method of inversion will yield unbounded states $\hat{x}_\ell(k)$ as k increases. Thus, $\hat{\mathbf{g}}^{-1}$ is derived via stable inversion rather than direct inversion. Note, though, that (4.19) also admits the use of other stable approximate inverse models for $\hat{\mathbf{g}}^{-1}$ should they be available.

4.3 Novel Stable Inversion Development

This section proves a relaxed set of sufficient conditions for the convergence of Picard iteration to the unique solution to the stable inversion problem, i.e. the unique solution to (4.11) from Section 4.1. This enables stable inversion—and thus ILC—for a new class of system representations capturing simultaneous feedback and feedforward control. Additionally, a new initial Picard iterate prescription is given to suit the broadened scope of stable inversion, and a procedure for practical implementation is described. This procedure enables the derivation of $\hat{\mathbf{g}}^{-1}$.

4.3.1 Fixed-Point Problem Solution

The standard Picard iterative solver [110, ch. 9] for (4.11) is

$$\tilde{\eta}_{(m+1)}(k) = \sum_{\kappa=-\infty}^{\infty} \phi(k - \kappa) (\tilde{f}_\eta(\tilde{\eta}_{(m)}(\kappa - 1), \hat{y}(\kappa - 1), \kappa - 1) - \tilde{A}\tilde{\eta}_{(m)}(\kappa - 1)) \quad (4.21)$$

where the parenthetical subscript $(m) \in \mathbb{Z}_{\geq 0}$ is the Picard iteration index.

To prove that (4.21) converges to a unique solution, [101] makes the assumptions¹ that

$$(Z1) \quad \hat{f}(0, 0, k) = 0 \quad \forall k, \text{ and}$$

$$(Z2) \quad \tilde{\eta}_{(0)}(k) = 0 \quad \forall k.$$

The first assumption is violated for many representations of systems incorporating both feedback and feedforward control. An example of such a system is given in Section 4.4, where u is the feedforward control input and the feedback control is part of the time-varying dynamics of \hat{f} . This feedback control influences \hat{x} regardless of whether or not $u(k) = 0$. While there may often be

¹The continuous-time literature also makes these assumptions [99, 100]

a change of variables that enables satisfaction of (Z1), (4.1a-4.1c) already imposes constraints on the states and outputs, and for many systems it is unlikely for there to exist a change of variables satisfying both assumptions.

Furthermore, while for systems satisfying (Z1), (Z2) may be the zero-input state trajectory, this is untrue for systems violating (Z1). For these systems, the zero state trajectory (Z2) is essentially arbitrary, and may degrade the quality of low- m Picard iterates if far from the solution trajectory. This seriously jeopardizes convergence because the computational complexity of the Picard iteration solution grows exponentially with the number of iterations. It is thus desirable to reach a satisfactory solution in as few iterations as possible, i.e. it is desirable to have high-quality low- m iterates.

Thus, this work presents a new set of sufficient conditions for the unique convergence of (4.21) that relaxes (Z1), (Z2). Before proof of this, several definitions are presented.

Definition 4.1 (Lifted Matrices and Third-Order Tensors). Given the vector and matrix functions of time $a(k) \in \mathbb{R}^n$ and $B(k) \in \mathbb{R}^{n \times n}$, the corresponding lifted matrix and third order tensor are given by upright bold notation: $\mathbf{a} \in \mathbb{R}^{n \times \mathcal{K}}$ and $\mathbf{B} \in \mathbb{R}^{n \times n \times \mathcal{K}}$. \mathcal{K} is the time dimension, and may be ∞ . Elements of the lifted objects are $\mathbf{a}^{i,k} := a^i(k)$ and $\mathbf{B}^{i,j,k} := B^{i,j}(k)$.

Definition 4.2 (Matrix and Third-Order Tensor Norms). $\|\cdot\|_\infty$ refers to the ordinary ∞ -norm when applied to vectors, and is the matrix norm induced by the vector norm when applied to matrices (i.e. the maximum absolute row sum). Additionally, the entry-wise $(\infty, 1)$ -norm is defined for the matrices and third-order tensors \mathbf{a} and \mathbf{B} from Definition 4.1 as

$$\|\mathbf{a}\|_{\infty,1} := \sum_{k \in \mathcal{K}} \|a(k)\|_\infty \quad \|\mathbf{B}\|_{\infty,1} := \sum_{k \in \mathcal{K}} \|B(k)\|_\infty \quad (4.22)$$

Definition 4.3 (Local Approximate Linearity [99, 101]). \tilde{f}_η is locally approximately linear in $\tilde{\eta}(k)$ and its $\tilde{\eta}(k) = 0$ dynamics, in a closed s -neighborhood around $(\tilde{\eta}(k) = 0, \tilde{f}_\eta(0, \hat{y}(k), k) = 0)$, with Lipschitz constants $K_1, K_2 > 0$ if $\exists s > 0$ such that for any vectors

- $a(k), b(k) \in \mathbb{R}^{n_\eta}$ with $\|\cdot\|_\infty \leq s \forall k$, and
- $\varphi(k), \vartheta(k) \in \mathbb{R}^{\mu+1}$ such that $\|\tilde{f}_\eta(0, \varphi(k), k)\|_\infty, \|\tilde{f}_\eta(0, \vartheta(k), k)\|_\infty \leq s \forall k$

the following is true $\forall k$

$$\begin{aligned} & \left\| (\tilde{f}_\eta(a(k), \varphi(k), k) - Aa(k)) - (\tilde{f}_\eta(b(k), \vartheta(k), k) - Ab(k)) \right\|_\infty \\ & \leq K_1 \|a(k) - b(k)\|_\infty + K_2 \left\| \tilde{f}_\eta(0, \varphi(k), k) - \tilde{f}_\eta(0, \vartheta(k), k) \right\|_\infty \end{aligned} \quad (4.23)$$

With these definitions a new set of sufficient conditions for Picard iteration convergence may be established.

Theorem 4.1. *The Picard iteration (4.21) converges to a unique solution to (4.10) if the following sufficient conditions are met.*

$$(A4.1) \quad \|\tilde{\eta}_{(0)}\|_{\infty,1} \leq s$$

$$(A4.2) \quad \forall k \exists \hat{y}(k) = \hat{y}^\dagger(k) \text{ such that } \tilde{f}_\eta(0, \hat{y}^\dagger(k), k) = 0$$

$$(A4.3) \quad \tilde{f}_\eta \text{ is locally approximately linear in the sense of (4.23)}$$

$$(A4.4) \quad K_1 \|\varphi\|_{\infty,1} < 1$$

$$(A4.5) \quad \frac{\|\varphi\|_{\infty,1} K_2 \|\tilde{f}_\eta(0, \hat{y})\|_{\infty,1}}{1 - \|\varphi\|_{\infty,1} K_1} \leq s$$

where $\|\tilde{f}_\eta(0, \hat{y})\|_{\infty,1} = \sum_{k=-\infty}^{\infty} \|\tilde{f}_\eta(0, \hat{y}(k), k)\|_{\infty}$ and φ are defined by Definition 4.1; i.e. φ is the lifted tensor version of (4.12).

Proof. This proof shares the approach of [101] in establishing the Cauchy nature of the Picard sequence. It is also influenced by the proofs of Picard iterate local approximate linearity for continuous-time systems in [99].

Proof that (4.21) converges to a unique fixed point begins with an induction showing that $\tilde{\eta}_{(m)}(k)$ remains in the locally approximately linear neighborhood $\forall k, m$. The base case of this induction is given by (A4.1). Then under the premise

$$\|\tilde{\eta}_{(m)}\|_{\infty,1} \leq s \tag{4.24}$$

the induction proceeds as follows. Here, ellipses indicate the continuation of a line of mathematics.

By the Picard iterative solver (4.21):

$$\|\tilde{\eta}_{(m+1)}\|_{\infty,1} = \sum_{k=-\infty}^{\infty} \left\| \sum_{\kappa=-\infty}^{\infty} \phi(k - \kappa) \left(\tilde{f}_\eta(\tilde{\eta}_{(m)}(\kappa - 1), \hat{y}(\kappa - 1), \kappa - 1) - A\tilde{\eta}_{(m)}(\kappa - 1) \right) \right\|_{\infty} \cdots \tag{4.25}$$

By the triangle inequality:

$$\cdots \leq \sum_{k=-\infty}^{\infty} \sum_{\kappa=-\infty}^{\infty} \|\phi(k - \kappa) \left(\tilde{f}_\eta(\tilde{\eta}_{(m)}(\kappa - 1), \hat{y}(\kappa - 1), \kappa - 1) - A\tilde{\eta}_{(m)}(\kappa - 1) \right)\|_{\infty} \cdots \tag{4.26}$$

By the fact that for matrix norms induced by vector norms $\|Ba\| \leq \|B\| \|a\|$ for matrix B and vector a :

$$\cdots \leq \sum_{k=-\infty}^{\infty} \sum_{\kappa=-\infty}^{\infty} \|\phi(k - \kappa)\|_{\infty} \|\tilde{f}_{\eta}(\tilde{\eta}_{(m)}(\kappa - 1), \hat{\mathcal{Y}}(\kappa - 1), \kappa - 1) - A\tilde{\eta}_{(m)}(\kappa - 1)\|_{\infty} \cdots \quad (4.27)$$

$$\cdots = \sum_{\kappa=-\infty}^{\infty} \|\tilde{f}_{\eta}(\tilde{\eta}_{(m)}(\kappa - 1), \hat{\mathcal{Y}}(\kappa - 1), \kappa - 1) - A\tilde{\eta}_{(m)}(\kappa - 1)\|_{\infty} \sum_{k=-\infty}^{\infty} \|\phi(k - \kappa)\|_{\infty} \cdots \quad (4.28)$$

By the fact that $\sum_{k=-\infty}^{\infty} \|\phi(k - \kappa)\|_{\infty}$ has the same value $\forall \kappa$

$$\cdots = \|\boldsymbol{\Phi}\|_{\infty,1} \sum_{\kappa=-\infty}^{\infty} \|\tilde{f}_{\eta}(\tilde{\eta}_{(m)}(\kappa - 1), \hat{\mathcal{Y}}(\kappa - 1), \kappa - 1) - A\tilde{\eta}_{(m)}(\kappa - 1)\|_{\infty} \cdots \quad (4.29)$$

By (A4.2):

$$\begin{aligned} \cdots = \|\boldsymbol{\Phi}\|_{\infty,1} \sum_{\kappa=-\infty}^{\infty} & \left\| \left(\tilde{f}_{\eta}(\tilde{\eta}_{(m)}(\kappa - 1), \hat{\mathcal{Y}}(\kappa - 1), \kappa - 1) - A\tilde{\eta}_{(m)}(\kappa - 1) \right) \right. \\ & \left. - \left(\tilde{f}_{\eta}(0, \hat{\mathcal{Y}}^{\dagger}(\kappa - 1), \kappa - 1) - A(0) \right) \right\|_{\infty} \cdots \end{aligned} \quad (4.30)$$

By (A4.3):

$$\cdots \leq \|\boldsymbol{\Phi}\|_{\infty,1} \sum_{\kappa=-\infty}^{\infty} K_1 \|\tilde{\eta}_{(m)}(\kappa - 1)\|_{\infty} + K_2 \|\tilde{f}_{\eta}(0, \hat{\mathcal{Y}}(\kappa - 1), \kappa - 1)\|_{\infty} \cdots \quad (4.31)$$

$$\cdots = \|\boldsymbol{\Phi}\|_{\infty,1} \left(K_1 \|\tilde{\boldsymbol{\eta}}_{(m)}\|_{\infty,1} + K_2 \|\tilde{\mathbf{f}}_{\eta}(0, \hat{\mathcal{Y}})\|_{\infty,1} \right) \cdots \quad (4.32)$$

By (A4.4), both sides of (A4.5) can be multiplied by the denominator in (A4.5) without changing the inequality direction. Thus by (4.24) and algebraic rearranging of (A4.5)

$$\cdots \leq \|\boldsymbol{\Phi}\|_{\infty,1} \left(K_1 s + K_2 \|\tilde{\mathbf{f}}_{\eta}(0, \hat{\mathcal{Y}})\|_{\infty,1} \right) \leq s \quad (4.33)$$

$\therefore \|\tilde{\boldsymbol{\eta}}_{(m)}\|_{\infty,1} \leq s \forall m$. Because $\|\tilde{\boldsymbol{\eta}}_{(m)}\|_{\infty,1} \geq \|\tilde{\eta}_{(m)}(k)\|_{\infty} \forall k$, this implies that $\tilde{\eta}_{(m)}(k)$ is within the locally approximately linear neighborhood $\forall m, k$.

To show that (4.21) converges to a unique fixed point, define

$$\Delta\tilde{\eta}_{(m)}(k) := \tilde{\eta}_{(m+1)}(k) - \tilde{\eta}_{(m)}(k) \quad (4.34)$$

Then, by a nearly identical induction

$$\|\Delta\tilde{\eta}_{(m+1)}\|_{\infty,1} \leq \|\boldsymbol{\varphi}\|_{\infty,1} K_1 \|\Delta\tilde{\eta}_{(m)}\|_{\infty,1} \quad (4.35)$$

By (A4.4)

$$\lim_{m \rightarrow \infty} \|\Delta\tilde{\eta}_{(m)}\|_{\infty,1} = 0 \quad (4.36)$$

which implies

$$\lim_{m \rightarrow \infty} \|\Delta\tilde{\eta}_{(m)}(k)\|_{\infty} = 0 \quad \forall k \quad (4.37)$$

$\therefore \forall k$ the sequence $\{\tilde{\eta}_m(k)\}$ is a Cauchy sequence, and thus the fixed point $\tilde{\eta}(k) = \lim_{m \rightarrow \infty} \tilde{\eta}_{(m)}(k)$ is unique. □

Neither the preceding presentation nor the nonlinear stable inversion prior art [101] explicitly discusses the intuitive foundation of stable inversion: evolving the stable modes of an inverse system forwards in time from an initial condition and evolving the unstable modes backwards in time from a terminal condition. Unlike for linear time invariant (LTI) systems, this intuition is not put into practice directly for nonlinear systems because the similarity transforms that completely decouple the stable and unstable modes of linear systems do not necessarily decouple the stable and unstable modes of nonlinear systems. However, the same principle underpins this work. This is evidenced by the fact that the intuitive LTI stable inversion is recovered from (4.11) when \hat{f} is LTI, as illustrated briefly below.

For LTI \hat{f} , \tilde{f} takes the form

$$\tilde{\eta}(k+1) = \tilde{A}\tilde{\eta}(k) + \tilde{B}\hat{y}(k) \quad (4.38)$$

$$\begin{bmatrix} \tilde{\eta}_s(k+1) \\ \tilde{\eta}_u(k+1) \end{bmatrix} = \begin{bmatrix} \tilde{A}_s & 0 \\ 0 & \tilde{A}_u \end{bmatrix} \begin{bmatrix} \tilde{\eta}_s(k) \\ \tilde{\eta}_u(k) \end{bmatrix} + \begin{bmatrix} \tilde{B}_s \\ \tilde{B}_u \end{bmatrix} \hat{y}(k) \quad (4.39)$$

Then the implicit solution (4.11) becomes the explicit solution

$$\tilde{\eta}(k) = \sum_{\kappa=-\infty}^{\infty} \phi(k-\kappa) \tilde{B}\hat{y}(\kappa-1) \quad (4.40)$$

$$\begin{bmatrix} \tilde{\eta}_s(k) \\ \tilde{\eta}_u(k) \end{bmatrix} = \begin{bmatrix} \sum_{\kappa=-\infty}^k \tilde{A}_s^{k-\kappa} \tilde{B}_s \hat{y}(\kappa-1) \\ -\sum_{\kappa=k+1}^{\infty} \tilde{A}_u^{k-\kappa} \tilde{B}_u \hat{y}(\kappa-1) \end{bmatrix} \quad (4.41)$$

$$= \begin{bmatrix} \tilde{A}_s \tilde{\eta}_s(k-1) + \tilde{B}_s \hat{y}(k-1) \\ \tilde{A}_u^{-1} \tilde{\eta}_u(k+1) - \tilde{A}_u^{-1} \tilde{B}_u \hat{y}(k) \end{bmatrix} \quad (4.42)$$

which is the forward evolution of the stable modes and backward evolution of the unstable modes

where the initial and terminal conditions at $k = \pm\infty$ are zero.

4.3.2 Initial Picard Iterate $\tilde{\eta}_{(0)}$ Selection and Implementation

This subsection addresses the need to select a new initial Picard iterate $\tilde{\eta}_{(0)}(k)$ in the absence of (Z2). Also addressed is the fact that (4.21) is a purely theoretical, rather than implementable, solution because it contains infinite sums along an infinite timeline.

In the context of ILC, the learned feedforward control action is often intended to be a relatively minor adjustment to the primary action of the feedback controller. Thus, choosing $\tilde{\eta}_{(0)}(k)$ to be the feedback-only trajectory, i.e. the zero-feedforward-input trajectory, is akin to warm-starting the fixed-point solving process. This trajectory is given by

$$\begin{aligned} \hat{x}(k+1) &= \hat{f}(\hat{x}(k), 0, k) & \hat{x}(0) &= 0_{n_x} \\ \tilde{\eta}_{(0)}(k) &= V^{-1} \begin{bmatrix} 0_{\mu \times \mu} & 0_{\mu \times n_\eta} \\ 0_{n_\eta \times \mu} & I_{n_\eta \times n_\eta} \end{bmatrix} \hat{x}(k) \end{aligned} \quad (4.43)$$

for $k \in \{0, \dots, N - \mu\}$.

An implementable version of (4.21) is given by

$$\tilde{\eta}_{(m+1)}(k) = \sum_{\kappa=1}^{N-\mu+1} \phi(k-\kappa) (\tilde{f}_\eta(\tilde{\eta}_{(m)}(\kappa-1), \hat{y}(\kappa-1), \kappa-1) - \tilde{A}\tilde{\eta}_{(m)}(\kappa-1)) \quad (4.44)$$

for $k \in \{1, \dots, N - \mu\}$, fixing the initial condition $\tilde{\eta}_{(m)}(0) = 0_{n_\eta} \forall m$.

Note that (4.44) is equivalent to assuming $\tilde{\eta}_{(m)}(k) = 0$, $\hat{y}(k) = 0$, and $\tilde{f}_\eta(0, 0, k) = 0$ for $k \in (-\infty, -1] \cup [N - \mu + 1, \infty)$ and extracting the $k \in [1, N - \mu]$ elements of $\tilde{\eta}_{(m+1)}(k)$ generated by (4.21). These assumptions correspond to a lack of control action prior to $k = 0$ and a reference trajectory that brings the system back to its zero initial condition with enough trailing zeros for the system to settle by $k = N - \mu$. This is typical of repetitive motion processes, but admittedly may preclude some other ILC applications.

Furthermore, for the first Picard iteration ($m + 1 = 1$) these assumptions yield identical (4.44)- and (4.21)-generated $\tilde{\eta}_{(1)}(k)$ on $k \in [0, N - \mu]$. Because output tracking of NMP systems in general requires preactuation, for this range of k to contain a practical control input trajectory there must be sufficient leading zeros in the reference starting at $k = 0$. For the following Picard iterates the theoretical and implementable trajectories are unlikely to be equal, but can be made closer the more leading zeros are included in the reference.

Ultimately, applying (4.44) for any number of iterations $m_{\text{final}} \geq 1$ yields an expression for each time step of $\tilde{\eta}_{(m_{\text{final}})}(k)$ whose only variable parameters are the elements of \hat{y} . This is because

the recursion calling $\tilde{\eta}_{(m_{\text{final}})}(k)$ terminates at the known trajectory $\tilde{\eta}_{(0)}(k)$, and because $\hat{y}(k) = 0$ for $k \in \{0, \dots, \mu - 1\}$ due to the known initial condition $\hat{x}(0) = 0$. The concatenation of these expressions plugged into the inverse output function (4.5b) yields the lifted inverse system model

$$\hat{\mathbf{g}}^{-1}(\hat{\mathbf{y}}) = \begin{bmatrix} \hat{f}^{\mu-1}(\tilde{\eta}_{(m_{\text{final}})}(0), \hat{\mathcal{U}}(0), 0) \\ \hat{f}^{\mu-1}(\tilde{\eta}_{(m_{\text{final}})}(1), \hat{\mathcal{U}}(1), 1) \\ \vdots \\ \hat{f}^{\mu-1}(\tilde{\eta}_{(m_{\text{final}})}(N - \mu), \hat{\mathcal{U}}(N - \mu), N - \mu) \end{bmatrix} \quad (4.45)$$

which enables the synthesis of the ILILC learning matrix (4.19). With this, the complete synthesis of ILILC with stable inversion—starting from a model in the normal form (4.1)—can be summarized by Procedure 4.1.

Procedure 4.1 ILILC Synthesis with Stable Inversion

- 1: Derive the minimal state space representation \hat{f}_{η} and $\hat{f}^{\mu-1}$ (from (4.5)) of the conventional inverse of (4.1).
 - 2: Apply similarity transform V (from (4.9)) to derive the inverse state dynamics representation \tilde{f}_{η} (from (4.10)) with decoupled stable and unstable linear parts.
 - 3: Use (4.43)-(4.44) to derive the inverse system state $\tilde{\eta}_{(m_{\text{final}})}$ as a function of $\hat{\mathbf{y}}$ at each point in time $k \in \{0, \dots, N - \mu\}$.
 - 4: Derive the lifted inverse model $\hat{\mathbf{g}}^{-1}$ via (4.45).
 - 5: Use an automatic differentiation tool to derive $\frac{\partial \hat{\mathbf{g}}^{-1}}{\partial \hat{\mathbf{y}}}$ as a function of \mathbf{y} , i.e. the learning matrix L_{ℓ} from (4.19).
 - 6: Compute $L_{\ell} = \frac{\partial \hat{\mathbf{g}}^{-1}}{\partial \hat{\mathbf{y}}}(\mathbf{y}_{\ell})$ at each trial for the ILC law (3.7).
// Steps 3-4 are greatly facilitated by using a computer algebra system. CasADi can provide this functionality in addition to automatic differentiation.
-

4.4 Validation

This section presents validation of the fundamental claim that the original NILC fails for models with unstable inverses and that the newly proposed ILILC framework—when used with stable inversion—succeeds. Additionally, while the intent of ILC is to account for model error, overly erroneous modeling can cause violation of (C2.3), which may cause divergence of the ILC law. Thus this section also probes the performance and robustness of ILILC with stable inversion over increasing model error in physically motivated simulations.

The ILILC law (3.7), (4.19) is applied as a reference shaping tool to a feedback control system (sometimes called “series ILC”). This represents the common scenario of applying a higher level

controller to “closed source” equipment. The resultant system (3.8) is a nonlinear time-varying system with relative degree $\mu = 2$.

Modeling error is simulated by synthesizing the ILC laws from a nominal “control model” of the example system, and applying the resultant control inputs to a set of “truth models” featuring random parameter errors and the injection of process and measurement noise. Finally, to give context to the results for ILILC with stable inversion, identical simulations are run with a benchmark technique that does not require modification for NMP systems: gradient ILC.

4.4.1 Benchmark Technique: Gradient ILC

Aside from those using NILC, the authors know of no prior art explicitly addressing ILC synthesis from discrete-time nonlinear (particularly nonlinear in the input) time-varying models with relative degree greater than 1. However, with automatic differentiation, “gradient ILC” is nearly as easily synthesized from this class of models as it is from the LTI models it was proposed for in [111].

The most straightforward form of Gradient ILC is gradient descent applied to the optimization problem

$$\arg \min_{\mathbf{u}} \frac{1}{2} \mathbf{e}^T \mathbf{e} \quad (4.46)$$

which yields the ILC law

$$\mathbf{u}_{\ell+1} = \mathbf{u}_{\ell} + \gamma \frac{\partial \hat{\mathbf{g}}}{\partial \mathbf{u}} (\mathbf{u}_{\ell})^T \mathbf{e}_j \quad (4.47)$$

where $\gamma > 0$ is the gradient descent step size. Note that (4.47) is free of the matrix inversion that historically inhibited the application of NILC to systems with unstable inverses.

γ is a tuning parameter that influences the performance-robustness trade off of (4.47). Reducing γ improves the probability that (4.47) will converge for some unknown model error, but may also reduce the rate of convergence. For the sake of comparing the convergence rates between gradient ILC and ILILC, here we choose γ such that the two methods have comparable probabilities of convergence over the battery of random model errors tested: $\gamma = 1.1$.

4.4.2 Example System

Consider the system pictured in Figure 4.1, consisting of a pendulum fixed to the mass center of a cart on a rail. This subsection presents the first-principles continuous-time equations of motion for this plant, the method for converting these dynamics to the discrete-time normal form (4.1), and the control architecture of the system.

The cart is subjected to an applied force c , and viscous damping occurs both between the cart and the rail and between the pendulum and the cart. Equations of motion for this plant are given

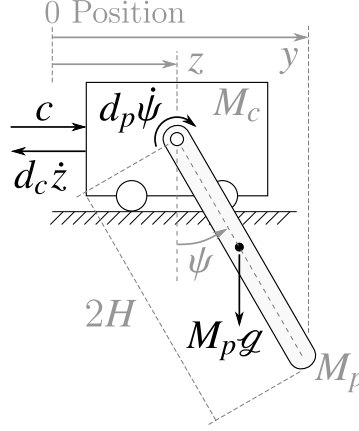


Figure 4.1: Cart and pendulum system. Dimension, position, and mass annotations are in grey. Force and torque annotations are in black.

by

$$\ddot{\psi} = -3 \left(HM_p (c + \omega_c) \cos(\psi) + d_p (M_c + M_p) \dot{\psi} + \right. \\ \left. H^2 M_p^2 \sin(\psi) \cos(\psi) \dot{\psi}^2 + gH (M_c M_p + M_p^2) \sin(\psi) - \right. \\ \left. d_c H M_p \cos(\psi) \dot{z} \right) \frac{1}{H^2 M_p (4(M_c + M_p) - 3M_p \cos^2(\psi))} \quad (4.48)$$

$$\ddot{z} = (4H (c + \omega_c) + 3d_p \cos(\psi) \dot{\psi} + \\ 4H^2 M_p \sin(\psi) \dot{\psi}^2 + 3gH M_p \sin(\psi) \cos(\psi) - \\ 4d_c H \dot{z}) \frac{1}{H (4(M_c + M_p) - 3M_p \cos^2(\psi))} \quad (4.49)$$

where $\psi(k)$ is the pendulum angle, $z(k)$ is the cart's horizontal position, $g = 9.8 \frac{\text{m}}{\text{s}^2}$ is gravitational acceleration, and the process noise $\omega_c(k)$ is a random sample from a normal distribution with 0 mean and standard deviation $3.15\text{E}-2\text{N}$. H is the pendulum half-length, M_c and M_p are the cart and pendulum masses, and d_c and d_p are the cart-rail and pendulum-cart damping coefficients, respectively. The time argument of ω_c , ψ , z and their derivatives has been dropped for compactness.

The output to be tracked is the pendulum tip's horizontal position, y . Obtaining a discrete-time state space model of this system in the normal form (4.1) requires first a change of coordinates

such that the desired output is a state, and then discretization. The change of coordinates is

$$\psi = \arcsin\left(\frac{y-z}{2H}\right) \quad (4.50)$$

with associated derivative substitutions

$$\dot{\psi} = \frac{\dot{y} - \dot{z}}{2H\sqrt{1 - \frac{(y-z)^2}{4H^2}}} \quad (4.51)$$

$$\ddot{\psi} = \frac{\sec(\psi)(\ddot{y} - \ddot{z} + 2H\sin(\psi)\dot{\psi}^2)}{2H} \quad (4.52)$$

Then the equations of motion are solved for in terms of the new coordinates. In the present case (4.48)-(4.52) can be solved for $\ddot{y}(k)$ and $\ddot{z}(k)$ as functions of $y(k)$, $z(k)$, $\dot{y}(k)$, and $\dot{z}(k)$. Next, forward Euler discretization is applied recursively to the equations of motion to reformulate the state dynamics in terms of discrete time increments rather than derivatives, as is required by the normal form. The innermost layer of the recursion is the first derivatives

$$\dot{y}(k) = \frac{y(k+1) - y(k)}{T_s} \quad \dot{z}(k) = \frac{z(k+1) - z(k)}{T_s} \quad (4.53)$$

where the sample period $T_s = 0.016$ s in this case. These can be plugged into $\ddot{y}(k)$ and $\ddot{z}(k)$ to eliminate their dependence on derivatives. The next—and in this case final—layer is the forward Euler discretization of the second derivatives. The outermost layer can be rearranged to yield the discrete-time equations of motion

$$\begin{aligned} y(k+2) &= \ddot{y}(k)T_s^2 + 2y(k+1) - y(k) \\ z(k+2) &= \ddot{z}(k)T_s^2 + 2z(k+1) - z(k), \end{aligned} \quad (4.54)$$

which are directly used to define the state dynamics f in terms of the state vector $x(k) = [y(k), y(k+1), z(k), z(k+1)]^T$. The explicit expressions of (4.54) are too long to print here, but can be easily obtained in Mathematica, MATLAB symbolic toolbox, etc. via the algebra described in (4.50)-(4.54).

The output must track the reference $r(k)$ given in Figure 4.2. To accomplish this the plant is equipped with a full-state feedback controller modeled as

$$c(k) = \kappa_0 r^*(k) - \begin{bmatrix} \kappa_1 & \kappa_2 & \kappa_3 & \kappa_4 \end{bmatrix} x(k) \quad (4.55)$$

$$r^*(k) = r(k) + u(k) \quad (4.56)$$

Here, $r^*(k)$ is the effective reference and $u(k)$ is the control input generated by the ILC law. In

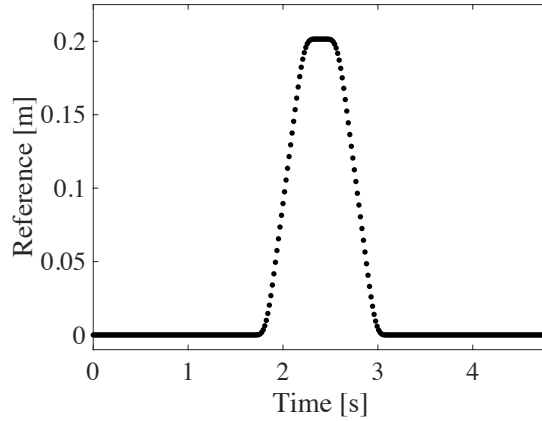


Figure 4.2: Reference

other words, the ILC law adjusts the reference delivered to the feedback controller to eliminate the error transients inherent to feedback control. Finally, the error signal input to the ILC law is subject to measurement noise $\omega_y(k)$

$$e(k) = r(k) - y(k) - \omega_y(k) \quad (4.57)$$

where the noise's distribution has 0 mean and standard deviation $5E-5$ m.

The ILC law itself is synthesized from a “control model” that is identical in structure to the “truth model” presented above, but has $\hat{\omega}_c = \hat{\omega}_y = 0$ and uses the model parameters tabulated in Table 4.1. Stable inversion for the synthesis of learning matrix (4.19) is performed with a single Picard iteration, i.e. $m_{\text{final}} = 1$ in (4.45). To simulate model error, the hatless truth model parameters differ from the behatted control model parameters in a manner detailed in Section 4.4.3. This ultimately results in the system block diagram given in Figure 4.3.

4.4.3 Simulation and Analysis Methods

Let $\hat{e}_\theta \in \mathbb{R}^{10}$ be a vector of the control model parameters in Table 4.1. Then a truth model can be specified by the vector θ , generated via

$$e_\theta = \left(\mathbf{1}_{10 \times 1} e_{e_\theta}^T \odot I + I \right) \hat{e}_\theta \quad (4.58)$$

where \odot is the Hadamard product and $e_{e_\theta} \in \mathbb{R}^{10}$ is a random sample of a uniform distribution. Under (4.58), each element of e_{e_θ} is the relative error between the corresponding elements of e_θ and \hat{e}_θ . Thus, $\|e_{e_\theta}\|_2$ provides a scalar metric for the model error between the control model and a given truth model. The range $\|e_{e_\theta}\|_2 \in [0, 0.1]$ is divided into 20 bins of equal width, and 50

Table 4.1: Cart-Pendulum Control Model Parameters

Parameter	Symbol	Value
Cart Mass	\hat{M}_c	0.5 kg
Pendulum Mass	\hat{M}_p	0.25 kg
Pendulum Half-Length	\hat{H}	0.225 m
Cart-Rail Damping Coefficient	\hat{d}_c	$10 \frac{\text{kg}}{\text{s}}$
Pendulum-Cart Damping Coefficient	\hat{d}_p	$0.01 \frac{\text{kg m}^2}{\text{s}}$
Full State Feedback Gain 0	$\hat{\kappa}_0$	630
Full State Feedback Gain 1	$\hat{\kappa}_1$	-5900
Full State Feedback Gain 2	$\hat{\kappa}_2$	5900
Full State Feedback Gain 3	$\hat{\kappa}_3$	-3700
Full State Feedback Gain 4	$\hat{\kappa}_4$	4300

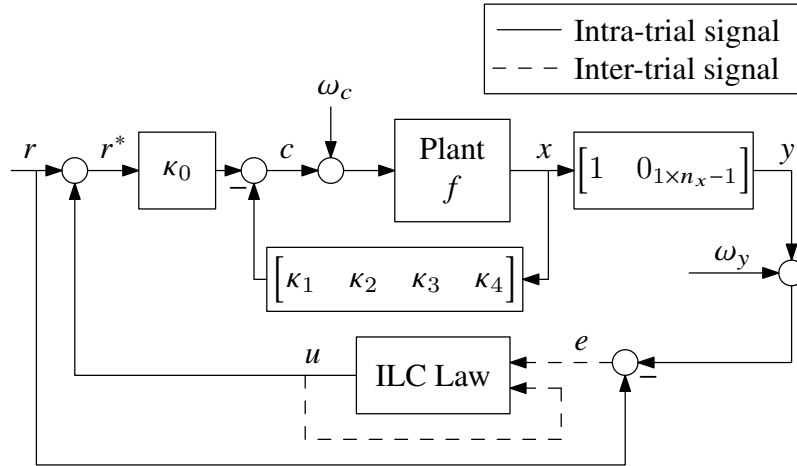


Figure 4.3: System Block Diagram. The control law outputting u is synthesized from the control models defined by the behatted parameters of Table 4.1 and by $\omega_c(k) = \omega_y(k) = 0$. The plant and controller gain blocks are defined with the truth model parameters generated according to Section 4.4.3. Inter-trial signals from trial ℓ are stored and used to compute the input for trial $\ell + 1$.

truth models are generated for each bin. Both ILC schemes are applied to each truth model with 50 trials, and $u_0(k) = 0 \forall k$. A full set of 50 trials of one of the ILC laws applied to a single truth model is referred to as a “simulation.” The results of these simulations are used to characterize the probability of convergence and rate of convergence of each ILC law.

For each iteration of a simulation, the normalized root mean square error (NRMSE) is given by

$$\text{NRMSE}_\ell := \frac{\text{RMS}(\mathbf{e}_\ell)}{\|\mathbf{r}\|_\infty} \quad (4.59)$$

A simulation is deemed convergent if there exists ℓ^* such that NRMSE_ℓ is less than some tolerance for all $\ell \geq \ell^*$. This work uses a tolerance of $5\text{E-}4$, which is close to the NRMSE floor created by noise.

Let $\ell^{\beta,\tau,\lambda}$ be the minimum ℓ^* for truth model $\tau \in [1, 50]$ in bin $\beta \in [1, 20]$ under ILC law $\lambda \in \{\text{ILILC}, \text{gradient ILC}\}$, and let C be the set of all (β, τ) for which both ILILC and gradient ILC converge. Then the mean transient convergence rate

$$\mathcal{R}_\lambda = \text{mean}_{C, \ell \in [1, \ell^{\beta,\tau,\lambda}]} \left(\frac{\text{NRMSE}_\ell^{\beta,\tau,\lambda}}{\text{NRMSE}_{\ell-1}^{\beta,\tau,\lambda}} \right) \quad (4.60)$$

offers a numerical performance metric. Note that [34] gives a theoretical convergence analysis for the ILC structure (3.7) in general (covering NILC, ILILC, and gradient ILC). This analysis can be used to lower bound performance (i.e. upper bound convergence rate) via multiple parameters computed from the learning matrix L_ℓ and the true dynamics \mathbf{g} . The mean transient convergence rate (4.60) may thus serve as a specific, measurable counterpart to any theoretical worst-case-scenario analyses performed via the formulas in [34].

Finally, to verify the fundamental necessity and efficacy of ILILC for systems with unstable inverses, 2 trials of traditional stable-inversion-free NILC (3.7), (3.15) are applied to each truth model.

4.4.4 Results and Discussion

The condition number of $\frac{\partial \hat{\mathbf{g}}}{\partial \mathbf{u}}(\mathbf{u}_0)$ is $1\text{E}17$. Attempted inversion of this matrix in MATLAB yields an inverse matrix with average nonzero element magnitude of $4\text{E}13$ and max element magnitude of $3\text{E}16$. Consequently, \mathbf{u}_1 generated by (3.7), (3.15) has an average element magnitude of $2\text{E}10$ m and a max element magnitude of $8\text{E}11$ m, which is so large that \mathbf{y}_1 and $\frac{\partial \hat{\mathbf{g}}}{\partial \mathbf{u}}(\mathbf{u}_1)$ contain NaN elements for all simulations. Conversely, while some simulations using ILILC, i.e. (3.7), (4.19), diverge due to excessive model error, the majority converge. This validates the fundamental claim that the direct application of Newton’s method in NILC is insufficient for systems with unstable inverses, and

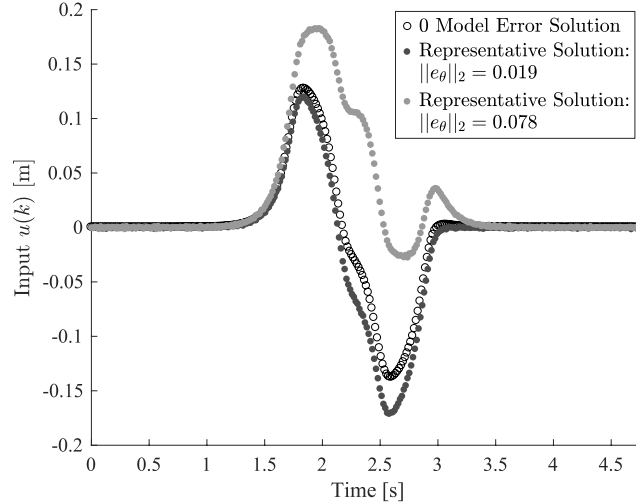


Figure 4.4: Representative input solution trajectories from low- and high-model-error ILILC simulations compared with the solution to the zero-model-error problem. The zero-model-error solution is the input trajectory that would be chosen for feedforward control in the absence of learning, and differs notably from both minimum-error trajectories found by ILILC with stable inversion.

that slight modification of the learning matrix and the incorporation of stable inversion addresses this gap.

To accompany the quantitative metric $\|e_\theta\|_2$, Figure 4.4 offers a qualitative sense of the degree of model error in this study by comparing two representative ILILC solution trajectories $u_{50}(k)$ with the solution to the $\|e_\theta\|_2 = 0$, $\omega_c(k) = \omega_y(k) = 0$ scenario. The lower-model-error representative solution is from within the range of $\|e_\theta\|_2$ for which all simulations converged, while the higher-model-error solution comes from a bin in which some simulations diverged. A more detailed analysis of the boundaries in θ -space determining convergence or divergence of a simulation is beyond the scope of this work. However, the given trajectories illustrate that even in the conservative subspace defined by the 100% convergent bins learning bridges a visible performance gap, and that beyond this subspace there are far greater performance gains to be had.

Finally, a statistical comparison of the performance and robustness of ILILC with stable inversion and gradient ILC is given in Figure 4.5. The tuning of gradient ILC indeed yields comparable robustness to ILILC, with ILILC 97% as likely to converge as gradient ILC over all simulations. The convergence rates of the two ILC schemes, however, differ substantially, with gradient ILC taking over 3 times as many trials as ILILC to converge on average. The mean transient convergence rate values tabulated in Table 4.2 give a more portable quantification of ILILC’s advantage, having a convergence rate nearly half that of gradient ILC’s.

This analysis confirms that ILILC with stable inversion is an important addition to the engineer’s toolbox because it enables ILC synthesis from nonlinear non-minimum phase models and

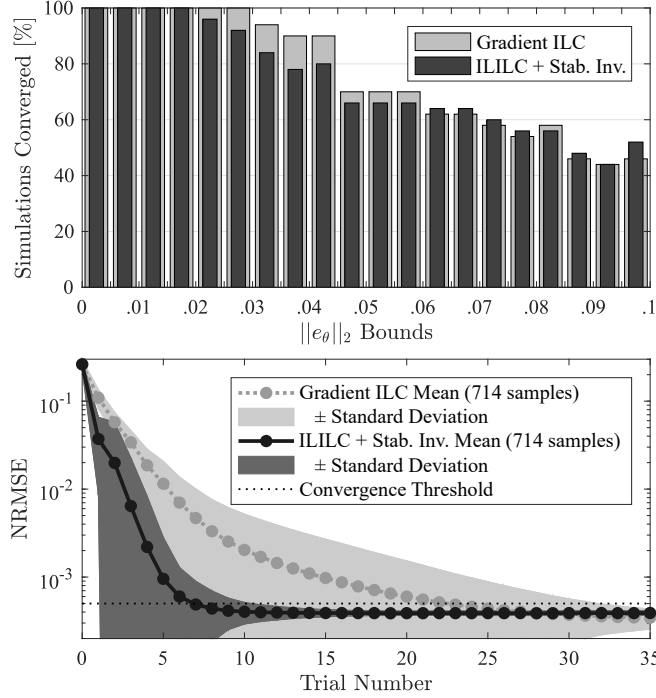


Figure 4.5: *Top*: Histogram giving the percentage of simulations converged in each bin of the model error metric $\|e_\theta\|_2$. *Bottom*: Mean value of NRMSE for each ILC trial over all simulations that are convergent for both gradient ILC and ILILC with stable inversion. This illustrates that for comparable robustness to model error, ILILC converges substantially faster than gradient ILC.

Table 4.2: Transient Convergence Rates for ILILC and Gradient ILC

ILC Law	Mean	Standard Deviation
Gradient ILC	0.76	0.17
ILILC + Stab. Inv.	0.41	0.27

delivers the fast convergence characteristic of algorithms based on Newton’s method.

4.5 Conclusion

This chapter introduces and validates a new ILC synthesis scheme applicable to nonlinear time-varying systems with unstable inverses and relative degree greater than 1. This is done with the support of nonlinear stable inversion, which is advanced from the prior art via proof of convergence for an expanded class of systems and methods for improved practical implementation. In all, this results in a new, broadly implementable ILC scheme displaying a competitive convergence speed under benchmark testing.

Future work may focus on further broadening the applicability of ILILC by relaxing reference and initial condition repetitiveness assumptions, and on the extension of ILILC with a potentially adaptive tuning parameter or other means to enable the exchange of some speed for robustness when called for. Levenberg-Marquardt-Fletcher algorithms may offer one source of inspiration for such work.

CHAPTER 5

Hybrid Systems with Unstable Inverses: Stable Inversion of Piecewise Affine Systems

As discussed in Chapter 1, despite the call for it [46], little work has been done on the feedforward control of PWA systems. Naturally, a lack of feedforward control research in general implies a lack of research on the more specific problem of feedforward control for NMP PWA systems.

Thus, while the combination of ILILC and stable inversion is promising for the ILC of PWA systems with NMP dynamics, there are two major gaps in the literature that must be filled before such control can be realized. First, there does not exist any published theory on stable inversion for PWA systems (or hybrid systems of any kind). Second, there does not exist sufficient literature on the conventional closed-form PWA system inversion prerequisite for stable inversion.

The most relevant prior art on PWA system inversion is Sontag’s foundational work on piecewise linear systems [112]. Sontag proposes that these systems are potentially invertible-with-delay, and explains the signal time shifting necessary to accommodate this delay. This serves as a beginning for the concept of the relative degree of a PWA system. However, these concepts require further development to account for the fact that a PWA system’s apparent relative degree may change during switching between component models and the fact that PWA systems may have multiple inverses. Additionally, Sontag leaves the derivation of the inverse dynamics other than the delay open as a “nontrivial part” of the inversion process. Finally, for reference tracking it is desirable to invert a system without delay. This frequently results in anticausal inverses—those in which future reference values are required to compute a current input—but this is no problem for typical feedforward control scenarios where the entire reference is known in advance.

Further work of Sontag [113] delves into the abstract algebra of piecewise linear functions and includes the useful facts that it is decidable whether two sets are isomorphic under piecewise linear

Content of this chapter also to be submitted as:

I. A. Spiegel, N. Strijbosch, R. de Rozario, T. Oomen and K. Barton, “Stable Inversion of Piecewise Affine Systems with Application to Feedforward and Iterative Learning Control,” in *IEEE Transactions on Automatic Control*. Copyright may be transferred without notice, after which this version may no longer be accessible.

functions, that the class of piecewise linear functions is closed under composition, and that if a piecewise linear function has an inverse, it has a piecewise linear inverse. These facts are promising and may support dynamical systems research, but are still quite distant from the problem of actually finding the inverse of a dynamical system. Additionally, beyond the suggestion of a direction for future work in abstract algebra, no information is given on the uniqueness of the inverse. Finally, these results do not apply to time-varying systems, which must be considered if one is to perform feedforward control of a system also subject to feedback control with a time-varying reference.

In short, the lack of general PWA system inversion theory stymies the output reference tracking control of a broad range of practical systems, especially those with NMP models, for which ILC-based workarounds are currently inapplicable. The present work fills this gap by contributing

1. formal inversion formulas for a class of PWA systems,
2. sufficient conditions for inverse uniqueness and the corresponding explicit inverse representations,
3. stable inversion theory and implementation methods for PWA models with NMP components, and
4. a simulation validation of this theory via the NILC of an NMP PWA system.

Section 5.1 formally defines the class of PWA systems treated in this work and a concept of relative degree for deterministic hybrid systems in general. Section 5.2 proves inverse PWA system formulas and sufficient conditions for inverse uniqueness. Section 5.3 presents the stable inversion theory for PWA systems. Section 5.4 presents and discusses the validation of the inversion and stable inversion theory via the ILILC of an NMP system. Finally, Section 5.5 presents conclusions and recommendations for future work.

5.1 System Definition

A variety of similar discrete-time PWA system definitions appear in the literature. For the sake of familiarity and simplicity, the following time-varying system definition uses a representation similar to [2] and [114].

Definition 5.1 (PWA System). A PWA system is given by

$$\begin{aligned} x_{k+1} &= A_{q,k}x_k + B_{q,k}u_k + F_{q,k} \\ y_k &= C_{q,k}x_k + D_{q,k}u_k + G_{q,k} \end{aligned} \quad \text{for } x_k \in Q_q \quad (5.1)$$

where $k \in \mathbb{Z}$ is the time-step index, $x \in \mathbb{R}^{n_x}$, $u \in \mathbb{R}^{n_u}$, and $y \in \mathbb{R}^{n_y}$ are the state, input, and output vectors, and $Q_q \in Q$ where Q is the set of “locations,” i.e. a set of disjoint regions with union equal to \mathbb{R}^{n_x} . Each location Q_q is the union of a set of disjoint convex polytopes. Here, a convex polytope is defined simply as an intersection of half spaces. Additionally, let the relative degree of the q^{th} component model be denoted μ_q for $q \in \llbracket 1, |Q| \rrbracket$ ($\llbracket \cdot \rrbracket$ indicates a closed set of integers).

To facilitate both mathematical analysis and controller synthesis, the remainder of the chapter uses the equivalent closed-form representation

$$x_{k+1} = \mathbf{A}_k x_k + \mathbf{B}_k u_k + \mathbf{F}_k \quad (5.2a)$$

$$y_k = \mathbf{C}_k x_k + \mathbf{D}_k u_k + \mathbf{G}_k \quad (5.2b)$$

with the upright, bold, capital letter notation defined as

$$\mathbf{M}_k := \sum_{q=1}^{|Q|} M_{q,k} K_q(\delta_k) \quad (5.3)$$

$$K_q(\delta_k) := 0^{\prod_{i=1}^{|\Delta_q^*|} \|\delta_{q,i}^* - \delta_k\|} = \begin{cases} 1 & \delta_k \in \Delta_q^* \\ 0 & \text{otherwise} \end{cases} \quad (5.4)$$

$$\delta_k = \delta(x_k) := H(Px_k - \beta) \quad (5.5)$$

where \mathbf{M} and $M_{q,k}$ stand in for any of $\{\mathbf{A}, \mathbf{B}, \mathbf{F}, \mathbf{C}, \mathbf{D}, \mathbf{G}\}$, and $\{A_{q,k}, B_{q,k}, F_{q,k}, C_{q,k}, D_{q,k}, G_{q,k}\}$, respectively. H is the Heaviside step function evaluated element-wise on its vector argument, K_q is the binary-output selector function for the q^{th} location, $\Delta_q^* = \{\delta_{q,1}^*, \delta_{q,2}^*, \dots\}$ is the set of binary vector signatures of the q^{th} location, $P \in \mathbb{R}^{n_p \times n_x}$ is a matrix consisting of concatenated hyperplane orientation vectors, and $\beta \in \mathbb{R}^{n_p}$ is a vector of hyperplane offsets. For more information about closed form representations of piecewise defined systems, see Chapter 3.

Furthermore, the following assumptions are made for all systems

(A5.1) $x_0 \in X_0$, where X_0 is the set of initial conditions from which all locations $Q_q \in Q$ are reachable in finite time

(A5.2) the system is single-input-single-output (SISO),

$$n_u = n_y = 1$$

(A5.3) switching depends only on the states, not the input

(A5.4) all component models have the same relative degree, μ_c , for all time, $\mu_q = \mu_c \forall q \in \llbracket 1, |Q| \rrbracket$ and $\forall k$

Note that while the assumption (A5.3) is implied by (5.5), the other assumptions are not implied by the system representation (5.2)-(5.5).

Finally, this work introduces the concept of the “global dynamical relative degree:”

Definition 5.2 (Global Dynamical Relative Degree). The *global dynamical relative degree* of a SISO PWA system is the smallest number $\mu_g \geq 0$ such that the explicit expression of $y_{k+\mu_g}$ in terms of component state space matrices, selector functions, x_k , and u_i , $i \geq k$ contains u_k outside of a selector function for all switching sequences on the interval $[[k, k + \mu_g]]$.

This μ_g is essentially the traditional relative degree, but neglecting inputs appearing in selector functions. This neglect is introduced to avoid situations in which the only explicit appearance of the input in the output function is within the Heaviside function, leading to a potentially infinite number of input values yielding the same output. Such non-injectiveness would make inversion unusually challenging. The assumption (A5.3) is made for similar reasons.

5.2 Conventional PWA System Inversion

This section presents the conventional exact inverses of PWA systems under assumptions (A5.1)-(A5.4). Conventional inversion is the process of

(Step 1) obtaining an expression for the previewed output $y_{k+\mu_g}$ in terms of x_k , $\mathbf{M}_{k+\kappa}$, and $u_{k+\kappa}$ where $\kappa \geq 0$,

(Step 2) solving the previewed output equation for u_k in terms of x_k , $\mathbf{M}_{k+\kappa}$, and $u_{k+\kappa+1}$, and finally

(Step 3) taking this expression of u_k as the output function of the inverse system, and plugging it in to (5.2a) to obtain the state transition formula of the inverse system.

Note that $y_{k+\mu_g}$ is necessarily an explicit function of u_k by Definition 5.2.

For systems with $\mu_g = 0$, this inverse system is unique, and can be expressed explicitly. For systems with $\mu_g \geq 1$, there may be multiple solutions to the problem of solving $y_{k+\mu_g}$ for u_k (Step 2), and thus the inverse system cannot be expressed explicitly without additional assumptions. This section gives both the general, implicit inverse system for $\mu_g \geq 1$ systems and sufficient conditions for the uniqueness of system inversion for $\mu_g \in \{1, 2\}$ systems along with the corresponding explicit inverse systems.

5.2.1 Unique Exact Inversion For $\mu_g = 0$

Lemma 1 (Relative Degree of 0). *The global dynamical relative degree of a reachable SISO PWA system, i.e. a PWA system satisfying (A5.1) and (A5.2), is 0 if and only if the relative degree of all*

component models are 0 for all time:

$$\mu_q = 0 \quad \forall q \in \llbracket 1, |Q| \rrbracket, \forall k \iff \mu_g = 0 \quad (5.6)$$

Proof. First, the forward implication is proven directly.

$$\mu_q = 0 \quad \forall q, k \implies D_{q,k} \neq 0 \quad \forall q, k \quad (5.7)$$

$$D_{q,k} \neq 0 \quad \forall q, k \implies \mathbf{D}_k \neq 0 \quad \forall k \quad (5.8)$$

$$\mathbf{D}_k \neq 0 \quad \forall k \implies (5.2b) \text{ always explicitly contains } u_k \quad (5.9)$$

$$\therefore \mu_q = 0 \quad \forall q \in Q \implies \mu_g = 0 \quad (5.10)$$

Now the backwards implication is proven by proving the contrapositive.

$$\exists q, k \text{ s.t. } \mu_q \neq 0 \implies \exists q, k \text{ s.t. } D_{q,k} = 0 \quad (5.11)$$

By (A5.1), there exists some finite sequence of inputs to bring the system to this location Q_q at some time step k such that $\mathbf{D}_k = D_{q,k} = 0$, and (5.2b) becomes

$$y_k = \mathbf{C}_k x_k + \mathbf{G}_k \quad (5.12)$$

which is not an explicit function of u_k , meaning $\mu_g \neq 0$.

$$\therefore \neg (\mu_q = 0 \quad \forall q \in \llbracket 1, |Q| \rrbracket, \forall k) \implies \neg (\mu_g = 0) \quad (5.13)$$

By (5.10) and (5.13), (5.6) must be true. \square

Theorem 5.1 ($\mu_g = 0$ PWA System Inverse). *The inverse of a PWA system satisfying (A5.1)-(A5.4) with $\mu_c = 0$ is itself a PWA system satisfying (A5.1)-(A5.4) and is given by*

$$x_{k+1} = \bar{\mathbf{A}}_k x_k + \bar{\mathbf{B}}_k y_k + \bar{\mathbf{F}}_k \quad (5.14)$$

$$u_k = \bar{\mathbf{C}}_k x_k + \bar{\mathbf{D}}_k y_k + \bar{\mathbf{G}}_k \quad (5.15)$$

where

$$\begin{aligned} \bar{\mathbf{A}}_k &= \mathbf{A}_k - \mathbf{B}_k \mathbf{D}_k^{-1} \mathbf{C}_k & \bar{\mathbf{B}}_k &= \mathbf{B}_k \mathbf{D}_k^{-1} & \bar{\mathbf{F}}_k &= \mathbf{F}_k - \mathbf{B}_k \mathbf{D}_k^{-1} \mathbf{G}_k \\ \bar{\mathbf{C}}_k &= -\mathbf{D}_k^{-1} \mathbf{C}_k & \bar{\mathbf{D}}_k &= \mathbf{D}_k^{-1} & \bar{\mathbf{G}}_k &= -\mathbf{D}_k^{-1} \mathbf{G}_k \end{aligned}$$

such that y_k is the input of the inverse system and u_k is the output.

Proof. (Step 1) is satisfied by (5.2b) and (Step 2) by

$$u_k = \mathbf{D}_k^{-1}(y_k - \mathbf{C}_k x_k - \mathbf{G}_k) \quad (5.16)$$

Equation (5.16) is always well-defined because by Lemma 1 $\mu_c = 0 \implies \mu_g = 0$, which in turn implies $\mathbf{D}_k \neq 0 \forall k$, and because \mathbf{D} is always scalar because the system is SISO by (A5.2). Plugging (5.16) into (5.2a) yields the inverse system state transition formula, satisfying (Step 3). \square

5.2.2 Non-unique Exact Inversion For $\mu_g \geq 1$

For systems with $\mu_g \geq 1$, (5.2b) does not explicitly contain u_k because $\mathbf{D}_k = 0 \forall k$; this is corollary to Lemma 1, Definition 5.2, and (A5.4). Consequently, (Step 1) necessitates the derivation of an explicit formula for the output preview $y_{k+\mu_g}$, i.e. the output at a time after the current time step k . This preview of future output is necessary for deriving an output equation that explicitly depends on the current input u_k .

Lemma 2 ($\mu_g \geq 1$ PWA System Output Preview). *Given a PWA system satisfying (A5.1)-(A5.4) with known global dynamical relative degree μ_g , the output function with minimum preview such that the function is explicitly dependent on an input term outside of the selector functions for any switching sequence is given by*

$$y_{k+\mu_g} = \mathbf{C}_k x_k + \mathcal{D}_k u_k + \mathcal{G}_k + \Psi_k(u_{k+1}, \dots, u_{k+\mu_g-1}) \quad (5.17)$$

with

$$\begin{aligned} \mathbf{C}_k &:= \mathbf{C}_{k+\mu_g} \left(\prod_{m=0}^{\mu_g-1} \mathbf{A}_{k+m} \right) & \mathcal{D}_k &:= \mathbf{C}_{k+\mu_g} \left(\prod_{m=1}^{\mu_g-1} \mathbf{A}_{k+m} \right) \mathbf{B}_k \\ \mathcal{G}_k &:= \mathbf{C}_{k+\mu_g} \sum_{s=0}^{\mu_g-1} \left(\left(\prod_{m=s+1}^{\mu_g-1} \mathbf{A}_{k+m} \right) \mathbf{F}_{k+s} \right) + \mathbf{G}_{k+\mu_g} \\ \Psi_k(u_{k+1}, \dots) &:= \mathbf{C}_{k+\mu_g} \sum_{s=1}^{\mu_g-1} \left(\left(\prod_{m=s+1}^{\mu_g-1} \mathbf{A}_{k+m} \right) \mathbf{B}_{k+s} u_{k+s} \right) \end{aligned}$$

where the factors in the products generated by \prod are ordered sequentially by the index m . The factor corresponding to the greatest value of the index must be on the left, and the factor corre-

sponding to the smallest value of the index must be on the right. For example,

$$\prod_{m=0}^2 \mathbf{A}_{k+m} \equiv \mathbf{A}_{k+2}\mathbf{A}_{k+1}\mathbf{A}_{k+0} \neq \mathbf{A}_{k+0}\mathbf{A}_{k+1}\mathbf{A}_{k+2} \quad (5.18)$$

because matrices do not necessarily commute. Additionally, if the lower bound on the product index exceeds the upper bound on the product index (an “empty product”), then the product resolves to the identity matrix. Similarly, empty sums resolve to 0. For example

$$\prod_{m=1}^0 \text{anything} \equiv I \quad \sum_{s=1}^0 \text{anything} \equiv 0 \quad (5.19)$$

Proof. Let the base case of the proof by induction be $\mu_g = 1$ such that

$$y_{k+1} = \mathbf{C}_{k+1} (\mathbf{A}_k x_k + \mathbf{F}_k + \mathbf{B}_k u_k) + \mathbf{G}_{k+1} \quad (5.20)$$

which is achieved equivalently from (5.17) and from the system definition by plugging (5.2a) into (5.2b) incremented by one time step (i.e. plugging the equation for x_{k+1} into the equation for y_{k+1}). The preview is minimal because, by Definition 5.2, $\mathbf{C}_{k+1}\mathbf{B}_k \neq 0$ for all switching sequences on $\llbracket k, k+1 \rrbracket$, and by Lemma 1 $\mu_g \geq 1 \implies \mathbf{D}_k = 0 \forall k$. In other words, for $\mu_g = 1$, (5.20) is always an explicit function of u_k . Thus, regardless of switching sequence, outputs further in the future, such as y_{k+2} , never need to be considered in order to explicitly relate the current input to an output.

Then consider (5.17) with $\mu_g = \nu$ as the foundation of the induction step. To prove (5.17) holds for $\mu_g = \nu + 1$, first increment (5.17) with $\mu_g = \nu$ by one time step, yielding

$$\begin{aligned} y_{k+\nu+1} = & \mathbf{C}_{k+\nu+1} \left(\prod_{m=0}^{\nu-1} \mathbf{A}_{k+1+m} \right) x_{k+1} + \mathbf{C}_{k+\nu+1} \left(\prod_{m=1}^{\nu-1} \mathbf{A}_{k+1+m} \right) \mathbf{B}_{k+1} u_{k+1} + \\ & \mathbf{C}_{k+\nu+1} \sum_{s=0}^{\nu-1} \left(\left(\prod_{m=s+1}^{\nu-1} \mathbf{A}_{k+1+m} \right) \mathbf{F}_{k+1+s} \right) + \mathbf{G}_{k+1+\nu} + \mathbf{C}_{k+\nu+1} \sum_{s=1}^{\nu-1} \left(\left(\prod_{m=s+1}^{\nu-1} \mathbf{A}_{k+1+m} \right) \mathbf{B}_{k+1+s} u_{k+1+s} \right) \end{aligned} \quad (5.21)$$

This can be simplified by first factoring out $\mathbf{C}_{k+\nu+1}$ and adjusting the product Π indices to subsume

the constant +1 in \mathbf{A}_{k+1+m} :

$$y_{k+\nu+1} = \mathbf{C}_{k+\nu+1} \left(\left(\prod_{m=1}^{\nu} \mathbf{A}_{k+m} \right) x_{k+1} + \left(\prod_{m=2}^{\nu} \mathbf{A}_{k+m} \right) \mathbf{B}_{k+1} u_{k+1} + \sum_{s=0}^{\nu-1} \left(\left(\prod_{m=s+2}^{\nu} \mathbf{A}_{k+m} \right) \mathbf{F}_{k+1+s} \right) \right. \\ \left. + \sum_{s=1}^{\nu-1} \left(\left(\prod_{m=s+2}^{\nu} \mathbf{A}_{k+m} \right) \mathbf{B}_{k+1+s} u_{k+1+s} \right) \right) + \mathbf{G}_{k+\nu+1} \quad (5.22)$$

Similarly, the sum \sum indices may be adjusted to subsume the constant +1 in \mathbf{F}_{k+1+s} , \mathbf{B}_{k+1+s} , and u_{k+1+s} . Because the sum index s also appears in the lower bound of the products, $m = s + 2$, the product index lower bound must also be adjusted.

$$y_{k+\nu+1} = \mathbf{C}_{k+\nu+1} \left(\left(\prod_{m=1}^{\nu} \mathbf{A}_{k+m} \right) x_{k+1} + \left(\prod_{m=2}^{\nu} \mathbf{A}_{k+m} \right) \mathbf{B}_{k+1} u_{k+1} + \sum_{s=1}^{\nu} \left(\left(\prod_{m=s+1}^{\nu} \mathbf{A}_{k+m} \right) \mathbf{F}_{k+s} \right) \right. \\ \left. + \sum_{s=2}^{\nu} \left(\left(\prod_{m=s+1}^{\nu} \mathbf{A}_{k+m} \right) \mathbf{B}_{k+s} u_{k+s} \right) \right) + \mathbf{G}_{k+\nu+1} \quad (5.23)$$

Finally, the two input terms (those containing u , arising from \mathcal{D}_{k+1} and Ψ_{k+1}) can be combined to achieve

$$y_{k+\nu+1} = \mathbf{C}_{k+\nu+1} \left(\left(\prod_{m=1}^{\nu} \mathbf{A}_{k+m} \right) x_{k+1} + \sum_{s=1}^{\nu} \left(\left(\prod_{m=s+1}^{\nu} \mathbf{A}_{k+m} \right) \mathbf{F}_{k+s} \right) \right. \\ \left. + \sum_{s=1}^{\nu} \left(\left(\prod_{m=s+1}^{\nu} \mathbf{A}_{k+m} \right) \mathbf{B}_{k+s} u_{k+s} \right) \right) + \mathbf{G}_{k+\nu+1} \quad (5.24)$$

which is a function of x_{k+1} and potentially u_{κ} for $\kappa \in \llbracket k+1, k+\nu+1 \rrbracket$. The dependence of $y_{k+\nu+1}$ on the input terms is conditioned on the switching sequence. Definition 5.2 implies that if $\mu_g = \nu+1$ there exists some switching sequence on $\llbracket k, k+\nu+1 \rrbracket$ such that the input coefficients in (5.24) are zero, i.e.

$$\exists \{x_{\kappa} \mid \kappa \in \llbracket k, k+\nu+1 \rrbracket\} \quad \text{s.t.} \quad \forall s \in \llbracket 1, \nu \rrbracket \quad \mathbf{C}_{k+\nu+1} \left(\prod_{m=s+1}^{\nu} \mathbf{A}_{k+m} \right) \mathbf{B}_{k+s} = 0 \quad (5.25)$$

Thus, to guarantee the expression for $y_{k+\nu+1}$ explicitly contains the input for all switching sequences, x_{k+1} in (5.24) must be expanded (via (5.2a)) to be in terms of x_k and u_k explicitly. The

resulting expression can be rearranged as follows:

$$y_{k+\nu+1} = \mathbf{C}_{k+\nu+1} \left(\left(\prod_{m=1}^{\nu} \mathbf{A}_{k+m} \right) (\mathbf{A}_k x_k + \mathbf{B}_k u_k + \mathbf{F}_k) + \sum_{s=1}^{\nu} \left(\left(\prod_{m=s+1}^{\nu} \mathbf{A}_{k+m} \right) \mathbf{F}_{k+s} \right) \right) + \Psi_k(u_{k+1}, \dots, u_{k+\nu}) + \mathbf{G}_{k+\nu+1} \quad (5.26)$$

$$y_{k+\nu+1} = \mathbf{C}_{k+\nu+1} \left(\left(\prod_{m=1}^{\nu} \mathbf{A}_{k+m} \right) \mathbf{A}_k x_k + \left(\prod_{m=1}^{\nu} \mathbf{A}_{k+m} \right) \mathbf{B}_k u_k + \sum_{s=1}^{\nu} \left(\left(\prod_{m=s+1}^{\nu} \mathbf{A}_{k+m} \right) \mathbf{F}_{k+s} \right) + \left(\prod_{m=1}^{\nu} \mathbf{A}_{k+m} \right) \mathbf{F}_k + \mathbf{G}_{k+\nu+1} \right) + \Psi_k(u_{k+1}, \dots, u_{k+\nu}) \quad (5.27)$$

$$y_{k+\nu+1} = \mathbf{C}_{k+\nu+1} \left(\left(\prod_{m=0}^{\nu} \mathbf{A}_{k+m} \right) x_k + \left(\prod_{m=1}^{\nu} \mathbf{A}_{k+m} \right) \mathbf{B}_k u_k + \sum_{s=0}^{\nu} \left(\left(\prod_{m=s+1}^{\nu} \mathbf{A}_{k+m} \right) \mathbf{F}_{k+s} \right) \right) + \mathbf{G}_{k+\nu+1} + \Psi_k(u_{k+1}, \dots, u_{k+\nu}) \quad (5.28)$$

Equation (5.28) is equation (5.17) for $\mu_g = \nu + 1$, thereby proving the lemma. \square

Using the output preview equation (5.17), a general PWA system inverse for $\mu_g \geq 1$ can be found in the same manner as for $\mu_g = 0$.

Theorem 5.2 (General $\mu_g \geq 1$ PWA System Inverse). *Given any PWA system satisfying (A5.1)-(A5.4) with known global dynamical relative degree $\mu_g \geq 1$, the inverse system with u_k as the output is given by the implicit, anticausal system*

$$x_{k+1} = \bar{\mathbf{A}}_k x_k + \bar{\mathbf{B}}_k y_{k+\mu_g} + \bar{\mathbf{F}}_k - \mathbf{B}_k \mathcal{D}_k^{-1} \Psi_k(u_{k+1}, \dots, u_{k+\mu_g-1}) \quad (5.29)$$

$$u_k = \bar{\mathbf{C}}_k x_k + \bar{\mathbf{D}}_k y_{k+\mu_g} + \bar{\mathbf{G}}_k - \mathcal{D}_k^{-1} \Psi_k(u_{k+1}, \dots, u_{k+\mu_g-1}) \quad (5.30)$$

where

$$\begin{aligned} \bar{\mathbf{A}}_k &= \mathbf{A}_k + \mathbf{B}_k \bar{\mathbf{C}}_k & \bar{\mathbf{B}}_k &= \mathbf{B}_k \bar{\mathbf{D}}_k & \bar{\mathbf{F}}_k &= \mathbf{F}_k + \mathbf{B}_k \bar{\mathbf{G}}_k \\ \bar{\mathbf{C}}_k &= -\bar{\mathbf{D}}_k \mathbf{C}_k & \bar{\mathbf{D}}_k &= \mathcal{D}_k^{-1} & \bar{\mathbf{G}}_k &= -\bar{\mathbf{D}}_k \mathbf{G}_k \end{aligned}$$

Proof. The sole term in Lemma 2's (5.17) containing u_k outside of a selector function is $\mathcal{D}_k u_k$. The

coefficient $\mathcal{D}_k = \mathbf{C}_{k+\mu_g} \left(\prod_{m=1}^{\mu_g-1} \mathbf{A}_{k+m} \right) \mathbf{B}_k$ is always scalar because the system is SISO, (A5.2), and always nonzero by Definition 5.2. Thus (5.17) can be divided by \mathcal{D}_k and u_k can be arithmetically maneuvered onto one side of the equation by itself, yielding (5.30).

Equation (5.30) is implicit in general because (5.17) cannot be uniquely solved for u_k in general. This is proven by presenting an example in which multiple input trajectories have the same output trajectory. Consider the two-location system

$$\begin{aligned} A_{1,k} &= \begin{bmatrix} 0 & 1 \\ 0 & 0 \end{bmatrix} & A_{2,k} &= \begin{bmatrix} 0 & 2 \\ 0 & 0 \end{bmatrix} & B_{1,k} &= B_{2,k} = \begin{bmatrix} 0 \\ 1 \end{bmatrix} \\ C_{1,k} &= C_{2,k} = \begin{bmatrix} 1 & 0 \end{bmatrix} \\ P &= \begin{bmatrix} 0 & 1 \end{bmatrix} & \beta &= 1.5 & \Delta_1^* &= \{1\} & \Delta_2^* &= \{2\} \end{aligned} \quad (5.31)$$

with F , D , and G matrices all equal to zero. Given $x_k = [0, 0]^T$, both $u_k = 2$ and $u_k = 1$ yield $y_{k+\mu_g} = 2$. Because there is not a unique solution to (5.17) for u_k , there does not exist an explicit formula for the solution (5.30).

The system is necessarily anticausal because u_k is necessarily a function of $y_{k+\mu_g}$ and $\mu_g > 0$. \square

Remark 5.1 (Inverse Implicitness). Analytically, the implicitness of (5.30) arises in $\bar{\mathbf{C}}_k$ through C_k , which is a function of $\mathbf{C}_{k+\mu_g}$ by definition, and $\mathbf{C}_{k+\mu_g}$ is a function of $x_{k+\mu_g}$ by (5.3)-(5.5). Finally, $x_{k+\mu_g}$ is a function of u_k via

$$\begin{aligned} x_{k+\mu_g} &= \left(\prod_{m=0}^{\mu_g-1} \mathbf{A}_{k+m} \right) x_k + \sum_{s=0}^{\mu_g-1} \left(\left(\prod_{m=s+1}^{\mu_g-1} \mathbf{A}_{k+m} \right) \mathbf{F}_{k+s} \right) + \\ &\quad \sum_{s=1}^{\mu_g-1} \left(\left(\prod_{m=s+1}^{\mu_g-1} \mathbf{A}_{k+m} \right) \mathbf{B}_{k+s} u_{k+s} \right) + \left(\prod_{m=1}^{\mu_g-1} \mathbf{A}_{k+m} \right) \mathbf{B}_k u_k \end{aligned} \quad (5.32)$$

following from $y_{k+\mu_g} = \mathbf{C}_{k+\mu_g} x_{k+\mu_g} + \mathbf{G}_{k+\mu_g}$ and Lemma 2.

Remark 5.2 (Input Preview and Inter-location Relative Degree). Note Ψ_k is written as a function of a set of previewed u -values. The written set of u -values is the maximum quantity of u -values that may be required by Ψ_k . Depending on the switching sequence, fewer previewed u -values may be required. In fact, by the definition of global dynamical relative degree μ_g , there must exist a switching sequence for which no previewed u -values are required, because otherwise μ_g would be

smaller. In other words, Definition 5.2 and Lemma 2 imply

$\exists \{x_k \mid \kappa \in \llbracket k, k + \mu_g \rrbracket\}$ s.t.

$$\begin{aligned} \forall s \in \llbracket 1, \mu_g - 1 \rrbracket \quad & \mathbf{C}_{k+\mu_g} \left(\prod_{m=s+1}^{\mu_g-1} \mathbf{A}_{k+m} \right) \mathbf{B}_{k+s} = 0 \\ & \wedge \mathbf{C}_{k+\mu_g} \left(\prod_{m=1}^{\mu_g-1} \mathbf{A}_{k+m} \right) \mathbf{B}_k \neq 0 \end{aligned} \quad (5.33)$$

For affine time-invariant systems without piecewise definition, there is never required input preview because the expressions claimed equal to zero in (5.33) reduce as

$$\mathbf{C}_{k+\mu_g} \left(\prod_{m=s+1}^{\mu_g-1} \mathbf{A}_{k+m} \right) \mathbf{B}_{k+s} = CA^{\mu_g-1-s}B \quad s \in \llbracket 1, \mu_g - 1 \rrbracket \quad (5.34)$$

which are always zero regardless of state sequence. However, it is important to emphasize that this is not the case for PWA systems. Even when the relative degrees of all component models are equal to μ_c , (A5.4), the inter-location relative degree may not be equal to μ_c . More formally

$$C_{1,k+1}B_{1,k} = 0 \wedge C_{2,k+1}B_{2,k} = 0 \not\Rightarrow C_{1,k+1}B_{2,k} = 0 \quad (5.35)$$

and

$$C_{1,k+1}B_{1,k} \neq 0 \wedge C_{2,k+1}B_{2,k} \neq 0 \not\Rightarrow C_{1,k+1}B_{2,k} \neq 0 \quad (5.36)$$

and this lack of conclusiveness regarding the inter-state relative degree generalizes to larger μ_c . In short, the inter-state relative degree may be either lower or higher than μ_c , and may be different for different switching sequences (with a maximum value of μ_g as given by Definition 5.2).

Because of the implicitness and potential requirement for input preview in the general PWA system inverse, it is nontrivial to use it for computing input trajectories from output trajectories. However, there are conditions under which inversion of a PWA system with $\mu_g \geq 1$ is unique, and the inverse itself becomes an explicit PWA system as is the case for $\mu_g = 0$. The remainder of this section provides such sufficient conditions for the cases of $\mu_g = 1$ and $\mu_g = 2$.

5.2.3 Unique Exact Inverses For $\mu_g \in \{1, 2\}$

First the “location-independent output function” assumption is introduced:

(A5.5) $\mathbf{C}_k = C_k$, $\mathbf{D}_k = D_k$, $\mathbf{G}_k = G_k$, with C_k, D_k, G_k indicating parameters that potentially vary with time but that are identical $\forall q \in \llbracket 1, |Q| \rrbracket$

Lemma 3 (Relative Degree of 1). *A PWA system satisfying (A5.1)-(A5.5) has a global dynamical relative degree of 1 if and only if the relative degree of all component models are 1 for all time:*

$$\mu_c = 1 \iff \mu_g = 1 \quad (5.37)$$

Proof. The forward implication follows directly from (A5.4), (A5.5), and $\mu_c = 1$:

$$\mu_c = 1 \implies D_{k+1} = 0 \wedge C_{k+1}B_{q,k} \neq 0 \quad \forall q \in \llbracket 1, |Q| \rrbracket \quad (5.38)$$

$$\implies \mathbf{D}_{k+1} = 0 \wedge \mathbf{C}_{k+1}\mathbf{B}_k \neq 0 \quad \forall k \quad (5.39)$$

This is equivalent to implying that the inter-location relative degree can be neither higher nor lower than $\mu_c = 1$ under (A5.4) and (A5.5)

$$\therefore \mu_c = 1 \implies \mu_g = 1 \quad (5.40)$$

The backward implication follows from (5.33) (i.e. the combination of Definition 5.2 and Lemma 2), which implies

$$\mu_g = 1 \implies \exists \{x_k, x_{k+1}\} \text{ s.t. } \mathbf{C}_{k+1}\mathbf{B}_k \neq 0 \quad (5.41)$$

Then, by (A5.4), (A5.5), and the fact that $\mu_g = 1 \implies \mathbf{D}_k = 0$ by Lemma 1, one finds that $\mathbf{C}_{k+1}\mathbf{B}_k = C_{k+1}B_k \neq 0 \implies \mu_c = 1$. Therefore (5.37) is true. \square

Corollary 5.2.1 (Unique Inverse of $\mu_g = 1$ PWA Systems). *The inverse of a PWA system satisfying (A5.1)-(A5.5) with $\mu_c = 1$ is given by the following explicit, anticausal PWA system.*

$$x_{k+1} = \bar{\mathbf{A}}_k x_k + \bar{\mathbf{B}}_k y_{k+1} + \bar{\mathbf{F}}_k \quad (5.42)$$

$$u_k = \bar{\mathbf{C}}_k x_k + \bar{\mathbf{D}}_k y_{k+1} + \bar{\mathbf{G}}_k \quad (5.43)$$

where

$$\begin{aligned} \bar{\mathbf{A}}_k &= \mathbf{A}_k + \mathbf{B}_k \bar{\mathbf{C}}_k & \bar{\mathbf{B}}_k &= \mathbf{B}_k \bar{\mathbf{D}}_k & \bar{\mathbf{F}}_k &= \mathbf{F}_k + \mathbf{B}_k \bar{\mathbf{G}}_k \\ \bar{\mathbf{C}}_k &= -\bar{\mathbf{D}}_k C_{k+1} \mathbf{A}_k & \bar{\mathbf{D}}_k &= (C_{k+1} \mathbf{B}_k)^{-1} & \bar{\mathbf{G}}_k &= -\bar{\mathbf{D}}_k (C_{k+1} \mathbf{F}_k + G_{k+1}) \end{aligned}$$

Proof. $\mu_g = 1$ by Lemma 3. Plugging (A5.5) and $\mu_g = 1$ into (5.30) yields

$$u_k = (\mathbf{C}\mathbf{B}_k)^{-1}(y_{k+1} - C(\mathbf{A}_k x_k + \mathbf{F}_k) - G) \quad (5.44)$$

which is explicit. Note that $(\mathbf{C}\mathbf{B}_k)^{-1}$ is always well defined because it is scalar by (A5.2) and is nonzero by $\mu_g = 1$ and Definition 5.2. \square

To derive explicit inverses for PWA systems with $\mu_g = 2$, (A5.5) is used along with the new “output-based switching” assumption. Assuming $\mu_g > 0$, this assumption is expressed as

$$(A5.6) \quad P = P_o \mathbf{C}_k \text{ and } \beta = \beta_o - P_o \mathbf{G}_k$$

where P_o and β_o contain the orientation vectors and offsets of hyperplanes in the output space \mathbb{R}^{n_y} .

Corollary 5.2.2 (Unique Inverse of $\mu_g = 2$ PWA Systems). *The inverse of a PWA system satisfying (A5.1)-(A5.6) with known global dynamical relative degree $\mu_g = 2$ is given by the following explicit, anticausal PWA system.*

$$x_{k+1} = \bar{\mathbf{A}}_k x_k + \bar{\mathbf{B}}_k y_{k+2} + \bar{\mathbf{F}}_k \quad (5.45)$$

$$u_k = \bar{\mathbf{C}}_k x_k + \bar{\mathbf{D}}_k y_{k+2} + \bar{\mathbf{G}}_k \quad (5.46)$$

where

$$\begin{aligned} \bar{\mathbf{A}}_k &= \mathbf{A}_k + \mathbf{B}_k \bar{\mathbf{C}}_k & \bar{\mathbf{B}}_k &= \mathbf{B}_k \bar{\mathbf{D}}_k & \bar{\mathbf{F}}_k &= \mathbf{F}_k + \mathbf{B}_k \bar{\mathbf{G}}_k \\ \bar{\mathbf{C}}_k &= -\bar{\mathbf{D}}_k C_{k+2} \mathbf{A}_{k+1} \mathbf{A}_k & \bar{\mathbf{D}}_k &= (C_{k+2} \mathbf{A}_{k+1} \mathbf{B}_k)^{-1} \\ \bar{\mathbf{G}}_k &= -\bar{\mathbf{D}}_k (C_{k+2} \mathbf{A}_{k+1} \mathbf{F}_k + C_{k+2} \mathbf{F}_{k+1} + G_{k+2}) \end{aligned}$$

Proof. Plugging (A5.5) and $\mu_g = 2$ into (5.30) yields

$$u_k = (C_{k+2} \mathbf{A}_{k+1} \mathbf{B}_k)^{-1} (y_{k+2} - C_{k+2} \mathbf{A}_{k+1} \mathbf{A}_k x_k - C_{k+2} \mathbf{A}_{k+1} \mathbf{F}_k - C_{k+2} \mathbf{F}_{k+1} - G_{k+2}) \quad (5.47)$$

In general, (5.47) would be implicit because of \mathbf{A}_{k+1} and \mathbf{F}_{k+1} ’s dependence on x_{k+1} , and thus u_k , via the selector functions

$$K_q(\delta(x_{k+1})) = 0^{\prod_{i=1}^{\Delta_q^*} \|\delta_{q,i}^* - H(P(\mathbf{A}_k x_k + \mathbf{B}_k u_k + \mathbf{F}_k) - \beta)\|} \quad (5.48)$$

However, under (A5.6) (in combination with (A5.5)) this becomes

$$K_q(\delta(x_{k+1})) = 0^{\prod_{i=1}^{\Delta_q^*} \|\delta_{q,i}^* - H(P_o C_{k+1} (\mathbf{A}_k x_k + \mathbf{F}_k) - \beta_o + P_o G_{k+1})\|} \quad (5.49)$$

which is not a function of u_k and is thus explicit.

The reduction of (5.48) to (5.49) relies on the fact that $C_{k+1}\mathbf{B}_k = 0 \forall k$. This is true for $\mu_g = 2$ systems under (A5.5) because $\mu_g = 2 \implies \mu_c > 1$ by Lemma 3. \square

Remark 5.3 (μ_c, μ_g Relationship). Note that unlike for relative degrees of 0 and 1, $\mu_c = 2 \not\Rightarrow \mu_g = 2$ under assumptions (A5.1)-(A5.6). If $n_x > 2$, there exists systems for which $\mu_c = 2$ but $\mu_g > 2$ due to inter-location dynamics.

5.3 Stable Inversion of PWA Systems

5.3.1 Exact Stable Inversion

For many PWA systems, evolving the inverse systems derived in Section 5.2 forward in time from an initial state at time $k = k_0$ and with a bounded reference $y_{k+\mu_g} = r_{k+\mu_g}$ will yield an inverse system trajectory u_k that is bounded for all $k \geq k_0$ and suitable for feedforward control. However, inverse PWA system instabilities may arise from NMP component dynamics, causing u_k to become unbounded under this conventional system evolution scheme, despite the bounded reference. In such cases, a bounded u_k may still be achievable on a bi-infinite timeline via stable inversion. Formally, the stable inversion problem may be given as follows.

Definition 5.3 (PWA Stable Inversion Problem Statement). Given an explicit inverse PWA system representation

$$x_{k+1} = \bar{\mathbf{A}}_k x_k + \bar{\mathbf{B}}_k y_{k+\mu_g} + \bar{\mathbf{F}}_k \quad (5.50a)$$

$$u_k = \bar{\mathbf{C}}_k x_k + \bar{\mathbf{D}}_k y_{k+\mu_g} + \bar{\mathbf{G}}_k \quad (5.50b)$$

and a reference trajectory $y_{k+\mu_g} = r_{k+\mu_g}$ known for all $k \in \mathbb{Z}$, a two point boundary value problem is formed by (5.50a) and the boundary conditions $x_{-\infty} = x_{\infty} = 0$. The solution to the stable inversion problem is the bounded bi-infinite time series $u_k \in \mathbb{R} \forall k$, which is generated by (5.50b) and the bounded bi-infinite solution x_k to the boundary value problem.

The following assumptions on system parameter boundedness and boundary conditions are common in some form across much stable inversion literature.

(A5.7) There exists a supremum to the norms of the inverse system matrices:

$$\sup_k \|\bar{\mathbf{A}}_k\|, \sup_k \|\bar{\mathbf{B}}_k\|, \sup_k \|\bar{\mathbf{F}}_k\|, \sup_k \|\bar{\mathbf{C}}_k\|, \sup_k \|\bar{\mathbf{D}}_k\|, \sup_k \|\bar{\mathbf{G}}_k\| \in \mathbb{R} \quad (5.51)$$

Any vector norm may be used, and the matrix norm is that induced by the vector norm.

(A5.8) The reference $y_{k+\mu_g}$ and bias terms $\bar{\mathbf{F}}_k, \bar{\mathbf{G}}_k$ decay to zero at the extremities of the bi-infinite time series:

$$\forall \varepsilon \in \mathbb{R}_{>0} \quad \exists \eta_1, \eta_2 \in \mathbb{Z} \quad \text{s.t.} \quad \left\| y_{k+\mu_g} \right\|, \left\| \bar{\mathbf{F}}_k \right\|, \left\| \bar{\mathbf{G}}_k \right\| < \varepsilon \quad \forall k \in (-\infty, \eta_1] \cup [\eta_2, \infty) \quad (5.52)$$

Additionally, stable inversion of PWA systems involves two challenges not faced in the stable inversion of linear systems. First, the dynamics of all locations and the inter-location dynamics must be simultaneously accounted for when decoupling the stable and unstable system modes. Second, there must be a way to manage switching in the two partial system evolutions. These challenges are manifested in the following assumptions.

(A5.9) There exists a similarity transform matrix $V \in \mathbb{R}^{n_x \times n_x}$ that decouples the stable and unstable modes of (5.50a). Formally this decoupling can be expressed as

$$V \bar{\mathbf{A}}_k V^{-1} = \begin{bmatrix} \tilde{\mathbf{A}}_k^s & \mathbf{0}_{n_s \times n_u} \\ \mathbf{0}_{n_u \times n_s} & \tilde{\mathbf{A}}_k^u \end{bmatrix} \quad \forall k \quad (5.53)$$

where n_s is the number of stable modes, n_u is the number of unstable modes, $n_s + n_u = n_x$, $\tilde{\mathbf{A}}_k^u$ has all eigenvalue magnitudes $> 1 \forall k$, and the free systems

$$z_{k+1}^s = \tilde{\mathbf{A}}_k^s z_k^s \quad z_{k+1}^u = (\tilde{\mathbf{A}}_k^u)^{-1} z_k^u \quad (5.54)$$

with appropriately sized state vectors z^s, z^u are globally uniformly asymptotically stable about the origin.

(A5.10a) Switching is exclusively dependent on the stable modes:

$$PV^{-1} = \begin{bmatrix} \tilde{P}^s & \mathbf{0}_{n_p \times n_u} \end{bmatrix} \quad (5.55)$$

(A5.10b) Switching is exclusively dependent on the unstable modes and all unstable states arising from (5.50) are reachable in one time step from some predecessor state for all k :

$$\left(PV^{-1} = \begin{bmatrix} \mathbf{0}_{n_p \times n_s} & \tilde{P}^u \end{bmatrix} \right) \wedge \left(\forall k, \forall \tilde{x}_{k+1}^u \in \mathcal{X}^u \subseteq \mathbb{R}^{n_u} \quad \text{Pre}(\{\tilde{x}_{k+1}^u\}) \neq \emptyset \right) \quad (5.56)$$

where $\tilde{x}_k^u = \begin{bmatrix} \mathbf{0}_{n_u \times n_s} & I_{n_u \times n_u} \end{bmatrix} V x_k$. \mathcal{X}^u is a set containing at least all solution values of \tilde{x}_{k+1}^u (see Section 5.3.2 for elaboration). $\text{Pre}(\mathcal{X})$ is the set of predecessor states whose

one-step successors belong to the set \mathcal{X} .

For detailed theorems on the sufficient conditions for uniform asymptotic stability of systems of the form (5.54), see [115].

As implied by the separation of (A5.10) into two opposing assumptions, the challenges associated with switching management precipitate different stable inversion procedures for the stable-mode-dependent switching and unstable-mode-dependent switching cases. In general, the trajectory of the modes upon which switching is dependent are computed first. This allows the switching signal for the overall system to be computed and given as an exogenous input to the evolution of the remaining modes.

The theorems for these cases are supported by the following notation for the decoupled system in addition to the above-defined $\tilde{\mathbf{A}}_k^j, \tilde{\mathbf{A}}_k^u, \tilde{\mathbf{P}}^j, \tilde{\mathbf{P}}^u$.

$$\begin{aligned}\tilde{x}_k^j &:= \mathcal{F}^j V x_k & \tilde{\mathbf{B}}_k^j &:= \mathcal{F}^j V \mathbf{B}_k & \tilde{\mathbf{F}}_k^j &:= \mathcal{F}^j V \tilde{\mathbf{F}}_k \\ \tilde{x}_k^u &:= \mathcal{F}^u V x_k & \tilde{\mathbf{B}}_k^u &:= \mathcal{F}^u V \mathbf{B}_k & \tilde{\mathbf{F}}_k^u &:= \mathcal{F}^u V \tilde{\mathbf{F}}_k\end{aligned}\quad (5.57)$$

where

$$\mathcal{F}^j := \begin{bmatrix} I_{n_s \times n_s} & 0_{n_s \times n_u} \end{bmatrix} \quad \mathcal{F}^u := \begin{bmatrix} 0_{n_u \times n_s} & I_{n_u \times n_u} \end{bmatrix} \quad (5.58)$$

Theorem 5.3 (PWA Stable Inversion with Stable-Mode-Dependent Switching). *Given an explicit inverse PWA system (5.50) satisfying (A5.7)-(A5.9) and (A5.10a), the solution to the stable inversion problem exists and can be found by first computing the stable mode time series \tilde{x}_k^j and location time series $\delta_k \forall k$ forwards in time via*

$$\delta_k = H (\tilde{\mathbf{P}}^j \tilde{x}_k^j - \beta) \quad (5.59)$$

$$\tilde{x}_{k+1}^j = \tilde{\mathbf{A}}_k^j \tilde{x}_k^j + \tilde{\mathbf{B}}_k^j y_{k+\mu_g} + \tilde{\mathbf{F}}_k^j \quad (5.60)$$

The location time series being now known, the unstable mode time series \tilde{x}_k^u can be computed backwards in time via

$$\tilde{x}_k^u = (\tilde{\mathbf{A}}_k^u)^{-1} (\tilde{x}_{k+1}^u - \tilde{\mathbf{B}}_k^u y_{k+\mu_g} - \tilde{\mathbf{F}}_k^u) \quad (5.61)$$

with δ_k input directly to the selector functions in (5.3). Finally the solution u_k is computed via (5.50b) with $x_k = V^{-1} \left[\left(\tilde{x}_k^j \right)^T, \left(\tilde{x}_k^u \right)^T \right]^T$.

Proof. The prescribed formula represents a solution to the stable inversion problem because

- by (A5.10a), (5.59) is equivalent to (5.5),

- by (A5.9), the concatenated evolutions of (5.60) and (5.61) are equivalent to (5.50a), and
- by (A5.7) and (A5.8), (5.60) and (5.61) decay to the form of (5.54) in the limits as k approaches ∞ or $-\infty$, and thus by (A5.9) the boundary conditions at these limits are satisfied.

The solution is guaranteed to exist because

- (5.59)-(5.61) and (5.50b) are all explicit functions with all variables in the right-hand side known due to the order of time series computation, and
- the outputs of (5.59)-(5.61) exist because the system parameters and input signals are bounded by (A5.7) and (A5.8), and $\tilde{\mathbf{A}}_k^u$ is guaranteed invertible by the eigenvalue condition of (A5.9).

□

Theorem 5.4 (PWA Stable Inversion with Unstable-Mode-Dependent Switching). *Given an explicit inverse PWA system (5.50) satisfying (A5.7)-(A5.9) and (A5.10b), the solution to the stable inversion problem exists and can be found in the following manner. First solve the implicit backward-in-time evolution of the unstable modes, (5.61), for \tilde{x}_k^u at each time step using any of the applicable algorithms (e.g. brute force search over all locations or computational geometry methods [116], see Section 5.3.2 for elaboration). For each time step at which one of the potentially multiple solution values of \tilde{x}_k^u is chosen (any selection method is valid), the location vector δ_k may be computed by*

$$\delta_k = H (\tilde{P}^u \tilde{x}_k^u - \beta) \quad (5.62)$$

The location time series being computed, δ_k may be directly plugged in to the selector functions in (5.3) to make the forward-in-time evolution of the stable modes, (5.60), explicit such that it can be evaluated at each time step for \tilde{x}_k^s . The solution u_k is then computed via (5.50b) with

$$x_k = V^{-1} \left[\left(\tilde{x}_k^s \right)^T, \left(\tilde{x}_k^u \right)^T \right]^T, \text{ as in Theorem 5.3.}$$

Proof. The prescribed formula represents a solution to the stable inversion problem for the same reasons as Theorem 5.3, but with the first proposition of (A5.10b)—i.e. $PV^{-1} = [0_{n_p \times n_s}, \tilde{P}^u]$ —used in place of (A5.10a). The solution is guaranteed to exist because

- the second proposition of (A5.10b) guarantees the solution set of (5.61) is non-empty,
- the PWA nature of the original inverse system (5.50) enables application of existing algorithms guaranteed to find $\text{Pre}(\{\tilde{x}_{k+1}^u\})$ and thus solve (5.61) [116], and
- with solutions to (5.61) chosen $\forall k$, the remaining equations are explicit with bounded outputs for the same reasons as in Theorem 5.3.

□

Note that while [116] focuses on PWA systems with time-invariant components, only the one-step predecessor set need be computed at each time step. Thus, because a time-varying system is indistinguishable from a time-invariant system over a single time step, the algorithms of [116] are still applicable.

5.3.2 Practical Considerations

The most immediate issue with Theorems 5.3 and 5.4 is that, while they provide an exact solution to the stable inversion problem, their procedures cannot be implemented because of the infinite nature of the time series involved. This issue applies to past works on stable inversion as well, and the same means of addressing the issue is taken here. Namely, an approximate solution is obtained by prescribing a finite reference $r_{k+\mu_g}$ for $k \in \llbracket 0, N - \mu_g \rrbracket$ and strictly enforcing the boundary conditions on only the initial/terminal states of the stable/unstable mode evolution. In other words, $x_0^j = 0$ and $x_{N-\mu_g}^u = 0$ but $x_{N-\mu_g}^j$ and x_0^u may be nonzero.

In general the closer x_k^j and x_k^u come to decaying to zero by $k = N - \mu_g$ and $k = 0$, respectively, the higher quality the approximation of the u_k time series will be. In other words, the closer u_k comes to returning $y_{k+\mu_g} = r_{k+\mu_g}$ when input to the original system from which the inverse (5.50) was derived. To achieve this high quality approximation, one may specify $r_{k+\mu_g}$ to begin and end with a number of zero elements to allow space for the u_k time series to contain the pre- and post-actuation typically necessary for the control of NMP systems. The number of zero elements required to achieve a satisfactorily low error is case dependent. One typical heuristic is to ensure that the durations of the leading and trailing zeros are approximately equal to the system settling time.

In addition to the practical need for finite references with leading and trailing zeros, the case of unstable-mode-dependent switching warrants special attention regarding implementation.

First, consider methods to solve the implicit equation (5.61) at each time step. Any method will consist of two parts: identifying a set of valid solutions and then choosing one of them. Choosing a solution can be formalized as the minimization of some cost function, $\|x_{k+1}^u - x_k^u\|$ being a straightforward and universally applicable option. If the inverse system (5.50) has exclusively unstable modes, input-based costs such as $\|u_k\|$ and $\|u_{k+1} - u_k\|$ may also be used. Note that any such optimization is combinatorial, i.e. the decision variable can only take on values from a particular finite set. For the problem considered here, the cardinality of this set is at most the number of locations $|Q|$ in the system. This is because each location contains at most one solution to (5.61) due to the eigenvalue condition in (A5.9) making $(\tilde{\mathbf{A}}_k^u)^{-1}$ full rank and thus one-to-one.

Having an upper bound of one solution per location leads to a direct method for deriving the set of valid solutions to (5.61). For each location $Q_q \in Q$, compute

$$\left(\tilde{A}_{q,k}^u\right)^{-1} \left(\tilde{x}_{k+1}^u - B_{q,k}^u r_{k+\mu_g} - F_{q,k}^u\right) \quad (5.63)$$

and check whether the result lies in Q_q . If so, the result is a solution to (5.61). Naturally, logic relating to solution selection criteria may be incorporated to reduce computational cost, e.g. checking locations in order of proximity to the current location to avoid checking all locations in the case that the solution selection cost function is something like $\|x_{k+1}^u - x_k^u\|$. Alternatively, $\text{Pre}\left(\{\tilde{x}_{k+1}^u\}\right)$ may be derived whole using the computational-geometry-supported algorithms of [116]. As noted in [116], the algorithm of least cost may be case-dependent.

Finally, consider verification of the existence of a solution to the stable inversion problem with unstable-mode-based switching. The verification method recommended here is to first verify (A5.7)-(A5.9) and the first proposition of (A5.10b) directly, then run the procedure given in Theorem 5.4 for finding a solution. If (A5.7)-(A5.9) and the first proposition of (A5.10b) have been verified, then the procedure is guaranteed to find a solution to (5.61) if a solution exists. Equivalently, failure to find a solution implies no solution exists.

This method is recommended over directly attempting to verify the second proposition of (A5.10b) because this second proposition may be conservative, difficult to verify, and yield very limited computational savings over the recommended method. The conservativeness arises from the choice of set of possible \tilde{x}_{k+1}^u values, \mathcal{X}^u . It is unlikely for one to possess knowledge of the solution \tilde{x}_{k+1}^u values prior to actually solving the stable inversion problem, so \mathcal{X}^u may need to be set much larger than necessary to ensure it contains the solution trajectory. This containment is necessary for truth of the proposition to imply verification of solution existence. Conversely, the proposition may evaluate to false despite containing a true solution if \mathcal{X}^u also contains unreachable states. Selection of \mathcal{X}^u may thus be a delicate, challenging task.

The expectation of high computational cost arises from the subtle discrepancy between the capabilities of established PWA system verification methods and the second proposition of (A5.10b). Multiple methods exist for verifying the reachability/controllability of a PWA system to a target set \mathcal{X}^u [116, 117]. However, these methods typically verify whether at least one element of the target set is reachable, whereas (A5.10b) requires verification that every element of the target set is reachable. In other words, the computational savings one might expect from existing reachability/controllability verification schemes may not be available.

In short, the second proposition of (A5.10b) is useful for specifying a condition under which a solution is guaranteed to exist, and thus for the derivation and proof of Theorem 5.4. But it is not recommended as a tool for existence verification. This is not a significant loss, however, because

the procedure given in Theorem 5.4 for finding a solution is itself a valid verification tool.

5.4 Validation: Application to ILC

This section uses the stable inversion theory of Section 5.3, and thus also the conventional inversion theory of Section 5.2, to simulate the application of ILILC to a PWA system with NMP component dynamics: an inkjet printhead positioning system. This system uses feedback and feedforward control simultaneously. In addition to ILILC, for benchmarking purposes a number of other controllers are applied to the system:

- feedback-only control (i.e. zero feedforward input),
- learning-free PWA stable inversion (i.e. stable inversion without ILILC),
- gradient ILC, and
- P-type ILC.

P-type ILC is used as a benchmark in addition to the gradient ILC benchmark introduced in Chapter 4 because P-type ILC is among the most common forms of ILC used in industry, is considered by many to be a form of “model-free” ILC, and like gradient ILC does not necessarily cause instability when applied to systems with NMP dynamics. Details for the formulation of all ILC schemes are given in Section 5.4.2.

These simulations are subject to a variety of model errors and other disturbances to validate the stable-inversion-supported learning controller’s practicality. In other words, the controller is synthesized from a “control model” and applied to a “truth model” representing a physical system. The control model features mismatches in parameter values, sample rate, model order, and relative degree.

Additionally, the truth model is subject to copious process noise and measurement noise. While the physical system has virtually no output-measurable noise, the injection here is done as a preliminary test to ensure that noise does not corrupt the learning process beyond the remedial power of conventional filtering.

5.4.1 Example System

The truth model is based on the physical desktop inkjet printhead positioning testbed at the Eindhoven University of Technology, pictured in Figure 5.1. The input to this system is an applied motor voltage, c_k , and the output is the printhead position along a 0.3 m guide rail, y_k^P , measured by a linear optical encoder with a resolution of 50 μm . The applied motor voltage c_k is the sum of

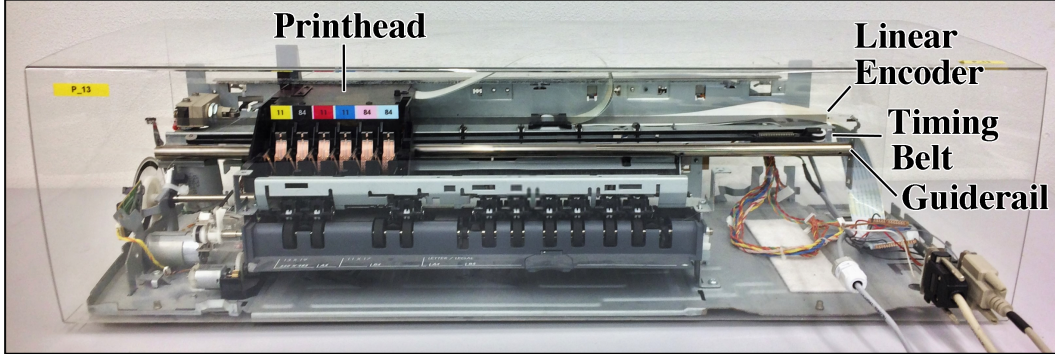


Figure 5.1: Photo of desktop inkjet printer with the case removed. The motor actuates the printhead motion along a guide rail via a timing belt, and the motion is measured by a linear optical encoder with resolution of $50\ \mu\text{m}$ (about 600 dots per inch).

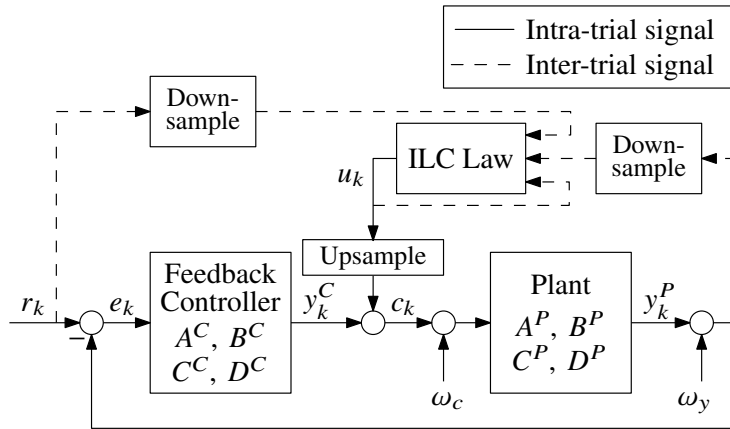


Figure 5.2: System block diagram. The plant block uses the truth model of the printer system obtained by experimental system identification while the ILC law is synthesized using the control model. The down-sample and upsample blocks account for the difference in sample period between the ILC law and the truth model.

a feedback component, y_k^C , and feedforward component, u_k . Finally, to add additional disturbance to the simulation, Gaussian white process noise ω_c (zero mean, standard deviation $0.03\ \text{V}$) and measurement noise ω_y (zero mean, standard deviation $50\ \mu\text{m}$) are added at the input and output of the plant, respectively. This ultimately results in the block diagram of Figure 5.2.

System identification of the printer yields a discrete-time LTI model, which is used as the truth model. Truncation-based model order reduction by 1 (MATLAB function `balred`), zero-order-hold-based sample period reduction by a factor of 2 (MATLAB function `d2d`), and random perturbation of model parameters results yields a new LTI model, which is used as the control model and can be represented by the state space system $(\hat{A}^P, \hat{B}^P, \hat{C}^P, \hat{D}^P)$ with state vector $\hat{x}^P \in \mathbb{R}^{n_{\hat{x}^P}}$.

To account for the change in sample period, truth model output signals are decimated by a

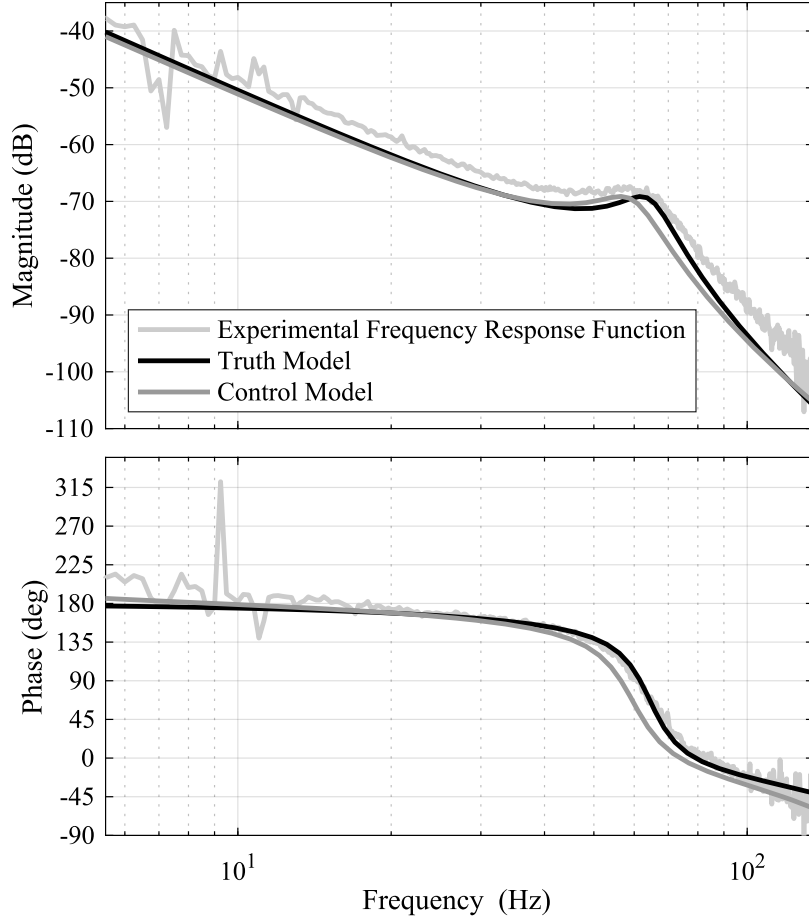


Figure 5.3: Bode plot of the experimental plant data, truth model of the plant, and control model of the plant.

factor of 2 before being input to the ILC law and ILC law output signals are upsampled by a factor of 2 with a zero order hold before being applied to the truth model. Parameters for the truth and control models are given in terms of pole, zero, and gain values in Table 5.1. A Bode plot of the experimental data, truth model, and control model are given in Figure 5.3.

The feedback controller is of identical structure and tuning for the truth and control models, but has different parameter values due to the difference in sample period between the two models. In either case, the feedback controller is composed of a second order lowpass filter given by the discrete-time transfer function

$$C^{LP}(z) = \frac{bz(z+1)}{z^2 + a_1z + a_2} \quad (5.64)$$

in series with a hybrid Proportional-Derivative (PD) controller. The proportional gain K_p is set to a high value when the reference-output error is greater than some magnitude threshold, and is set

to a lower value otherwise:

$$C^{PD}(z) = \frac{\left(K_p + \frac{K_d}{T_s}\right)z - \frac{K_d}{T_s}}{z} \quad (5.65)$$

$$K_p = \begin{cases} K_{p,1} & |e_{k-1}| \leq e_{\text{switch}} \\ K_{p,2} & |e_{k-1}| > e_{\text{switch}} \end{cases} \quad (5.66)$$

where T_s is the sample period in seconds and K_d is the derivative gain. Note that switching is the error of the previous time step rather than the current time step in order for switching to be state-based, and thus satisfy (A5.3). Mathematically this switching is made state-based by augmenting the minimal state-space representation of $C^{PD}(z)C^{LP}(z)$ with an extra state that stores the error input to the lowpass filter. In other words, the feedback controller model is given by

$$\hat{A}^C = \begin{bmatrix} 0 & 1 & 0 \\ -a_2 & -a_1 & 0 \\ 0 & 0 & 0 \end{bmatrix} \quad \hat{B}^C = \begin{bmatrix} 0 \\ 1 \\ 1 \end{bmatrix} \quad (5.67)$$

$$\hat{C}^C = -b \left[\frac{K_d(1+a_2)}{T_s} + K_p a_2 \quad \frac{K_d a_1}{T_s} + K_p (a_1 - 1) \right] \quad (5.68)$$

$$\hat{D}^C = \left[b \left(K_p + \frac{K_d}{T_s} \right) \right] \quad (5.69)$$

with state vector $\hat{x}_k^C \in \mathbb{R}^{n_x^C}$ having its final element equal to e_{k-1} . Parameter values for the feedback controller are given in Table 5.1. For both the truth model and the control model, the lowpass filter has a roll off frequency of 40 Hz and a damping ratio of 0.7.

To perform stable inversion of the system dynamics from the feedforward input to the output, a monolithic PWA model of the form (5.2) is needed. This is given by

$$\hat{x}_{k+1} = \hat{\mathbf{A}}_k \hat{x}_k + \hat{\mathbf{B}}_k u_k + \hat{\mathbf{F}}_k \quad (5.70)$$

$$\hat{y}_k = \hat{\mathbf{C}}_k \hat{x}_k + \hat{\mathbf{D}}_k u_k + \hat{\mathbf{G}}_k \quad (5.71)$$

where

$$\hat{\mathbf{A}}_k = \begin{bmatrix} \hat{A}^P - \hat{B}^P \hat{D}^C \hat{C}^P & \hat{B}^P \hat{C}^C \\ -\hat{B}^C \hat{C}^P & \hat{A}^C \end{bmatrix} \quad \hat{\mathbf{B}}_k = \begin{bmatrix} \hat{B}^P \\ 0_{n_x^C \times 1} \end{bmatrix} \quad \hat{\mathbf{F}}_k = \begin{bmatrix} \hat{B}^P \hat{D}^C \\ \hat{B}^C \end{bmatrix} r_k \quad (5.72)$$

$$\hat{\mathbf{C}}_k = \begin{bmatrix} \hat{C}^P & 0_{1 \times n_x^C} \end{bmatrix} \quad \hat{\mathbf{D}}_k = 0 \quad \hat{\mathbf{G}}_k = 0 \quad \hat{x}_k = \begin{bmatrix} \hat{x}_k^P \\ \hat{x}_k^C \end{bmatrix} \quad (5.73)$$

Table 5.1: Simulation Model Parameters

	Truth Model	Control Model
Plant Poles	$0.88 \pm 0.37i$	$0.67 \pm 0.61i$
	1.00	0.99
	1.00	1.00
	0	N/A
Plant Zeros	-5.10	33.10
	-0.44	-2.21
	0.16	0.16
Plant Gain	$2.42E-7$	$2.38E-7$
a_1	-1.65	-1.31
a_2	0.70	0.50
b	0.027	0.093
K_d	3	3
$K_{p,1}$	40	40
$K_{p,2}$	160	160
e_{switch}	2 mm	2 mm
T_s	0.001 s	0.002 s

This system is NMP, as it has all the zeros of the plant model given in Table 5.1 (as well as additional zeros).

The monolithic control model has two locations based on the switching of K_p in \hat{C}^C and \hat{D}^C . Let the location $q = 1$ correspond to low error with $K_{p,1}$ and $q = 2$ correspond to high error and $K_{p,2}$. Then the switching parameters are

$$P = \begin{bmatrix} 0_{1 \times n_{\hat{x}}P + n_{\hat{x}}C - 1} & -1 \\ 0_{1 \times n_{\hat{x}}P + n_{\hat{x}}C - 1} & 1 \end{bmatrix} \quad \beta = \begin{bmatrix} -e_{\text{switch}} \\ -e_{\text{switch}} \end{bmatrix} \quad (5.74)$$

$$\Delta_1^* = \left\{ \begin{bmatrix} 1 \\ 1 \end{bmatrix} \right\} \quad \Delta_2^* = \left\{ \begin{bmatrix} 1 \\ 0 \end{bmatrix}, \begin{bmatrix} 0 \\ 1 \end{bmatrix} \right\} \quad (5.75)$$

Note that $\delta = [0, 0]^T$ is not reachable, and thus need not be included in Δ_2^* .

This monolithic model is of global dynamical relative degree $\mu_g = 1$ and satisfies (A5.1)-(A5.5), enabling the use of Corollary 5.2.1 for derivation of the conventional inverse. The resultant inverse system satisfies (A5.7)-(A5.10a), enabling the use of stable inversion for the generation of stable inverse state trajectories. The decoupling similarity transform V is derived by the MATLAB function `canon` applied to the dynamics of location 1.

Finally, the reference r_k for the truth model to track is given in Figure 5.4.

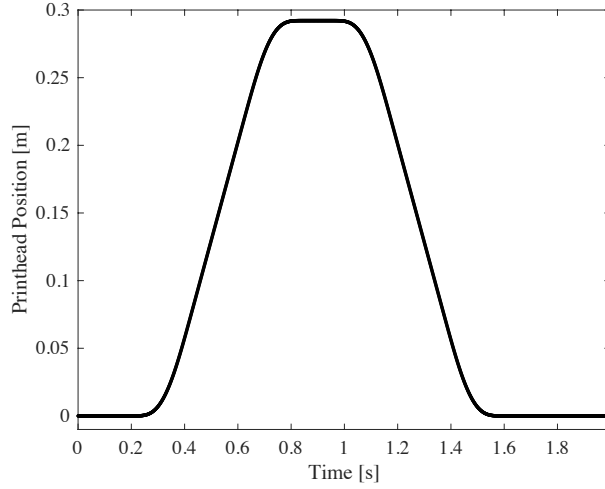


Figure 5.4: Reference. The reference is 1999 samples long for the truth model, and is downsampled to 1000 samples for the control model.

5.4.2 ILC Schemes

5.4.2.1 Invert-Linearize ILC

In Chapter 4, ILILC is presented as a means to derive the trial-varying learning matrix L_ℓ of the classical ILC law

$$\mathbf{u}_{\ell+1} = \mathbf{u}_\ell + L_\ell (\mathbf{r} - \mathbf{y}_\ell) \quad (3.7)$$

where $\ell \in \mathbb{Z}_{\geq 0}$ is the iteration index, \mathbf{u} , \mathbf{r} , $\mathbf{y} \in \mathbb{R}^{N-\mu_g+1}$ are the lifted vectors (i.e. time series vectors)

$$\mathbf{u}_\ell = \begin{bmatrix} u_{\ell,0} & u_{\ell,1} & \cdots & u_{\ell,N-\mu_g} \end{bmatrix}^T \quad (5.76)$$

$$\mathbf{r}_\ell = \begin{bmatrix} r_{\ell,\mu_g} & r_{\ell,\mu_g+1} & \cdots & r_{\ell,N} \end{bmatrix}^T \quad (5.77)$$

$$\mathbf{y}_\ell = \begin{bmatrix} y_{\ell,\mu_g} & y_{\ell,\mu_g+1} & \cdots & y_{\ell,N} \end{bmatrix}^T \quad (5.78)$$

and $N \in \mathbb{Z}_{>\mu_g}$ is the number of time steps in a trial of the output reference tracking task (the number of samples is $N + 1$).

To derive L_ℓ , ILILC calls for a lifted input-output model inverse $\hat{\mathbf{g}}^{-1} : \mathbb{R}^{N-\mu_g+1} \rightarrow \mathbb{R}^{N-\mu_g+1}$ taking in the *measured* output \mathbf{y} and outputting the control signal \mathbf{u} *predicted* to yield \mathbf{y} when input to the true, unknown system. Equivalently, $\hat{\mathbf{g}}^{-1}$ takes in the *model* output $\hat{\mathbf{y}}$ and outputs the control signal \mathbf{u} that yields $\hat{\mathbf{y}}$ when input to the known model *approximating* the true system.

This $\hat{\mathbf{g}}^{-1}$ must be closed-form, such that the ILILC learning matrix

$$L_\ell = \frac{\partial \hat{\mathbf{g}}^{-1}}{\partial \hat{\mathbf{y}}} (\mathbf{y}_\ell) \quad (4.19)$$

can be derived via an automatic differentiation tool such as CasADi [37]. Here, $\frac{\partial \hat{\mathbf{g}}^{-1}}{\partial \hat{\mathbf{y}}}$ is the Jacobian (in numerator layout) of $\hat{\mathbf{g}}^{-1}$ with respect to $\hat{\mathbf{y}}$. Furthermore, as stated in Chapter 4, when the known system model is NMP, $\frac{\partial \hat{\mathbf{g}}^{-1}}{\partial \hat{\mathbf{y}}}$ is likely to be ill-conditioned unless $\hat{\mathbf{g}}^{-1}$ is synthesized using stable inverse trajectories. For a PWA system satisfying (A5.7)-(A5.10a), Theorem 5.3 provides a method for generating these closed-form state trajectories; given trial-invariant conditions $\tilde{x}_{\ell,0}^j = 0$ and $\tilde{x}_{\ell,N-\mu_g}^u = 0$, each element of the time series x_k and δ_k is a function only of $\hat{\mathbf{y}}$. Then $\hat{\mathbf{g}}^{-1}$ is given by

$$\hat{\mathbf{g}}^{-1} = \begin{bmatrix} \hat{\mathbf{C}}_0 \hat{x}_0 + \hat{\mathbf{D}}_0 y_{\mu_g} + \hat{\mathbf{G}}_0 \\ \hat{\mathbf{C}}_1 \hat{x}_1 + \hat{\mathbf{D}}_1 y_{1+\mu_g} + \hat{\mathbf{G}}_1 \\ \vdots \\ \hat{\mathbf{C}}_{N-\mu_g} \hat{x}_{N-\mu_g} + \hat{\mathbf{D}}_{N-\mu_g} y_N + \hat{\mathbf{G}}_{N-\mu_g} \end{bmatrix} \quad (5.79)$$

Finally, for the particular example system studied here, the common practice (see, e.g. [4]) of adding filters to the ILC law is implemented. Two filters are used. First, a zero-phase-shift version of the feedback controller's lowpass filter is applied to the input and output of the ILC law. In lifted form, the feedback controller's filter is given by the lower diagonal, square, Toeplitz matrix \mathcal{F} whose first column is the unit magnitude impulse response of the lowpass filter (5.64) on $k \in \llbracket 0, N - \mu_g \rrbracket$. The zero phase shift is achieved by first filtering the signals forwards in time, and then backwards in time. The resultant lifted zero-phase-shift lowpass filter is

$$\mathcal{Q} = \mathcal{I} \mathcal{F} \mathcal{I} \mathcal{F} \quad (5.80)$$

where \mathcal{I} is a square matrix with ones on the antidiagonal and zeros elsewhere. Second, to eliminate time series edge effects the first 35 and last 35 samples of the 1000 sample ILC law output are forced to zero. These edge effects may arise because the finite stable inversion trajectories have nearly zero—rather than zero—initial conditions for the unstable modes and similar for the terminal conditions of the stable modes. In lifted form this filter is given by the identity matrix with the first 35 and last 35 diagonal elements set to zero, notated as \mathcal{E} .

Thus, the ILILC law used here is ultimately given by

$$\mathbf{u}_{\ell+1} = \mathcal{E} \mathcal{Q} (\mathbf{u}_\ell + L_\ell (\mathbf{r} - \mathcal{Q} \mathbf{y}_\ell)) \quad (5.81)$$

with $\mathbf{u}_0 = 0$ and $y_{\ell,k} = y_{\ell,k}^P + \omega_y$.

5.4.2.2 Gradient and Lifted P-Type ILC

Gradient ILC and lifted P-type ILC both also use the filtered ILC law (5.81), but with different definitions of L_ℓ .

Gradient ILC uses

$$L_\ell = \gamma \frac{\partial \hat{\mathbf{g}}}{\partial \mathbf{u}}(\mathbf{u}_\ell)^T \quad (5.82)$$

as in Chapter 4, where γ is the learning gain and $\hat{\mathbf{g}}$ is the lifted system input-output model

$$\hat{\mathbf{y}}_\ell = \hat{\mathbf{g}}(\mathbf{u}_\ell) \quad (5.83)$$

which can be synthesized via (3.11)-(3.12).

P-type ILC is typically expressed without lifting as [118]

$$u_{\ell+1,k} = u_{\ell,k} + \mathcal{P} (r_{\ell,k+\mu} - y_{\ell,k+\mu}) \quad (5.84)$$

where \mathcal{P} is a constant scalar learning gain and μ is the system relative degree (here the global dynamical relative degree μ_g is used). In lifted form, (5.84) manifests as the trial invariant learning matrix

$$L_\ell = \mathcal{P} I_{N-\mu_g+1 \times N-\mu_g+1} \quad \forall \ell \quad (5.85)$$

which can be plugged into the filtered learning law (5.81). At this time, there is no literature prescribing a stable synthesis procedure for the P-type ILC of PWA systems. In fact, the literature lacks application of either gradient ILC or P-type ILC to PWA models. However, because of its simplicity it is ubiquitous in industry and often synthesized heuristically, much like the PID feedback control for which it was named. Thus, P-type ILC makes for an important benchmark.

Tuning of the learning gains for both benchmark methods is described in Section 5.4.3.

5.4.3 Methods

The presented stable inversion theory's ability to derive the inverse of a non-minimum phase PWA model is tested by applying $\mathbf{u} = \hat{\mathbf{g}}^{-1}(\mathbf{r})$ to the control model. Then, to assess a more practical utility, five independent simulations with the truth model are performed. First, a simulation is run with the feedforward input fixed to zero for all time, yielding a feedback-only simulation to serve as a baseline against which the four feedforward controllers can be compared. Next, learning-free stable inversion is applied to the truth model. In other words, a simulation is run with $\mathbf{u} = \hat{\mathbf{g}}^{-1}(\mathbf{r})$. The remaining three simulations each use one of the ILC techniques described Section 5.4.2 (ILILC, gradient ILC, or P-type ILC) with 9 trials (8 learning operations). For all ILC simulations, \mathbf{u}_0 is the zero vector.

The primary metric for assessing control performance in a given trial is the normalized root mean square error (NRMSE) of the truth model, defined as

$$\text{NRMSE} = \frac{\text{RMS}_{k \in \llbracket 0, N \rrbracket} (e_k)}{\|\mathbf{r}\|_\infty} \quad (5.86)$$

The peak error magnitude $\max_k (|e_k|)$ is also considered.

For gradient ILC and P-type ILC, tuning of the learning gains is done to achieve the most aggressive stable controller possible. Specifically γ and \mathcal{P} are chosen as the largest whole number such that the NRMSE decreases monotonically over all trials or drops below the convergence tolerance, set to 0.0005 here. These numbers are found via a line search over many ILC simulations using the given truth and control model, varying only the learning gains. By this method, $\gamma = 4255$ (dimensionless) and $\mathcal{P} = 27 \frac{\text{V}}{\text{m}}$. If the learning gains are increased above these values, the benchmark ILC schemes begin to exhibit instability.

5.4.4 Results and Discussion

When $\mathbf{u} = \hat{\mathbf{g}}^{-1}(\mathbf{r})$ is input to the noise-free control model (5.70)-(5.71) from which it was derived, the resulting NRMSE and peak error magnitude are $1\text{E}-7$ and 49 nm. This is nearly zero compared to the other simulation errors, tabulated in Table 5.2, and what error there is can be attributed to the approximation error expected of finite-time stable inversion, as discussed in Section 5.3.2. This validates the fundamental theoretical contributions of this chapter: the stable inversion—and thus also conventional inversion—of PWA systems.

To analyze the more practical application of these techniques to the truth model, Figure 5.5 plots the evolution of the ILC schemes' NRMSEs over the iteration process, and Figures 5.6 and 5.7 plot the input and error time series for the five simulations. Specifically, Figure 5.6 compares the learning-free simulations to ILILC and Figure 5.7 compares ILILC against the other benchmark learning techniques. The NRMSE and peak error magnitude for these simulations are tabulated in Table 5.2.

Because the model error is relatively small, learning-free stable inversion does yield some improvement (4%) over the feedback-only NRMSE. (Naturally, one expects that the NRMSE of learning-free stable inversion would grow if the model error increased). Learning-free stable inversion also reduces the peak error magnitude, which is a critical safety criterion in many applications, by 28%. However, because of the model error that does exist, all of the ILC schemes defeat learning-free stable inversion in both metrics. P-type ILC shows the least improvement, but still yields a 40% reduction in NRMSE from learning-free stable inversion. This improvement is dwarfed by that of ILILC, however, which yields a 70% NRMSE improvement from gradient ILC

Table 5.2: NRMSE and Peak Error Magnitude of Truth Model Simulations

	NRMSE	Peak Error Magnitude
Feedback-Only	$5.6\text{E-}3$	3.9 mm
Learning-Free Stable Inversion	$5.4\text{E-}3$	2.8 mm
P-type ILC - Final Trial	$3.1\text{E-}3$	2.1 mm
Gradient ILC - Final Trial	$1.2\text{E-}3$	1.1 mm
ILILC - Final Trial	$3.6\text{E-}4$	0.34 mm

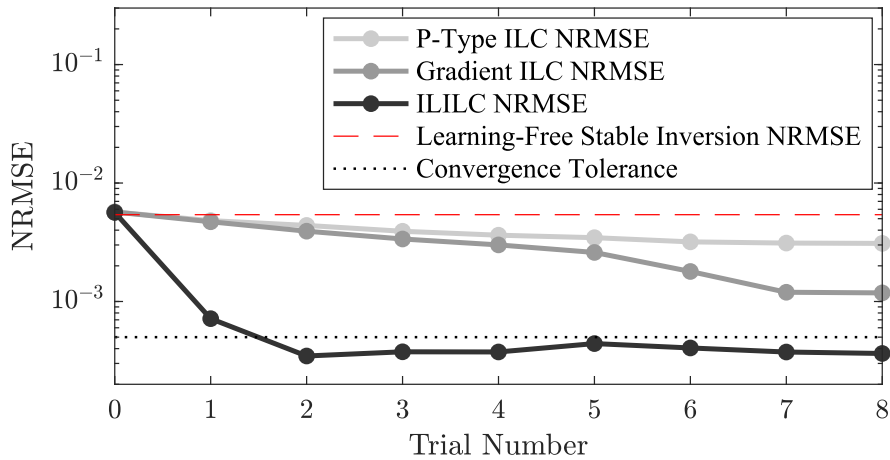


Figure 5.5: NRMSE of each ILC trial, illustrating convergence of ILILC to a plateau determined by the noise injected to the system, and dramatically surpassing the convergence speed of both benchmark ILC techniques. The NRMSE of the learning-free stable inversion simulation is also pictured. It is 4% smaller than the feedback-only simulation (ILILC trial 0), but is much larger than the performance achievable with learning. Because the noise injected in this chapter is of the same distribution and injection location as the noise in Chapter 4, the same convergence threshold can be used to approximate the minimum NRMSE achievable by ILILC.

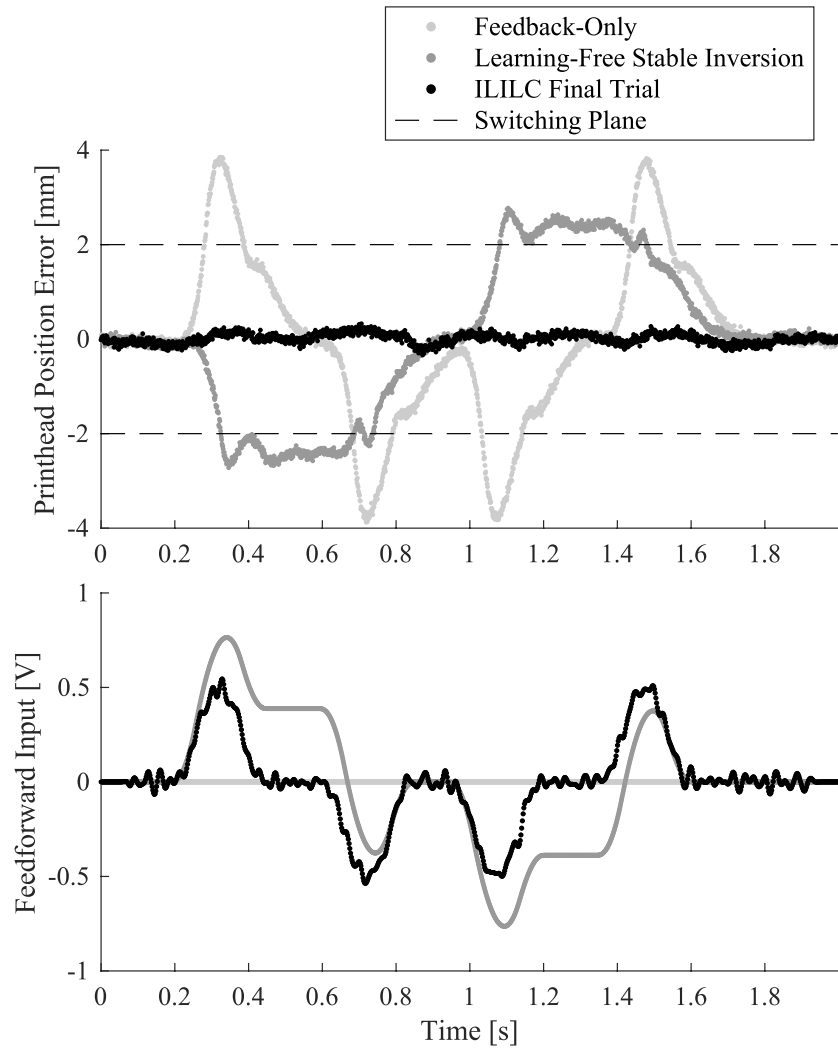


Figure 5.6: Error (top) and Input (bottom) time series data for the feedback-only simulation, learning-free stable inversion simulation, and the final trial of the ILILC simulation. Both stable inversion and ILILC perform as expected, but due to model error learning is required to reap the full benefit of feedforward control.

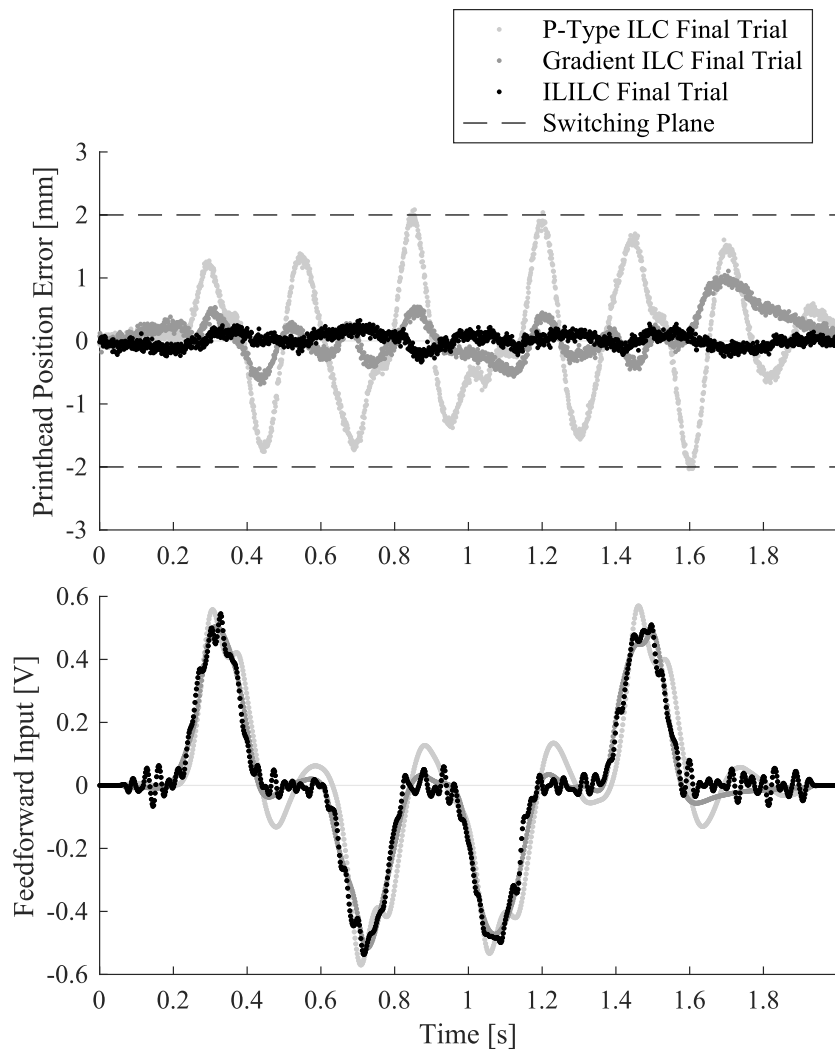


Figure 5.7: Error (top) and Input (bottom) time series data for the three ILC simulations. Even the worst-performing ILC technique—P-type ILC—yields a reduction in maximum error magnitude when compared to the learning-free techniques of Figure 5.6, but ILILC clearly yields the lowest-error performance. This superiority is in spite of ILILC acquiring more high frequency content via learning than the other ILC schemes, which appear less noisy but appear to contain higher amplitude, lower frequency oscillations that degrade performance.

(the next best technique), or equivalently, a 93% improvement from learning-free stable inversion.

In addition to these quantitative metrics, inspection of Figure 5.7 reveals a qualitative comparison worth making between the ILC schemes: that of noise acquisition. While even qualitatively, ILILC clearly demonstrates the highest quality reference tracking, it also accumulates the most noise in its learned feedforward input. There may be applications in which this noise acquisition is unattractive. However, it must also be noted that gradient ILC and P-type ILC are not free from unwanted frequency content. P-type ILC especially appears to develop mid-frequency oscillations that substantially degrade performance. Gradient ILC is more subtle; its main source of error appears to be oscillations arising from overshoot of the feedforward input. As a final note, it is unclear at this time whether the noise acquisition of the ILILC simulation is a result of the Newton-like learning intrinsic to ILILC or the stable inversion used to eliminate the inverse instability.

In all, this validation constitutes the first demonstration of ILC applied to any hybrid system with NMP component dynamics. Because stable inversion is a required part of the highest performing ILC scheme used here, this validates the utility of this chapter's theoretical contributions for high performance control.

5.5 Conclusion

This chapter has derived theory for the inversion of a class of PWA systems. This includes the implicit inverse formula for systems of any relative degree and the explicit formulas for systems with global dynamical relative degree (a concept introduced in this work) of 0, 1, or 2, along with the proof of sufficient conditions for the inverse of the original PWA system to be explicit. Additionally, for cases in which the inverse system is unstable, a stable inversion procedure is created, along with proof of the sufficient conditions for the procedure to be applicable.

The ability to analytically produce inverse system models for hybrid systems has multiple applications in controls. Demonstrated here is the newfound ability to apply ILC to PWA systems with unstable inverses to achieve low error output reference tracking.

There are many avenues for future work. Of particular interest is the relaxation of the constraints on relative degree. For some hybrid systems, it may be desirable to have locations in which the input cannot affect the output, and the state is governed by natural dynamics alone. In such cases the global dynamical relative degree would be undefined (infinite), which is not considered here. There may also be more cases in which different locations feature different component relative degrees, which would violate (A5.4). Relaxing these constraints would dramatically expand the class of systems addressed. Extension to multi-input-multi-output systems and input-based switching would also be significant contributions.

CHAPTER 6

Conclusion

6.1 Synthesis of Research Contributions

Spurred by the long-term goal of achieving high performance droplet volume control in e-jet printing, this dissertation makes substantial contributions to both the modeling of e-jet printing and the control theory necessary to leverage those models. At each stage, practical obstacles give rise to novel scientific and mathematical research.

First, while Chapter 2 presents significant new progress in the traditional physics-based modeling of meniscus electrohydrodynamics, the inability of traditional models to completely capture the ejection process from end to end motivates the development of hybrid e-jet modeling frameworks. Likewise, the inability to process the computer-vision-based jet measurements fast enough for real-time feedback control motivates the study of ILC for this system. Finally, the lack of ILC theory for hybrid systems in the preexisting literature serves as the impetus for the controls research making up Chapters 3-5.

The first of these chapters lays the groundwork for the remaining hybrid systems and ILC research by providing a closed-form PWD system representation and integrating it with NILC. Based on the original convergence analysis for NILC, one might expect the performance of this integration to be mostly uniform across all PWD models. However, while the lifted model derivation given in Chapter 3 is guaranteed to have a theoretically invertible Jacobian if the relative degree is constant over the trial, this does not account for the practical ability to compute the inverse. As found in Chapter 4, this practical ability is compromised when the system model has an unstable inverse. Such NMP systems are not negligible edge cases. They arise when modeling many practical motion control devices—a key application space for ILC—from piezoactuators [7] to DC motor and tachometer assemblies [39]. Thus, to leave the issue of NMP hybrid systems unaddressed would be to deliver more of a minefield than a control theory.

Chapters 4-5 sweep this minefield by introducing the new ILILC framework, integrating it with stable inversion, and developing the first theory for the stable inversion of hybrid systems.

Ultimately this enables ILC synthesis from a model of the physical device that originally sounded the alarm on NILC of NMP systems, an inkjet printhead positioning system.

6.2 Broader Impacts

Both the hybrid e-jet modeling research and the control theory research in this dissertation have ramifications beyond the validations presented here, and beyond the intended future use for droplet volume control. In fact, the broader impacts of hybrid e-jet modeling have already begun to manifest.

Within the world of e-jet printing, the hybrid models provided by this dissertation serve as an end-to-end process model that is more easily interpreted and analyzed by human researchers than computational multiphysics models. Because of this, the physics-driven hybrid model is currently being used for the benchmarking and development of such sophisticated partial-differential-equation-based simulations.

This dissertation’s modeling contributions have also gained attention in the broader AM community, outside of e-jet-specific research. The promotion and validation of hybrid modeling for e-jet printing helped pave the way for the proposal of a more general hybrid AM modeling framework, which was used for modeling the multi-level workflow of FDM [119]. There is also great promise for more thorough hybrid modeling of the physical dynamics of FDM: research has been published identifying distinct dynamic regimes FDM may occupy depending on the physical state of the printhead and filament [85]. Additionally, because AM processes are mostly open loop at this time, they are compelling candidates for ILC. In other words, there is evidence of a rich field of systems whose modeling would benefit from following in the footsteps of this dissertation, and whose control may benefit directly.

To see the broader impacts of Chapters 3-5, it may be beneficial to revisit the “castle-of-building-blocks” visualization from Figure 1.1. Such a revisitation is given in Figure 6.1, which illustrates a number of new classes of control systems that may be enabled by the fundamental contributions of this work. Most obviously, where there are contributions to inversion and stable inversion theory, there is opportunity for feedforward control. While this dissertation focuses on ILC because of the performance advantages it yields over learning-free methods, one should not discount the importance of ordinary feedforward control, for it can be applied in non-repetitive scenarios where the learning mechanisms of most ILC schemes may falter.

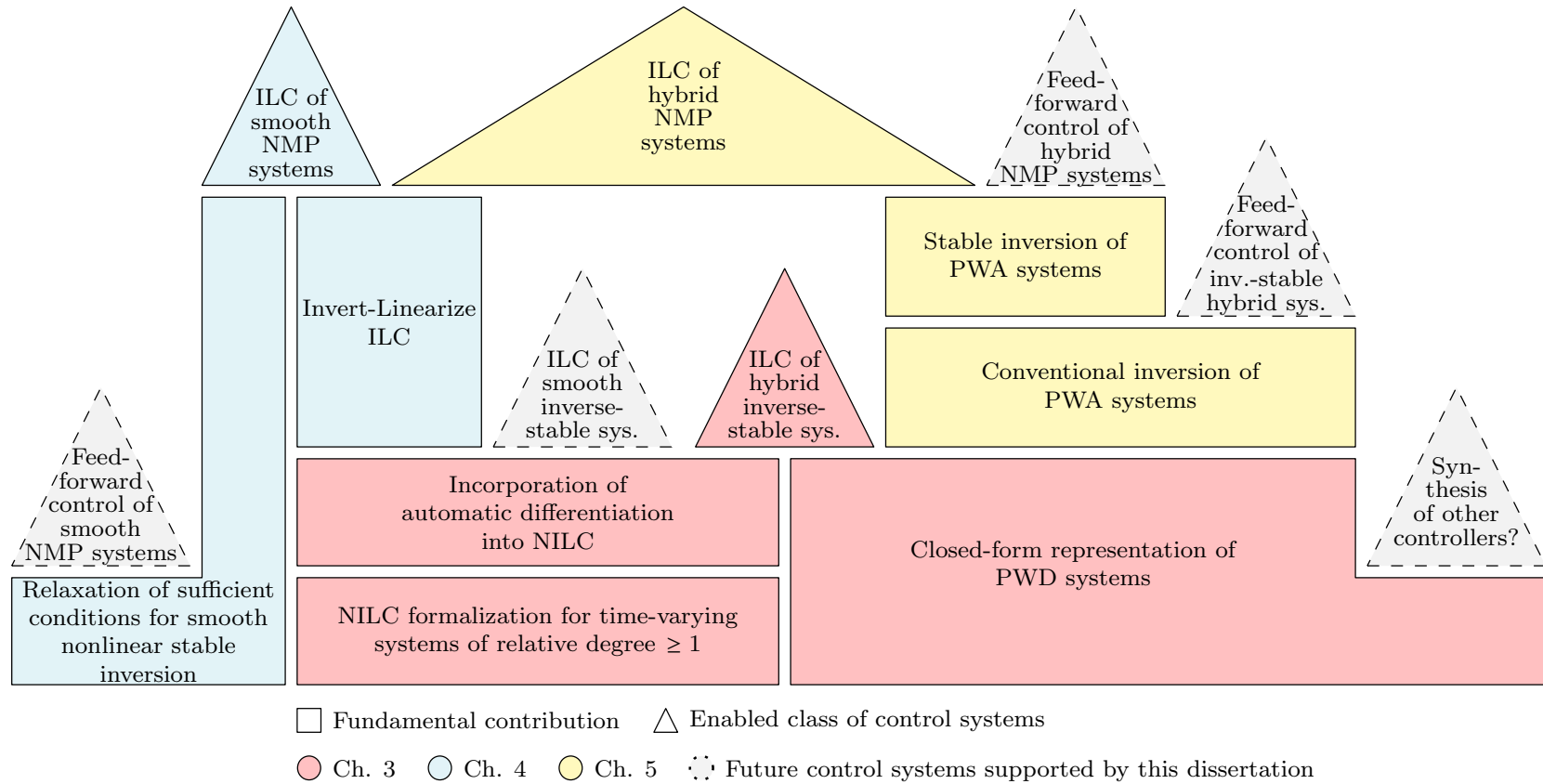


Figure 6.1: Castle of Control Contributions, revisited for visualization of this dissertation's potential broader impacts. These may take the form of other new classes of control systems leveraging the theoretical contributions presented here.

The ability to generate feedforward control signals can also be useful in scenarios where feedback control is a primary focus. A concrete example is given by [46], where a combined feedback/feedforward control scheme for PWA system reference tracking is derived, but is limited based on the availability of the feedforward signal. This dissertation alleviates that limitation.

Finally, a further impact on feedback control may be possible with the closed-form PWD representation. The new ability to holistically differentiate a hybrid state transition function or output function may facilitate the synthesis of a diverse range of controllers, e.g. feedback linearization.

6.3 Future Directions

Clearly, these potential broader impacts themselves constitute a large arena for future work. In particular, investigations into the hybrid modeling of other AM technologies and the use of the closed-form PWD system representation for feedback control synthesis may be valuable contributions. Of course, further progress towards the original long-term objective of e-jet droplet volume control is of primary interest.

The three main challenges to overcome here are the need for point-to-point ILC, managing the trade-off between time-based location transitions and model stability, and encoding the limits of the safe printing region into the model.

Clearly, the droplet volume modeling of the PWA e-jet model (the second proposed model, Section 2.3) is necessary to achieve droplet volume control. However, it is undesirable to require reference specification for the entire droplet volume time series; only the final droplet volume value matters. ILC with reference specification for only a subset of the trial time series exists and is called point-to-point ILC [120], but has not been combined with either NILC or hybrid models. This leaves a gap between the prior art and the needs of e-jet printing.

Additionally, while the PWA e-jet model introduces droplet volume modeling, it removes state-based transitions and replaces them with time-based transitions. Time-based transitions cannot be altered by ILC, but the time of transition will certainly change in practice if the input voltage changes in magnitude from trial to trial. This makes state-based switching desirable. To achieve state-based transitions, dynamical modeling of the meniscus position is necessary. This presents an issue for ILC because a linear model fit to meniscus position data during the approach location is likely to be unstable (this may be deduced from Figure 2.8), and asymptotic model stability is prerequisite to ILC in general [4].

Constrained system identification or extension of the physics-focused e-jet model's build-up or jetting locations may enable stable modeling of the meniscus position. However, this is unlikely to completely solve the e-jet ILC problem. Stable linear modeling during jetting implies that the meniscus position may be completely controllable during jetting (potentially with all control ac-

tions experiencing the same time delay modeled for the physics-focused model's jetting location). There is no evidence to suggest this degree of controllability in practice. Basing ILC on this assumption may have undesirable results. For example, if a droplet volume is desired to be smaller than it was for trial ℓ , ILC may request a large negative voltage during jetting to arrest the jet or remove material from the substrate. This may be possible according to the LTI component models, but may not be possible in reality, and attempts to do so may take the physical system outside the regime in which the model is applicable. Such risks lead to the final gap identified for the ILC of e-jet printing: encoding of the safe input range.

In other words, a major area for future work in e-jet modeling is the prediction and encoding of the boundaries of the subcritical regime. This is both a performance and safety issue. Attempts to project subcritical regime behavior beyond the regime limits may result in failure to eject, misplaced droplets due to tilted ejection angles, or destruction of the nozzle via flooding or arcing.

Beyond e-jet printing, there are also exciting control theory developments to be built directly off the contributions of this dissertation. Two meaningful areas for future work are identified. First is the investigation of compatibility between the closed-form PWD representation and forms of ILC not using lifted models. While ILILC's sufficient conditions for convergence are very broad, in some cases it may be desirable to prioritize computational cost. In such cases the large matrix operations in lifted ILC may be a disadvantage. Thus, the use of the closed-form PWD representation to synthesize filter-based ILC, such as that of [121], may be valuable.

Second is the relaxation of the assumptions under which an NMP PWA system may be controlled via ILILC. Currently, these assumptions are those of PWA stable inversion, but ILILC can admit other inverse system approximations as well. Thus, assumption relaxation efforts could focus on improving PWA stable inversion or introducing a new stable inverse approximation method.

Finally, it must be remembered that the research and new engineering tools provided here were developed in large part as a response to the *unexpected* challenges that leapt up from physical systems. Surely nature's surprises are not exhausted.

APPENDIX A

Neglect of Inverse Instability by Non-NILC Prior Art

This appendix demonstrates that the sufficient conditions for convergence proposed by past works [13, 14, 15, 16] on ILC for discrete-time nonlinear systems are in actuality not sufficient for some cases of systems having unstable inverses. This is done by running model-error-free ILC simulations that are guaranteed to converge by the past works, and observing them to diverge instead.

Each of [13, 14, 15, 16] proposes sufficient conditions for the convergence $\lim_{\ell \rightarrow \infty} \mathbf{e}_\ell = \mathbf{0}_{N-\mu+1}$ of a particular ILC scheme applied to a particular class of nonlinear dynamics. All of these classes of nonlinear dynamics are supersets of the SISO LTI dynamics

$$x_\ell(k+1) = Ax_\ell(k) + Bu_\ell(k) \tag{A.1a}$$

$$y_\ell(k) = Cx_\ell(k) \tag{A.1b}$$

with relative degree $\mu = 1$, i.e. $CB \neq 0$. Additionally, assume (A.1) is stable and $x_\ell(0)$ is such that $y_\ell(0) = r_\ell(0) \forall \ell$. Given a system of this structure, the ILC schemes and convergence conditions of the past work reduce to the following.

From [13] the learning law is

$$u_{\ell+1}(k) = u_\ell(k) + L_\ell(k) (\gamma_1 e_\ell(k+1) + \gamma_0 e_\ell(k)) \tag{A.2}$$

where $L \in \mathbb{R}$ is a potentially time-varying and trial-varying part of the learning gain and $\gamma_1, \gamma_0 \in \mathbb{R}$ are trial-invariant, time-invariant learning gains with $\gamma_1 \neq 0$. The learning laws of [14, 15, 16] are special cases of (A.2): [14] sets $\gamma_1 = 1, \gamma_0 = -1$, [15] sets $\gamma_1 = 1, \gamma_0 = 0$, and [16] sets $\gamma_1 = 1$ and leaves γ_0 free.

Each work presents a different variation of convergence analysis, but all propose a sufficient condition of the form

$$(CA.1) \quad |1 - L_\ell(k)\gamma_1 CB| < 1 \quad \forall k, \ell .$$

In [13, 15, 16] (CA.1) is used exactly, while the convergence analysis in [14] implies the additional sufficient condition

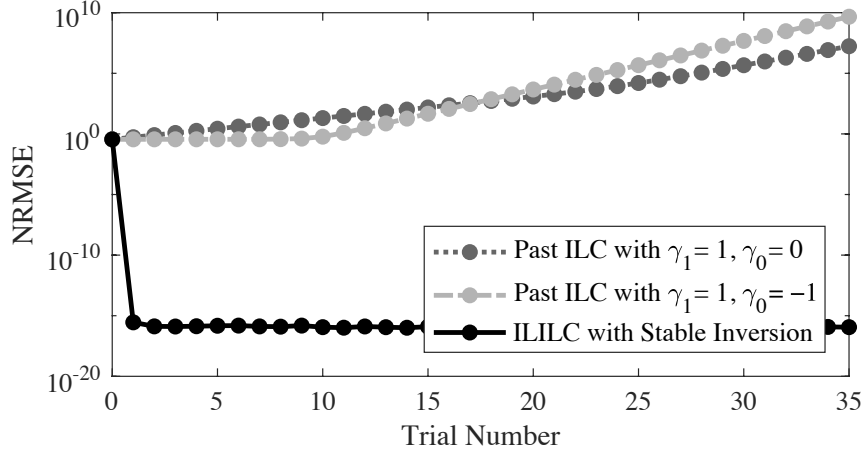


Figure A.1: NRMSE versus trial number of past works' ILC schemes (A.2) applied with learning gain (A.4) to the system (A.3). These NRMSEs monotonically increase, confirming the inability of the past work on ILC with discrete-time nonlinear systems to account for unstable inverses. The NRMSE trajectory yielded by the stable-inversion-supported ILILC scheme proposed by this article is also displayed. The convergence of this ILC scheme when applied to (A.3) reiterates its ability to control such non-minimum phase systems.

$$(CA.2) \quad \|A\| > 1$$

where any consistent norm may be chosen for $\|\cdot\|$.

Consider the example system and learning gain

$$\begin{aligned}
 A &= \begin{bmatrix} -0.3 & -0.79 & 0.53 \\ 0 & 0.5 & 1 \\ 0 & -0.36 & 0.5 \end{bmatrix} & B &= \begin{bmatrix} 0 \\ 0 \\ 1.34 \end{bmatrix} \\
 C &= \begin{bmatrix} 0.7 & 1.1 & -0.74 \end{bmatrix} & x_\ell(0) &= 0 \quad \forall \ell
 \end{aligned} \tag{A.3}$$

$$L_\ell(k) = 0.5(CB)^{-1} \quad \forall k, \ell \tag{A.4}$$

with the reference given in Figure 4.2. This system has an unstable inverse.

The plant (A.3) satisfies (CA.2), and with (A.4) it satisfies (CA.1) for $\gamma_1 = 1$. Thus, according to [13, 14, 15, 16] the ILC scheme (A.2) is guaranteed to yield tracking error convergence in a model-error-free simulation. However, Figure A.1 shows that the tracking error diverges under (A.2), meaning that satisfaction of (CA.1) and (CA.2) is not actually sufficient for the convergence of all systems (A.1) under the learning law (A.2). This illustrates that the failure to account for phenomena arising from inverse instability is not unique to NILC, but rather pervades the literature on ILC with discrete-time nonlinear systems.

BIBLIOGRAPHY

- [1] P. Tabuada, *Verification and Control of Hybrid Systems*. New York: Springer US, 2009. <https://doi.org/10.1007/978-1-4419-0224-5>
(Back reference pages: vii, 2, 3, and 54)
- [2] W. P. M. H. Heemels, B. De Schutter, and A. Bemporad, “Equivalence of hybrid dynamical models,” *Automatica*, vol. 37, no. 7, pp. 1085–1091, 2001. [https://doi.org/10.1016/S0005-1098\(01\)00059-0](https://doi.org/10.1016/S0005-1098(01)00059-0)
(Back reference pages: vii, 2, 3, and 94)
- [3] C. G. Cassandras and S. Lafortune, *Introduction to Discrete Event Systems*, 2nd ed. New York: Springer Science+Business Media, 2008. <https://doi.org/10.1007/978-0-387-68612-7>
(Back reference pages: vii, 2, 14, and 54)
- [4] D. A. Bristow, M. Tharayil, and A. G. Alleyne, “A survey of iterative learning control,” *IEEE Control Systems Magazine*, vol. 26, no. June, pp. 96–114, 2006. <https://doi.org/10.1109/MCS.2006.1636313>
(Back reference pages: vii, 3, 118, and 128)
- [5] C. C. de Wit, B. Siciliano, and G. Bastin, *Theory of Robot Control*. Springer-Verlag, 1996. <https://doi.org/10.1007/978-1-4471-1501-4>
(Back reference pages: viii, 4)
- [6] F. R. Hogan and A. Rodriguez, “Feedback Control of the Pusher-Slider System: A Story of Hybrid and Underactuated Contact Dynamics,” in *Proceedings of the Twelfth Workshop on the Algorithmic Foundations of Robotics*, K. Goldberg, P. Abbeel, K. Bekris, and L. Miller, Eds. Springer International Publishing, 2020, pp. 800–815. https://doi.org/10.1007/978-3-030-43089-4_51
(Back reference pages: viii, 3)
- [7] G. Schitter, R. W. Stark, and A. Stemmer, “Sensors for closed-loop piezo control: Strain gauges versus optical sensors,” *Measurement Science and Technology*, vol. 13, pp. N47–N48, 2002. <https://doi.org/10.1088/0957-0233/13/4/404>
(Back reference pages: viii, 5, and 125)

- [8] T. H. Cho, N. Farjam, C. R. Allemang, C. P. Pannier, E. Kazyak, C. Huber, M. Rose, O. Trejo, R. L. Peterson, K. Barton, and N. P. Dasgupta, “Area-Selective Atomic Layer Deposition Patterned by Electrohydrodynamic Jet Printing for Additive Manufacturing of Functional Materials and Devices,” *ACS Nano*, vol. 14, pp. 17262–17272, 2020. <https://doi.org/10.1021/acsnano.0c07297>
(Back reference page: viii)
- [9] Z. Afkhami, B. Iezzi, D. Hoelzle, M. Shtein, and K. Barton, “Electrohydrodynamic Jet Printing of One-Dimensional Photonic Crystals: Part I—An Empirical Model for Multi-Material Multi-Layer Fabrication,” *Advanced Materials Technologies*, vol. 2000386, pp. 1–8, 2020. <https://doi.org/10.1002/admt.202000386>
(Back reference page: viii)
- [10] C. T. Freeman, “Upper Limb Electrical Stimulation Using Input-Output Linearization and Iterative Learning Control,” *IEEE Transactions on Control Systems Technology*, vol. 23, no. 4, pp. 1546–1554, 2015. <https://doi.org/10.1109/TCST.2014.2363412>
(Back reference page: 2)
- [11] Q. Yu, Z. Hou, and J. X. Xu, “D-Type ILC Based Dynamic Modeling and Norm Optimal ILC for High-Speed Trains,” *IEEE Transactions on Control Systems Technology*, vol. 26, no. 2, pp. 652–663, 2018. <https://doi.org/10.1109/TCST.2017.2692730>
(Back reference page: 2)
- [12] W. Rafajłowicz, P. Jurewicz, J. Reiner, and E. Rafajłowicz, “Iterative Learning of Optimal Control for Nonlinear Processes with Applications to Laser Additive Manufacturing,” *IEEE Transactions on Control Systems Technology*, vol. 27, no. 6, pp. 2647–2654, 2019. <https://doi.org/10.1109/TCST.2018.2865444>
(Back reference page: 2)
- [13] T.-J. Jang, H.-S. Ahn, and C.-H. Choi, “Iterative learning control for discrete-time nonlinear systems,” *International Journal of Systems Science*, vol. 25, no. 7, pp. 1179–1189, 1994. <https://doi.org/10.1080/00207729408949269>
(Back reference pages: 2, 3, 70, 130, and 131)
- [14] S. S. Saab, “Discrete-Time Learning Control Algorithm for a Class of Nonlinear Systems,” in *Proceedings of 1995 American Control Conference*. Seattle: IEEE, 1995, pp. 2793–2743. <https://doi.org/10.1109/ACC.1995.532347>
(Back reference pages: 2, 3, 70, 130, and 131)
- [15] D. Wang, “Convergence and robustness of discrete time nonlinear systems with iterative learning control,” *Automatica*, vol. 34, no. 11, pp. 1445–1448, 1998. [https://doi.org/10.1016/S0005-1098\(98\)00098-3](https://doi.org/10.1016/S0005-1098(98)00098-3)
(Back reference pages: 2, 3, 70, 130, and 131)
- [16] M. Sun and D. Wang, “Initial shift issues on discrete-time iterative learning control with system relative degree,” *IEEE Transactions on Automatic Control*, vol. 48, no. 1, pp. 144–148, 2003. <https://doi.org/10.1109/TAC.2002.806668>
(Back reference pages: 2, 3, 70, 130, and 131)

- [17] F. D. Torrisi and A. Bemporad, “HYSDEL - A tool for generating computational hybrid models,” *IEEE Transactions on Control Systems Technology*, vol. 12, no. 2, pp. 235–249, 2004. <https://doi.org/10.1109/TCST.2004.824309>
(Back reference pages: 3, 16, and 69)
- [18] J.-H. Kim, S. Hayakawa, T. Suzuki, K. Hirana, Y. Matsui, S. Okuma, N. Tsuchida, M. Shimizu, and S. Kido, “Modeling of Human Driving Behavior Based on Expression as Hybrid Dynamical System,” *Transaction of the Society of Instrument and Control Engineers*, vol. 40, no. 2, pp. 180–188, 2004. <https://doi.org/10.9746/sicetr1965.40.180>
(Back reference page: 3)
- [19] I. Hiskens and M. Pai, “Hybrid systems view of power system modelling,” in *2000 IEEE International Symposium on Circuits and Systems. Emerging Technologies for the 21st Century. Proceedings (IEEE Cat No.00CH36353)*. Geneva: IEEE, 2000, pp. 228–231. <https://doi.org/10.1109/ISCAS.2000.856300>
(Back reference page: 3)
- [20] I. Hiskens, “Stability of hybrid system limit cycles: application to the compass gait biped robot,” in *Proceedings of the 40th IEEE Conference on Decision and Control (Cat. No.01CH37228)*, no. December, 2001, pp. 774–779. <https://doi.org/10.1109/2001.980200>
(Back reference page: 3)
- [21] M. Saez, F. Maturana, K. Barton, and D. Tilbury, “Anomaly Detection and Productivity Analysis for Cyber-Physical Systems in Manufacturing,” in *2017 13th IEEE Conference on Automation Science and Engineering (CASE)*, Xi’an, 2017, pp. 23–29. <https://doi.org/10.1109/COASE.2017.8256070>
(Back reference page: 3)
- [22] I. Spiegel, I. Kovalenko, D. Hoelzle, P. M. Sammons, and K. L. Barton, “Hybrid modeling and identification of jetting dynamics in electrohydrodynamic jet printing,” in *2017 IEEE Conference on Control Technology and Applications (CCTA)*, Aug 2017, pp. 695–701. <https://doi.org/10.1109/CCTA.2017.8062543>
(Back reference pages: 3, 10, 12, 24, 25, 28, and 44)
- [23] R. Chi, Z. Hou, and J. Xu, “Adaptive ILC for a class of discrete-time systems with iteration-varying trajectory and random initial conditions,” *Automatica*, vol. 44, no. 8, pp. 2207–2213, 2008. <https://doi.org/10.1016/j.automatica.2007.12.004>
(Back reference pages: 3, 70)
- [24] H.-J. Shieh and C.-H. Hsu, “An adaptive approximator-based backstepping control approach for piezoactuator-driven stages,” *IEEE Transactions on Industrial Electronics*, vol. 55, no. 4, pp. 1729–1738, 2008. <https://doi.org/10.1109/TIE.2008.917115>
(Back reference page: 3)
- [25] C. M. Hackl, N. Hopfe, A. Ilchmann, M. Mueller, and S. Trenn, “Funnel Control for Systems with Relative Degree Two,” *SIAM Journal on Control and Optimization*, vol. 51, no. 2, pp. 1046–1060, 2013. <https://doi.org/10.1137/100799903>
(Back reference page: 3)

- [26] H. Geniele, R. V. Patel, and K. Khorasani, “End-Point Control of a Flexible-Link Manipulator: Theory and Experiments,” *IEEE Transactions on Control Systems Technology*, vol. 5, no. 6, pp. 556–570, 1997. <https://doi.org/10.1109/87.641401>
(Back reference pages: 3, 5)
- [27] U. Münz, A. Papachristodoulou, and F. Allgöwer, “Robust consensus controller design for nonlinear relative degree two multi-agent systems with communication constraints,” *IEEE Transactions on Automatic Control*, vol. 56, no. 1, pp. 145–151, 2011. <https://doi.org/10.1109/TAC.2010.2084150>
(Back reference page: 3)
- [28] G. Escobar, R. Ortega, H. Sira-Ramirez, J.-P. Vilain, and I. Zein, “An experimental comparison of several nonlinear controllers for power converters,” *IEEE Control Systems Magazine*, vol. 19, no. 1, pp. 66–82, 1999. <https://doi.org/10.1109/37.745771>
(Back reference pages: 3, 5)
- [29] H. De Battista and R. J. Mantz, “Dynamical variable structure controller for power regulation of wind energy conversion systems,” *IEEE Transactions on Energy Conversion*, vol. 19, no. 4, pp. 756–763, 2004. <https://doi.org/10.1109/TEC.2004.827705>
(Back reference pages: 3, 5)
- [30] H. M. Gutierrez and P. I. Ro, “Magnetic servo levitation by sliding-mode control of nonaffine systems with algebraic input invertibility,” *IEEE Transactions on Industrial Electronics*, vol. 52, no. 5, pp. 1449–1455, 2005. <http://doi.org/10.1109/TIE.2005.855651>
(Back reference page: 3)
- [31] P. K. Khosla and T. Kanade, “Experimental Evaluation of Nonlinear Feedback and Feedforward Control Schemes for Manipulators,” *The International Journal of Robotics Research*, vol. 7, no. 1, pp. 18–28, 1988. <https://doi.org/10.1177/027836498800700102>
(Back reference page: 3)
- [32] R. E. Kalman, “Phase-plane analysis of automatic control systems with nonlinear gain elements,” *Transactions of the American Institute of Electrical Engineers, Part II: Applications and Industry*, vol. 73, no. 6, pp. 383–390, 1955. <https://doi.org/10.1109/tai.1955.6367086>
(Back reference pages: 3, 6)
- [33] M. Garcia, A. Chatterjee, A. Ruina, and M. Coleman, “The Simplest Walking Model: Stability, Complexity, and Scaling,” *Journal of Biomechanical Engineering*, vol. 120, no. 2, pp. 281–288, 1998. <https://doi.org/10.1115/1.2798313>
(Back reference page: 3)
- [34] K. E. Avrachenkov, “Iterative learning control based on quasi-Newton methods,” in *Proceedings of the 37th IEEE Conference on Decision & Control*, no. December. Tampa: IEEE, 1998, pp. 170–174. <https://doi.org/10.1109/CDC.1998.760615>
(Back reference pages: 4, 58, 61, 62, 66, and 89)

- [35] J.-X. Xu and Y. Tan, *Linear and Nonlinear Iterative Learning Control*, M. Thoma and M. Morari, Eds. Berlin: Springer-Verlag, 2003, vol. 404. <https://doi.org/10.1007/3-540-44845-4>
(Back reference page: 4)
- [36] T. Lin, D. H. Owens, and J. Hätönen, “Newton method based iterative learning control for discrete non-linear systems,” *International Journal of Control*, vol. 79, no. 10, pp. 1263–1276, 2006. <https://doi.org/10.1080/00207170600821187>
(Back reference pages: 4, 59)
- [37] J. A. E. Andersson, J. Gillis, G. Horn, J. B. Rawlings, and M. Diehl, “CasADi: a software framework for nonlinear optimization and optimal control,” *Mathematical Programming Computation*, vol. 11, pp. 1–36, 2019. <https://doi.org/10.1007/s12532-018-0139-4>
(Back reference pages: 4, 62, and 118)
- [38] U. Naumann, “Exact first and second derivatives by automatic differentiation,” *Proceedings in Applied Mathematics and Mechanics*, vol. 7, no. 1, pp. 1 140 205–1 140 206, 2008. <https://doi.org/10.1002/pamm.200700844>
(Back reference pages: 4, 62)
- [39] S. Awtar and K. C. Craig, “Electromagnetic Coupling in a dc Motor and Tachometer Assembly,” *Journal of Dynamic Systems, Measurement, and Control*, vol. 126, no. 3, pp. 684–691, 2004. <https://doi.org/10.1115/1.1789543>
(Back reference pages: 5, 125)
- [40] M. Tomizuka, “Zero Phase Error Tracking Algorithm for Digital Control,” *Journal of Dynamic Systems, Measurement and Control*, vol. 109, no. 1, pp. 65–68, 1987. <https://doi.org/10.1115/1.3143822>
(Back reference page: 5)
- [41] J. van Zundert, J. Bolder, S. Koekebakker, and T. Oomen, “Resource-efficient ILC for LTI/LTV systems through LQ tracking and stable inversion: Enabling large feedforward tasks on a position-dependent printer,” *Mechatronics*, vol. 38, pp. 76–90, 2016. <http://doi.org/10.1016/j.mechatronics.2016.07.001>
(Back reference page: 5)
- [42] G. Ferrari-Trecate, M. Muselli, D. Liberati, and M. Morari, “A clustering technique for the identification of piecewise affine systems,” *Automatica*, vol. 39, no. 2, pp. 205–217, 2003. [https://doi.org/10.1016/S0005-1098\(02\)00224-8](https://doi.org/10.1016/S0005-1098(02)00224-8)
(Back reference page: 6)
- [43] J. H. Bonsel, R. H. B. Fey, and H. Nijmeijer, “Application of a dynamic vibration absorber to a piecewise linear beam system,” *Nonlinear Dynamics*, vol. 37, no. 3, pp. 227–243, 2004. <https://doi.org/10.1023/B:NODY.0000044646.70030.31>
(Back reference page: 6)

- [44] D. Mignone, G. Ferrari-Trecate, and M. Morari, “Stability and stabilization of continuous piecewise affine and hybrid systems: An LMI approach,” in *Proceedings of the 39th IEEE Conference on Decision and Control*, vol. 1. Sydney: IEEE, 2000. <https://doi.org/10.1109/CDC.2000.912814>
(Back reference page: 6)
- [45] M. di Bernardo, U. Montanaro, and S. Santini, “Hybrid Model Reference Adaptive Control of Piecewise Affine Systems,” *IEEE Transactions on Automatic Control*, vol. 58, no. 2, pp. 304–316, 2013. <https://doi.org/10.1109/TAC.2012.2212516>
(Back reference pages: 6, 54)
- [46] N. van de Wouw and A. Pavlov, “Tracking and synchronisation for a class of PWA systems,” *Automatica*, vol. 44, no. 11, pp. 2909–2915, 2008. <http://doi.org/10.1016/j.automatica.2008.04.015>
(Back reference pages: 6, 93, and 128)
- [47] D. Totah, “Ankle-Foot Orthosis Stiffness: Biomechanical Effects, Measurement and Emulation,” Ph.D. dissertation, University of Michigan, 2020. <https://deepblue.lib.umich.edu/handle/2027.42/163219>
(Back reference pages: xiii, 8)
- [48] M. H. Fatehi, M. Eghtesad, and R. Amjadifard, “Modelling and control of an overhead crane system with a flexible cable and large swing angle,” *Journal of Low Frequency Noise Vibration and Active Control*, vol. 33, no. 4, pp. 395–410, 2014. <https://doi.org/10.1260/0263-0923.33.4.395>
(Back reference pages: xiii, 8)
- [49] M. I. Solihin, Wahyudi, and A. Legowo, “Fuzzy-tuned PID anti-swing control of automatic gantry crane,” *Journal of Vibration and Control*, vol. 16, no. 1, pp. 127–145, 2010. <https://doi.org/10.1177/1077546309103421>
(Back reference pages: xiii, 8)
- [50] H. Qi and J. Mazumder, “Numerical simulation of heat transfer and fluid flow in coaxial laser cladding process for direct metal deposition,” *Journal of Applied Physics*, vol. 100, pp. 024 903:1–11, 2006. <https://doi.org/10.1063/1.2209807>
(Back reference page: 9)
- [51] J. Gonzalez, J. Mireles, Y. Lin, and R. Wicker, “Characterization of ceramic components fabricated using binder jetting additive manufacturing technology,” *Ceramics International*, vol. 42, pp. 10 559–10 564, 2016. <https://doi.org/10.1016/j.ceramint.2016.03.079>
(Back reference page: 9)
- [52] M. Singh, H. Haverinen, P. Dhagat, and G. Jabbour, “Inkjet printing - process and its applications,” *Advanced Materials*, vol. 22, pp. 673–685, 2010. <https://doi.org/10.1002/adma.200901141>
(Back reference page: 9)

- [53] R. Piner, J. Zhu, F. Xu, S. Hong, and C. Mirkin, ““Dip-Pen” Nanolithography,” *Science*, vol. 283, pp. 661–663, 1999. <https://doi.org/10.1126/science.283.5402.661>
(Back reference page: 9)
- [54] C. Sun, N. Fang, D. Wu, and X. Zhang, “Projection micro-stereolithography using digital micro-mirror dynamic mask,” *Sensors and Actuators A*, vol. 121, pp. 113–120, 2005. <https://doi.org/10.1016/j.sna.2004.12.011>
(Back reference page: 9)
- [55] I. Gibson, D. Rosen, and B. Stucker, *Additive Manufacturing Technologies: 3D Printing, Rapid Prototyping, and Direct Digital Manufacturing*, 2nd ed. New York: Springer, 2015. <https://doi.org/10.1007/978-1-4939-2113-3>
(Back reference page: 10)
- [56] S. Lee, J. Kim, J. Choi, H. Park, J. Ha, Y. Kim, J. Rogers, and U. Paik, “Patterned oxide semiconductor by electrohydrodynamic jet printing for transparent thin film transistors,” *Applied Physics Letters*, vol. 100, pp. 102108:1–4, 2012. <https://doi.org/10.1063/1.3691177>
(Back reference page: 10)
- [57] K. Choi, M. Zubair, and H. Dang, “Characterization of flexible temperature sensor fabricated through drop-on-demand electrohydrodynamics patterning,” *Japanese Journal of Applied Physics*, vol. 53, pp. 05HB02:1–5, 2014. <https://doi.org/10.7567/JJAP.53.05HB02>
(Back reference page: 10)
- [58] M. Poellmann, K. Barton, S. Mishra, and A. W. Johnson, “Patterned hydrogel substrates for cell culture with electrohydrodynamic jet printing,” *Macromolecular Bioscience*, vol. 11, pp. 1164–1168, 2011. <https://doi.org/10.1002/mabi.201100004>
(Back reference page: 10)
- [59] Y. Han, C. Wei, and J. Dong, “Droplet formation and settlement of phase-change ink in high resolution electrohydrodynamic (EHD) 3D printing,” *Journal of Manufacturing Processes*, vol. 20, no. 3, pp. 485–491, 2015. <https://doi.org/10.1016/j.jmapro.2015.06.019>
(Back reference page: 10)
- [60] Y. Jang, I. Hartarto Tambunan, H. Tak, V. Dat Nguyen, T. Kang, and D. Byun, “Non-contact printing of high aspect ratio Ag electrodes for polycrystalline silicone solar cell with electrohydrodynamic jet printing,” *Applied Physics Letters*, vol. 102, no. 12, p. 123901, 2013. <https://doi.org/10.1063/1.4798332>
(Back reference page: 10)
- [61] J.-U. Park, M. Hardy, S. J. Kang, K. Barton, K. Adair, D. K. Mukhopadhyay, C. Y. Lee, M. S. Strano, A. G. Alleyne, J. G. Georgiadis, P. M. Ferreira, and J. A. Rogers, “High-resolution electrohydrodynamic jet printing,” *Nature Materials*, vol. 6, no. 10, pp. 782–789, 2007. <https://doi.org/10.1038/nmat1974>
(Back reference page: 10)

- [62] P. Sammons, S. Bollineni, R. Sibal, and K. Barton, “Temperature and Humidity Variation Effect on Process Behavior in Electrohydrodynamic Jet Printing of a Class of Optical Adhesives,” in *28th Annual International Solid Freeform Fabrication Symposium*. Austin, TX: University of Texas, Austin, 2017, pp. 1784–1794. <http://sffsymposium.engr.utexas.edu/sites/default/files/2017/Manuscripts/TemperatureandHumidityVariationEffectonProce.pdf> (Back reference page: 10)
- [63] Z. Afkhami, C. P. Pannier, L. Aarnoudse, D. Hoelzle, and K. Barton, “Spatial Iterative Learning Control for Multi-material Three-Dimensional Structures,” *ASME Letters in Dynamic Systems and Control*, vol. 1, no. 1, p. 011011, 2021. <https://doi.org/10.1115/1.4046576> (Back reference page: 10)
- [64] Z. Wang, C. P. Pannier, K. Barton, and D. J. Hoelzle, “Application of robust monotonically convergent spatial iterative learning control to microscale additive manufacturing,” *Mechatronics*, vol. 56, pp. 157–165, 2018. <https://doi.org/10.1016/j.mechatronics.2018.09.003> (Back reference page: 10)
- [65] B. Altin, Z. Wang, D. J. Hoelzle, and K. Barton, “Robust Monotonically Convergent Spatial Iterative Learning Control: Interval Systems Analysis via Discrete Fourier Transform,” *IEEE Transactions on Control Systems Technology*, vol. 27, no. 6, pp. 2470–2483, 2019. <https://doi.org/10.1109/TCST.2018.2868039> (Back reference page: 10)
- [66] F. J. Higuera, S. E. Ibáñez, A. J. Hijano, and I. G. Loscertales, “Pulsating emission of droplets from an electrified meniscus,” *Journal of Aerosol Science*, vol. 66, pp. 193–208, 2013. <http://doi.org/10.1016/j.jaerosci.2013.09.001> (Back reference page: 11)
- [67] W. Wei, Z. Gu, S. Wang, Y. Zhang, K. Lei, and K. Kase, “Numerical simulation of the cone-jet formation and current generation in electrostatic spray - modeling as regards to space charged droplet effect,” *Journal of Micromechanics and Microengineering*, vol. 23, pp. 015 004:1–11, 2013. <https://doi.org/10.1088/0960-1317/23/1/015004> (Back reference page: 11)
- [68] R. Collins, J. Jones, M. Harris, and O. Basaran, “Electrohydrodynamic tip streaming and emission of charged drops from liquid cones,” *Nature Physics*, vol. 4, pp. 149–154, 2008. <https://doi.org/10.1038/nphys807> (Back reference page: 11)
- [69] C. P. Pannier, M. Diagne, I. A. Spiegel, D. J. Hoelzle, and K. Barton, “A dynamic model of drop spreading in electrohydrodynamic jet printing,” *Journal of Manufacturing Science and Engineering*, vol. 139, pp. 111 008:1–6, 2017. <https://doi.org/10.1115/1.4037436> (Back reference pages: 11, 28, and 29)

- [70] W. Carter, G. C. Popell, J. Samuel, and S. Mishra, “A Fundamental Study and Modeling of the Micro-Droplet Formation Process in Near-Field Electrohydrodynamic Jet Printing,” *Journal of Micro and Nano-Manufacturing*, vol. 2, no. 2, p. 021005, 2014. <https://doi.org/10.1115/1.4027099>
(Back reference page: 11)
- [71] H. Choi, J.-U. Park, O. Park, P. Ferreira, J. Georgiadis, and J. Rogers, “Scaling laws for jet pulsations associated with high-resolution electrohydrodynamic printing,” *Applied Physics Letters*, vol. 92, pp. 123 109:1–3, 2008. <https://doi.org/10.1063/1.2903700>
(Back reference page: 11)
- [72] R. Collins, K. Sambath, M. Harris, and O. Basaran, “Universal scaling laws for the disintegration of electrified drops,” *Proceedings of the National Academy of Sciences*, vol. 110, pp. 4905–4910, 2013. <https://doi.org/10.1073/pnas.1213708110>
(Back reference page: 11)
- [73] C. Chen, D. Saville, and I. Aksay, “Scaling laws for pulsed electrohydrodynamic drop formation,” *Applied Physics Letters*, vol. 89, pp. 124 103:1–3, 2006. <https://doi.org/10.1063/1.2356891>
(Back reference page: 11)
- [74] L. Larrondo and R. S. J. Manley, “Electrostatic fiber spinning from polymer melts. III. Electrostatic deformation of a pendant drop of polymer melt,” *Journal of Polymer Science: Polymer Physics Edition*, vol. 19, no. 6, pp. 933–940, 1981. <https://doi.org/10.1002/pol.1981.180190603>
(Back reference page: 18)
- [75] G. Joffre, B. Prunet-Foch, S. Berthomme, and M. Cloupeau, “Deformation of liquid menisci under the action of an electric field,” *Journal of Electrostatics*, vol. 13, no. 2, pp. 151–165, 1982. [https://doi.org/10.1016/0304-3886\(82\)90005-5](https://doi.org/10.1016/0304-3886(82)90005-5)
(Back reference page: 18)
- [76] M. T. Harris and O. A. Basaran, “Capillary Electrohydrodynamics of Conducting Drops Hanging From Nozzle in Electric Field,” *Journal of Colloid and Interface Science*, vol. 161, no. 2, pp. 389–413, 1993. <https://doi.org/10.1006/jcis.1993.1482>
(Back reference page: 18)
- [77] G. S. Wright, P. T. Krein, and J. C. Chato, “Factors affecting dynamic electrical manipulation of menisci,” *IEEE Transactions on Industry Applications*, vol. 29, no. 1, pp. 103–112, 1993. <https://doi.org/10.1109/28.195895>
(Back reference page: 18)
- [78] J. Yang, H. Kim, B. Cho, and J. Chung, “Modeling of sessile droplet oscillation on electrohydrodynamic jetting nozzle at constant back pressure,” *Journal of Mechanical Science and Technology*, vol. 28, no. 7, pp. 2815–2823, 2014. <https://doi.org/10.1007/s12206-014-0635-z>
(Back reference page: 18)

- [79] J. F. Calero, J. C. Chato, P. T. Krein, J. M. Crowley, and G. S. Wright, “The Electrohydrostatics of A Conductive Liquid Meniscus,” in *Conference Record of the 1988 IEEE Industry Applications Society Annual Meeting*, 1988, pp. 1547–1551. <https://doi.org/10.1109/IAS.1988.25262>
(Back reference page: 18)
- [80] H. H. Woodson and J. R. Melcher, *Electromechanical Dynamics v.2: Fields, Forces, and Motion*. New York: John Wiley and Sons, Inc., 1968. https://ocw.mit.edu/ans7870/resources/woodson/textbook/emd_part2.pdf
(Back reference page: 18)
- [81] K. L. Kaiser, “Maximum Electric Field and Breakdown Table,” in *Electromagnetic Compatibility Handbook*. Boca Raton: CRC Press, 2004, ch. 10.16, pp. 10–51 to 10–53.
(Back reference page: 20)
- [82] A. L. Yarin, S. Koombhongse, and D. H. Reneker, “Taylor Cone and Jetting from Liquid Droplets in Electrospinning of Nanofibers,” *Journal of Applied Physics*, vol. 90, no. 9, pp. 4836–4846, 2001. <https://doi.org/10.1115/DSCC2015-9995>
(Back reference pages: 24, 26)
- [83] C. Pannier, Z. Wang, D. Hoelzle, and K. Barton, “A model of liquid drop spreading for electrohydrodynamic jet printing,” in *Proceedings of the ASME 2015 Dynamic Systems and Control Conference*, 2015, p. 9995. <https://doi.org/10.1115/DSCC2015-9995>
(Back reference page: 28)
- [84] Norland Products Incorporated, “Norland Optical Adhesive 81 Technical Data Sheet.” <http://www.norlandprod.com/literature/81tds.pdf>
(Back reference page: 28)
- [85] J. Plott, X. Tian, and A. Shih, “Measurement and Modeling of Forces in Extrusion-Based Additive Manufacturing of Flexible Silicone Elastomer with Thin Wall Structures,” *Journal of Manufacturing Science and Engineering, Transactions of the ASME*, vol. 140, no. 9, pp. 1–11, 2018. <https://doi.org/10.1115/1.4040350>
(Back reference pages: 53, 126)
- [86] J. Zhao and D. J. Hill, “On stability, L_2 -gain and H_∞ control for switched systems,” *Automatica*, vol. 44, no. 5, pp. 1220–1232, 2008. <https://doi.org/10.1016/j.automatica.2007.10.011>
(Back reference page: 54)
- [87] N. van de Wouw, A. V. Pavlov, K. Y. Pettersen, and H. Nijmeijer, “Output Tracking Control of PWA Systems,” in *Proceedings of the 45th IEEE Conference on Decision and Control*. San Diego, CA, USA: IEEE, 2006, pp. 2637–2642. <https://doi.org/10.1109/CDC.2006.377028>
(Back reference page: 54)

- [88] L. O. Chua and S. M. Kang, "Section-Wise Piecewise-Linear Functions: Canonical Representation, Properties, and Applications," *Proceedings of the IEEE*, vol. 65, no. 6, pp. 915–929, 1977. <https://doi.org/10.1109/PROC.1977.10589>
(Back reference pages: 54, 55)
- [89] A. Bemporad and M. Morari, "Control of systems integrating logic, dynamics, and constraints," *Automatica*, vol. 35, no. 3, pp. 407–427, 1999. [https://doi.org/10.1016/S0005-1098\(98\)00178-2](https://doi.org/10.1016/S0005-1098(98)00178-2)
(Back reference page: 55)
- [90] E. Chicurel-Uziel, "Exact, single equation, closed-form solution of vibrating systems with piecewise linear springs," *Journal of Sound and Vibration*, vol. 245, no. 2, pp. 285–301, 2001. <https://doi.org/10.1006/jsvi.2001.3568>
(Back reference page: 56)
- [91] M. Donà, A. Palmeri, and M. Lombardo, "Exact closed-form solutions for the static analysis of multi-cracked gradient-elastic beams in bending," *International Journal of Solids and Structures*, vol. 51, no. 15-16, pp. 2744–2753, 2014. <https://doi.org/10.1016/j.ijsolstr.2014.02.020>
(Back reference page: 56)
- [92] R. B. Hetnarski and J. Ignaczak, "Generalized Thermoelasticity: Closed-Form Solutions," *Journal of Thermal Stresses*, vol. 16, no. 4, pp. 473–498, 1993. <https://doi.org/10.1080/01495739308946241>
(Back reference page: 56)
- [93] J. Kim, L. Li, S. Wu, H. Wang, Y. Takita, H. Takeuchi, K. Araki, J. Fan, and J. L. Drewniak, "Closed-form expressions for the maximum transient noise voltage caused by an ic switching current on a power distribution network," *IEEE Transactions on Electromagnetic Compatibility*, vol. 54, no. 5, pp. 1112–1124, 2012. <https://doi.org/10.1109/TEMC.2012.2194786>
(Back reference page: 56)
- [94] M. Ochmann, "Closed form solutions for the acoustical impulse response over a masslike or an absorbing plane," *The Journal of the Acoustical Society of America*, vol. 129, no. 6, pp. 3502–3512, 2011. <https://doi.org/10.1121/1.3570947>
(Back reference page: 56)
- [95] A. Bhattacharyya, J. K. Schueller, B. P. Mann, J. C. Ziegert, T. L. Schmitz, F. J. Taylor, and N. G. Fitz-Coy, "A closed form mechanistic cutting force model for helical peripheral milling of ductile metallic alloys," *International Journal of Machine Tools and Manufacture*, vol. 50, no. 6, pp. 538–551, 2010. <http://doi.org/10.1016/j.ijmachtools.2010.03.003>
(Back reference page: 56)
- [96] B. F. Peng and J. P. Conte, "Closed-form solutions for the response of linear systems to fully nonstationary earthquake excitation," *Journal of Engineering Mechanics*, vol. 124, no. 6, pp. 684–693, 1998. [https://doi.org/10.1061/\(ASCE\)0733-9399\(1998\)124:6\(684\)](https://doi.org/10.1061/(ASCE)0733-9399(1998)124:6(684))
(Back reference page: 56)

- [97] M. Sun and D. Wang, “Analysis of Nonlinear Discrete-Time Systems with Higher-Order Iterative Learning Control,” *Dynamics and Control*, vol. 11, no. 1, pp. 81–96, 2001. <https://doi.org/10.1023/A:1017912319985>
(Back reference page: 59)
- [98] C. T. Freeman, “Newton-method based iterative learning control for robot-assisted rehabilitation using FES,” *Mechatronics*, vol. 24, no. 8, pp. 934–943, 2014. <http://doi.org/10.1016/j.mechatronics.2014.04.001>
(Back reference page: 62)
- [99] S. Devasia, D. Chen, and B. Paden, “Nonlinear inversion-based output tracking,” *IEEE Transactions on Automatic Control*, vol. 41, no. 7, pp. 930–942, 1996. <https://doi.org/10.1109/9.508898>
(Back reference pages: 71, 77, 78, and 79)
- [100] S. Devasia and B. Paden, “Stable Inversion For Nonlinear Nonminimum-phase Time-varying Systems,” *IEEE Transactions on Automatic Control*, vol. 43, no. 2, pp. 283–288, 1998. <http://doi.org/10.1109/9.661082>
(Back reference pages: 71, 77)
- [101] G. Zeng and L. R. Hunt, “Stable inversion for nonlinear discrete-time systems,” *IEEE Transactions on Automatic Control*, vol. 45, no. 6, pp. 1216–1220, 2000. <http://doi.org/10.1109/9.863610>
(Back reference pages: 71, 72, 77, 78, 79, and 81)
- [102] J. J. A. Eksteen and P. S. Heyns, “Improvements in stable inversion of NARX models by using Mann iteration,” *Inverse Problems in Science and Engineering*, vol. 24, no. 4, pp. 667–691, 2016. <http://doi.org/10.1080/17415977.2015.1055262>
(Back reference page: 73)
- [103] D. A. Belsley, E. Kuh, and R. E. Welsch, *Regression Diagnostics: Identifying Influential Data and Sources of Collinearity*. Hoboken, NJ: John Wiley & Sons, Inc., 1980. <https://doi.org/10.1002/0471725153>
(Back reference page: 75)
- [104] S. M. Rump, “Inversion of extremely ill-conditioned matrices in floating-point,” *Japan Journal of Industrial and Applied Mathematics*, vol. 26, no. 2-3, pp. 249–277, 2009. <https://doi.org/10.1007/BF03186534>
(Back reference page: 75)
- [105] B. Chu and D. Owens, “Singular Value distribution of non-minimum phase systems with application to iterative learning control,” in *Proceedings of the 52nd IEEE Conference on Decision and Control*. Florence: IEEE, 2013, pp. 6700–6705. <https://doi.org/10.1109/CDC.2013.6760950>
(Back reference page: 75)

- [106] K. L. Moore, *Iterative Learning Control for Deterministic Systems*. London: Springer-Verlag, 1993. <https://doi.org/10.1007/978-1-4471-1912-8>
(Back reference page: 75)
- [107] M. Norrlöf and S. Gunnarsson, “Time and frequency domain convergence properties in iterative learning control,” *International Journal of Control*, vol. 75, no. 14, pp. 1114–1126, 2002. <https://doi.org/10.1080/00207170210159122>
(Back reference page: 75)
- [108] B. G. Dijkstra, “Iterative Learning Control with Application to a Wafer Stage,” Ph.D. dissertation, Delft University of Technology, 2004. <http://resolver.tudelft.nl/uuid:b29a7fa2-6bee-4b59-8aaf-b7b016e1eeba>
(Back reference page: 75)
- [109] J. H. Lee, K. S. Lee, and W. C. Kim, “Model-based iterative learning control with a quadratic criterion for time-varying linear systems,” *Automatica*, vol. 36, no. 5, pp. 641–657, 2000. [https://doi.org/10.1016/S0005-1098\(99\)00194-6](https://doi.org/10.1016/S0005-1098(99)00194-6)
(Back reference page: 75)
- [110] R. P. Agarwal, *Difference Equations and Inequalities: Theory, Methods, and Applications*, 2nd ed., E. J. Taft and Z. Nashed, Eds. New York: Marcel Dekker, Inc., 2000. <https://doi.org/10.1201/9781420027020>
(Back reference page: 77)
- [111] D. H. Owens, J. J. Hatonen, and S. Daley, “Robust monotone gradient-based discrete-time iterative learning control,” *International Journal of Robust and Nonlinear Control*, vol. 19, pp. 634–661, 2009. <https://doi.org/10.1002/rnc.1338>
(Back reference page: 84)
- [112] E. D. Sontag, “Nonlinear Regulation: The Piecewise Linear Approach,” *Transactions on Automatic Control*, vol. 26, no. 2, pp. 346–358, 1981. <https://doi.org/10.1109/TAC.1981.1102596>
(Back reference page: 93)
- [113] —, “Remarks on piecewise-linear algebra,” *Pacific Journal of Mathematics*, vol. 98, no. 1, pp. 183–201, 1982. <https://doi.org/10.2140/pjm.1982.98.183>
(Back reference page: 93)
- [114] Y. Gao, Z. Liu, and H. Chen, “Robust H_∞ control for constrained discrete-time piecewise affine systems with time-varying parametric uncertainties,” *IET Control Theory and Applications*, vol. 3, no. 8, pp. 1132–1144, 2009. <https://doi.org/10.1049/iet-cta.2008.0182>
(Back reference page: 94)
- [115] G. Chen and Y. Yang, “Stability analysis of discrete-time switched linear time-varying systems based on function-dependent LMIs,” *IEEE Access*, vol. 8, pp. 19 221–19 229, 2020. <https://doi.org/10.1109/ACCESS.2020.2968636>
(Back reference page: 108)

- [116] S. V. Raković, E. C. Kerrigan, D. Q. Mayne, and J. Lygeros, “Reachability analysis of discrete-time systems with disturbances,” *IEEE Transactions on Automatic Control*, vol. 51, no. 4, pp. 546–561, 2006. <https://doi.org/10.1109/TAC.2006.872835>
(Back reference pages: 109, 110, and 111)
- [117] A. Bemporad, G. Ferrari-Trecate, and M. Morari, “Observability and controllability of piecewise affine and hybrid systems,” *IEEE Transactions on Automatic Control*, vol. 45, no. 10, pp. 1864–1876, 2000. <https://doi.org/10.1109/TAC.2000.880987>
(Back reference page: 111)
- [118] J. D. Ratcliffe, J. J. Hätönen, P. L. Lewin, E. Rogers, T. J. Harte, and D. H. Owens, “P-type iterative learning control for systems that contain resonance,” *International Journal of Adaptive Control and Signal Processing*, vol. 19, no. 10, pp. 769–796, 2005. <https://doi.org/10.1002/acs.878>
(Back reference page: 119)
- [119] E. C. Balta, D. M. Tilbury, and K. Barton, “A digital twin framework for performance monitoring and anomaly detection in fused deposition modeling,” in *IEEE International Conference on Automation Science and Engineering*. IEEE, 2019, pp. 823–829. <https://doi.org/10.1109/COASE.2019.8843166>
(Back reference page: 126)
- [120] C. T. Freeman and Y. Tan, “Iterative Learning Control With Mixed Constraints for Point-to-Point Tracking,” *IEEE Transactions on Control Systems Technology*, vol. 21, no. 3, pp. 604–616, may 2013. <https://doi.org/10.1109/TCST.2012.2187787>
(Back reference page: 128)
- [121] N. Strijbosch, I. Spiegel, K. Barton, and T. Oomen, “Monotonically Convergent Iterative Learning Control for Piecewise Affine Systems,” in *21st IFAC World Congress*. Berlin: IFAC, 2020. <http://www.dct.tue.nl/toomen/files/StrijboschSpiBarOom2020.pdf>
(Back reference page: 129)